

An Experimental and Phenomenological Dissection of Beauty-Quark Decays into Light Leptons

Dissertation

zur

Erlangung der naturwissenschaftlichen Doktorwürde
(Dr. sc. nat.)

vorgelegt der

Mathematisch-naturwissenschaftlichen Fakultät

der

Universität Zürich

von

Davide Lancierini

aus

Italien

Promotionskommission

Prof. Dr. Nicola Serra (Vorsitz)

Prof. Dr. Gino Isidori

Prof. Dr. Laura Baudis

Dr. Patrick Owen

Zürich, 2023

Abstract

The Standard Model of particle physics represents the status of the art of our understanding of Nature at the tiniest scales. It was conceived in the first half of the twentieth century and consolidated during the following years in a fascinating interplay between experimental evidences and their interpretation in a rigorous theoretical framework, which in turn allowed for conjecturing new predictions that would then receive further experimental testing. This virtuous circle culminated with the confirmation of the Spontaneous Symmetry Breaking mechanism, which was hypothesised in the early sixties but received experimental confirmation through the discovery of the Higgs particle ten years ago. Despite its success in explaining phenomena ranging from subnuclear to atomic scales, several open theoretical questions and compelling experimental observations indicate the Standard Model is the low energy limit of a wider picture that contains it. Therefore, searches for extensions of the Standard Model are conducted at the Large Hadron Collider where particle physics experiments look for signatures of New Physics, and in particular, LHCb is specialised in precision measurements of observables that search for such signatures using an indirect approach. These searches can be performed by testing an approximate symmetry of the Standard Model known as Lepton Flavour Universality, which predicts that processes involving different lepton species are distinguished only by mass related effects, and hence precisely calculable within the Standard Model. In this thesis, the measurement of R_K , a Lepton Flavour Universality probe that compares rates of $b \rightarrow s\ell^+\ell^-$ transitions to different light leptons species, is presented, using the full dataset of pp collisions collected at LHCb. Moreover we provide a verification of the correct modelling of radiative effects in $b \rightarrow s\ell^+\ell^-$ decays to light leptons, which constitute a source of Lepton Flavour Universality violation within the Standard Model. Finally we provide a general method to interpret the global significance of Flavour Anomalies within the Standard Model Effective Theory framework. Not only this method allows for the determination of the global significance in a conservative way, as far as the long-distance charm-loop effects are concerned, but also it allows to incorporate present and future measurements for which the form factors are not yet calculated.

Table of contents

List of figures	ix
List of tables	xvii
1 Introduction	1
1.1 History of the Standard Model	2
1.1.1 A new player in the game	2
1.1.2 Objects in the mirror don't look as you'd expect	3
1.1.3 A heavier sibling of the electron	5
1.1.4 The "strange" path to new fundamental particles	7
1.1.5 Symmetry as a guiding principle	10
1.1.6 A "massive" problem	12
1.1.7 The colour and flavour of particle physics	13
1.1.8 Yet another symmetry is questioned	15
1.1.9 A third heavier family	16
1.2 The Standard Model	19
1.2.1 The electroweak sector	19
1.2.1.1 Assigning particles to representations of $SU(2)_L \times U(1)_Y$	19
1.2.1.2 Electroweak unification	21
1.2.2 Spontaneous symmetry breaking	25
1.2.3 Fermion mass generation and the flavour sector	29
1.2.3.1 The CKM matrix	30
1.2.3.2 Lepton masses	31
1.3 Beyond the Standard Model	34
1.3.1 Unanswered questions in the Standard Model	34
1.3.2 The Standard Model as a low energy effective theory	37
1.3.2.1 A systematic approach to identifying the New Physics structure	37

1.3.2.2	$b \rightarrow s\ell^+\ell^-$ transitions	38
1.3.2.3	Sandwiching the currents	40
1.4	The Large Hadron Collider	42
1.4.1	The LHCb experiment at the LHC	43
1.4.1.1	Tracking system	45
1.4.1.2	Particle identification	48
1.4.1.3	Calorimeters	50
1.4.1.4	The muon system	51
1.4.1.5	The trigger system	52
1.4.2	Overview of latest $b \rightarrow s\ell^+\ell^-$ results	53
1.4.2.1	Differential semi-leptonic branching fractions	53
1.4.2.2	Angular observables	55
1.4.2.3	Purely leptonic branching fractions	57
1.4.2.4	Ratios of branching fractions	59
1.5	Personal contributions	61
	References	63
	Appendix 1.A Appendix to Chapter 1	75
1.A.1	The optical theorem	75
1.A.2	Applications of the optical theorem	77
1.A.2.1	Decay widths and unstable particles	77
1.A.2.2	Unitarity bound	78
1.A.3	General facts about $SU(N)$	81
1.A.4	Symmetries and interactions	83
1.A.4.1	<i>global</i> vs. <i>local</i> gauge invariance	83
1.A.4.2	Non-abelian (Yang-Mills) gauge theories	85
2	QED in $\bar{B} \rightarrow \bar{K}\ell^+\ell^-$ LFU ratios:	
	Theory versus Experiment, a Monte Carlo Study	89
2.1	Introduction	89
2.2	Monte Carlo Framework	92
2.2.1	Generalities	92
2.2.2	Basic strategy of the Monte Carlo approach	93
2.2.3	Numerical procedure	94
	2.2.3.0.1	95
2.3	Direct Comparison with PHOTOS at the Short Distance Level	96
2.3.1	Parameterisation of the short distance amplitude	96

2.3.2	Comparison of our Monte Carlo with PHOTOS	96
2.4	Adding Long Distance (Charmonium Resonances)	100
2.4.1	Parameterisation of the charm amplitude	101
2.4.2	Study of the J/Ψ -resonance interference term in our Monte Carlo	102
2.4.3	J/Ψ and $\Psi(2S)$, including the resonant mode via a semi-analytic approach	105
2.5	Outlook and Conclusions	109
References		111
Appendix 2.A	Appendix to Chapter 2	114
2.A.1	Kinematics	114
2.A.2	More Detail on the Charm Parameterisation	115
2.A.3	Supplementary plots	117
2.A.4	Values of f^{th} used in the Monte Carlo Simulations	117
3	Test of lepton flavour universality in beauty quark-decays	121
3.0.1	Experimental setup	131
3.0.2	Analysis description	132
3.0.2.1	Event selection	132
3.0.2.2	Multivariate selection	134
3.0.2.3	Calibration of simulation	135
3.0.2.4	Likelihood fit	136
3.0.2.5	Additional cross-checks	141
3.0.2.6	Systematic uncertainties	141
References		145
Appendix 3.A	Appendix to Chapter 3	159
Appendix 3.B	Branching fraction measurements	159
Appendix 3.C	Fits to the $B^+ \rightarrow \psi(2S)K^+$ resonant mode	160
Appendix 3.D	Effect of q^2 migration	162
Appendix 3.E	Overview of R_K measurements	164
4	On the significance of new physics in $b \rightarrow s\ell^+\ell^-$ decays	167
4.1	Introduction	167
4.2	Effective Lagrangian and selection of the observables	169
4.3	Statistical Method	172
4.4	Results	174
4.5	Conclusion and discussion	175

References	179
5 A general effective field theory description of $b \rightarrow s\ell^+\ell^-$ lepton universality ratios	187
5.1 Introduction	187
5.2 General expression of R_X in terms of Wilson coefficients	189
5.2.0.0.1 Numerical estimate of the $\langle\eta_X^i\rangle$	192
5.2.0.0.2 Impact of four-fermion operators.	193
5.3 Global combination of current measurements	195
5.4 Impact of future measurements	197
5.5 Conclusions	199
References	203

List of figures

1.1	Schematic diagram for the $e\nu_e \rightarrow \mu\nu_\mu$ process in the Fermi theory . . .	6
1.2	Fundamental, anti-fundamental and adjoint representations of $SU(3)_F$ for the u, d, s baryon octet, also known as "The Eightfold Way"	9
1.3	Schematic view of the Aharonov-Bohm "Gedankenexperiment": two electron beams originating from the same source are collected on a screen on the opposite side of a solenoid. The magnetic field inside the solenoid is screened inside the solenoid.	11
1.4	Schematic view of the wave function shift induced by the field A_μ , responsible for the Aharonov-Bohm effect	11
1.5	Schematic view of the accelerator complex at CERN [99]	42
1.6	Angular (left) and rapidity (right) correlation between two heavy quarks in $Q\bar{Q}$ production [104], simulated using PYTHIA8 and the CTEQ6 NLO parton distribution functions.	43
1.7	Side view of the LHCb detector [103], the beam is aligned with the z axis	44
1.8	Geometry of the VELO r and ϕ sensors. For the ϕ sensor, strips belonging to two adjacent modules are represented in order to show the stereo angle [103]	46
1.9	Layout of one TT (left) and of the four TT layers (right) [103]	47
1.10	Perspective view of the magnet, with dimensions in millimeters (left) and measured on-axis magnetic field, for both "up" and "down" polarities (right)	47
1.11	Side view schematic layout of RICH-I (left) and RICH-II (right) detectors [103].	49
1.12	Left: reconstructed Cherenkov angle for isolated tracks as a function of their momentum; the Cherenkov bands for μ, π, K are clearly visible. Right: Same quantity as obtained from simulation, for different particles and radiators.	49

1.13	Left: side view of the LHCb Muon Detector [103]. Right: geometry of a quadrant, with each rectangle representing a chamber. [103]	51
1.14	Differential branching ratios $d\Gamma/q^2$ of $B^+ \rightarrow K^+\mu^+\mu^-$ (top left) $B^+ \rightarrow K^{*+}\mu^+\mu^-$ (top right) and $B_s^0 \rightarrow \phi\mu^+\mu^-$ (bottom). A deficit with respect to the SM prediction in the intermediate q^2 region is observed for all modes, however the large theory error bands don't allow to draw unambiguous conclusions.	54
1.15	Comparisons of the measured $d\Gamma/dq^2$ for $\Lambda_b^0 \rightarrow \Lambda\mu^+\mu^-$ decays with respect to theoretical predictions that use different assumptions in the derivation of the form factors. Relaxing the static b hypothesis (right) reduces the tension with the SM prediction.	55
1.16	Comparison of measurements of P'_5 in bins of q^2 as obtained from ATLAS, Belle, CMS and Run I LHCb data [120] (top left) and using data collected during Run I and 2016 [121] (top right). Measurements of P'_5 (bottom left) using $B^+ \rightarrow K^{*+}\mu^+\mu^-$ decays [122] and F_L (bottom right) using $B_s^0 \rightarrow \phi\mu^+\mu^-$ decays [124], in bins of q^2 , using Run I + Run II datasets collected at LHCb.	57
1.17	Contour plots for ATLAS [129], CMS [130] and LHCb [131] combined measurements (top left) and CMS measurement [132] (top right) of time-integrated and CP -averaged $B_s \rightarrow \mu^+\mu^-$ and prompt $B_d \rightarrow \mu^+\mu^-$ branching fractions. The plots in the bottom row show the comparisons of the latest CMS measurements with the previous ones of the same quantities.	58
1.18	Measurements of LFU universality probes using different hadronic systems, all connected by $b \rightarrow s\ell^+\ell^-$ transitions comparing muons to electron decay rates. For each plot, the corresponding channel is indicated below.	60
1.19	Decomposition of the full elastic scattering amplitude as sum of powers of 1PI transition amplitudes. This is resummed as a geometric series leading to the propagator term in Eq. (1.113)	77
1.20	Argand diagram for the partial wave decomposition coefficients $a_j(s)$. The area delimited by the circumference is the one allowed by the optical theorem	80

2.1	Differential distributions in q_0^2 for the short distance transition only: NLO over LO for muons in blue (top left) and for electrons in red (top right) in our MC, with appropriate cuts as in Tab. 2.1. The normalisation of these upper plots is arbitrary (cf. main text). The double ratios of our MC versus the PHOTOS framework, shown in the middle and bottom plots, are free of ambiguities.	97
2.2	Differential distributions in q^2 for the short distance transition only: The notation is the same as in Fig. 2.1.	98
2.3	Double ratio of the q^2 -spectrum, with and without the inclusion of interference effects induced by the J/Ψ -resonance, for electron and muons, using the respective reference m_B^{rec} cuts in Tab. 2.1. For numerical stability we use $m_e \rightarrow 10m_e$ (as indicated by the darker shade in red). The phase of the J/Ψ amplitude, relative to the SD term, is set to $\delta_{J/\Psi} = 1.47$	103
2.4	Same plots as in Fig. 2.3 with the relative phase of the J/Ψ amplitude set to $\delta_{J/\Psi} = 0$	104
2.5	Plots with the resonant mode cut out (cf. main text for explanation). For $q^2 < 6 \text{ GeV}^2$ the interference effects are small, even in the electron case (confirming the plot in Fig. 2.4), and do not indicate any contamination to R_K in particular. The corresponding plot without the LO normalisation can be found in App. 2.A.3 in Fig. 2.8.	106
2.6	Same plots as in Fig. 2.5 including resonant modes: (left) for electrons and (right) for muons respectively. It is noted that at $q^2 = 6 \text{ GeV}^2$, the effect is noticeable for electrons and care has to be taken (cf. main text). For the electrons, the plot ends at $q^2 = 6 \text{ GeV}^2$ since beyond this value the effects are too large (at $q^2 = (7, 8) \text{ GeV}^2$ we find, approximately, (6.5, 40) and (8.4, 73) for +charm and -charm respectively). We have checked that resummation slightly tames the effect but qualitatively, it remains the same. The muon plot looks deceptively similar to the one in Fig. 2.5 for $q^2 < 8 \text{ GeV}^2$ but differences arise thereafter. The corresponding plot without the LO normalisation can be found in App. 2.A.3 in Fig. 2.9.	107

-
- 2.7 Short distance (form factor) plots, in the $\cos \theta_\ell$ -variable, NLO over LO for muons in blue (top left) and for electrons in red (top right) in our MC, with appropriate cuts as in Tab. 2.1. The normalisation of these plots is not meaningful (cf. main text). However, double ratios, shown in the middle and bottom, of our Monte Carlo versus the PHOTOS framework are free of ambiguities. 118
- 2.8 Same plots as in Fig. 2.5 without LO-normalisation. 119
- 2.9 Same plots as in Fig. 2.6 without LO-normalisation. 119
- 3.1 Contributions to $B^+ \rightarrow K^+ \ell^+ \ell^-$ decays in the SM and possible new physics models. A B^+ meson, consisting of \bar{b} and u quarks, decays into a K^+ , containing \bar{s} and u quarks, and two charged leptons, $\ell^+ \ell^-$. (Left) The SM contribution involves the electroweak bosons γ , W^+ and Z^0 , and the up-type quarks \bar{u} , \bar{c} and \bar{t} . (Right) A possible new physics contribution to the decay with a hypothetical leptoquark (LQ) which, unlike the electroweak bosons, could have different interaction strengths with the different types of leptons. 122
- 3.2 Candidate invariant mass distributions. Distribution of the invariant mass $m_{(J/\psi)}(K^+ \ell^+ \ell^-)$ for candidates with (left) electron and (right) muon pairs in the final state for the (top) nonresonant $B^+ \rightarrow K^+ \ell^+ \ell^-$ signal channels and (bottom) resonant $B^+ \rightarrow J/\psi (\rightarrow \ell^+ \ell^-) K^+$ decays. The fit projection is superimposed, with dotted lines describing the signal contribution and solid areas representing each of the background components described in the text and listed in the legend. In the resonant-mode distributions, some fit components are too small to be visible. 126
- 3.3 Differential $r_{J/\psi}$ measurement. The distributions of (left) the B^+ transverse momentum, p_T , and (right) the ratio $r_{J/\psi}$ relative to its average value $\langle r_{J/\psi} \rangle$ as a function of p_T . The p_T spectrum of the $B^+ \rightarrow J/\psi K^+$ decays is similar to that of the corresponding $B^+ \rightarrow K^+ \ell^+ \ell^-$ decays such that the measurement of $r_{J/\psi}$ tests the kinematic region relevant for the R_K measurement. The lack of any dependence of the value of $r_{J/\psi} / \langle r_{J/\psi} \rangle$ as a function of $B^+ p_T$ demonstrates control of the efficiencies. Uncertainties on the data points are statistical only. 128

-
- 3.4 Comparison between R_K measurements. In addition to the LHCb result, the measurements by the BaBar [15] and Belle [13] collaborations, which combine $B^+ \rightarrow K^+ \ell^+ \ell^-$ and $B^0 \rightarrow K_S^0 \ell^+ \ell^-$ decays, are also shown. The vertical dashed line indicates the SM prediction. 130
- 3.5 Simulated $K^+ e^-$ mass distributions for signal and various cascade background samples. The signal is represented by the orange shaded region and the various cascade background contributions by red, dark blue and light blue shaded regions. The distributions are all normalised to unity. (Left, with log y -scale) the bremsstrahlung correction to the momentum of the electron is applied, resulting in a tail to the right. The region to the left of the vertical dashed line is rejected. (Right, with linear y -scale) the mass is computed only from the track information. The notation $\pi_{[\rightarrow e^-]}^-$ ($e_{[\rightarrow \pi^-]}^-$) is used to denote an pion (electron) that is reconstructed as an electron (pion). The region between the dashed vertical lines is rejected. 134
- 3.6 Candidate invariant mass distributions. Distribution of the invariant mass $m(K^+ \ell^+ \ell^-)$ for nonresonant candidates in the (left) sample previously analysed [11] and (right) the new data sample. The top row shows the fit to the muon modes and the subsequent rows the fits to the electron modes triggered by (second row) one of the electrons, (third row) the kaon and (last row) by other particles in the event. The fit projections are superimposed, with dotted lines describing the signal contribution and solid areas representing each of the background components described in the text and listed in the legend. 138
- 3.7 Candidate invariant mass distributions. Distribution of the invariant mass $m_{J/\psi}(K^+ \ell^+ \ell^-)$ for resonant candidates in the (left) sample previously analysed [11] and (right) the new data sample. The top row shows the fit to the muon modes and the subsequent rows the fits to the electron modes triggered by (second row) one of the electrons, (third row) the kaon and (last row) by other particles in the event. The fit projections are superimposed, with dotted lines describing the signal contribution and solid areas representing each of the background components described in the text and listed in the legend. 139

- 3.8 Likelihood function from the fit to the nonresonant $B^+ \rightarrow K^+\ell^+\ell^-$ candidates in terms of the ratio between the likelihood value (L) and that found by the fit (L_{\max}) as a function of R_K . The extent of the dark, medium and light blue regions shows the values allowed for R_K at 1σ , 3σ and 5σ levels. The red line indicates the prediction from the SM. 140
- 3.9 Differential $r_{J/\psi}$ measurement. (Top) distributions of the reconstructed spectra of (left) the angle between the leptons, $\alpha(\ell^+, \ell^-)$, and (right) the minimum p_T of the leptons for $B^+ \rightarrow K^+\ell^+\ell^-$ and $B^+ \rightarrow J/\psi(\rightarrow \ell^+\ell^-)K^+$ decays. (Bottom) the single ratio $r_{J/\psi}$ relative to its average value $\langle r_{J/\psi} \rangle$ as a function of these variables. In the electron minimum p_T spectra, the structure at 2800 MeV/c is related to the trigger threshold. Uncertainties on the data points are statistical only. 142
- 3.10 Double differential $r_{J/\psi}$ measurement. (Left) the value of $r_{J/\psi}$, relative to the average value of $r_{J/\psi}$, measured in two-dimensional bins of the maximum lepton momentum, $p(\ell)$, and the opening angle between the two leptons, $\alpha(\ell^+, \ell^-)$. (Right) the bin definition in this two-dimensional space together with the distribution for $B^+ \rightarrow K^+e^+e^-$ ($B^+ \rightarrow J/\psi(\rightarrow e^+e^-)K^+$) decays depicted as red (blue) contours. Uncertainties on the data points are statistical only. 143
- 3.11 Branching fractions of (blue) $B^+ \rightarrow K^+e^+e^-$ from this paper and (black) $B^+ \rightarrow K^+\mu^+\mu^-$ from Ref. [37] including the q^2 bin $15.0 < q^2 < 22.0 \text{ GeV}^2/c^4$. The SM predictions (red area) from Refs. [166,167] are also shown. 159
- 3.12 Candidate invariant mass distributions. Distribution of the invariant mass $m_{\psi(2S)}(K^+\ell^+\ell^-)$ for $B^+ \rightarrow \psi(2S)K^+$ resonant candidates in the (left) sample previously analysed [11] and (right) the new data sample. The top row shows the fit to the muon modes, the combinatorial component is included in the fit but is too small to be seen. The subsequent rows show the fits to the electron modes triggered by (second row) one of the electrons, (third row) the kaon and (last row) by other particles in the event. The fit projections are superimposed. 161
- 3.13 Distribution of $m(K^+e^+e^-)$ in simulated $B^+ \rightarrow K^+e^+e^-$ decays. The orange shaded area corresponds to $B^+ \rightarrow K^+e^+e^-$ candidates with true q^2 outside the interval of interest. The green and purple components correspond to candidates with $q_{\text{true}}^2 > 6.0 \text{ GeV}^2/c^4$ and $q_{\text{true}}^2 < 1.1 \text{ GeV}^2/c^4$, respectively. (Left) linear and (right) logarithmic scales are shown. 162

- 3.14 Distribution of the invariant mass $m(K^+e^+e^-)$ for $B^+ \rightarrow K^+e^+e^-$ candidates. The fit projection is superimposed, with a black dotted line describing the signal contribution and solid areas representing each of the background components described in the text and listed in the legend. For illustration, the expected distribution of signal candidates with $q_{\text{true}}^2 < 1.1 \text{ GeV}^2/c^4$ or $q_{\text{true}}^2 > 6.0 \text{ GeV}^2/c^4$ is shown as a grey dashed and dotted line. 163
- 3.15 Comparison between R_K measurements. The measurements by the BaBar [15] and Belle [13] collaborations combine $B^+ \rightarrow K^+\ell^+\ell^-$ and $B^0 \rightarrow K_S^0\ell^+\ell^-$ decays. 164
- 3.16 Comparison between R_K measurements. The measurements by the BaBar [15] and Belle [13] collaborations combine $B^+ \rightarrow K^+\ell^+\ell^-$ and $B^0 \rightarrow K_S^0\ell^+\ell^-$ decays. The previous LHCb measurement [11], superseded by the present result, is also shown. 165
- 3.17 Comparison between R_K measurements. The measurements by the BaBar [15] and Belle [13] collaborations combine $B^+ \rightarrow K^+\ell^+\ell^-$ and $B^0 \rightarrow K_S^0\ell^+\ell^-$ decays. The previous LHCb measurements [11] and [130], superseded by the present result, are also shown. 165
- 4.1 $\Delta\chi^2$ distribution extracted from pseudo-experiments (blue) for fitting the best one/two WCs varying the SM, compared to the theoretical χ^2 distribution with one/two degrees of freedom (red). 173
- 4.2 $\Delta\chi^2$ distribution (blue) for SM pseudo-experiments in the general 9 WC fit basis (top) and the reduced 5 WC basis (bottom). The data is shown as a vertical red line on the plot. 174
- 5.1 Integrated hadronic parameters $\langle\eta_X^i\rangle$, defined in Eq. (5.16), extracted from $B^0 \rightarrow K^{*0}(\rightarrow K\pi)\mu^+\mu^-$ as a function of q_{min}^2 , setting $q_{\text{max}}^2 = 6 \text{ GeV}^2$. 195
- 5.2 Distribution of the likelihood ratio for pseudo-experiments under the SM hypothesis along with the value obtained from data. Results are shown under the same conditions as in Ref. [33] and also when the measurements of R_{pK} is included. 197
- 5.3 Distribution of the likelihood ratio for pseudo-experiments under the SM hypothesis along with the value obtained from data. The distribution is overlaid with a scenario including hypothetical non-exclusive R_X measurements along with their expected sensitivities (blue). An azimov dataset [27] is used to estimate the expectation value for the significance. 201

List of tables

1.1	Organisation of the fermion content of the SM in multiplets of $SU(3)_C \times SU(2)_L \times U(1)_Y$	23
2.1	Relation between the cut on the reconstructed mass m_B^{rec} and the maximal value of q_0^2 affecting the spectrum at a given q^2 -value, after photon radiation, according to ((2.14)). The specific values of m_B^{rec} are fixed to the same values used in the LHCb analysis of R_K [24].	100
2.2	Data of charmonium resonances included in our analysis as taken from [25]. The J/Ψ mass uncertainty is negligibly small.	101
2.3	f^{th} for different cases. When the resonance is “on”, the interference of the Breit-Wigner term of the J/ψ and the rare mode is included (but not the square of the Breit-Wigner term). $10e$ is a ‘fake’ lepton that has an ‘intermediate’ mass (between the muon and the electron), and we take $m_{10e} = 10 m_e$. When the resonance is “off” (ie. only rare mode), the full range of q_0^2 is integrated over. When $\delta_{J/\psi} = 0$, the q_0^2 integration is restricted in the region $q_0^2 \leq 9.5905 \text{ GeV}^2$, whereas when $\delta_{J/\psi} = 1.47$, the q_0^2 integration is restricted in the region $q_0^2 \leq 9.585 \text{ GeV}^2$. $E_{\gamma, \text{cut}}^{(i)}$ is given in GeV units.	120
3.1	Nonresonant and resonant mode q^2 and $m(K^+\ell^+\ell^-)$ ranges. The variables $m(K^+\ell^+\ell^-)$ and $m_{J/\psi}(K^+\ell^+\ell^-)$ are used for nonresonant and resonant decays, respectively.	133
3.2	Yields of the nonresonant and resonant decay modes obtained from the fits to the data. The quoted uncertainty is the combination of statistical and systematic effects.	137

5.1	Limits placed on the hadronic nuisance parameters. The default values are determined by a conservative extrapolation from $B^0 \rightarrow K^*(892)^0$ matrix elements (see section 5.2.a). The larger interval for $\langle \eta_{pK}^{77} \rangle$ compared to $\langle \eta_{K\pi, K\pi\pi}^{77} \rangle$ takes into account the different q^2 ranges in the experimental measurements [12]. The values in the last column correspond to an extremely conservative extrapolation assuming large non-local matrix elements of four-quark operators (see section 5.2.b).	193
5.2	Change of the significance of the new-physics hypothesis in $b \rightarrow s\ell^+\ell^-$ decays adding hypothetical measurements of R_{pK} , $R_{K\pi}$, and $R_{K\pi\pi}$, with full run I and run II statistics, under two different hypotheses for the central values.	199

Chapter 1

Introduction

This chapter is aimed at introducing the subject matter of my dissertation which is based on the articles published during my PhD at the University of Zürich.

The first section, Sec. 1.1 is not mandatory for their comprehension, however it places them in the historical context of the development of our current understanding of the microscopic world: the Standard Model (SM).

The reader who is interested in revising the formulation of this theory in terms of gauge fields and spontaneous symmetry breaking can refer to the (non-exhaustive) review in Sec. 1.2.1 and Sec. 1.2.2, in particular, the consequences of spontaneously broken SM gauge symmetries, such as fermion and boson masses generation and the flavour sector are outlined in Sec. 1.2.3.

Despite its fascinating success in describing nature at scales spanning several order of magnitudes, the SM is an incomplete theory and Sec. 1.3.1 aims at outlining such open questions, while Sec. 1.3.2 suggests useful tools to answer them.

As expressed by T. Lee, a theoretical physicist who formulated pivotal aspects of the SM as we know it today:

1. Without theorists, experimentalists tend to falter.
2. Without experimentalists, theorists tend to drift.

Therefore, one of the best current laboratories for testing the SM at its intensity frontier, the LHCb experiment, is outlined in Sec. 1.4.1, and an overview on the latest measurements of $b \rightarrow s\ell^+\ell^-$ processes is presented Sec. 1.4.2. Throughout this chapter we adopt natural units for which $\hbar = c = 1$.

1.1 History of the Standard Model

*The universe is simple;
it's the explanation that's complex.*

W. Allen

1.1.1 A new player in the game

What is now the most precisely verified theory in particle physics, the Standard Model, did not follow a linear path through its development. In fact, it was 1896 when the french physicist H. Becquerel, hoping to demonstrate a link between minerals that glow when exposed to strong light and a new type of electromagnetic radiation called X-rays, discovered radioactivity by accident. On 26 February 1896 [1], after placing uranium salts wrapped in black paper on top of a photographic plate, he observed that the salts caused a blackening of the plate despite the paper in between. Becquerel concluded that invisible radiation that could pass through paper was causing the plate to react as if exposed to light. Subsequently, E. Rutherford, continued these experiments and discovered in 1899 different kinds of radiation defined by their penetrating power [2]: α -particles, that did not leave any trace on the Becquerel plates since they were absorbed by the black wrapping paper, and β -particles, that have a 100-times greater penetrating power than α -particles. In 1900, Becquerel measured the mass-to-charge ratio of the β -particles to conclude that these were in fact electrons. The puzzle, however, was far from being solved: some years later, in 1914, data collected by J. Chadwick [3] showed that the electron spectrum measured in a two-body β -decay

$${}^AZ \rightarrow {}^A(Z+1) + \beta^-$$

was a continuous distribution instead of a Dirac δ , as one would naively expect from energy-momentum conservation applied to a two-body decay. The open letter by W. Pauli in 1930 [4] addressed to the radioactive attendants of the Gauverein meeting in Tübingen was a desperate remedy in order not to renounce to the conservation laws of energy and angular momentum. Pauli hypothesised the existence of a third, undetected element in the decay products of the β -decay of the nucleon, that had almost no rest mass and was electrically neutral:

$${}^AZ \rightarrow {}^A(Z+1) + \beta^- + \nu$$

It was Chadwick's discovery of the neutron in 1932 [5] that gave Fermi the inspiration to name *neutrino* this hypothetical particle in his first theory of β -decay [6], which can be regarded as the precursor of the theory of weak interactions. Assuming a close analogy with the QED description of electron-proton scattering, Fermi proposed to explain the β -decay as the contact interaction of two vector currents:

$$\mathcal{L}_{\beta\text{-decay}} \propto G_F (\bar{u}_p \gamma^\mu u_n) (\bar{u}_e \gamma_\mu u_\nu) \quad (1.1)$$

However, the difference with the QED paradigm is striking since the currents in this Lagrangian are charged.

In the same years (1932-1937) Heisenberg and Wigner, starting from the hypothesis that the proton and the neutron are two different states of the same object, gave birth to SU(2) of flavour and the isotopic spin. In analogy to the spin states of the electron wave-function, the neutron and the proton are spin up and spin down states of the nucleon.

$$\begin{pmatrix} n \\ p \end{pmatrix} \sim \begin{pmatrix} |\uparrow\rangle \\ |\downarrow\rangle \end{pmatrix}_e \quad (1.2)$$

According to this hypothesis the difference in mass between the proton and the neutron is exclusively due to the electromagnetic repulsion.

It was 20 years after being hypothesised that the elusive neutrino was first observed by C. L. Cowan and F. Reines [7], exploiting the inverse β reaction:

$$\bar{\nu}_e + p \rightarrow e^+ + n$$

initiated by anti-neutrinos produced at the nuclear facility of Savannah River Plant near Augusta in Georgia.

1.1.2 Objects in the mirror don't look as you'd expect

A few years later, in 1956, T. Lee and C. Yang [8] suggested that experimental data neither confirmed nor refuted spatial reflection invariance (parity conservation) in transitions governed by weak interactions. This led to the study of the directional properties of β -decay in a polarised sample of ^{60}Co cobalt by C. Wu et al. [9]. The observation of a preferred direction of emission for electrons in polarised nuclei was a clear signature of parity symmetry violation in β -decays. Moreover, to enforce angular momentum conservation, it was concluded that neutrinos emitted in β -decays could

only be left-handed or, in other words, that the projection of their spin along their direction of motion is always anti-parallel. This was later confirmed in 1958 in an experiment by M. Goldhaber et al. [10] which first measured the neutrino's helicity to be $h(\nu) = -1.0 \pm 0.3$ and concluded that anti-neutrinos are always right-helical ($h(\bar{\nu}) = +1$).

Following these results, the initial hypothesis formulated by E. Fermi in (1.1) required to be extended to a more general expression

$$\mathcal{L}_w = \sum_i \frac{G_i}{2} (\bar{u}_p \Gamma_i u_n) (\bar{u}_e \Gamma_i u_\nu) + \text{h.c.} \quad (1.3)$$

Which contains a sum over all possible bilinear covariants Γ_i with $i = \{S, V, T, A, P\}$. Eq. (1.1) is a special case in which $G_i = 0$ for $i \neq V$, leaving us with an expression that represented a purely vector interaction. However, each product of bilinear covariants in Eq. (1.3) is parity conserving, hence to include the experimental evidence of parity violation in weak interactions, the product of hadron and lepton currents in (1.3) needs to be modified as follows:

$$\mathcal{L}_w = \sum_i \frac{G_i}{2} (\bar{u}_p \Gamma_i u_n) (\bar{u}_e \Gamma_i (1 + C_i \gamma_5) u_\nu) + \text{h.c.} \quad (1.4)$$

Where G_i and C_i are scalar constants. It was at the Rochester conference held in 1957 where T. Lee and C. Yang presented two new operators P_L and P_R which projected a four component massless bispinor into two opposite helicity spinors [11].

$$P_R = \frac{1 + \gamma_5}{2} \quad P_L = \frac{1 - \gamma_5}{2} \quad (1.5)$$

and subsequently, R. P. Feynman (which in 1948 together with F. J. Dyson and Schwinger [12,13] developed the QED formalism, including radiative corrections), used these two new operators to replace the full spinors of the massive leptons contained in weak interactions with their left-chiral projections

$$u_e \rightarrow u_e^L = \frac{1 - \gamma_5}{2} u_e \quad \bar{u}_e \rightarrow \bar{u}_e^L = \bar{u}_e \frac{1 + \gamma_5}{2} \quad (1.6)$$

Plugging these chiral projections in the expression of the lepton current of (1.4) yields

$$(\bar{u}_e \Gamma_i (1 + C_i \gamma_5) u_\nu) \rightarrow \left(\bar{u}_e \Gamma_i (1 \mp C_i) \frac{1 \mp \gamma_5}{2} u_\nu \right) \quad (1.7)$$

where the top sign holds for $i \in \{V, A\}$ and the bottom sign for $i \in \{S, T, P\}$. The sign in the last term of the product is bound by experimental evidence to be the top one since weak interactions only couple to left-handed particles, hence this interaction can only involve V and A covariant forms. Moreover, for this whole term to be non-vanishing it must be that $C_i = -1$, yielding the weak Lagrangian:

$$\begin{aligned} \mathcal{L}_w &= \left[\frac{G_V}{2} \bar{u}_p \gamma_\mu u_n + \frac{G_A}{2} \bar{u}_p \gamma_5 \gamma_\mu u_n \right] [\bar{u}_e \gamma^\mu (1 - \gamma_5) u_\nu] \\ &= \frac{G_F}{\sqrt{2}} [\bar{u}_p \gamma_\mu (1 - g_A \gamma_5) u_n] [\bar{u}_e \gamma^\mu (1 - \gamma_5) u_\nu] + \text{h.c.} \end{aligned} \tag{1.8}$$

With $g_A = |G_A/G_V| = 1.26$ experimentally determined and $G_F \equiv G_V/\sqrt{2}$.

1.1.3 A heavier sibling of the electron

To proceed with our review of the SM history we have to do one step back in time to the mid-1930's when H. Yukawa made an attempt [14] to describe the force responsible for nucleons attraction through the exchange of an hypothetical charged boson. Yukawa also suggested that this new particle might be responsible for the β -decay, because it could decay into an electron-(anti)neutrino pair. After Anderson's discovery of the positron in 1932, Neddermeyer detected in 1937 [15] a particle that had a similar mass to the one predicted by Yukawa and its decay products included an electron. However, this was predicted to be responsible for the nuclear force and should have had very strong interactions with nuclei, but the detected particle was able to traverse thick layers of matter without any such interactions. The mass of this particle, which is the muon μ , was measured to be orders of magnitude greater than the one of the electron, but there were no indications that it could be an excited state of it, since decays of the kind $\mu^- \rightarrow e^- \gamma$, $\mu^- \rightarrow \mu^- e^+ e^-$ and $\mu^- \rightarrow e^- \gamma \gamma$ were not observed. While Yukawa's meson was later found to be the pion π , the muon is the particle that lead from a Fermi theory which is only useful in the description of β -decay to a theory which encompasses many interactions, a "universal" Fermi theory. The originator of the idea of a universal Fermi theory was B. Pontecorvo, who first noticed that the process of muon absorption $\mu^- + p \rightarrow n + \nu$ could be described using Fermi's theory (1.8), if the mass difference between e and μ is taken into account [16]. Hence he proposed in 1947 that the following decays were possible:

$$\mu^- \rightarrow e^- \nu \bar{\nu}, \quad \mu^+ \rightarrow e^+ \nu \bar{\nu} \quad (1.9)$$

and the electron produced in such decay should manifest a continuous energy spectrum. This observation was performed in 1949 by J. Steinberger [17] thus it became clear that β -decay was not the only interaction which could be described by the Fermi theory. In 1962 the existence of a second form of neutrino, the muon neutrino ν_μ , was shown by a team of scientists led by L. Lederman, M. Schwartz, and J. Steinberger [18]. Exploiting the large number of pion decays to μ and ν at the BNL's synchrotron, only reactions of the type $\bar{\nu}_\mu + p \rightarrow \mu^+ + n$ were observed, confirming the existence of a separate kind of neutrinos from the ones observed just a decade before, *i.e.* $\nu_\mu (\neq \nu_e)$. A doublet structure of the kind

$$\begin{pmatrix} \nu_e \\ e \end{pmatrix}_L \quad \begin{pmatrix} \nu_\mu \\ \mu \end{pmatrix}_L \quad (1.10)$$

is hypothesised, together with an extension to the muonic counterpart of the Lagrangian \mathcal{L}_w in Eq. (1.8)

$$\mathcal{L}_{V-A} = \mathcal{L}_w + \frac{G_F}{\sqrt{2}} \sum_{\ell=e,\mu} [\bar{u}_{\nu_\ell} \gamma_\mu (1 - \gamma_5) u_\ell] [\bar{u}_\ell \gamma^\mu (1 - \gamma_5) u_{\nu_\ell}] + \text{h.c.} \quad (1.11)$$

However the $V - A$ Lagrangian of Eq.(1.11) violates the unitarity bounds derived in Sec. 1.A.2.2. In fact, if we consider the process:

$$e^-(p_1) + \nu_\mu(p_2) \rightarrow \mu^-(k_1) + \nu_e(k_2)$$

The transition amplitude according to Eq. (1.11) reads:

$$\mathcal{M}(s, z) = -\frac{G_F}{\sqrt{2}} \bar{u}(k_2) \gamma_\alpha (1 - \gamma_5) u(p_1) \bar{u}(k_1) \gamma^\alpha (1 - \gamma_5) u(p_2) \quad (1.12)$$

In the massless lepton limit, taking the square modulus of the transition amplitude we obtain

$$|\mathcal{M}(s, z)|^2 \propto 32 G_F^2 s^2$$

Since the result doesn't depend on z , the partial wave decomposition will contain exclusively $a_0(s)$ term and $a_j(s) = 0$ for $j > 0$.

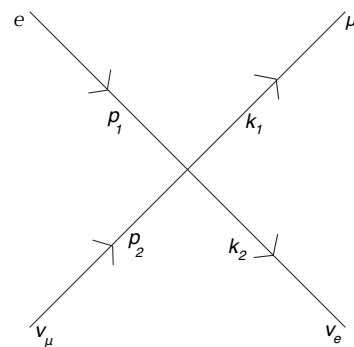


Fig. 1.1 Schematic diagram for the $e\nu_e \rightarrow \mu\nu_\mu$ process in the Fermi theory

$$a_0(s) = \frac{1}{32\pi} \int_{-1}^1 dz P_0(z) \sqrt{32} G_F s = \frac{G_F s}{2\sqrt{2}\pi} \quad (1.13)$$

The unitarity bound of Eq. (1.126) imposes that

$$\frac{G_F s}{2\sqrt{2}\pi} \leq 1 \quad (1.14)$$

Which, substituting the values for the Fermi constant, places an upper boundary on s of $\sqrt{s} \lesssim 875$ GeV. For higher energies the unitarity bounds are violated, and at the time of the formulation of the $V - A$ theory of weak interactions, this constituted exclusively a conceptual problem, since experimentally $\sqrt{s} \ll 875$ GeV. The hypothesis of a new mediator would have removed the s dependence of $a_0(s)$, however if massless it wouldn't have met the requirements imposed by experimental data that were suggesting an interaction with a limited range of 10^{-15} cm. An equally not viable option would have been the addition a massive mediator with an *ad-hoc* mass. since it would have introduced diagrams (such as $\ell^+ + \ell^- \rightarrow W^+ + W^-$) which, in turn, would violate the unitarity bounds. The problem of the mass of the force mediators was already clear to Feynman, since the *ad hoc* addition of a related mass term in the Lagrangian would have violated gauge invariance of QED. This posed a problem for any extension of QED which would include a massive mediator.

1.1.4 The "strange" path to new fundamental particles

Neglecting the mass problem, by the start of the 1940s, it seemed like physicists were getting a handle on the fundamental particles and their interactions. Properties of electrons, protons and neutrons, as well as neutrinos and even positrons were known and observed. However this status was soon due to end with the discovery in the early 1950's [19] of new particles, in an experiment using a cloud chamber to detect penetrating particles from cosmic ray showers. These "strange" particles were measured to be roughly 200 times heavier the proton, however they had unusual long lifetimes (10^{-8} s) for such heavy masses. Moreover they always came in pairs, but could decay independently from each other.

The decay modes of these charged strange particles also presented a puzzle that was of difficult solution in the hypothesis of parity conservation of the interaction responsible for their decay. These types of decays, into two or three pions, were labeled as follows:

$$\tau^\pm \rightarrow \pi^\pm \pi^+ \pi^-, \quad \tau^\pm \rightarrow \pi^\pm \pi^0 \pi^0, \quad \theta^\pm \rightarrow \pi^\pm \pi^0 \quad (1.15)$$

All three decays appeared to originate from particles (of unknown spin-parity) with nearly the same mass and lifetime, apparently having the same abundance ratio (independently of their production mechanism) and same interactions with heavy nuclei. While the first two decays of Eq. (1.15) could be described as two different decay modes of the same particle, the third one could not due to parity symmetry. The analysis of the experimental Dalitz plot distributions from [20] indicated that the spin-parity assignment for the two-pion final state, was not the same as the three body one, so - on the grounds that parity must be conserved in the decay - the two modes could not originate from the same state.

In the same years M. Gell-Man, K. Nishijima and A. Pais developed the idea that these particles had a property called "strangeness", to which the corresponding quantum number is associated. According to their hypothesis, strong nuclear forces involved in the production of such particles conserve strangeness, but weak nuclear forces responsible for their decays do not. This would explain why strange particles would always appear in pairs of total strangeness 0, and their relatively long decay time, since weak interactions tend to take longer to play out.

Up to that time though, evidence of parity violation was only found in weak processes involving at least two leptons. Given the difficulty of building a pseudo-scalar probe to test for parity violation in the $\theta - \tau$ system, since the two- and three-pion states cannot interfere directly, Lee and Yang suggested in 1956 The possibility of testing parity violation in a fully hadronic system using decays of hyperons. Soon after Lee and Yang's proposal, a large parity violating asymmetry in $\Lambda \rightarrow p\pi^-$ was indeed measured [21][22]. This eventually lead to the resolution of the $\theta - \tau$ puzzle: the two and three pion decays originate from a single particle, the Kaon (K^\pm) which can actually decay to states of opposite parity because the weak interactions inducing such decays do not respect parity symmetry.

M. Gell-Man, in 1963 [23], realised that a symmetry scheme, which he named "Eight-fold Way", would allow to group the eight known baryons in multiplets characterised by different isotopic spin values, much in the same way as the periodic table classifies the chemical elements. These multiplets represent the eight-dimensional adjoint representation of $SU_F(3)$ (See Fig. 1.2), and, according to his model, the phenomenological breaking of this symmetry is reflected in the mass spectrum of such multiplets, which would be degenerate in case of unbroken symmetry. The fact that also K and π mesons could fit into a similar multiplet scheme allowed Gell-Man to predict the existence of

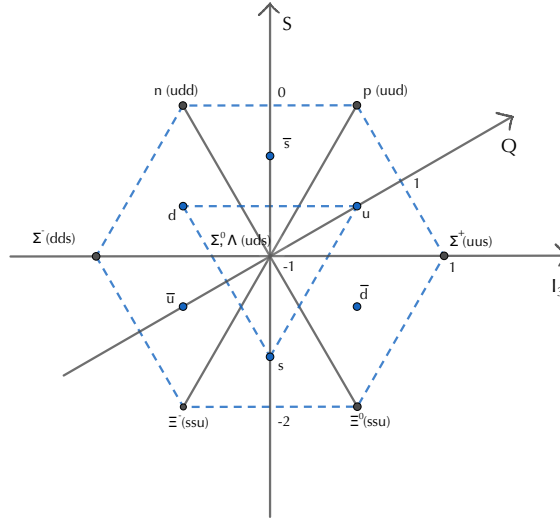


Fig. 1.2 Fundamental, anti-fundamental and adjoint representations of $SU(3)_F$ for the u, d, s baryon octet, also known as "The Eightfold Way"

an additional pseudo-scalar meson with 0 isotopic spin, the η meson. This model also predicted the realisation of the fundamental and anti-fundamental representations of $SU_F(3)$, *i.e.* three new elementary particles which he called "quarks".

It was in these years that, from experimental observations of equality of the couplings of $\bar{\nu}_e e, \bar{\nu}_\mu \mu$ currents to any other given current, and of the near equality of coupling constants describing the μ -decay and the nuclear β -decay lead to the idea of universality of charged current interactions. This however, was encountering difficulties in explaining the phenomenology of leptonic K and π decays. It was observed, in fact, that albeit strongly favoured from the available phase space, the $K^+ \rightarrow \mu^+ \nu_\mu$ happened 20 times less frequently than the same decay originating from a pion. This lead N. Cabibbo in 1963 to formulate a weaker form of universality [24] by introducing θ_C as the angle rotating the axial and vector currents responsible of $\Delta S = 0, \Delta Q = 1$ with respect to the ones governing $\Delta S = \Delta Q = 1$ transitions.

$$\frac{\Gamma(K^+ \rightarrow \mu^+ \nu_\mu)}{\Gamma(\pi^+ \rightarrow \mu^+ \nu_\mu)} \propto \tan^2 \theta_C$$

From experimental data $\theta_C \simeq 0.257$. The model introduced by N. Cabibbo received confirmation thanks to the possibility of explaining ratios of branching fractions of semi-leptonic decays of baryons. In particular it could explain the cancellation of the axial contribution to the process $\Sigma^- \rightarrow n + e^- + \bar{\nu}_e$, and its relative suppression with respect to $\Lambda \rightarrow p + e^- + \bar{\nu}_e$ decays.

It was clear that a doublet structure similar to the one for the leptons (1.10) was emerging

$$\begin{pmatrix} u \\ d' \end{pmatrix} \quad \begin{pmatrix} \\ s \end{pmatrix} \quad (1.16)$$

Where $d' = \cos \theta_C d + \sin \theta_C s$, *i.e.* the interaction basis appears rotated of θ_C with respect to the mass basis. This model paved the way for the Glashow–Iliopoulos–Maiani (GIM) mechanism which was developed a few years later and more generally to the Cabibbo–Kobayashi–Maskawa (CKM) matrix as we know it today.

1.1.5 Symmetry as a guiding principle

To proceed with our historical review of the SM we have once again to jump back in time to 1918 when the mathematician E. Noether discovered the profound connection between symmetries and conservation laws in physics [25]. Noether's theorem states that if the Lagrangian describing a system is symmetric (invariant) with respect to some transformation, then there must exist a conserved charge and a corresponding conserved current within the system which is associated with this symmetry. In the same year, Weyl's attempts to describe gravitation and electromagnetism within a unifying geometrical framework [26] paved the way for the correct understanding of the role of gauge invariance. Weyl's initial attempt of unification of general relativity and electromagnetism was not viable, however, in view of the development of quantum mechanics, he reinterpreted his speculative theory under a new perspective. In his 1929 work [27] he emphasised the role of gauge invariance as a constructive principle from which electromagnetism can be derived. In fact he showed that it possible to introduce in the Schrödinger equation the coupling of the electron with the electromagnetic field by performing a shift of the electron wave function $\psi \rightarrow e^{i\alpha(x)}\psi$.

The experimental verification of this principle was proposed by Aharonov-Bohm in 1959 [28] by placing a solenoid, shielded by a conductor, between two beams obtained from the same electron source (Fig. 1.3). The observation of an interference pattern on the screen produced by the variation of the magnetic field \vec{B} would confirm that the electron, even if never in contact with the magnetic field, would "feel" the auxiliary field $A_\mu(x)$, and the interference between the two beams would depend on the phase difference.

$$\oint \vec{A} \cdot d\vec{\ell} = \phi_B$$

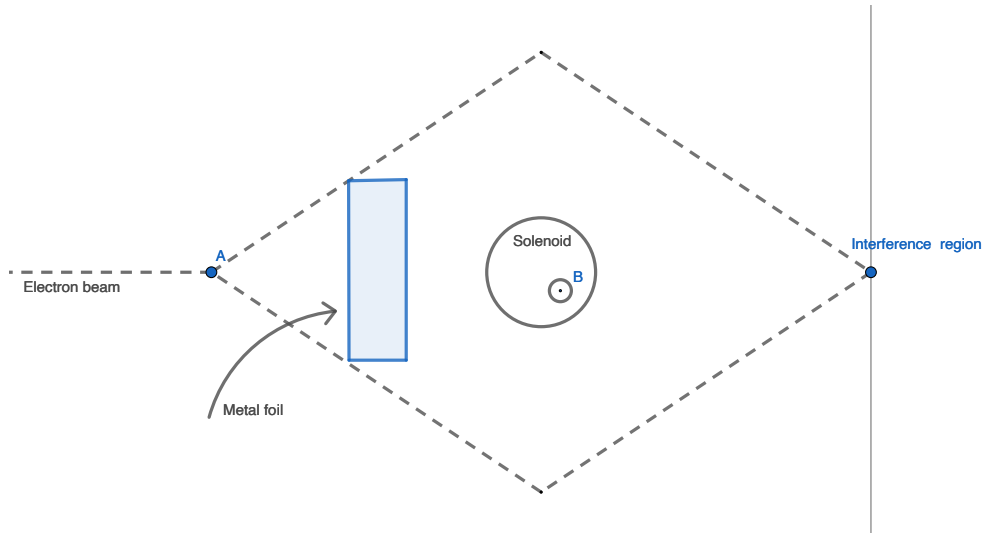


Fig. 1.3 Schematic view of the Aharonov-Bohm "Gedankenexperiment": two electron beams originating from the same source are collected on a screen on the opposite side of a solenoid. The magnetic field inside the solenoid is screened inside the solenoid.

All these effects depend only on the gauge-invariant quantity $\oint \vec{A} \cdot d\vec{\ell}$, so that in reality they can be expressed in terms of the fields inside the circuit, however, according to relativity, all fields must interact only locally. And since the electrons cannot reach the regions where the fields are, Aharonov and Bohm could not interpret such effects as due to the magnetic field \vec{B} . Another interesting point of this effect is that it would make the field $A_\mu(x)$ measurable, in spite of the fact, due to gauge invariance, that all the known physical quantities are left unchanged by a rescaling $A_\mu(x) \rightarrow A'_\mu(x) = A_\mu(x) + \partial\psi/\partial x_\mu$ where ψ is a continuous scalar function. To conserve locality and gauge invariance of the theory, Aharonov and Bohm where led to regarding $A_\mu(x)$ as a physical variable, *i.e.* that it is possible to define the physical difference between two quantum states which differ only by gauge transformation.

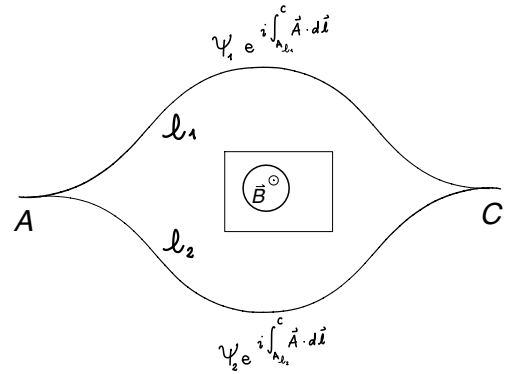


Fig. 1.4 Schematic view of the wave function shift induced by the field A_μ , responsible for the Aharonov-Bohm effect

1.1.6 A "massive" problem

In 1954 C. N. Yang and R. L. Mills [29], starting from the isospin doublet introduced earlier by Heisenberg and Wigner in Eq. (1.2), formulated Lagrangian that featured the $SU(2)$ symmetry of the isospin doublet. This theory predicted the existence of 3 gauge fields, or force mediators, which however had to be massless since a mass term added *by hand* would violate gauge invariance. Weak interactions and electromagnetism were combined by S. Glashow in 1961 [30] under the formulation of a Lagrangian that is invariant under $SU(2)_L \times U(1)_Y$ transformations. This theory, which included (3+1) massless gauge bosons, could not accommodate a fermion mass term $m\bar{\psi}\psi$ due to gauge invariance requirements. However, it allowed to establish a relation between electric charge Q , the third component of the weak isospin I_3 and the hypercharge Y

$$Q = I_3 + \frac{1}{2}Y \quad (1.17)$$

of the particle content of the Lagrangian. In order to get an insight on the interplay between gauge symmetries of the Lagrangian and the mass terms of the gauge bosons, again we have to step back in time to 1911 when dutch physicist H. K. Onnes discovered that mercury at cryogenic temperatures assumes a superconducting state, *i.e.* a state in which electric current could flow without any resistance imposed by the conductor. The experiment conducted in 1933 by W. Meissner and R. Ochsenfeld [31] provided a physical example of a gauge theory with a massive boson as a result of a spontaneous breaking of the gauge symmetry, in fact they showed that magnetic field is expelled from a superconductor during its transition to the superconducting state. The magnetic field inside the superconductor is null, except in a very limited ($\sim 10 \mu\text{m}$) superficial region. As initially hypothesised by W. Heisenberg 5 years before [32], this can be interpreted as the breaking of the rotational symmetry of the ferromagnetic material when it is cooled down below the critical temperature, causing the mediator of the electromagnetic interaction to acquire a mass and to penetrate only the superficial volume of the superconductor.

It was in this context that Y. Nambu and J. Goldstone [33,34] showed the necessary appearance of such massless bosons in models exhibiting spontaneous breaking of continuous symmetries. According to Nambu and Goldstone, if the vacuum state is non-invariant under a continuous symmetry of the theory, one massless state for each generator of the symmetry that is broken is expected. In 1963 P. Anderson [35] realised that for a gauge symmetric Lagrangian where this symmetry is spontaneously broken, the Nambu-Goldstone massless modes can combine with the Yang-Mills massless gauge

fields to produce a physical massive vector field. He remarked that, in elementary particle physics, *“the Goldstone zero-mass difficulty is not a serious one, because we can probably cancel it off against an equal Yang–Mills zero-mass problem”*. The relativistic formulation of this mechanism would be formulated one year later, in an independent but complementary way, by Brout, R F. Englert [36] and P. Higgs [37], however, P. Higgs appears to have been the first to discuss the existence in models like his of a massive mode, i.e. the "Higgs particle". After several attempts to apply Brout-Englert-Higgs ideas to the breaking of hadronic flavour symmetries without success, progress came in 1967 when S. Weinberg [38] and A. Salam [39] independently realised that the candidate for spontaneous symmetry breaking was the $SU(2)_L \times U(1)_Y$ model of leptonic electroweak interactions earlier proposed by S. Glashow [30]

$$SU(2)_L \times U(1)_Y \xrightarrow{\text{SSB}} U_{EM}(1)$$

The $U_{EM}(1)$ symmetry observed today, responsible for electric charge conservation and electromagnetic interactions, is a relic of a greater symmetry which is spontaneously broken by the scalar complex field

$$\begin{pmatrix} \phi^* \\ \phi \end{pmatrix} \quad (1.18)$$

In a process which gives mass to the gauge bosons, as well as to the fermion content of the theory. The search for direct or indirect signatures of this mechanism had just started.

1.1.7 The colour and flavour of particle physics

A few years later, deep inelastic scattering (DIS) experiments conducted by the MIT-SLAC collaboration at the Stanford Linear Accelerator Centre (SLAC) revealed the first signs that nucleons have an inner structure: as hypothesised by Gell-Man and Zweig, the quark model, which predicted elementary half integer spin particles as components of baryons and mesons, was confirmed. In the subsequent years, the combination of these results with others from neutrino-scattering in the Gargamelle bubble chamber at CERN, confirmed fractional electric charges of $+2/3|e|$ and $-1/3|e|$ of quarks. However the existence of bound quarks states such as $\Omega^-(sss)$ was posing a great problem for the quark model. In fact, since the wave function describing this ground state baryon is symmetric, it would contradict Pauli exclusion principle if its constituents are 3 identical quarks of spin 1/2.

The formulation by H. Fritzsch and M. Gell-Man of QCD as an unbroken $SU_C(3)$ Yang-Mills theory posed a solution to the statistics problem by introducing a new quantum number that the quarks possessed, the colour charge [40,41]. According to this theory all hadrons are singlets of the colour group: the baryon wave functions are totally antisymmetric combinations of the 3 colour indices (rgb), while the mesons wave functions are symmetric combinations of colour and anti-colour charges ($r\bar{r}, g\bar{g}, b\bar{b}$). The experimental confirmation of colour charge came from the ratio R

$$R(\sqrt{s} \lesssim 3 \text{ GeV}) = \frac{\sigma(e^+ + e^- \rightarrow \text{hadrons})}{\sigma(e^+ + e^- \rightarrow \mu^+ + \mu^-)} = N_C \sum_{f=u,d,s} Q_f^2/e^2 \quad (1.19)$$

The experimental data were in agreement with a ratio of $R = 2$, hence indicating that $N_C = 3$.

At the time a gauge theory for strong interactions was proposed, only three quarks were thought to exist: *up*, *down*, *strange*. Starting from the phenomenological observation that transitions such as $K^+ \rightarrow (\pi^0)\mu^+\nu_\mu$ have a branching fraction of $\sim 66\%$ ($\sim 3\%$) while $K^0 \rightarrow (\pi^0)\mu^+\mu^-$ amount to $\sim 10^{-7}$ (10^{-8})% of the total decay width, S. Glashow, J. Iliopoulos and L. Maiani (GIM) hypothesised the existence of a fourth quark, named *charm* [42]. In this model, both *down* and *strange* eigenstates are rotated with respect to the mass eigenstates by the Cabibbo angle θ_C .

$$\begin{pmatrix} u \\ d' \end{pmatrix} = \begin{pmatrix} c \\ s' \end{pmatrix}, \quad \begin{pmatrix} d' \\ s' \end{pmatrix} = \begin{pmatrix} \cos \theta_C & \sin \theta_C \\ -\sin \theta_C & \cos \theta_C \end{pmatrix} \begin{pmatrix} d \\ s \end{pmatrix} \quad (1.20)$$

Through the GIM mechanism, Flavour Changing Neutral Currents (FCNC) would only be possible at loop level, hence the suppression of $K^0 \rightarrow (\pi^0)\mu^+\mu^-$, while $\Delta S = 1$ processes are allowed only in weak charged current interactions. The existence of a fourth quark flavour was independently confirmed with the observation of a flavour-neutral vector meson with an invariant mass of $m_{J/\psi} = 3.097 \text{ GeV}$ by two independent collaborations. A bump in the electron positron pairs produced in high energy $p + \text{Be} \rightarrow e^+ + e^- + X$ collisions observed at the BNL's 30 GeV alternating-gradient-synchrotron, was named J by the first collaboration [43]. The same particle was produced in collisions of electrons and positrons in the SPEAR storage ring at the SLAC Laboratory [44] and was named ψ by the second collaboration. Both collaborations announced they had actually found the same particle, the $J/\psi(c\bar{c})$ in November 1974, in an event that due to the subsequent rapid changes in the field, became known as "November revolution".

Flavoured bound states of the charm quark, the D mesons, were first discovered by the SLAC-BNL Mark I collaboration at the SPEAR e^+e^- collider in 1976 using data collected at $3.6 < \sqrt{s} < 4.6$ GeV [45,46]. The first modes observed included the decays $D^0 \rightarrow K^-\pi^+$, $K^-\pi^+\pi^-\pi^+$ and $D^+ \rightarrow K^-\pi^+\pi^+$. Almost contemporarily to the discovery of the charm quark, the electroweak model, which predicted the existence of a neutral massive gauge boson carrying the weak force, obtained indirect confirmation. The first observations of weak neutral current induced leptonic [47] and hadronic processes [48] were performed at the Gargamelle bubble chamber at CERN in 1973. Events involving a neutrino-electron scattering process in the former case, or with an isolated vertex with hadrons produced in the latter case, were observed in the active volume of the chamber which consisted in nearly 12 cubic metres of heavy-liquid freon (CF₃Br). The direct detection of the weak W^\pm/Z bosons followed in 1983 [49,50], at the two moveable detectors UA1 and UA2 which collected data from proton-antiproton collisions at the SPS beam pipe at CERN, performing the first measurements of the electroweak gauge bosons' masses.

1.1.8 Yet another symmetry is questioned

To proceed our historical review of the Standard Model, we have once again to shift our attention from the gauge sector to the flavour sector. With the discovery of the charm quark, and the development of the gauge theories, it was becoming clear that the number of quarks was non-trivially related to the number of leptons. In particular $n_q = n_\ell$ to cancel gauge anomalies arising from symmetries which are exact at the classical level but explicitly broken at the quantum level. The kaon system, which led to the discovery of parity violation in hadrons through the $\theta - \tau$ puzzle, still had unexploited discovery potential in this regard. The neutral K mesons, form a special system of neutral particles. In fact, the K^0 and \bar{K}^0 are distinguished by a conserved quantum number as far as strong interactions are concerned, but are self-CP-conjugate as far as weak interactions are considered, since strangeness is not conserved in weak processes. This implies that $\pi^+\pi^-$ states obtained from a K^0 cannot be distinguished from those obtained from \bar{K}^0 and more generally, that processes such as $K^0 \leftrightarrow \bar{K}^0$ would be possible through the common virtual decay states. The two non self-conjugated states with definite strangeness:

$$CP|K^0\rangle = |\bar{K}^0\rangle \quad CP|\bar{K}^0\rangle = |K^0\rangle$$

can be linearly combined

$$|K_1\rangle = \frac{1}{\sqrt{2}} (|K^0\rangle + |\bar{K}^0\rangle) \quad |K_2\rangle = \frac{1}{\sqrt{2}} (|K^0\rangle - |\bar{K}^0\rangle)$$

to obtain states with definite CP eigenvalues

$$CP|K_1\rangle = +|\bar{K}_1\rangle \quad CP|\bar{K}_2\rangle = -|K_2\rangle$$

If weak interactions respect CP symmetry, the $K_{1/2}$ would only decay to CP even/odd states. In 1956 two neutral kaon states, named short-lived K_S and long-lived K_L , were discovered, with lifetimes:

$$\tau(K_S) = 0.89 \cdot 10^{-10} s \quad \tau(K_L) = 5.17 \cdot 10^{-8} s$$

Since the short-lived neutral kaon was observed to decay into two pions, while the long-lived one apparently only decayed into three-body final states, the K_S was identified with the $CP = +1$ eigenstate (K_1), and the K_L was identified with the $CP = -1$ eigenstate (K_2).

The factor of ~ 600 difference in their lifetimes, which is ascribed to the available phase space in their decays to two or three pions, has important experimental consequences: starting from a mixture of the two states, far enough from the production point the beam will contain exclusively the long lived K_L . In the experiment conducted by J. Christenson, J. Cronin, V. Fitch et al. [51] at the Brookhaven National Laboratories, K_L in a collimated beam were found to occasionally decay into two charged pions, violating CP conservation. Contrary to the case of parity violation, the physics community had a hard time accepting that CP could be violated. Two conclusive pieces of evidence came years later with the detection of the interference between the 2π states obtained from K_S and K_L decays in 1965, and with the measurement of the charge asymmetry of semi-leptonic $K_L \rightarrow \pi^+ \ell^- \bar{\nu}_\ell$ vs. $K_L \rightarrow \pi^- \ell^+ \nu_\ell$ decays in 1967. The efforts to incorporate CP violation phenomenology in the Standard Model framework lead M. Kobayashi, T. Maskawa, building on the work by N. Cabibbo (CKM), to propose the existence of an extra pair of quark beyond the four ones seen until then [52]. A CP violating phase would appear in the Standard Model Lagrangian if the multiplets of Eq. (1.20) were made by three quark flavours instead of two.

1.1.9 A third heavier family

Evidence of the existence of a third heavier lepton decaying into electrons and muons [53] were found a few years later, in 1975, by the SLAC-BNL Mark I collaboration

at the SPEAR e^+e^- storage ring. In the period from 1975-1978 more data from the SPEAR storage ring, as well as from the DORIS storage ring at the Deutsches Elektronen Synchrotron (DESY), confirmed the discovery and the interpretation of the $\mu - e$ production process as arising from a new heavy lepton, the τ . According to the pattern of the first two lepton generations, such a particle was predicted to also have an associated neutrino type, the ν_τ , which would be observed 20 years later by the DONUT experiment at Fermilab using nuclear emulsion targets [54]. The self consistency of the emerging theory describing elementary particles, which required equality between the number of quark and lepton families, made search for a third family of quarks even more compelling.

In 1977 L. Lederman et al. [55] presented the findings of E288, an experiment in the proton fixed-target facility at Fermilab. They observed an excess at 9.5 GeV in the di-muon mass spectrum of muons produced in $p + (\text{Cu, Pt}) \rightarrow \mu^+ + \mu^- + X$ (the name Υ comes from the assonance with *Oops-Leon* due to a clustering of di-electron data around 6 GeV that was later found to be a background fluctuation). The surprisingly small decay width of the $\Upsilon(1S)$ of ~ 53 keV (or, equivalently, its long decay time), is ascribed to the fact that at $\sqrt{s} < 2m_B$ the strong decay in two beauty flavoured mesons is kinematically prohibited, hence the decay proceeds through weak processes, which are typically slower. Studies on higher excited states such as $\Upsilon(2S)$ $\Upsilon(3S)$ and $\Upsilon(4S)$, with masses of $\sim 10, 10.36, 10.58$ GeV respectively, were later performed by the CLEO collaboration at the Cornell Electron Storage Ring (CESR) and ARGUS collaboration at DESY. These studies allowed to establish that the Υ states were $b\bar{b}$ resonances, and to derive the electric charge of $-1/3|e|$ of the b quark. The first Υ resonance that can decay in a pair of B -mesons is the $\Upsilon(4S)$, hence its considerably larger decay width (20 MeV) with respect to the lower states.

In the following 20 years, the rich phenomenology offered by b quarks was extensively studied. The first measures on inclusive decays and lifetime of b hadrons were performed at PEP (SLAC) and PETRA (DESY) in 1982 yielding a $c\tau_{X_b} \sim 490\mu m$, indicating that the B meson decays were governed by the weak interactions, involving transitions to lighter quark families, and hence suppressed by a CKM factor. In analogy to the neutral strange mesons, evidence for $B^0 \leftrightarrow \bar{B}^0$ oscillations were first found by the ARGUS collaboration [56] and their time dependence was subsequently studied in 1993 by the ALEPH collaboration [57] at the Z resonance. B factories such as BaBar at SLAC and Belle at KEKB, thanks to their asymmetric beam energies configuration, allowed for precise time dependent measurements on which CP asymmetries are crucially dependent.

Violation of the CP symmetry arising from the interference of mixing and decay amplitudes in B meson decays was found in 2001 by both BaBar [58] and Belle [59] exploiting the "golden mode" $B^0 \rightarrow J/\psi K_S$, while direct CP violation was established in 2004 by both Babar [60] and Belle [61] using $B^0 \rightarrow K^\pm \pi^\mp$ decays. Despite working in an extremely clean environment, e^+e^- colliders such as PEP, KEKB, and LEP suffer from low $b\bar{b}$ production cross section of $\mathcal{O}(1-6 \text{ nb})$. On the other hand hadron colliders, such as Tevatron ($p\bar{p}$) at Fermilab or LHC (pp) at CERN, profit from a significantly larger $\sigma_{b\bar{b}} = 100 - 600 \text{ mb}$ at $\sqrt{s} = 2 - 7 \text{ TeV}$ respectively. However, they suffer from a much lower signal to background ratio of $0.2 - 0.6\%$ (*cf.* $25 - 15\%$ at electron-positron colliders), due to the richer hadronic environment. Studies on B -meson physics are currently performed both at B factories such as Belle II at SuperKEKB and at hadron colliders by ATLAS, CMS and LHCb at the LHC. These studies are proving crucial for the advance of our knowledge on the Standard Model and to shape its possible extensions, as will be shown in the following chapters of this thesis.

The weak isospin partner of the b -quark, although predicted in 1977 with the discovery of the $\Upsilon(1S)$, was found only several years later: the top quark, which is the sixth and quite possibly last quark to be encapsulated in the Standard Model, was discovered in 1995 by the CDF [62] and D0 [63] experiments at Fermilab. The top quark plays a special role in the Standard Model picture since it behaves differently from all other quarks. In fact, its large mass, and correspondingly short lifetime ($\simeq 1/20$ the timescale for strong interactions), causes the top quark to decay before it hadronises, offering the opportunity to study its "bare" decay properties.

Moreover, from the sensitivity of electroweak observables to the mass of the top quark, the mass of the Higgs boson can be constrained without directly producing it.

It wasn't until 2012 that the first signature of a scalar particle was observed by the ATLAS [64] and CMS [65] collaborations each using $\sim 10 \text{ fb}^{-1}$ of pp collisions collected in 2011 and 2012 at the LHC. The decay channel for discovery of the Higgs particle was the $H \rightarrow \gamma\gamma$ indicating that a boson with a spin different from one was observed, hence it was compatible with the Standard Model predicted Higgs. In the years after its first observation, processes of vector boson fusion VVH [66,67] and the Higgs coupling to the top [68,69], bottom quarks [70,71] and τ leptons [72,73] were observed, confirming that the Higgs mechanism is actually responsible for the mass of the particles in the Standard Model. With the discovery of the Higgs particle, the long sought missing piece found its place in the Standard Model puzzle.

In the next section a more formal description of the structure of the Standard Model is given.

1.2 The Standard Model

*As far as I see,
all a priori statements in physics
have their origin in symmetry.*

H. Weyl

*C'est la dissymétrie, qui crée le
phénomène.*

P. Curie

1.2.1 The electroweak sector

1.2.1.1 Assigning particles to representations of $SU(2)_L \times U(1)_Y$

The experimental evidences collected up to the 1960's on weak and electromagnetic interactions (charged currents couple only with left-handed fermions, the existence of a massless photon and a neutral Z), except for the masses of the force mediators and the fermions, were encapsulated by S. Glashow in a Lagrangian that is symmetric under $SU(2)_L \times U(1)_Y$. In this model, representation of lepton fields are assigned according to their handedness:

$$L_L \equiv \frac{1}{2}(1 - \gamma_5) \begin{pmatrix} \nu_\ell^i \\ \ell^i \end{pmatrix} = \begin{pmatrix} \nu_{\ell L}^i \\ \ell_L^i \end{pmatrix}, \quad \ell_R^i \equiv \frac{1}{2}(1 + \gamma_5)\ell^i \quad (1.21)$$

The same applies for quarks:

$$Q_L^i \equiv \frac{1}{2}(1 - \gamma_5) \begin{pmatrix} u^i \\ d^i \end{pmatrix} = \begin{pmatrix} u_L^i \\ d_L^i \end{pmatrix}, \quad u_R^i \equiv \frac{1}{2}(1 + \gamma_5)u^i, \quad d_R^i \equiv \frac{1}{2}(1 + \gamma_5)d^i \quad (1.22)$$

Here, and throughout this section, $i = 1, 2, 3$ denotes the generation number. The weak isospin group $SU(2)_L$ is characterized by three generators, hence this gives rise to three gauge bosons, W^1, W^2 and W^3 and the coupling g . The generators t^a are the Pauli matrices $\sigma^a/2$ when acting on the gauge doublets and $t^a \equiv 0$ when acting on the gauge singlets. As far as the weak hypercharge $U(1)_Y$ is concerned, only one generator

is present, the gauge boson B with coupling g' and hypercharge $Y(\psi)$ whose value depends on the corresponding field.

The corresponding kinetic Lagrangian for the fermion fields reads

$$\begin{aligned} \mathcal{L}_\psi &= i\bar{L}_L^i \not{D} L_L^i + i\bar{Q}_L^i \not{D} Q_L^i \\ &+ i\bar{\ell}_R^i \not{D} \ell_R^i + i\bar{u}_R^i \not{D} u_R^i + i\bar{d}_R^i \not{D} d_R^i \end{aligned} \quad (1.23)$$

The covariant derivative in Eq. (1.23), which generates the interactions between the gauge bosons and the fermion fields, is defined as:

$$D^\mu = \partial^\mu - igW_i^\mu t_i - ig'B^\mu \frac{Y(\psi)}{2} \quad (1.24)$$

Any fermion mass term of the kind

$$m\bar{\psi}\psi = m(\bar{\psi}_L\psi_R + \bar{\psi}_R\psi_L) \quad (1.25)$$

is not admitted in Eq. (1.23) since it would spoil the gauge invariance of the theory. It is interesting to note that at this stage gauge bosons of $SU(2)_L \times U(1)_Y$ couple equally to charged fermions, or in other words, that the charges g, g' appearing in Eq. (1.2.1.2) do not depend on the fermion generations. Let's restrict our focus on leptonic terms, the extension to the quark sector is (for the moment) trivial. The Lagrangian in Eq. (1.23) is splitted in three parts:

$$\mathcal{L}_\psi = \mathcal{L}_\psi^{\text{kin}} + \mathcal{L}_\psi^{\text{cc}} + \mathcal{L}_\psi^{\text{nc}} \quad (1.26)$$

- A kinematic part containing the derivatives of the field, $\mathcal{L}_\psi^{\text{kin}}$:

$$\mathcal{L}_\psi^{\text{kin}} = i\bar{L}_L^i \not{D} L_L^i + i\bar{\nu}_{\ell R}^i \not{D} \nu_{\ell R}^i + i\bar{\ell}_R^i \not{D} \ell_R^i \quad (1.27)$$

- One involving only charged currents, $\mathcal{L}_\psi^{\text{cc}}$:

$$\mathcal{L}_\psi^{\text{cc}} = g W_\mu^1 \bar{L}_L^i \gamma^\mu \frac{\sigma_1}{2} L_L^i + g W_\mu^2 \bar{L}_L^i \gamma^\mu \frac{\sigma_2}{2} L_L^i \quad (1.28)$$

Since for example the action of σ^1 on the lepton doublets:

$$\sigma_1 L_L^i = \begin{pmatrix} 0 & 1 \\ 1 & 0 \end{pmatrix} \begin{pmatrix} \nu_L^i \\ \ell_L^i \end{pmatrix} = \begin{pmatrix} \ell_L^i \\ \nu_L^i \end{pmatrix} \implies \bar{L}_L^i \sigma_1 L_L^i = (\bar{\nu}_L^i, \quad \bar{\ell}_L^i) \begin{pmatrix} \ell_L^i \\ \nu_L^i \end{pmatrix} = \bar{\nu}_L^i \ell_L^i + \bar{\ell}_L^i \nu_L^i$$

exchanges $\ell_L^i \leftrightarrow \nu_L^i$. $\mathcal{L}_\psi^{\text{cc}}$ assumes a more familiar form if we take linear combinations of the generators W^1 and W^2 , $W_\mu^\pm = \frac{1}{\sqrt{2}}(W_\mu^1 \mp iW_\mu^2)$ allows to rewrite $\mathcal{L}_\psi^{\text{cc}}$ in a more familiar way:

$$\mathcal{L}_\psi^{\text{cc}} = \frac{g}{\sqrt{2}} \left[W_\mu^+ \bar{\nu}_L^i \gamma^\mu \ell_L^i + W_\mu^- \bar{\ell}_L^i \gamma^\mu \nu_L^i \right] \quad (1.29)$$

Where $W_\mu^\pm = \frac{1}{\sqrt{2}}(W_\mu^1 \pm iW_\mu^2)$ and $\sigma^\pm = \frac{1}{2}(\sigma^1 \pm i\sigma^2)$, ($\sigma^\pm \in \mathbb{R}$ and the i has entered the definition of W^\pm).

- And finally one involving only neutral currents $\mathcal{L}_\psi^{\text{nc}}$

$$\begin{aligned} \mathcal{L}_\psi^{\text{nc}} = & \frac{g}{2} W_\mu^3 \left[\bar{\nu}_L^i \gamma^\mu \nu_L^i - \bar{\ell}_L^i \gamma^\mu \ell_L^i \right] + \frac{g'}{2} B_\mu \left[Y(L) \left(\bar{\nu}_L^i \gamma^\mu \nu_L^i + \bar{\ell}_L^i \gamma^\mu \ell_L^i \right) \right. \\ & \left. + Y(\ell_R^i) \left(\bar{\ell}_R^i \gamma^\mu \ell_R^i \right) \right] \end{aligned} \quad (1.30)$$

Since it involves the diagonal $SU(2)_L$ generators t^3 .

1.2.1.2 Electroweak unification

If we focus on $\mathcal{L}_\psi^{\text{nc}}$ of Eq. (1.30), neither W_μ^3 nor B_μ can be interpreted as the photon field A_μ , since they couple to the neutrino. However since the fields are still massless, they can be rotated by means of an orthogonal matrix without affecting the Lagrangian. To do this, $\mathcal{L}_\psi^{\text{nc}}$ can be more conveniently expressed as:

$$\mathcal{L}_\psi^{\text{nc}} = g \bar{\Psi} \gamma^\mu \mathcal{T}_3 \Psi W_\mu^3 + g' \bar{\Psi} \gamma^\mu \frac{\mathcal{Y}}{2} \Psi B_\mu \quad (1.31)$$

With:

$$\Psi = \begin{pmatrix} \nu_L^i \\ \ell_L^i \\ \ell_R^i \end{pmatrix}, \quad \mathcal{T}_3 = \text{diag}(1/2, -1/2, 0), \quad \mathcal{Y} = \text{diag}(Y(\nu_L^i), Y(\ell_L^i), Y(\ell_R^i))$$

By performing a rotation of the fields B_μ and W_μ^3 by the Weinberg angle θ_W :

$$\begin{aligned} B_\mu &= A_\mu \cos \theta_W - Z_\mu \sin \theta_W \\ W_\mu^3 &= A_\mu \sin \theta_W + Z_\mu \cos \theta_W \end{aligned} \quad (1.32)$$

The Lagrangian in Eq. (1.31) is rewritten as

$$\mathcal{L}_\psi^{\text{nc}} = \bar{\Psi} \gamma^\mu \underbrace{\left[g \sin \theta_W \mathcal{T}_3 + g' \cos \theta_W \frac{\mathcal{Y}}{2} \right]}_{|e|\mathcal{Q}} \Psi A_\mu + \bar{\Psi} \gamma^\mu \left[g \cos \theta_W \mathcal{T}_3 - g' \sin \theta_W \frac{\mathcal{Y}}{2} \right] \Psi Z_\mu \quad (1.33)$$

A_μ can be identified with the photon field if

$$g \sin \theta_W \mathcal{T}_3 + g' \cos \theta_W \frac{\mathcal{Y}}{2} = |e|\mathcal{Q}, \quad \mathcal{Q} = \text{diag}(0, -1, 0, -1) \quad (1.34)$$

Hence $e = g' \cos \theta_W = g \sin \theta_W$ relating the electric charge to g and g' . Substituting this relation in Eq. (1.34) yields the Gell-Mann Nishijima formula $\mathcal{Q} = \mathcal{T}_3 + \frac{\mathcal{Y}}{2}$ (See Eq. (1.17)), which connects the third component of the weak isospin and electric charge to the hypercharges $Y(\psi)$. Up to now we did not include strong interactions in our treatment, however the inclusion of QCD is obtained by requiring the Lagrangian of Eq. (1.23) to be invariant under $SU(3)_C$, the gauge symmetry is then extended to:

$$G_{\text{SM}} = SU(3)_C \times SU(2)_L \times U(1)_Y \quad (1.35)$$

And the covariant derivative is extended:

$$D^\mu = \partial^\mu - g_s G_\mu^a \lambda_a - ig W_i^\mu t_i - ig' B^\mu \frac{Y(\psi)}{2} \quad (1.36)$$

to include the gluon fields G_μ^a . The λ_a are the generators of $SU(3)_C$, the Gell-Mann matrices, when acting on quark fields or $\lambda_a \equiv 0$ when acting on lepton fields. The assignments of fermion fields to multiplets of the SM gauge symmetries, and their corresponding charges, are summarised in Tab. (1.1). The model can be extended to include a right handed neutrino, however, as can be seen in Tab. (1.1), being a singlet under the SM gauge group, it is completely decoupled from SM fields.

Any mass term for the force mediators would spoil the gauge symmetry of the Lagrangian, this is in contradiction with experimental evidence of a short range weak interaction. Moreover, since the structure constants for $SU(2)_L$ are non zero, the theory

Table 1.1 Organisation of the fermion content of the SM in multiplets of $SU(3)_C \times SU(2)_L \times U(1)_Y$.

	$i = 1$	$i = 2$	$i = 3$	$SU(3)_C$	$SU(2)_L$	$U(1)_Y$	$Q = T_3 + \frac{Y}{2}$
Q_L^i	$\begin{pmatrix} u_L \\ d_L \end{pmatrix}$	$\begin{pmatrix} c_L \\ s_L \end{pmatrix}$	$\begin{pmatrix} t_L \\ b_L \end{pmatrix}$	3	2	$+\frac{1}{3}$	$+\frac{2}{3}$ $-\frac{1}{3}$
u_R^i	u_R	c_R	t_R	3	1	$+\frac{4}{3}$	$+\frac{2}{3}$
d_R^i	d_R	d_R	d_R	3	1	$-\frac{2}{3}$	$-\frac{1}{3}$
L_L^i	$\begin{pmatrix} \nu_{eL} \\ e_L \end{pmatrix}$	$\begin{pmatrix} \nu_{\mu L} \\ \mu_L \end{pmatrix}$	$\begin{pmatrix} \nu_{\tau L} \\ \tau_L \end{pmatrix}$	1	2	-1	0 -1
ν_R^i	ν_{eR}	$\nu_{\mu R}$	$\nu_{\tau R}$	1	1	0	0
e_R^i	e_R	μ_R	τ_R	1	1	-2	-1

will present cubic $W^+ + W^- \rightarrow \gamma/Z^0$ and quartic gauge bosons $W^+ + W^- \rightarrow W^+ + W^-$ interactions arising from the Yang-Mills Lagrangian:

$$\mathcal{L}_{\text{YM}}^{\text{kin}} = -\frac{1}{4}B_{\mu\nu}B^{\mu\nu} - \frac{1}{4}W_{\mu\nu}^i W^{i\mu\nu} \quad (1.37)$$

Where:

$$B_{\mu\nu} = \partial_\nu B_\mu - \partial_\mu B_\nu \quad (1.38)$$

$$W_{\mu\nu}^i = \partial_\nu W_\mu^i - \partial_\mu W_\nu^i - g\epsilon^{ijk}W_\mu^j W_\nu^k \quad (1.39)$$

These processes are of interest since amplitudes for elastic scattering of longitudinally polarised gauge bosons, such as for example $W_L^+ + W_L^- \rightarrow W_L^+ + W_L^-$ violate the unitarity bounds, if we include only the vertices appearing in the kinetic part of the gauge fields.

If we admit massive gauge bosons, in the $s \gg m_W^2$ limit, the amplitude is of the form:

$$\mathcal{M}(W_L^+ + W_L^- \rightarrow W_L^+ + W_L^-) \simeq \frac{g^2}{4m_W^2}(s + t) \quad (1.40)$$

Expanding the matrix element on partial waves, and taking the zero-th order term $a_0(s)$ we find

$$a_0(s) = \frac{1}{32\pi} \int_{-1}^1 dz P_0(z) \frac{g^2 s}{4m_W^2} (1+z) = \frac{G_F s}{16\sqrt{2}\pi} \quad (1.41)$$

Having used the relation $\frac{G_F}{\sqrt{2}} = \frac{g^2}{8m_W^2}$. The unitarity bound of Eq. (1.126) imposes that $|a_0(s)| \leq 1$, hence the vector boson model breaks down for $\sqrt{s} \gtrsim 2.5$ TeV if no additional diagram is considered in the process of longitudinal vector boson scattering.

1.2.2 Spontaneous symmetry breaking

In the Standard Model, fermion and gauge bosons masses arise from the spontaneous breaking of gauge invariance. In this mechanism, the mass terms arise from the kinetic energy term of a complex scalar doublet ϕ that undergoes a spontaneous symmetry breaking process. We introduce the four Hermitian fields, disposed in an $SU(2)_L$ doublet with hypercharge $Y(\phi) = 1$:

$$\phi = \begin{pmatrix} \phi^+ \\ \phi^0 \end{pmatrix} = \begin{pmatrix} \phi_1 + i\phi_2 \\ \phi_3 + i\phi_4 \end{pmatrix} \quad (1.42)$$

and add the following terms to the Standard Model Lagrangian, without breaking $SU(2)_L \times U(1)_Y$ gauge invariance:

$$\mathcal{L}_{\text{Higgs}} = (D_\mu \phi)^\dagger (D_\mu \phi) - V(\phi^\dagger \phi) \quad (1.43)$$

with:

$$V(\phi^\dagger \phi) = -\mu^2 \phi^\dagger \phi + \lambda (\phi^\dagger \phi)^2, \quad [\mu] = 1, [\lambda] = 0 \quad (1.44)$$

and the covariant derivative D_μ is defined as:

$$D_\mu = \partial_\mu - igW_\mu^i t^i - ig' \frac{Y(\phi)}{2} B_\mu \quad (1.45)$$

The idea at the basis of spontaneous symmetry breaking is that the lowest energy (vacuum) state does not respect the gauge symmetry and induces effective masses for particles propagating through it. The vector

$$v = \begin{pmatrix} \langle \phi_1 \rangle \\ \langle \phi_2 \rangle \\ \langle \phi_3 \rangle \\ \langle \phi_4 \rangle \end{pmatrix} = \text{constant} \quad (1.46)$$

whose components are the vacuum expectation values (VEV) of the scalar fields, are constants due to the fact that space is isotropic, and scalars since it is Lorentz invariant. Written in the basis Eq. (1.42), $V(\phi^\dagger \phi)$ is $O(4)$ invariant:

$$V(\phi) = -\frac{\mu^2}{2} \left(\sum_i^4 \phi_i^2 \right) + \lambda \left(\sum_i^4 \phi_i^2 \right)^2 \quad (1.47)$$

hence we can choose an axis in four-dimensional space such that $\langle \phi_i \rangle = 0$, for $i = 1, 2, 4$ and $\langle \phi_3 \rangle = \nu$. To determine ν we minimise $V(v)$:

$$V(\phi) \rightarrow V(v) = -\frac{1}{2}\mu^2\nu^2 + \lambda\nu^4 \quad (1.48)$$

If $\mu^2 < 0$ the minimum occurs at $\nu = 0$ which corresponds to empty space and $SU(2)_L \times U(1)_Y$ is unbroken at the minimum. On the other hand, if $\mu^2 > 0$ the $\nu = 0$ point is unstable, and the minimum of the potential appears at some non-zero value of ν which breaks the $SU(2)_L \times U(1)_Y$ symmetry.

$$V'(\nu) = \nu(-\mu^2 + \lambda\nu^2) = 0 \quad \rightarrow \quad \nu^2 = \frac{\mu^2}{2\lambda} \quad (1.49)$$

The vacuum state is degenerate in the sense that the solution ν can be brought in the solution $-\nu$ by a proper $O(4)$ transformation. Adding the Higgs field to the Lagrangian still leaves it $SU(2)_L \times U(1)_Y$ gauge invariant until the vacuum expectation value $\langle \phi_3 \rangle = \nu$ assumes a non-zero value and picks one of the degenerate vacuum configurations. Picking as the vacuum state

$$\phi \rightarrow \frac{1}{\sqrt{2}} \begin{pmatrix} 0 \\ \nu \end{pmatrix} \equiv v \quad (1.50)$$

The generators of $SU(2)_L \times U(1)_Y$, t_a and Y are broken, in fact:

$$\begin{aligned} \sigma^1 v &= \begin{pmatrix} 0 & 1 \\ 1 & 0 \end{pmatrix} \begin{pmatrix} 0 \\ \nu/\sqrt{2} \end{pmatrix} \neq 0, & \sigma^2 v &= \begin{pmatrix} 0 & -i \\ i & 0 \end{pmatrix} \begin{pmatrix} 0 \\ \nu/\sqrt{2} \end{pmatrix} \neq 0 \\ \sigma^3 v &= \begin{pmatrix} 1 & 0 \\ 0 & -1 \end{pmatrix} \begin{pmatrix} 0 \\ \nu/\sqrt{2} \end{pmatrix} \neq 0, & Y v &= Y(\phi) \begin{pmatrix} 0 \\ \nu/\sqrt{2} \end{pmatrix} \neq 0 \end{aligned} \quad (1.51)$$

The electric charge operator $\hat{Q} = T_3 + Y/2$ on the electrically neutral vacuum state leaves it invariant

$$\hat{Q}v = \frac{1}{2}(\sigma^3 + Y) \begin{pmatrix} 0 \\ \nu/\sqrt{2} \end{pmatrix} = \frac{1}{2} \begin{pmatrix} Y(\phi) + 1 & 0 \\ 0 & Y(\phi) - 1 \end{pmatrix} \begin{pmatrix} 0 \\ \nu/\sqrt{2} \end{pmatrix} \stackrel{Y(\phi)=1}{=} 0 \quad (1.52)$$

The unbroken generator of the electromagnetic charge gives rise to the residual $U(1)_{EM}$ symmetry. Rescaling and translating the doublet in Eq. (1.42)

$$\phi = \begin{pmatrix} \phi^+ \\ \phi^0 \end{pmatrix} = \frac{1}{\sqrt{2}} \exp \left[\frac{i\sigma_i \theta^i(x)}{\nu} \right] \begin{pmatrix} 0 \\ \nu + H(x) \end{pmatrix} \quad (1.53)$$

We can rotate away the fields $\theta^i(x)$ by an $SU(2)_L$ gauge transformation.

$$\phi \rightarrow \phi' = U(x)\phi = \frac{1}{\sqrt{2}} \begin{pmatrix} 0 \\ \nu + H(x) \end{pmatrix} \quad (1.54)$$

With $U(x) = \exp \left[-\frac{i\sigma_i \theta^i(x)}{\nu} \right]$. This gauge choice (unitary gauge) is equivalent to absorbing the three would-be Goldstone modes $\theta^i(x)$ which are "eaten up" by the three vector bosons W^\pm, Z that acquire a mass. Expanded around the vacuum state, the terms in the $\mathcal{L}_{\text{Higgs}}$ Eq. (1.43) are rewritten as:

$$V(\phi^\dagger\phi) = \underbrace{\frac{1}{2}(2\lambda\nu^2)H^2}_{(1.)} + \underbrace{\lambda\nu H^3 + \frac{\lambda}{4}H^4}_{(2.)} - \underbrace{\frac{\lambda\nu^4}{4}}_{(3.)} \quad (1.55)$$

- (.1) This term encodes the mass of the scalar field, $m_H = \sqrt{2\lambda}\nu$. The electroweak breaking scale ν is predicted by the theory, however the quartic coupling λ is unknown, so m_H is also not predicted.
- (.2) Cubic and quartic Higgs field self-interactions appear in the Lagrangian
- (.3) This constant term reflects the fact that V was chosen such that $V(0) = 0$, and therefore $V < 0$ at the minimum, and is discarded as an overall constant term, however this poses a problem when gravity is included since this vacuum energy density term is related to the cosmological constant.

and:

$$(D_\mu\phi)^\dagger(D_\mu\phi) \supset \left(\underbrace{1}_{(1.)} + \underbrace{\frac{H}{\nu}}_{(2.)} \right)^2 \left[\underbrace{\left(\frac{g\nu}{2}\right)^2}_{m_W^2} W_\mu^+ W^{-,\mu} + \frac{1}{2} \underbrace{\frac{\nu^2(g^2 + g'^2)}{4}}_{m_Z^2} Z_\mu Z^\mu \right] \quad (1.56)$$

- (.1) The the gauge bosons (W^\pm) and Z have acquired masses

$$m_W^2 = \frac{g^2\nu^2}{4}, \quad m_Z^2 = \frac{\nu^2(g^2 + g'^2)}{4} = \frac{m_W^2}{\cos^2\theta_W} \quad (1.57)$$

but thanks to the requirement of $Y(\phi) = 1$ the photon field A_μ did not. Moreover, by linking the Fermi theory of Eq. (1.11) with the electroweak model an explicit estimate of ν can be made:

$$\frac{G_F}{\sqrt{2}} = \left(\frac{g}{2\sqrt{2}} \right)^2 \frac{1}{m_W^2} \implies \nu = \sqrt{\frac{1}{\sqrt{2}} G_F} \quad (1.58)$$

Which from precise measurements of the μ decay time yields the electroweak breaking scale $\nu \simeq 246$ GeV. Below this scale, the gauge bosons "naturally" acquire their mass. Having measured $\sin^2 \theta_W \sim 0.23$ from neutral current scattering experiments, and $\alpha \sim 1/137$ being the fine structure constant

$$m_W = m_Z \cos \theta_W \sim \frac{(\pi\alpha/\sqrt{2}G_F)^{1/2}}{\sin \theta_W} \quad (1.59)$$

The masses of the gauge bosons are expected to be $m_W \sim 78$ GeV and $m_Z \sim 89$ GeV

- (.2) Cubic and quartic Higgs field self-interactions appear in the Lagrangian. In particular the cubic HVV couplings

$$\mathcal{L}_{\text{HVV}} \supset \underbrace{\frac{1}{2}g^2\nu W^{+\mu}W_\mu^-}_\propto m_W H + \underbrace{\frac{g\sqrt{g^2+g'^2}\nu}{4\cos\theta_W} Z^\mu Z_\mu^-}_\propto m_Z H \quad (1.60)$$

which induce vector boson fusion processes (VBF), are a probe of the Standard Model spontaneous symmetry breaking. In particular, their presence in the Lagrangian is a unique indication of the SSB pattern, since a term νHVV with $\nu = 0$ wouldn't have the correct energy dimensions to enter the Lagrangian.

1.2.3 Fermion mass generation and the flavour sector

Before the inclusion of an Higgs doublet, the Standard Model Lagrangian exhibits a *global* $U(3)^5$ flavour symmetry. In fact the kinetic Lagrangian of the fermion fields Eq. (1.23) is invariant for a rotation in flavour space:

$$U(3)^5 = U(3)_{Q_L} \times U(3)_{d_R} \times U(3)_{u_R} \times U(3)_{L_L} \times U(3)_{e_R} \quad (1.61)$$

The SSB mechanism breaks this global symmetry to a smaller symmetry group. The fermions masses are generated through Yukawa interaction terms:

$$\begin{aligned} \mathcal{L}_{\text{Yukawa}} = & - Y_d^{ij} \bar{Q}_L^i \phi d_R^{\prime j} + h.c. \\ & - Y_u^{ij} \bar{Q}_L^i \phi_c u_R^{\prime j} + h.c. \\ & - Y_\ell^{ij} \bar{L}_L^i \phi \ell_R^{\prime j} + h.c. \end{aligned} \quad (1.62)$$

Where

$$\phi_c + i\sigma_2 \phi^* = \frac{1}{\sqrt{2}} \begin{pmatrix} \nu + H(x) \\ 0 \end{pmatrix} \quad (1.63)$$

All terms in Eq. (1.62) are gauge invariant and renormalizable since the Y are dimensionless 3×3 complex matrices in generation space, spanned by the indices i, j . The primed Q'_L, u' and d' indicate that these states are expressed as gauge interaction eigenstates, hence a linear combination of the mass eigenstates u^i, d^i .

After SSB, in unitary gauge, the Yukawa terms become:

$$\begin{aligned} \mathcal{L}_{\text{Yukawa}} = & - \left(1 + \frac{H}{\nu}\right) \left[M_d^{ij} \bar{d}_L^i d_R^{\prime j} + M_u^{ij} \bar{u}_L^i u_R^{\prime j} + M_\ell^{ij} \bar{\ell}_L^i \ell_R^{\prime j} \right] + h.c. \\ = & \mathcal{L}_{\text{Yukawa}}^{\text{quarks}} + \mathcal{L}_{\text{Yukawa}}^{\text{leptons}} \end{aligned} \quad (1.64)$$

Where $M_f^{ij} = Y_f^{ij} \nu / \sqrt{2}$ are 3×3 fermion mass matrices. Gauge symmetry violating mass terms $\propto \bar{\psi}_L \psi_R$ for the fermions have appeared in the Lagrangian.

1.2.3.1 The CKM matrix

We focus first on $\mathcal{L}_{\text{Yukawa}}^{\text{quarks}}$. This Lagrangian exhibits the global symmetry in Eq. (1.61), which is broken to an accidental symmetry by the SSB mechanism:

$$U(3)_{Q_L} \times U(3)_{d_R} \times U(3)_{u_R} \rightarrow U(1)_B \quad (1.65)$$

which reflects baryon number conservation. While $U(3)^3$ has 27 generators (9 real parameters and 18 phases) $U(1)_B$ has only one phase generator. This broken symmetry allows to rotate away 26 unphysical parameters by moving to a more convenient basis. The Yukawa matrices for the quark sector are 3×3 complex matrices, which contain a total of 36 parameters (18 real parameters and 18 phases) so the number of physical parameters reduces to

$$N_{\text{phys}}^{\text{real}} = 18 - 9 = 9, \quad N_{\text{phys}}^{\text{phases}} = 18 - 17 = 1 \quad (1.66)$$

of which 6 are the quark masses, 3 are the CKM matrix mixing angles and 1 is the CP violating phase of the CKM matrix. To identify the physical states, the mass matrices in $\mathcal{L}_{\text{Yukawa}}^{\text{quarks}}$ are diagonalised by separate unitary transformations for the left and the right-handed fields

$$(U_L^f)^\dagger M_f U_R^f = \Lambda^f, \quad f = u, d \quad (1.67)$$

Where the matrix Λ^f has diagonal real and positive entries, the physical quark masses

$$\Lambda^u = \text{diag}(m_u, m_c, m_t), \quad \Lambda^d = \text{diag}(m_d, m_s, m_b) \quad (1.68)$$

These unitary transformations can be reabsorbed in the field definitions rotating from the interaction eigenstates to the mass eigenstates:

$$\bar{f}_L^i M_f^{ij} f_R^j = \underbrace{\bar{f}_L^i U_L^f}_{\bar{f}_L^i} \underbrace{(U_L^f)^\dagger M_f^{ij} U_R^f}_{\Lambda^f} \underbrace{(U_R^f)^\dagger f_R^j}_{f_R^j} = \sum_{i=1}^3 m_f^i \bar{f}_L^i f_R^i, \quad f = u, d \quad (1.69)$$

Adopting the mass eigenstates basis, the quark $\mathcal{L}_{\text{Yukawa}}^{\text{quarks}}$ assumes the form:

$$\mathcal{L}_{\text{Yukawa}}^{\text{quarks}} = - \sum_f m_f \left(1 + \frac{H}{\nu} \right) (\bar{f}_L f_R + \bar{f}_R f_L), \quad f = (u, d, c, s, t, b) \quad (1.70)$$

A few remarks are due at this point:

- A coupling between fermions and the Higgs (Yukawa coupling) has appeared in the Lagrangian, whose strength is proportional to the fermions' mass. This coupling is flavour diagonal and doesn't generate flavour changing Higgs interactions.
- The interaction basis are brought into the mass eigenstates by two unitary rotations. In components:

$$f_L^{\prime j} = (U_L^f)_{ij} f_L^j, \quad f_R^{\prime j} = (U_R^f)_{ij} f_R^j, \quad f = u, d \quad (1.71)$$

These rotations don't affect the kinetic terms since the rotation matrices are space-time independent. However, since we rotated independently the two components of the same $SU(2)_L$ doublet, a flavour non-diagonal coupling between quarks and the W boson arises, for example:

$$\frac{g}{\sqrt{2}} \bar{u}_L^i W^+ d_L^i + h.c. \rightarrow \frac{g}{\sqrt{2}} \bar{u}_L^i \left((U_L^u)^\dagger U_L^d \right)_{ij} W^+ d_L^j \quad (1.72)$$

From which the unitary matrix $V_{\text{CKM}} = (U_L^u)^\dagger U_L^d$ is defined. The CKM matrix V_{CKM} is a complex unitary matrix and its entries are determined experimentally.

1.2.3.2 Lepton masses

Moving to the lepton Yukawas we write

$$\mathcal{L}_{\text{Yukawa}}^{\text{leptons}} = -Y_\ell^{ij} \bar{L}_L^i \phi \ell_R^j - Y_\nu^{ij} \bar{L}_L^i \phi_c \nu_R^j + h.c. \quad (1.73)$$

The second term in this Lagrangian would extend the Glashow-Weinberg-Salam model and generate Dirac type masses for the neutrinos, however, experimental evidence sets upper bounds for the neutrino masses of $\mathcal{O}(0.1)$ eV which is several orders of magnitude smaller than the vacuum expectation value ν implying, $Y_\nu \sim 0$. Alternative mechanisms to the SSB, such as for example the Seesaw mechanism, are possible candidates for explaining the masses of the neutrinos, as well as their peculiar lightness with respect to the other SM fermion fields.

In the SM, where $Y_\nu = 0$, the Lagrangian of Eq. (1.73) exhibits a $U(3)^2$ global symmetry, which is broken to the lepton family number conservation:

$$U(3)^2 = U(3)_{LL} \times U(3)_{eR} \rightarrow U(1)_e \times U(1)_\mu \times U(1)_\tau \quad (1.74)$$

Therefore, in the lepton case, the number of broken generators is 15 which allow to rotate away the same amount of unphysical parameters

$$N_{\text{phys}}^{\text{real}} = 9 - 6 = 3, \quad N_{\text{phys}}^{\text{phases}} = 9 - 9 = 0 \quad (1.75)$$

The three real parameters we are left with are identified as the three charged lepton masses. To see this explicitly let's express Eq. (1.73) in the unitary gauge:

$$\mathcal{L}_{\text{Yukawa}}^{\text{leptons}} = - \left(1 + \frac{H}{\nu} \right) \left[M_{\ell}^{ij} \bar{\ell}_L^i \ell_R^j \right] + h.c. \quad (1.76)$$

Having neglected the neutrino masses, *i.e.* $Y_{\nu} = 0$. In analogy to the quark sector, we rotate to the mass eigenstates basis by a bi-unitary transformation:

$$\Lambda_{\ell} = (U_L^{\ell})^{\dagger} M_{\ell} U_R^{\ell} = \text{diag}(m_e, m_{\mu}, m_{\tau}) \quad (1.77)$$

which allows to write:

$$\ell_L^j = (U_L^{\ell})_{ij} \ell_L^j, \quad \ell_R^j = (U_R^{\ell})_{ij} \ell_R^j \quad (1.78)$$

and:

$$\mathcal{L}_{\text{Yukawa}}^{\text{leptons}} = - \sum_{\ell} m_{\ell} \left(1 + \frac{H}{\nu} \right) (\bar{\ell}_L \ell_R + \bar{\ell}_R \ell_L), \quad \ell = e, \mu, \tau \quad (1.79)$$

The following remarks can be made:

- Since $Y_{\nu} = 0$ in the Standard Model, the three neutrino mass eigenstates are degenerate with eigenvalues 0. There is nothing to distinguish them except weak interactions, so they are simply defined as weak interaction partners of the charged leptons $\nu_e, \nu_{\mu}, \nu_{\tau}$. This freedom allows to align the neutrino mass eigenstates to the charged leptons mass eigenstates:

$$\nu_{\ell L}^j = (U_L^{\ell})_{ij} \nu_{\ell, L}^j \quad (1.80)$$

And the charged current gauge interaction terms read:

$$\frac{g}{\sqrt{2}} \bar{\nu}_L^i W^+ \ell_L^i + h.c. \rightarrow \frac{g}{\sqrt{2}} \bar{\nu}_L^i \underbrace{(U_L^{\ell})_{ji}^* (U_L^{\ell})_{ij}}_{\mathbb{1}} W^+ \ell_L^i + h.c. = \frac{g}{\sqrt{2}} \bar{\nu}_L^i W^+ \ell_L^i + h.c. \quad (1.81)$$

No flavour changing charged currents arise in the leptons sector, hence, in the Standard Model, not only to the total lepton number is conserved, but also the number of leptons of a specific family is (see Eq. (1.74)).

- As opposed to the quark sector, the Yukawa couplings for the leptons are small compared to their gauge couplings.

$$\frac{\sqrt{2}m_\ell}{\nu} \sim \mathcal{O}(10^{-2} - 10^{-6}) \ll g, g' \quad (1.82)$$

in practice, the only terms in the Standard Model Lagrangian which lead to observable differences between the leptons are their masses. This leads to another accidental symmetry in the Standard Model, which is referred to as Lepton Flavour Universality (LFU) which is approximate since it is only broken by kinematic effects in the Standard Model.

1.3 Beyond the Standard Model

*The more original a discovery,
the more obvious it seems afterwards.*

A. Koestler

1.3.1 Unanswered questions in the Standard Model

The Standard Model of electroweak interactions is a renormalizable field theory which predicts or is consistent with a stunning range of experimental facts, from low energy β -decays to high energy collider experiments. As outlined in the previous sections, among the most remarkable achievements for this theory are the ability to predict the existence (and masses) of the W and Z bosons, the existence of the charm quark, as necessitated by the GIM mechanism, and the existence of a third family of fermions, as required by CP violating experimental evidences.

The charged current weak interactions, as described by the generalized Fermi theory, were successfully incorporated, as was quantum electrodynamics. The consistency between theory and experiment indirectly tested the radiative corrections and allowed the successful prediction of the top quark mass and the constraints on the Higgs mass, which were confirmed with its discovery in 2012.

When combined with quantum chromodynamics for the strong interactions, the Standard Model is almost certainly the approximately correct description of the elementary particles and their interactions down to at least 10^{-16} cm.

Nevertheless, there are still fundamental unanswered questions which suggest the necessity for an extension of the Standard Model. A (non exhaustive) list follows:

- Gravity: the gravitational force is not included in a common framework together with the other three fundamental interactions described by the Standard Model. In fact, general relativity is not a quantum theory, and the proposed solutions for a quantum theory of gravity do not yield a renormalizable theory. In addition there is another difficulty related to gravity, namely the cosmological constant in Eq. (1.55). As an overall constant, it has no significance for microscopic interactions, however, it assumes great importance when the Standard Model is extended to include gravity because it couples to the cosmological constant, or vacuum energy density. Given the measured mass of $m_H \sim 125$ GeV, $\Lambda_{\text{SSB}} \sim 10^8$ GeV⁴, however, from cosmological observations, $\Lambda_{\text{obs.}} \sim 10^{-46}$ GeV⁴ [74] and

would involve a cancellation to ~ 50 orders of magnitude precision to link these two quantities. [75]

- Matter-antimatter asymmetry: The Standard Model doesn't have sufficient CP violation sources to explain the observed asymmetry between baryons and antibaryons in the Universe. [76]
- Dark Matter: Several experimental observations have shown that the matter described by the Standard Model is just a small fraction of the matter content of the Universe, the rest corresponds to Dark Matter which possesses only gravitational interactions with the known physics [77,76]. Possible NP candidates for this phenomena are Weakly Interacting Massive Particles (WIMP), and efforts to detect their signatures are carried both at collider, such as for example CMS [78] and fixed target experiments such as XENON [79] (See [80] for a review).
- The hierarchy problem and fine tuning: The tree-level Higgs mass receives corrections due to a top-quark loop [81]

$$\delta m_H^2 = \frac{3G_F m_t^2}{\sqrt{2}\pi^2} \Lambda^2 \sim (0.27\Lambda)^2 \quad (1.83)$$

which are quadratically divergent with respect to the next higher scale in the theory Λ . In absence of a higher scale Λ could be interpreted as an ultraviolet cutoff necessary to render m_H observable. However, experimental observations indicate that the Standard Model is embedded in some larger theory that cuts off the momentum integral at the finite scale of new physics. Hence, the natural scale for m_H would be $\mathcal{O}(\Lambda)$, which in the case of the Planck scale $M_P = G_N^{-1/2} \sim 10^{19}$ GeV or of grand unification theories $M_{\text{GUT}} \sim 10^{16}$ GeV, which is much larger than the measured value. If there is no new physics below these scales then there must be a fine-tuned cancellation between the bare value and the correction, to ~ 30 decimal places. This is known as the fine-tuning problem.

- Evidence for neutrino masses: Since the inception of the Fermi theory of weak interactions, neutrinos played a special role in advancing our understanding of nature. In the Standard Model, the unitary transformation that rotated neutrinos interaction eigenstates to mass eigenstates was chosen to be the same as the one acting on their charged isospin partners. This is possible thanks to their massless-ness in the theory, and renders them undistinguishable if not for the weak interactions they give rise to. However, neutrino flavour oscillations, which

are sensitive to their non-zero masses or mass differences, are experimentally observed (See [82,83] for a review). This gives rise to a mixing matrix V_{PMNS} , with 3 mixing angles and a CP violating phase in the lepton sector. As opposed to its quark counterpart V_{CKM} , V_{PMNS} exhibits a non flavour-diagonal pattern [84,85]. Moreover, given the fact that the neutrinos are the only neutral fermion in the Standard Model, they could receive their mass not only via the Higgs mechanism, but also via a lepton number violating Majorana term. This motivates the huge experimental effort to search for signatures induced by this class of operators such as the neutrinoless double beta decay $0\nu 2\beta$ (See [86] for a review) or lepton flavour violating (LFV) modes such as $\mu^- \rightarrow e^- e^+ e^-$ [87,88].

- The flavour puzzle: The Standard Model has too much arbitrariness to be the final story. If we include neutrino masses the model has 25 free parameters: 20 belong to the flavour sector (12 fermion masses, 6 mixing angles and 2 CP violation phases (+ 2 possible Majorana phases)) while 5 determine the gauge sector with 3 coupling 1 the Higgs mass and 1 VEV. Moreover the Standard Model gives no explanation as to why fermions appear in three generations with such hierarchical pattern of masses, which spans over 10^{-5} orders of magnitude from the top quark to the electron.

The Standard Model is therefore considered an incomplete theory and a huge amount of both experimental and theoretical efforts are addressed to shed light towards its extensions. Experimentally, these efforts can be classified in two complimentary approaches:

- Direct searches: Aim at producing and observing the decay of new particles or mediators. The reach of this approach is limited by the energy in the centre of mass, which has to be enough to produce the new particles on-shell.
- Indirect searches: Aim at observing the indirect effects of NP contributions to SM processes. These contributions would arise from virtual loops which involve new particles or interactions, therefore this approach allows to probe energy scales far beyond those accessible to present particle accelerators in a complimentary way with respect to direct searches.

Both these approaches contribute on constraining the possible shapes New Physics (NP) can assume, which are systematically developed in an Effective Field Theory Framework (EFT).

1.3.2 The Standard Model as a low energy effective theory

1.3.2.1 A systematic approach to identifying the New Physics structure

In presence of NP, the SM is considered as the low energy limit of a more general Lagrangian which includes operators of dimension $d > 4$ which are written in terms of SM fields and suppressed by inverse powers of the NP scale Λ .

This approach is similar to the one that lead Fermi to hypothesise a four-fermion operator between two currents (Fig. 1.1) when formulating his theory of weak interactions. The four-fermion operator is a result of integrating out the unknown heavy degrees of freedom and contracting the W mediator exchange to a contact interaction. In doing so we obtain a dimensionful coupling constant, and a $d > 4$ operator in the Lagrangian. The SM Lagrangian when considered as an Effective Field Theory (EFT) can be written as [89]:

$$\mathcal{L}_{\text{SMEFT}} = \mathcal{L}_{\text{SM}} + \underbrace{\sum_{d>4} \sum_{n=1}^{N_d} \frac{c_n^{(d)}}{\Lambda^{d-4}} Q_n^{(d)}(\text{SM fields})}_{\Delta\mathcal{L}_{d>4}} \quad (1.84)$$

The operators $Q_n^{(d)}$ in $\Delta\mathcal{L}_{d>4}$ respect the gauge symmetries of the SM, and their coefficients are strongly constrained from present data, in particular:

- The only $d = 5$ electroweak structure [90] violates the total lepton number and describes non-vanishing Majorana-type masses for the left handed neutrinos. The upper limits on neutrino masses and lepton number conservation strongly suppress these contributions.
- Given that the Higgs naturally tends to become as heavy as the heaviest degree of freedom in the underlying theory Eq. (1.83), from the Higgs mass measurement we are lead to expect that NP should be characterised by Λ_{NP} of a few TeV. Sizeable contributions should arise for operators involving the Higgs field and fields strongly coupled to the Higgs, such as the third generation quarks. Present data constrains these contributions to $\Delta\mathcal{L}_{d>4}$ to have very small coefficients.
- Experimental observations also impose strong constraints on $d = 6$ operators that do not explicitly violate symmetries of the \mathcal{L}_{SM} such as the ones contributing to flavour-changing processes, if we are to expect $\Lambda_{\text{NP}} \sim \mathcal{O}(\text{TeV})$
- As discussed in Sec. 1.2.3, the SM Lagrangian exhibits *accidental symmetries* leading to baryon number and lepton number conservation. The strong constraints

on baryon and lepton number violating terms (from proton decay time lower limits and smallness of neutrino masses) impose that the $\mathcal{O}(\text{TeV})$ NP terms must preserve those symmetries and suggests a multi-scale structure in the SMEFT.

The hierarchical way in which the flavour symmetry of the gauge sector is broken by Yukawa couplings induces *approximate accidental symmetries* for lighter leptons Eq. (1.82), and the search for their possible violation represents a very sensitive probe to search for physics beyond the Standard Model. The b quark properties (for example its relatively long decay time, and high mass hence large number of available decay modes) render the B meson phenomenology an excellent physics laboratory for indirect BSM searches.

1.3.2.2 $b \rightarrow s\ell^+\ell^-$ transitions

As we have seen in the previous sub-section, EFT allows to factorise effects which are typical of separate physics scales. Hence it becomes handy in describing rare processes involving heavy flavoured meson decays [91], since they are governed by two different energy scales: the electroweak scale, characterised by the (W^\pm, Z) and the top quark masses, and Λ_{QCD} , which is related to the hadronisation processes. By integrating out the heavy degrees of freedom in the SM Lagrangian we obtain an effective theory written in terms of light SM field operators:

$$\mathcal{L}_{eff}^{b \rightarrow s} = \frac{4G_F}{\sqrt{2}} \sum_i \mathcal{C}_i(\mu) \mathcal{Q}_i(\mu) \quad (1.85)$$

Where the \mathcal{C}_i are the effective couplings (Wilson Coefficients, WC) and the index i spans the complete basis of operators \mathcal{Q}_i which give rise to the $b \rightarrow s$ transition. The renormalisation scale μ , which these terms depend on, acts as a separator scale between short distance (perturbative) effects which are embedded in the $\mathcal{C}_i(\mu)$, and the long-distance (non-perturbative) contributions given by the $\mathcal{Q}_i(\mu)$. The modification with respect to the SM predictions due to NP amplitudes is systematically treated by considering their contribution to the \mathcal{C}_i at $\mu \sim m_W$ and subsequently by running the $\mathcal{C}_i(\mu)$ values to lower scales $\mu \sim m_B$ with the use of renormalisation group equations. This leads to a shift in the Wilson coefficients with respect to the SM prediction, in the presence of NP.

$$\mathcal{C}_i = \mathcal{C}_i^{\text{SM}} + \mathcal{C}_i^{\text{NP}} \quad (1.86)$$

The effective Lagrangian inducing FCNC $b \rightarrow s$ transitions can be classified in terms of light SM fields operator content, Lorentz and gauge structures of the couplings as [89]:

$$\mathcal{L}_{\text{eff}}^{b \rightarrow s} = \mathcal{L}_{4(q)}^{b \rightarrow s} + \mathcal{L}_{\text{FCNC}}^{b \rightarrow s} \quad (1.87)$$

The first part $\mathcal{L}_{4(q)}^{b \rightarrow s}$ includes four quark operators inducing $b \rightarrow s q \bar{q}$ processes:

$$\mathcal{L}_{4(q)}^{b \rightarrow s} = 4 \frac{G_F \lambda_t}{\sqrt{2}} \left[\sum_{i=1,2} \mathcal{C}_i(\mu) \mathcal{Q}_i(\mu) \right] + \mathcal{O} \left(\frac{\lambda_u}{\lambda_t} \right) + \mathcal{O}(\mathcal{C}_{3\dots 6}) + h.c. \quad (1.88)$$

Where $\lambda_q = V_{qb}^* V_{qs}$. Here we have used CKM unitarity to express $\lambda_t = -\lambda_c + \mathcal{O}(\lambda_u)$. Four-quark operators such as $\mathcal{Q}_{3\dots 6}$, which induce $b \rightarrow s q \bar{q}$ transition via a gluon exchange (QCD penguins) are characterised by small $\mathcal{C}_i(\mu = m_b)$ within the SM [92], while $\mathcal{Q}_1^{(c)}$ and $\mathcal{Q}_2^{(c)}$ are generated at tree-level by a W exchange. The ones with the largest Wilson coefficients are:

$$\begin{aligned} \mathcal{Q}_1^{(c)} &= (\bar{s}_L \gamma^\mu t^a c_L) (\bar{c}_L \gamma_\mu t^a b_L), \\ \mathcal{Q}_2^{(c)} &= (\bar{s}_L \gamma^\mu c_L) (\bar{c}_L \gamma_\mu b_L), \end{aligned} \quad (1.89)$$

The second part contains relevant operators since they give rise to non-vanishing $b \rightarrow s \ell^+ \ell^-$ tree level matrix elements:

$$\mathcal{L}_{\text{FCNC}}^{b \rightarrow s} = 4 \frac{G_F \lambda_t}{\sqrt{2}} \left[\mathcal{C}_7(\mu) \mathcal{Q}_7(\mu) + \sum_{i=9,10} \sum_{\ell} \mathcal{C}_i^\ell(\mu) \mathcal{Q}_i^\ell(\mu) \right] + \mathcal{O}(g_s \mathcal{C}_8) + h.c. \quad (1.90)$$

$$\begin{aligned} \mathcal{Q}_7 &= \frac{e}{16\pi^2} m_b (\bar{s}_L \sigma^{\mu\nu} b_R) F_{\mu\nu}, \\ \mathcal{Q}_9^\ell &= \frac{e}{16\pi^2} (\bar{s}_L \gamma^\mu b_L) (\bar{\ell} \gamma_\mu \ell), \\ \mathcal{Q}_{10}^\ell &= \frac{e}{16\pi^2} (\bar{s}_L \gamma^\mu b_L) (\bar{\ell} \gamma_\mu \gamma_5 \ell). \end{aligned} \quad (1.91)$$

These operators correspond to the local $b \rightarrow s \gamma$ transition, and $b \rightarrow s \ell^+ \ell^-$ through vector and axial vector lepton currents, respectively. Due to the V-A structure, the set of operators $\mathcal{Q}'_{7,9,10}$ obtained by flipping the chirality of the quark spinors in Eq. (1.91) are strongly suppressed within the SM. This is also valid for the scalar currents:

$$\mathcal{Q}_{S_1}^\ell = \frac{e}{16\pi^2}(\bar{s}_L b_R)(\bar{\ell}_R \ell_L), \quad \mathcal{Q}_{S_2}^\ell = \frac{e}{16\pi^2}(\bar{s}_R b_L)(\bar{\ell}_L \ell_R) \quad (1.92)$$

Which receive strong helicity suppression in the SM due to the smallness of the lepton masses. Moreover, the smallness of the SM Yukawa couplings for leptons is reflected in the fact that $\mathcal{C}_i^\ell(\mu)$ is independent on the lepton generation ℓ . All of these stringent constraints motivate the search for deviations from SM predictions in the Wilson coefficients appearing in the SMEFT describing $b \rightarrow s\ell^+\ell^-$ transitions.

1.3.2.3 Sandwiching the currents

The decay amplitudes for exclusive B decays are obtained in terms of expectation values of the effective operators \mathcal{Q}_i [89,93]:

$$\mathcal{M}(B \rightarrow H_s \ell^+ \ell^-) = \langle H_s \ell^+ \ell^- | \mathcal{Q}_i | B \rangle \quad (1.93)$$

Where H_s is a meson containing a strange quark. These matrix element encode the long-distance (non perturbative) QCD effects, two are the dominant sources of uncertainties on their determination:

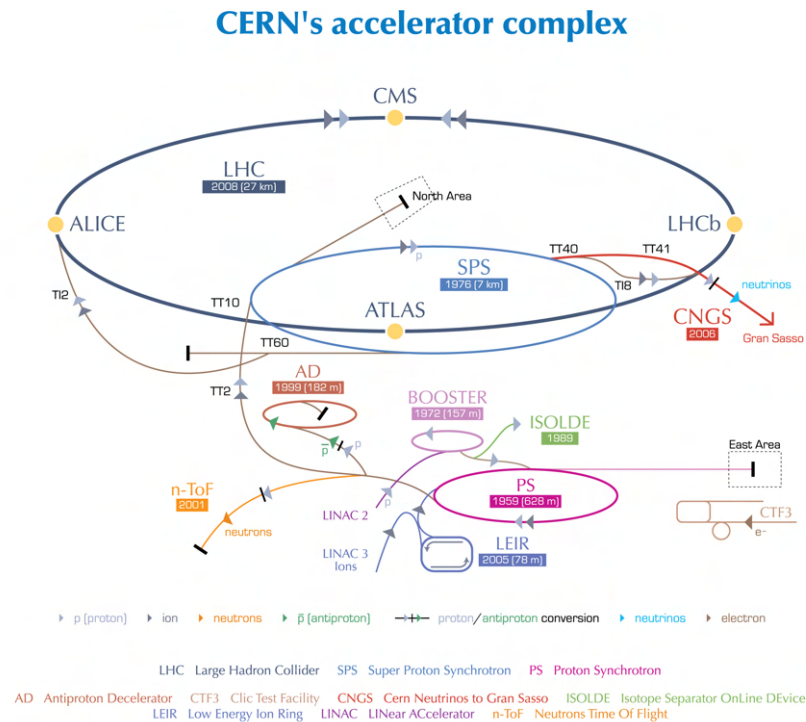
- Form factors: For bilinear quark operators, such as for example $\mathcal{Q}_{9,10}^\ell$, the hadronic and leptonic currents in the matrix element factorise as $\mathcal{M} = H_{\mu\nu} L^{\mu\nu}$. While the lepton current is treated perturbatively, the $H_{\mu\nu}$ is expressed in terms of non-perturbative scalar functions, indicated as *QCD form factors*, and are expressed as combinations of the B and H_s meson momenta which give $H^{\mu\nu}$ a Lorentz covariant form. Despite the non-perturbative nature of the form factors, important theoretical efforts for are carried out to obtain them from Light Cone Sum Rules [94,95] (valid at low $q^2 = (p_B - p_{H_s})^2$) or Lattice QCD (valid at high q^2) [96].
- Charm-loop effects: The factorisation that allowed to separate hadronic and leptonic currents doesn't hold for four-quark operators. The situation gets complicated by the fact that $\mathcal{Q}_{1,2}^{(c)}$ arise at tree level in the SM, hence their coefficients are large. These effects, which are indicated as *charm-loop*, are estimated by means of a Λ_{QCD}/m_c expansion [97] or by a more general data driven method based on analyticity of the function describing them [98]. Both estimates suggest these effect are small, however, since there is no general consensus on the hypothesis at their basis, they are affected by large theoretical uncertainties.

Nonetheless, the fact that these non-perturbative uncertainties are lepton flavour universal allows to build observables and test statistics which cancel their impact on the results, as will be shown in the following chapters. In the next section measurements of the observables sensitive to these NP contributions are presented, together with LHCb which is currently the current world leading particle physics experiment in precision of their determination.

1.4 The Large Hadron Collider

*La sapienza è figliuola della
sperienza.*

L. da Vinci



European Organization for Nuclear Research | Organisation européenne pour la recherche nucléaire

© CERN 2008

Fig. 1.5 Schematic view of the accelerator complex at CERN [99]

The Large Hadron Collider (LHC) is a particle accelerator and collider at the European Organisation for Nuclear Research (CERN) laboratory. It is placed in the 27 km circumference tunnel located approximately 100 m underground which previously hosted the Large Electron Positron Collider (LEP). Proton beams circulating at the LHC are first gradually accelerated in the injection chain composed by other accelerators formerly built at CERN for previous experiments, as illustrated in Fig. 1.5 [99], up to the Super Proton Synchrotron (SPS) where they reach an energy of 450 GeV. At this stage they are injected in the concentric LHC rings, where the two proton beams circulate in opposite directions. A complex system of superconducting magnetic multipoles, operating at 1.9 K and producing an 8.3 T magnetic field, bend and focus the beam around its trajectory in the acceleration process. At the design energies of

7 TeV and 14 TeV for Run-I and Run-II,, respectively stable circulating proton beams are focused by the magnets in 2800 bunches, each consisting of 1.15×10^{11} protons and collide at the frequency of bunch crossing (20 – 40 MHz). These parameters contribute directly at reaching the LHC design instantaneous luminosity of $10^{34} \text{ cm}^{-2} \text{ s}^{-1}$.

The proton beams cross at four interaction points where the main experiments are located: ALICE [100], ATLAS [101], CMS [102], LHCb [103]. While ALICE focuses on the study of quark-gluon plasma processes through heavy ion collisions, ATLAS and CMS aim at studying the direct production of NP particles and LHCb is designed to investigate phenomena related to heavy flavour physics.

1.4.1 The LHCb experiment at the LHC

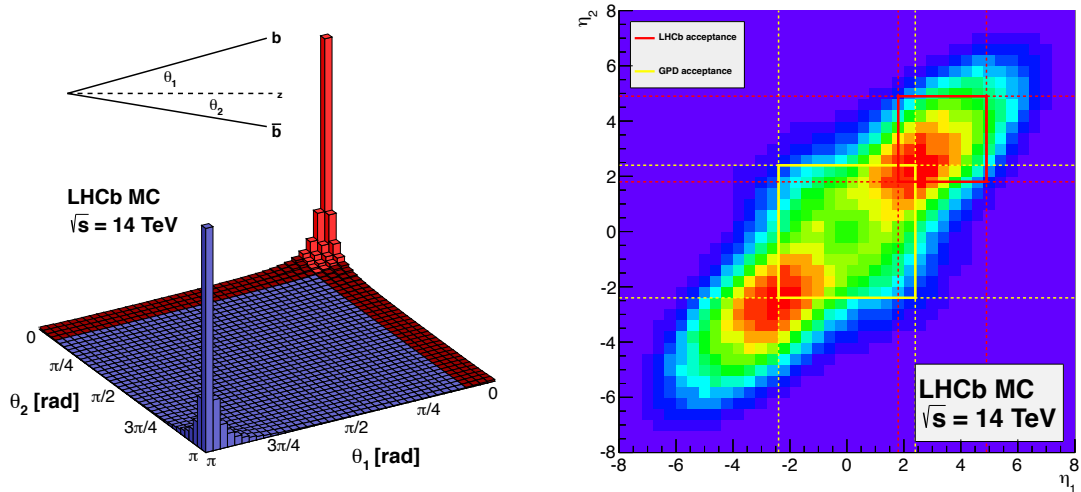


Fig. 1.6 Angular (left) and rapidity (right) correlation between two heavy quarks in $Q\bar{Q}$ production [104], simulated using PYTHIA8 and the CTEQ6 NLO parton distribution functions.

The expected rate for a process is obtained by the product of the luminosity times its corresponding cross section. At leading order, the differential cross section for heavy flavour quark pair production at hadron collisions is given by [105]:

$$\frac{d}{dyd\bar{y}dp_T^2}\sigma(pp \rightarrow Q\bar{Q}) = \frac{\pi}{4m_T^4} \frac{1}{[1 + \cosh(y - \bar{y})]^2} \sigma_{\text{partonic}}(q\bar{q}, gg \rightarrow Q\bar{Q}) \quad (1.94)$$

Where y, \bar{y} are the rapidities of the heavy quark produced, $m_T^2 = p_\perp^2 + m^2$ is the transverse mass. For a fixed value of m_T , the cross section is heavily suppressed when

the difference in rapidity becomes large. This implies once a detector has registered the b quark, there is a large probability that the \bar{b} will be nearby in rapidity as shown in Fig. 1.6.

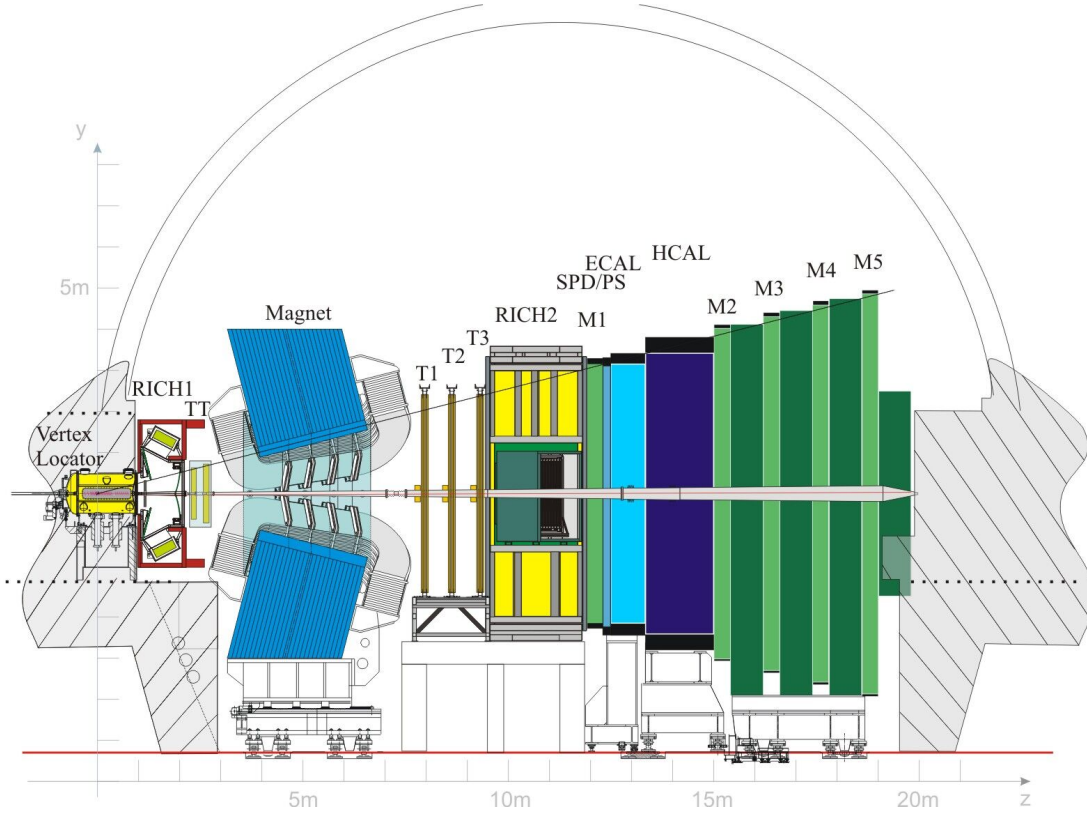


Fig. 1.7 Side view of the LHCb detector [103], the beam is aligned with the z axis

At 14 TeV the total pp cross section is 100 mb, of which inelastic processes amount to 70% [106]. Heavy quark pair production through strong interactions is dominated by $c\bar{c}$ and $b\bar{b}$ pair production with the latter being expected $\sim 500 \mu\text{b}$ at the LHC design energy. Motivated by the strong rapidity correlations between heavy quark pairs produced at high energy, the LHCb detector [103] is a single-arm spectrometer with forward angle coverage of 10 mrad to 300 (250) mrad in the bending (non-bending) plane, corresponding to a pseudorapidity coverage of $2 < \eta < 5$ where $\eta = -\ln[\tan \theta]$ with θ defined as the polar angle with respect to the beam direction (See Fig. 1.7). In the LHCb acceptance, the $b\bar{b}$ pair production cross section was measured to be [107]:

$$\begin{aligned}
\sigma(pp \rightarrow b\bar{b}X)[@ 7 \text{ TeV}] &= 72 \pm 0.3 \pm 6.8 \text{ } \mu\text{b} \\
\sigma(pp \rightarrow b\bar{b}X)[@ 13 \text{ TeV}] &= 144 \pm 1 \pm 21 \text{ } \mu\text{b}
\end{aligned}
\tag{1.95}$$

Which, extrapolated with simulation to the full solid angle correspond to $\sim 295 \text{ } \mu\text{b}$ and $\sim 560 \text{ } \mu\text{b}$ respectively. Hence $\sim 25\%$ of $b\bar{b}$ pairs produced are contained in the detector's acceptance. In such a harsh hadronic environment, the optimal detector performance is obtained by tuning the beam focus at its interaction point independently from the other interaction points. In its Run-I and Run-II data taking periods, the LHCb ran at instantaneous luminosities of $\sim 4 \times 10^{32} \text{ cm}^{-2} \text{ s}^{-1}$, roughly an order of magnitude lower than CMS and ATLAS. Although levelling the luminosity corresponds to reduced interactions rates, it has the advantage of reducing the pile-up (number of pp collisions per bunch crossing), consequently the occupancy in the detector remains low yielding easier to analyse events, and the radiation damage is reduced. This will allow LHCb to maintain the optimal luminosity for the experiment in its subsequent Upgrades. In these conditions roughly $10^5 b\bar{b}$ pairs per second would be produced in LHCb acceptance. The LHCb detector layout can be described by three components, each optimised to maximally exploit the study of beauty and charm hadron decays: a tracking system, a particle identification (PID) and trigger systems:

1.4.1.1 Tracking system

The relatively long ($\mathcal{O}(1 \text{ ps})$) lifetime and the relativistic boost combine to yield an average flight distance of few millimetres for a b -hadron in the detector, therefore the identification of secondary vertices (SV) at short distance from the interaction point is of crucial importance to discriminate b -hadron decays against the underlying event originated by charged particles in the pp collision. An excellent SV resolution is for example required for precision studies of systems with a high oscillation frequencies such as the $B_s - \bar{B}_s$ system. This is achieved by the combined effort of three sub-detectors:

- The VERTex LOcator (VELO): operating at 2×10^{-7} mbar vacuum and at a temperature of -7°C , the VELO consists of 42 silicon microstrip detectors arranged along the beam, each providing a measurement of the r and ϕ charged tracks coordinates, with pitches of $40 - 100 \text{ } \mu\text{m}$. It is the closest sub-detector to the interaction point surrounding the beam at 7 mm from its axis, and for detector safety reasons, it is composed by two retractible semi-circular halves which are

moved close to the beam after the injection and energy ramping procedure is completed. It reaches impact parameter (IP) resolution of $\leq 35 \mu\text{m}$ for particles with $p_T > 1 \text{ GeV}$.

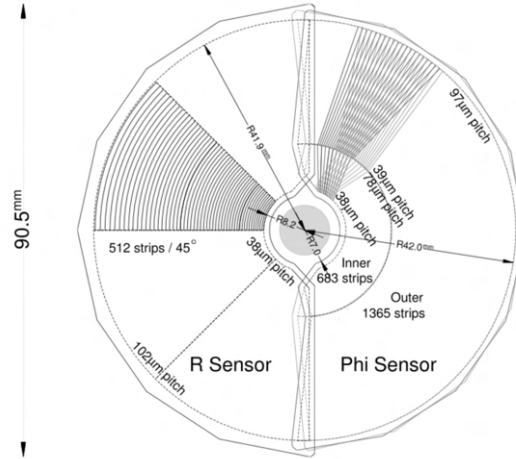


Fig. 1.8 Geometry of the VELO r and ϕ sensors. For the ϕ sensor, strips belonging to two adjacent modules are represented in order to show the stereo angle [103]

- The Silicon Tracker (ST): The Silicon Tracker is composed by two sub-detectors: the Tracker Turicensis (TT) which is located upstream of the magnet and the Inner Tracker (IT), downstream of the bending magnet. Both are equipped with silicon microstrip sensors disposed in a cross-shaped fashion, however while the TT covers the entire acceptance of the detector, with a total effective area of around 8 m^2 , the IT covers a smaller effective area of 4 m^2 . Each of the tracking stations follows a $x - u - v - x$ arrangement with vertical strips in each of the two x layers, and strips rotated by an angle of $\pm 5^\circ$ in the u, v layers (Fig. 1.9). A similar microstrip pitch of $180 - 190 \mu\text{m}$ for both detectors has been chosen to minimise radiation damage and obtain a single hit resolution of $50 \mu\text{m}$.
- The Outer Tracker (OT): The Outer Tracker is the outer part of the downstream tracking station, where the incident particles flux is reduced with respect to the inner regions. It is composed by a coarse array of lower-priced drift tubes filled with a $\text{Ar CO}_2 \text{ O}_2$ (70% - 28% - 2%) gas admixture which guarantees a drift-time $\tau_D < 50 \text{ ns}$ and a resolution on the drift coordinate $\sim 200 \mu\text{m}$. The three modules (T1, T2 and T3) are disposed according to the same stereo angle as the IT/TT and extend the IT active area to fully cover the LHCb acceptance.

The spectrometer magnet (Fig. 1.10), placed between TT and T1, is a warm magnet which provides an integrated field of about 4 Tm and allows to measure the charged

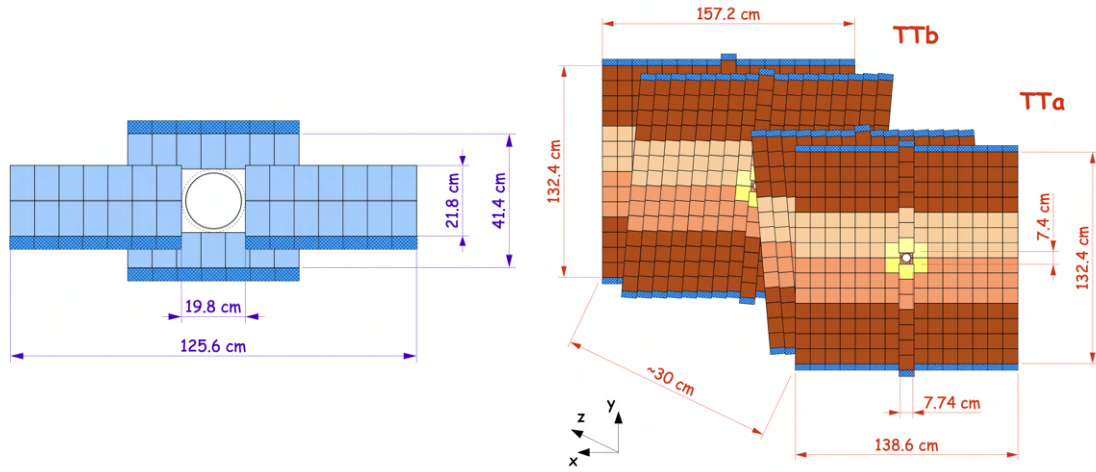


Fig. 1.9 Layout of one TT (left) and of the four TT layers (right) [103]

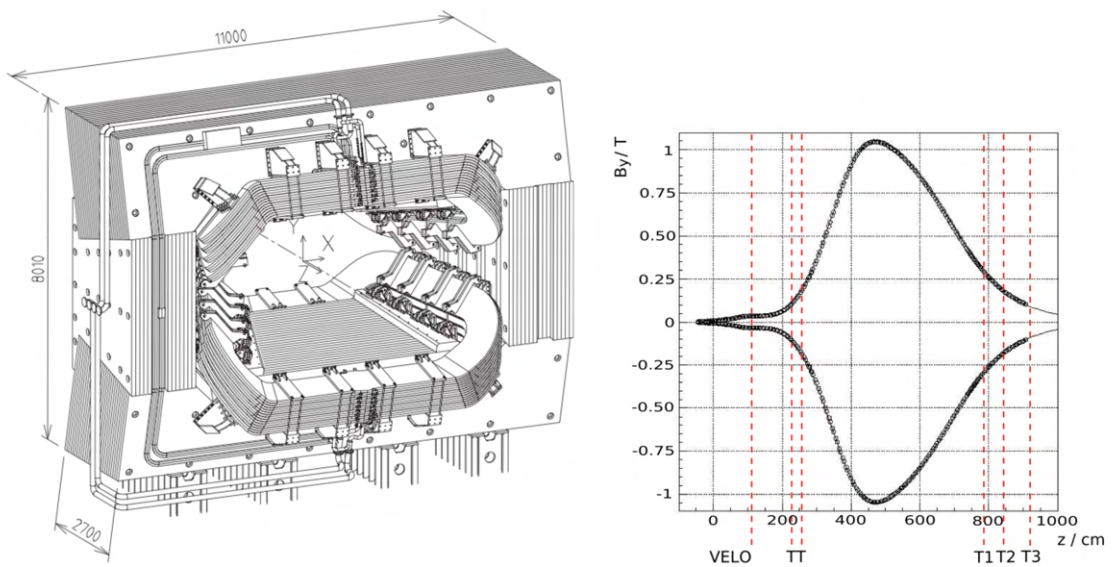


Fig. 1.10 Perspective view of the magnet, with dimensions in millimeters (left) and measured on-axis magnetic field, for both "up" and "down" polarities (right)

particles' momenta with a resolution of $\delta p/p \sim 0.5\%$ for momenta up to 200 GeV by bending their trajectories in the horizontal plane. The current in the magnet is periodically inverted, and comparable amounts of data are collected in each polarity configuration in order to reduce the impact of systematic effects due to detection asymmetries.

1.4.1.2 Particle identification

Excellent particle identification capabilities are fundamental to study heavy hadron decays at LHCb, where the separation between π^\pm - $K^\pm - p$ as well as e^\pm - π^\pm signatures is crucial. The former relies on the information collected at the two Ring Imaging Cherenkov (RICH) detectors, while the latter heavily relies on the information collected at the electromagnetic calorimeters (ECAL) which are detailed in the next subsection. Since the momenta of the B mesons is greater at greater polar angles, two RICH detector subsystems are deployed:

- **RICH1**: Placed between the VELO and the TT, RICH1 covers the entire LHCb acceptance and contains an admixture of aerogel¹ (SO₂) and (C₄F₁₀) which allow a momentum operation range of 1 – 60 GeV. Being placed upstream, light spherical mirrors are employed within the detector acceptance to minimise the material budget, while the optical system is placed outside acceptance, achieving a radiation length (including radiators) of $\simeq 8\%X_0$. Moreover the low angle acceptance is limited by the beam pipe which traverses the detector, the Hybrid Photon Detectors (HPDs) are screened from the dipolar field of the magnet.
- **RICH2**: is located between the last tracking station and the first muon station and equipped with C₄F₁₀ radiator which covers the higher momentum range of 15 – 100 GeV and a limited acceptance of acceptance from ± 15 mrad to ± 120 mrad (horizontal) and ± 100 mrad (vertical).

Cherenkov light is collected by HPDs and its spatial position is measured to obtain information on the particle velocity. This, combined with momentum information from the tracking systems allows to infer the particles mass, and therefore their type (*e.g.* pion, proton, kaon).

¹The aerogel radiator was employed in the RICH detectors only during Run I data taking period

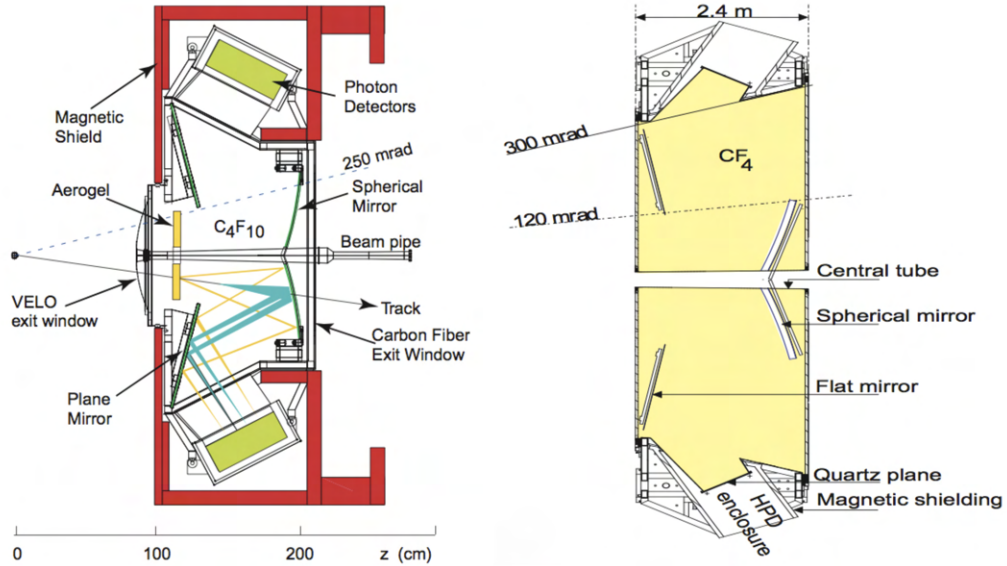


Fig. 1.11 Side view schematic layout of RICH-I (left) and RICH-II (right) detectors [103].

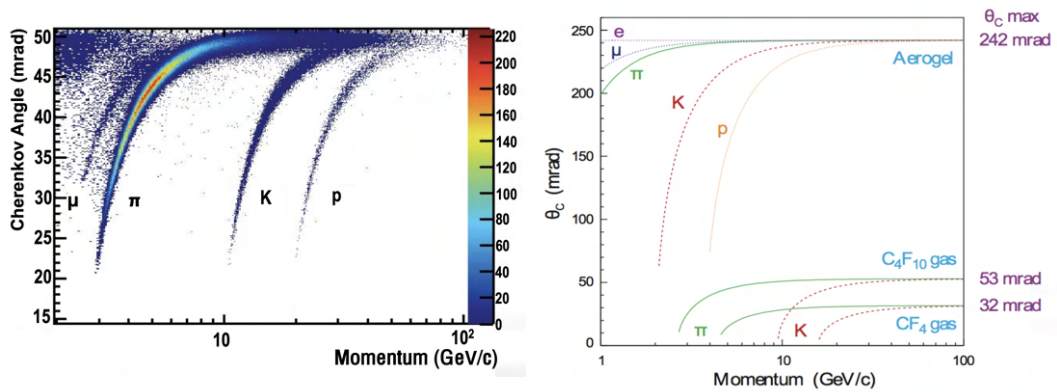


Fig. 1.12 Left: reconstructed Cherenkov angle for isolated tracks as a function of their momentum; the Cherenkov bands for μ , π , K are clearly visible. Right: Same quantity as obtained from simulation, for different particles and radiators.

1.4.1.3 Calorimeters

Calorimeters are of paramount importance at the LHCb detector since they are deputed to e^\pm - π^\pm discrimination, to energy and position measurement of electrons photons and hadrons, and to selection of candidates with high transverse energy at the first (hardware) trigger level (L0) deciding after just 4 μ s after the interaction took place. In particular The stringent performance requirements define the general structure and the characteristics of the calorimeter system and the associated electronics. The calorimeter system is composed of three main components:

- The Scintillating Pad Detector (SPD) and Preshower (PS) detectors. The SPD improves the separation of electrons and photons before entering the calorimeters while the PS, placed after a $2.5X_0$ (15 mm) lead converter, improves the electron/charged pion separation by measurement of the longitudinal partitioning of the EM shower.
- An Electromagnetic Calorimeter (ECAL): the π^\pm/e^\pm separation relies heavily on the ECAL which is composed by alternating layers of scintillators and lead. At this point the major background component for triggers based on the electron signature in the calorimeter is still dominated by upstream γ conversions for which no PID information is available yet, this requires full containment of the EM showers for optimal energy resolution, hence the thickness of the ECAL of 25 radiation lengths (X_0). The granularity of the ECAL in the transverse dimension increases with the distance from the beam pipe, to adapt to the non-uniform detector occupancy.
- The Hadronic Calorimeter (HCAL): The HCAL, which is in charge of triggering high transverse energy hadrons, consists of a sampling calorimeter made from 26 layers of iron and scintillating tiles, as absorber and active material, respectively. The segmentation of the tiles is transverse to the beam-pipe, hence they are placed parallel to the beam axis for a total of $5.6\lambda_i(\text{Fe})$ (~ 20 cm) interaction lengths.

The obtained energy resolution is found to be [108]:

$$\frac{\sigma_E}{E} \simeq \begin{cases} \frac{9\%}{\sqrt{E(\text{GeV})}} \oplus 0.8\% & \text{for the ECAL and} \\ \frac{69\%}{\sqrt{E(\text{GeV})}} \oplus 9\% & \text{for the HCAL.} \end{cases} \quad (1.96)$$

Where the first uncertainty is related to the stochasticity of shower development and the second is related to detector resolution.

1.4.1.4 The muon system

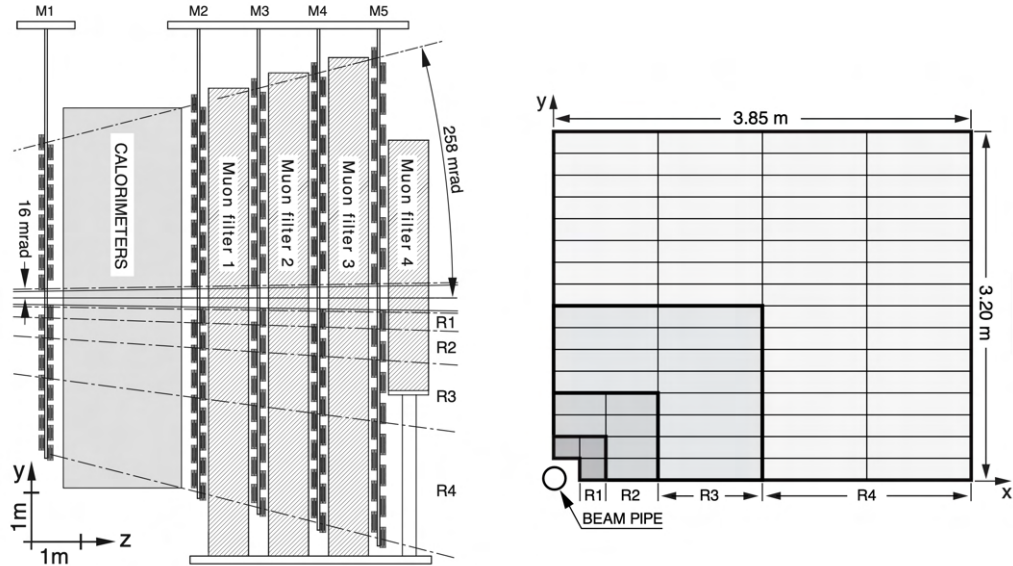


Fig. 1.13 Left: side view of the LHCb Muon Detector [103]. Right: geometry of a quadrant, with each rectangle representing a chamber. [103]

Muon triggering and muon identification are of fundamental for LHCb physics program. Muon final states are present *e.g.* in CP sensitive B decays such as $B_d^0 \rightarrow J/\psi(\mu\mu)K_S^0$ and $B_s^0 \rightarrow J/\psi(\mu\mu)\phi$, or helicity suppressed $B_{s/d}^0 \rightarrow \mu^+\mu^-$ or FCNC $B^0 \rightarrow K^{*0}\mu^+\mu^-$ rare decays, which are sensitive to NP models as outlined in the previous chapters. The muon systems provide information for the high- p_T muon triggers at the L0 level, as well as muon identification information for the subsequent stages of trigger (HLT1 and HLT2) and offline analysis.

The muon systems consist of 5 rectangular stations placed along the beam axis covering an acceptance of 20 – 306 mrad(16 – 258 mrad) in the bending (non-bending) plane. Energetic muons are able to pass through several meters of material losing only a small fraction of their energy, for this reason muon detectors are placed at the farthest point from the interaction point. The stations are disposed as M1(ECAL-HCAL)M2-M5 and the ones after the calorimeters are interspaced by layers of 80 cm or iron, to select penetrating muons: for a muon to traverse the whole system, whose length corresponds to ~ 20 interaction lengths, the minimum energy has to be ~ 6 GeV. All muon stations are equipped with multi-wire proportional chambers, with the exception

of M1 for which gas electron multiplier detectors (GEM) are employed, due to higher radiation harshness. While M1-M2-M3 improve the p_T^μ input for the trigger (at this stage $\delta p_T^\mu \sim 20\%$), M4-M5 provide binary information to the trigger system. The geometry of the 5 stations scales transversally with the distance from the interaction point and spatial information on the muon tracks is obtained by partitioning the muon chambers along the plane perpendicular to the beam axis. Their granularity scales with the distance from the beam axis so that the incident particle flux is constant.

1.4.1.5 The trigger system

Considering the high rate of collisions and the large number of track in the underlying event compared to the small fraction of interesting decays of a $b\bar{b}$ pair inside LHCb acceptance, a trigger system is needed to identify events of interest and reduce the rate to manageable levels to be stored on disk for offline analysis. The LHCb trigger is organised in two stages (levels):

- L0 Trigger The L0 Trigger system reduces the output rate to 1 MHz which is the maximum rate at which the whole detector can be read out. Due to its large mass, B decay products are typically characterise by high transverse momenta and energy hence, the L0 trigger selects the highest E_T hadron, electron or γ from the calorimeters or the single/di-muon candidates with highest p_T . To do so it reads information from calorimeters, PS and SPD or the muon stations. An estimate of the total number of tracks is also provided by the SPD. A Decision Unit (DU) collects all the collected information until now and derives the final trigger decision for each bunch crossing. Not only the L0 trigger reduces the rate to a writeable amount, but also to a level that is compatible to the computing power of the next stage, the HLT.
- High Level Trigger (HLT) In order to reduce the rate to the writeable 5 kHz and 12.5 kHz rates in Run I and Run II respectively, software based HLT makes use of the of the full information from the detector to select events filtered by the L0 and organise them in separate alleys based on more complex quantities than the one of L0 such as kinematical, topological and particle identification variables, as well as geometrical variables and invariant masses.

1.4.2 Overview of latest $b \rightarrow s\ell^+\ell^-$ results

In this subsection, an overview of the latest measurements of observables governed by the underlying FCNC $b \rightarrow s\ell^+\ell^-$ transition is presented. These, together with LFU tests in $b \rightarrow c\ell\nu$ decays, are collectively referred to as "Flavour Anomalies", and, although none of those measurements exhibits a discrepancy larger than the golden value of 5σ , they present an interesting pattern of global and coherent deviations with respect to the corresponding SM expectations. These observables consist of semi-leptonic or leptonic branching fractions, angular observables and ratios of branching fractions. While the SM prediction for semi-leptonic branching fractions and angular observables suffer from potentially large theoretical uncertainties related to form factors determination and charm-loop contributions (See Sec. 1.3.2.3), they are experimentally clean thanks to the fact that they are measured using muons in the final state, which traverse the detector almost undisturbed up to the muon stations.

On the other hand, purely leptonic branching fractions and ratios of semi-leptonic branching fractions are of clean determination within the SM, thanks to the fact that they are free from QCD related uncertainties, nonetheless they pose non-trivial experimental challenges since the former class of observables is loop, CKM and helicity suppressed and hence extremely rare, while the latter class of observables involves detection of electrons which, among other problems, lose a significant amount of energy to bremsstrahlung radiation and are affected by lower reconstruction efficiency with respect to muons.

1.4.2.1 Differential semi-leptonic branching fractions

The LHCb experiment measured the differential branching fractions of several decay channels governed by the $b \rightarrow s\mu^+\mu^-$ transition, each involving different spectator quarks, as a function of the dimuon invariant mass q^2 . These consist of mesonic transitions $B^{0,(+)} \rightarrow K^{0,(+)}\mu^+\mu^-$ and $B^+ \rightarrow K^{*+}\mu^+\mu^-$ [109], $B^0 \rightarrow K^{*0}\mu^+\mu^-$ [110], and $B_s^0 \rightarrow \phi\mu^+\mu^-$ [111] decays, and baryonic transitions such as $\Lambda_b^0 \rightarrow \Lambda\mu^+\mu^-$ decays [112]. Apart from overall normalisation parameters, such as for example the Fermi coupling constant and elements of the CKM matrix, the differential decay rates depend on the Wilson Coefficients $\mathcal{C}_i(\mu)$, hence their measurement gives potential direct access to NP contributions which would induce a shift on their value with respect to the SM prediction. As can be seen in Fig. 1.14, all of the measured differential decay rates $d\Gamma/dq^2$ involving $b \rightarrow s\mu^+\mu^-$ processes have lower measured values than the SM prediction, in particular in the region below the charmonium resonances, for

$1 \lesssim q^2 / \text{GeV}^2 \lesssim 6$. However, the broad theoretical uncertainties represented by solid coloured bands reduce the significance of such deviations.

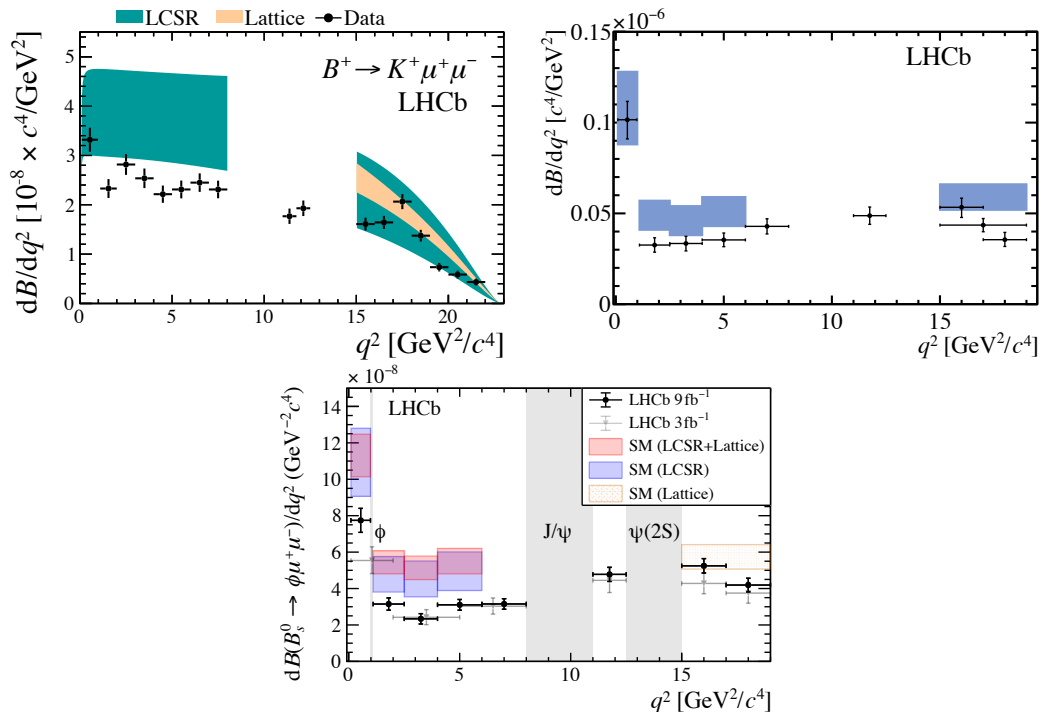


Fig. 1.14 Differential branching ratios $d\Gamma/q^2$ of $B^+ \rightarrow K^+ \mu^+ \mu^-$ (top left) $B^+ \rightarrow K^{*+} \mu^+ \mu^-$ (top right) and $B_s^0 \rightarrow \phi \mu^+ \mu^-$ (bottom). A deficit with respect to the SM prediction in the intermediate q^2 region is observed for all modes, however the large theory error bands don't allow to draw unambiguous conclusions.

The $\Lambda_b^0 \rightarrow \Lambda \mu^+ \mu^-$ differential decay rate, in fact, is an example of how the significance of the deviations with respect to the SM predictions of absolute branching fractions depends on determination of non-perturbative quantities and on experimental inputs. An example of the former case can be seen in Fig. 1.15 where the two SM predictions for the differential decay rate are both obtained with Lattice QCD calculations, however the result shown in the right subfigure relaxes the static approximation and treats the b quark relativistically in the form factors derivation, thus reducing the theoretical uncertainties and therefore the significance of the tension with respect to the SM prediction [113,114]. On the other hand, an example for the latter case is shown in [115]. Since the $\Lambda_b^0 \rightarrow \Lambda \mu^+ \mu^-$ differential decay rate is measured relative to the control channel $\Lambda_b^0 \rightarrow \Lambda J/\Psi$, the absolute $\Lambda_b^0 \rightarrow \Lambda \mu^+ \mu^-$ decay rate depends on the experimental input of f_{Λ_b} . In [115] it is shown that the tension with the SM expectation at high q^2 is greatly reduced when including results on f_{Λ_b} from TeVatron

data only, given its strong dependence on the b -quark production processes and the b -quark transverse momentum.

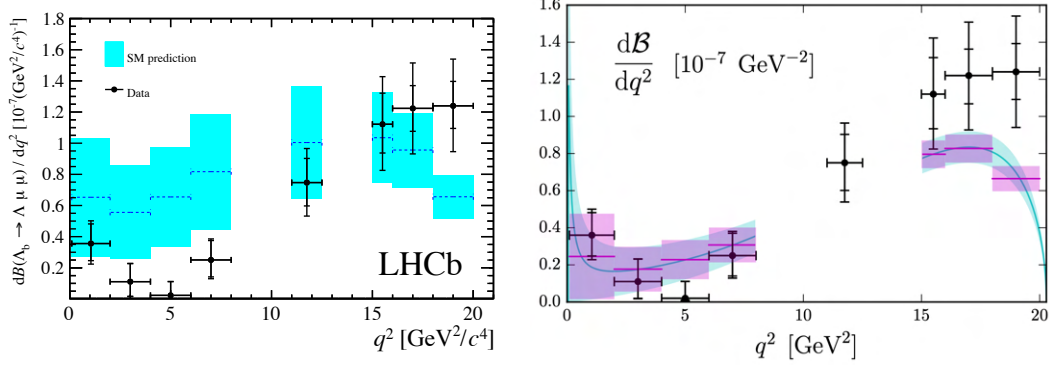


Fig. 1.15 Comparisons of the measured $d\Gamma/dq^2$ for $\Lambda_b^0 \rightarrow \Lambda\mu^+\mu^-$ decays with respect to theoretical predictions that use different assumptions in the derivation of the form factors. Relaxing the static b hypothesis (right) reduces the tension with the SM prediction.

1.4.2.2 Angular observables

In case of a vector hadron in the final state, *e.g.* the decay $B^0 \rightarrow K^{*0}(K^+\pi^-)\ell^+\ell^-$, a rich series of angular observables is accessible thanks to the non-trivial angular dependence of the b -hadron decay width. The number of independent variables needed to describe a process involving n final states is $2n - 3$, hence the decay rate is expressed in terms of 5 independent variables: the invariant mass of the $K^+\pi^-$ system $m_{K\pi}$, the dilepton invariant mass q^2 and the set of angular variables $\vec{\Omega} = (\cos\theta_l, \cos\theta_K, \phi)$ as [116]:

$$\frac{d^5\Gamma}{dm_{K\pi}dq^2d\vec{\Omega}} \propto \sum_i I_i(q^2, m_{K\pi}) f_i(\vec{\Omega}) \quad (1.97)$$

Where the $f_i(\vec{\Omega})$ are combinations of spherical harmonics which depend on θ_l (the angle between one of the leptons' spatial momentum and the B meson direction in the dilepton rest frame), θ_K (the angle between the K^+ spatial momentum and the B meson momentum in the K^{*0} rest frame) and ϕ (the angle between the plane of the dilepton pair and the plane of the K and π originated from the K^{*0} in the B rest frame). Assuming an on-shell K^{*0} of narrow width and integrating over $m_{K\pi}$ the $I_i(q^2)$ are q^2 dependent *angular observables*. Starting from the parametrisation of Eq. (1.97), a set of CP -averaged and CP -asymmetric observables can be built:

$$\begin{aligned}
S_i(q^2) &= \frac{I_i(q^2) + \bar{I}_i(q^2)}{(d\Gamma + d\bar{\Gamma})/dq^2} \\
A_i(q^2) &= \frac{I_i(q^2) - \bar{I}_i(q^2)}{(d\Gamma + d\bar{\Gamma})/dq^2}
\end{aligned}
\tag{1.98}$$

Where the \bar{I}_i and $\bar{\Gamma}$ refer to the CP conjugated decays. The observables S_i and A_i are extracted by fitting the decay rate via (un)binned maximum likelihood fits to the angular distributions of the final state particles, or by adopting the method of moments. In analogy to the differential branching fractions, they are sensitive to short distance (the Wilson Coefficients $\mathcal{C}_i(\mu)$), and long distance (form factors and charm-loop effects) contributions, whose SM predictions suffer from sizeable uncertainties due to their non-perturbative nature. To reduce the impact of said uncertainties an optimised set of observables, which consist of combinations of the longitudinal fraction $F_L \left(\stackrel{m_\ell \rightarrow 0}{\simeq} S_1 \right)$ and S_{3-9} , has been engineered [117,118]. Among these, P'_5 :

$$P'_5 = \frac{S_5}{F_L \sqrt{1 - F_L}} \tag{1.99}$$

received much attention in the recent years due to the deviation in the intermediate q^2 bin which was first observed by LHCb in 2013 [119] using 1 fb^{-1} of data, and subsequently confirmed in 2016 and 2020 expanding the analysed dataset to 3 fb^{-1} (Fig. 1.18 (top left) [120]) and 4.7 fb^{-1} (Fig. 1.18 (top right)[121]) respectively. Although with larger uncertainty, the same observable measured using the isospin partner decay $B^+ \rightarrow K^{*+}(\rightarrow K_s^0 \pi^+) \mu^+ \mu^-$ using 9 fb^{-1} of pp collision data Fig. 1.18 [122], exhibits a similar tension as the neutral B^0 mode. Complimentary information provided by the very low q^2 angular analysis of $B^0 \rightarrow K^{*0}(K^+ \pi^-) e^+ e^-$ [123] place stringent constraints on possible NP contributions on Wilson Coefficients to which these observables are particularly sensitive to, such as $\mathcal{C}_7^{(\prime)}$. Thanks to the copious quantity of b -mesons produced at LHCb, the determination of angular observables exploiting decays governed by the $b \rightarrow s \ell^+ \ell^-$ transition but with different spectator quarks, such as $B_s^0 \rightarrow \phi(K^+ K^-) \mu^+ \mu^-$ decays was performed using the full dataset collected (Fig. 1.18) [124].

In addition to the efforts from the theory community to hone in on the theoretical determination of non-local matrix elements [125], improvement of the experimental determination of the binned angular observables is foreseen exploiting the full dataset collected by LHCb, together with several unbinned q^2 and angular analyses which,

albeit with different degrees of model dependence, aim to pin down the size of the charm-loop contribution, defined in Sec 1.3.2.3 (*e.g.* [126]).

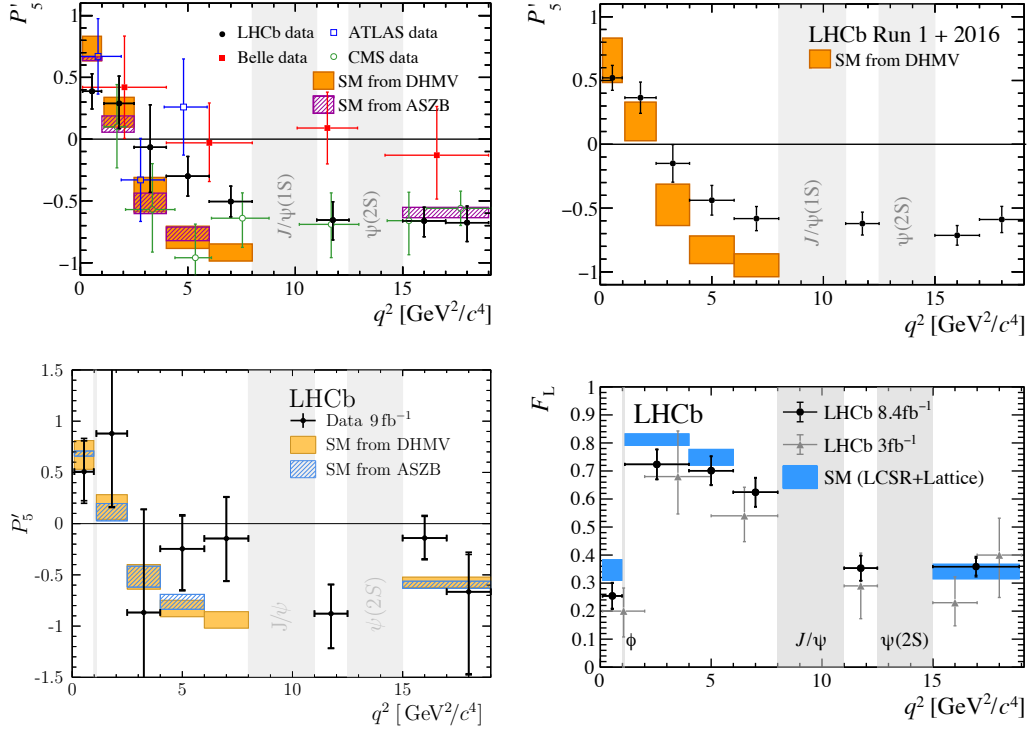


Fig. 1.16 Comparison of measurements of P'_5 in bins of q^2 as obtained from ATLAS, Belle, CMS and Run I LHCb data [120] (top left) and using data collected during Run I and 2016 [121] (top right). Measurements of P'_5 (bottom left) using $B^+ \rightarrow K^{*+} \mu^+ \mu^-$ decays [122] and F_L (bottom right) using $B_s^0 \rightarrow \phi \mu^+ \mu^-$ decays [124], in bins of q^2 , using Run I + Run II datasets collected at LHCb.

1.4.2.3 Purely leptonic branching fractions

Of more clean and precise SM prediction than the previously reviewed observables are the purely leptonic branching fractions of b -mesons such as $B_{s,d} \rightarrow \mu^+ \mu^-$, where the non-perturbative contributions reduce to decay constants f_{B_s, B_d} . They are proportional to the meson vacuum matrix elements, and are obtained using Lattice QCD calculations to percent level precision. This leads to a SM determination of branching ratio of $\mathcal{O}(2 - 5\%)$ precision [127,128].

The $B_{s,d} \rightarrow \mu^+ \mu^-$ decay rate is sensitive to vector couplings $\mathcal{C}_{10}^{(\prime)}$ as well as combinations of pseudo-scalar and scalar couplings $\mathcal{C}_S - \mathcal{C}'_S$ and $\mathcal{C}_P - \mathcal{C}'_P$ and place stringent constraint on NP models which would predict an enhancement of these contributions.

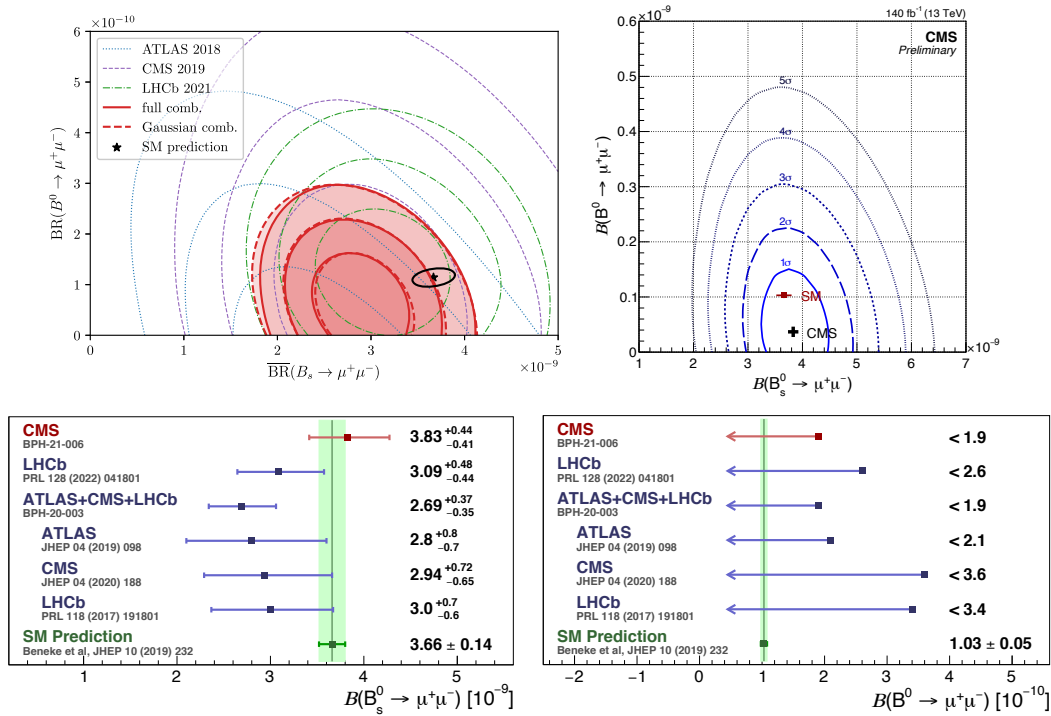


Fig. 1.17 Contour plots for ATLAS [129], CMS [130] and LHCb [131] combined measurements (top left) and CMS measurement [132] (top right) of time-integrated and CP -averaged $B_s \rightarrow \mu^+\mu^-$ and prompt $B_d \rightarrow \mu^+\mu^-$ branching fractions. The plots in the bottom row show the comparisons of the latest CMS measurements with the previous ones of the same quantities.

The combinations of ATLAS [129], CMS [130] and LHCb [131] measurements of time-integrated and CP -averaged $B_s \rightarrow \mu^+\mu^-$ branching fraction and upper limits on the prompt $B_d \rightarrow \mu^+\mu^-$ branching fractions are displayed in Fig. 1.17 (top left) [133] and found to be in $\sim 2\sigma$ tension with the SM prediction. In summer 2022 CMS updated the measurement of the $B_s \rightarrow \mu^+\mu^-$ branching fraction and the upper limit on the $B_d \rightarrow \mu^+\mu^-$ decay rate by analysing 140 fb^{-1} of data collected in the 2016-2018 data taking period [132], superseding the previous analysis. The results are shown in Fig. 1.17 (top right) and are in 1σ agreement with the SM. As can be seen in the summary plot in Fig. 1.17 (bottom left) the latest CMS measurement is singled out by its central value, greater than the SM expectation, as opposed to all previous measurements of this quantity.

As opposed to the differential semi-leptonic branching fractions and angular observables, purely leptonic branching fractions are precisely determined within the SM, however, their strong suppression poses challenges to their experimental determination and is limited by the statistical uncertainty. The sensitivity to the $B_s \rightarrow \mu^+\mu^-$ branch-

ing fraction is expected to be competitive with the SM prediction [134] by the end of Upgrade II of the LHCb detector [135].

1.4.2.4 Ratios of branching fractions

As detailed in Sec. 1.2.3.2, accidental symmetries are an excellent opportunity to test beyond SM effects. A LFU breaking sensitive class of observable consists of R_H ratios, which in case of a b -hadron X_b decaying to a well defined meson system containing an s squark H_s , compare the ratio of semi-leptonic branching fractions of muons with respect to electrons in the final state, in the dilepton mass-squared range $q_{\min}^2 < q^2 < q_{\max}^2$ [136,137]:

$$R_H \equiv \frac{\int_{q_{\min}^2}^{q_{\max}^2} \frac{d\mathcal{B}(X_b \rightarrow H_s \mu^+ \mu^-)}{dq^2} dq^2}{\int_{q_{\min}^2}^{q_{\max}^2} \frac{d\mathcal{B}(X_b \rightarrow H_s e^+ e^-)}{dq^2} dq^2}. \quad (1.100)$$

In the SM, deviations of LFU observables from unity are governed by kinematic and radiative effects, which for ratios involving light leptons are of $\mathcal{O}(\%)$ [138,139], due to their small mass compared to that of b quarks. Moreover since charm-loop contributions are LFU, they cancel in ratios of branching fractions to different leptons, rendering the SM prediction free from uncertainties relative to long-distance effects. LFU ratios involving B decays to K (Fig. 1.18b), K^{*0} (Fig. 1.18a), K_S and K^{*+} (Fig. 1.18d) mesons were measured by the LHCb [140–142], Belle [143–146] and BaBar [147] collaborations. Most precise measurements of these LFU observables from the LHCb experiment exhibit, in the low q^2 region, discrepancies ranging from 1.4σ to 2.5σ from the SM expectations. LHCb measured the analogous LFU ratio involving baryonic A_b^0 decays with $H_s = pK^-$ (Fig. 1.18c) exhibiting compatibility with unity at the level of one standard deviation [148]. As for the case of purely leptonic B decays, current LFU measurements are dominated by the statistical uncertainty, which, in turn, is driven by the uncertainty on the yield of the electron channel. However, the improved electron detection efficiency at the future LHCb Upgrades coupled with the higher luminosity reached at the LHC would allow to reach sub-percent precision on the determination of observables sensitive to LFU violation.

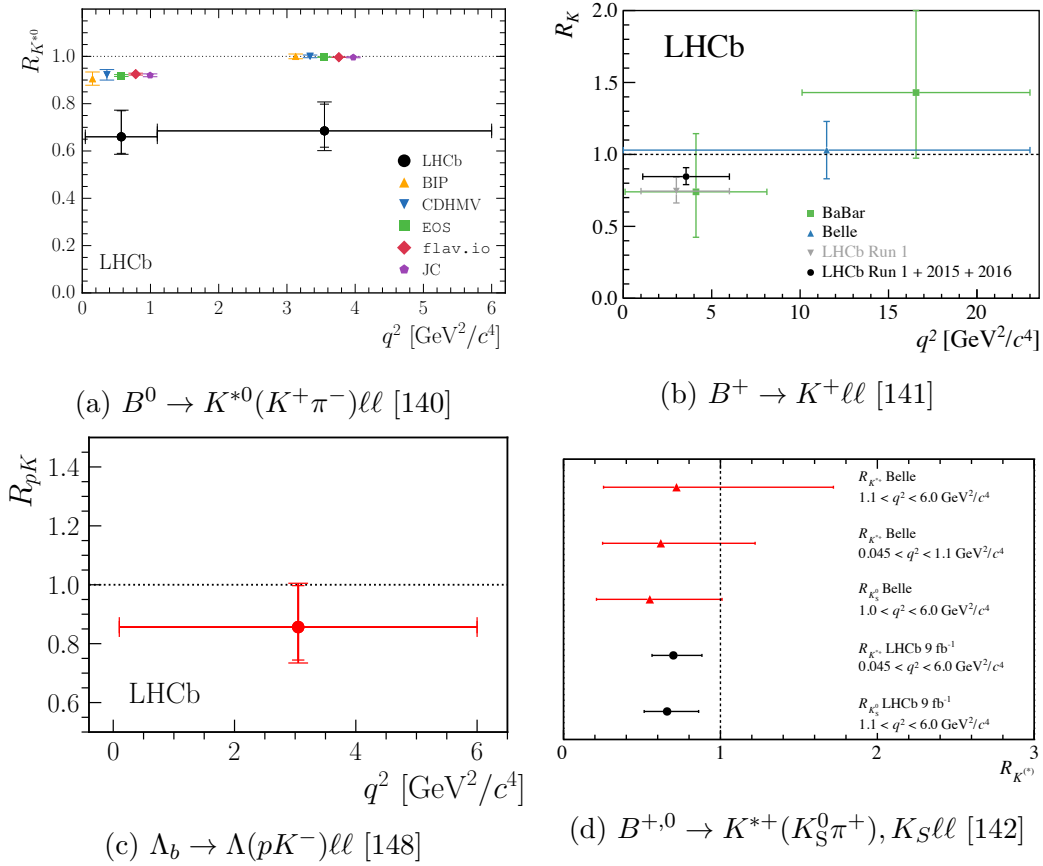


Fig. 1.18 Measurements of LFU universality probes using different hadronic systems, all connected by $b \rightarrow s\ell^+\ell^-$ transitions comparing muons to electron decay rates. For each plot, the corresponding channel is indicated below.

1.5 Personal contributions

Time is an illusion.

Lunchtime doubly so.

D. Adams

In the following chapters of this dissertation, original work performed during my PhD is presented, and is organised as follows:

- As stated in 1.2.3.2, mass related effects can induce lepton flavour non universality within the SM. In case of muon/electrons differences these consist of QED effects, which are taken into account by experimental collaborations via Monte Carlo simulations such as PHOTOS, which performs leading log approximations when simulating the radiative process. In Chapter 2 [149] we present a custom simulation built on a full NLO computation for $B^0 \rightarrow K^0 \ell^+ \ell^-$ decays and compare the QED induced effects in both the q^2 and $\cos \theta_l$ distributions in the two approaches.
- In Sec. 1.3.2.3 the theoretical limitations related to the absolute determination of $b \rightarrow s \ell^+ \ell^-$ observables such as the branching ratios and angular observables are introduced. The fact that these contributions are lepton flavour universal can be exploited to cancel their impact on the SM prediction when taking ratios of branching fractions. In Chapter 3 [150] the test of LFU using $B^+ \rightarrow K^+ \ell^+ \ell^-$ using the full Run-I and Run-II dataset collected at LHCb is presented.
- Multiple efforts from the theory community are aimed at establishing the *local* significance of the $b \rightarrow s \ell^+ \ell^-$ anomalies by fitting the Wilson Coefficients. These methods are perfectly defined for testing particular models, however they cannot be used to assess a global significance unless all of the involved Wilson Coefficients are introduced, and are susceptible of SM uncertainties arising from non-perturbative QCD effects. In Chapter 4 [151] we address this problem by defining a new method of assessing the global significance of $b \rightarrow s \ell^+ \ell^-$ results which is insensitive to the uncertainties arising from LFU contributions induced by potentially underestimated charm-loop effects.
- The application of the method outlined in the previous point is expanded to the more general $H_b \rightarrow X_s \ell^+ \ell^-$ transitions in Chapter 5 [152]. Not only this allows to evaluate for the first time in a global significance fit the result for R_{pK} [148], but also to include in the global significance estimate LFU ratios which have

still an indefinite formulation in terms of form factors and are being measured at LHCb.

References

- [1] H Bequerel. Sur les radiations émises par phosphorescence. *Comptes Rendus*, 122:420–421, 1896.
- [2] E. Rutherford M.A. B.Sc. Viii. uranium radiation and the electrical conduction produced by it. *The London, Edinburgh, and Dublin Philosophical Magazine and Journal of Science*, 47(284):109–163, 1899.
- [3] J Chadwick. Intensitätsverteilung im magnetischen Spectrum der β -Strahlen von radium B + C. *Verhandl. Dtsc. Phys. Ges.*, 16:383, 1914.
- [4] W. Pauli. Dear radioactive ladies and gentlemen. *Phys. Today*, 31N9:27, 1978.
- [5] J. Chadwick. The Existence of a Neutron. *Proceedings of the Royal Society of London Series A*, 136(830):692–708, June 1932.
- [6] E. Fermi. Tentativo di una Teoria Dei Raggi β . *Il nuovo cimento*, 11:1–19, January 1933.
- [7] C. L. Cowan, F. Reines, F. B. Harrison, H. W. Kruse, and A. D. McGuire. Detection of the free neutrino: A Confirmation. *Science*, 124:103–104, 1956.
- [8] T. D. Lee and C. N. Yang. Question of parity conservation in weak interactions. *Phys. Rev.*, 104:254–258, Oct 1956.
- [9] C. S. Wu, E. Ambler, R. W. Hayward, D. D. Hoppes, and R. P. Hudson. Experimental test of parity conservation in beta decay. *Phys. Rev.*, 105:1413–1415, Feb 1957.
- [10] M. Goldhaber, L. Grodzins, and A. W. Sunyar. Helicity of neutrinos. *Phys. Rev.*, 109:1015–1017, Feb 1958.
- [11] T. D. Lee and C. N. Yang. Parity nonconservation and a two-component theory of the neutrino. *Phys. Rev.*, 105:1671–1675, Mar 1957.

-
- [12] Richard P. Feynman. Relativistic cut-off for quantum electrodynamics. *Phys. Rev.*, 74:1430–1438, Nov 1948.
- [13] F. J. Dyson. The radiation theories of tomonaga, schwinger, and feynman. *Phys. Rev.*, 75:486–502, Feb 1949.
- [14] H. Yukawa. On the interaction of elementary particles. i. *Proceedings of the Physico-Mathematical Society of Japan. 3rd Series*, 17:48–57, 1935.
- [15] Seth H. Neddermeyer and Carl D. Anderson. Note on the nature of cosmic-ray particles. *Phys. Rev.*, 51:884–886, May 1937.
- [16] B. Pontecorvo. Nuclear capture of mesons and the meson decay. *Phys. Rev.*, 72:246–247, Aug 1947.
- [17] J. Steinberger. On the range of the electrons in meson decay. *Phys. Rev.*, 75:1136–1143, Apr 1949.
- [18] G. Danby, J-M. Gaillard, K. Goulianos, L. M. Lederman, N. Mistry, M. Schwartz, and J. Steinberger. Observation of high-energy neutrino reactions and the existence of two kinds of neutrinos. *Phys. Rev. Lett.*, 9:36–44, Jul 1962.
- [19] Butler Dr. C. Rochester Dr., G. Evidence for the existence of new unstable elementary particles. *Nature*, 160:855.857, Dec 1947.
- [20] J. Orear, G. Harris, and S. Taylor. Spin and parity analysis of bevatron τ mesons. *Phys. Rev.*, 102:1676–1684, Jun 1956.
- [21] F. S. Crawford, M. Cresti, M. L. Good, K. Gottstein, E. M. Lyman, F. T. Solmitz, M. L. Stevenson, and H. K. Ticho. Detection of Parity Nonconservation in Lambda Decay. *Phys. Rev.*, 108:1102–1103, 1957.
- [22] Fred R. Eisler et al. Demonstration of parity nonconservation in hyperon decay. *Physical Review*, 108:1353–1355, 1957.
- [23] M Gell-Mann. The eightfold way: A theory of strong interaction symmetry.
- [24] Nicola Cabibbo. Unitary symmetry and leptonic decays. *Phys. Rev. Lett.*, 10:531–533, Jun 1963.
- [25] Emmy Noether. Invariant variation problems. *Transport Theory and Statistical Physics*, 1(3):186–207, jan 1971.

-
- [26] H. Weyl. *Gravitation und Elektrizität*, pages 147–159. Vieweg+Teubner Verlag, Wiesbaden, 1923.
- [27] H. Weyl. Elektron und gravitation. i. *Zeitschrift für Physik*, 56:330–352, May 1929.
- [28] Y. Aharonov and D. Bohm. Significance of electromagnetic potentials in the quantum theory. *Phys. Rev.*, 115:485–491, Aug 1959.
- [29] C. N. Yang and R. L. Mills. Conservation of isotopic spin and isotopic gauge invariance. *Phys. Rev.*, 96:191–195, Oct 1954.
- [30] Sheldon L. Glashow. Partial-symmetries of weak interactions. *Nuclear Physics*, 22(4):579–588, 1961.
- [31] Ochsenfeld R. Meissner, W. Ein neuer effekt bei eintritt der supraleitfähigkeit. *Naturwissenschaften*, 21:787–788, Nov 1933.
- [32] W. Heisenberg. Zur theorie des ferromagnetismus. *Z. Physik*, 49:619–636, May 1928.
- [33] Yoichiro Nambu. Quasi-particles and gauge invariance in the theory of superconductivity. *Phys. Rev.*, 117:648–663, Feb 1960.
- [34] J. Goldstone. Field theories with « superconductor » solutions. *Nuovo Cim*, 19:154–164, Sept 1961.
- [35] P. W. Anderson. Plasmons, gauge invariance, and mass. *Phys. Rev.*, 130:439–442, Apr 1963.
- [36] F. Englert and R. Brout. Broken symmetry and the mass of gauge vector mesons. *Phys. Rev. Lett.*, 13:321–323, Aug 1964.
- [37] Peter W. Higgs. Broken symmetries and the masses of gauge bosons. *Phys. Rev. Lett.*, 13:508–509, Oct 1964.
- [38] Steven Weinberg. A model of leptons. *Phys. Rev. Lett.*, 19:1264–1266, Nov 1967.
- [39] A. Salam. Elementary particle physics: Relativistic groups and analyticity. *Proceedings of the Eighth Nobel Symposium*, page 367, 1968.
- [40] Harald Fritzsch and Murray Gell-Mann. Current algebra: Quarks and what else? *eConf*, C720906V2:135–165, 1972.

-
- [41] H. Fritzsch, M. Gell-Mann, and P. Minkowski. Vectorlike weak currents and new elementary fermions. *Physics Letters B*, 59(3):256–260, 1975.
- [42] S. L. Glashow, J. Iliopoulos, and L. Maiani. Weak interactions with lepton-hadron symmetry. *Phys. Rev. D*, 2:1285–1292, Oct 1970.
- [43] J. J. et al. Aubert. Experimental observation of a heavy particle j . *Phys. Rev. Lett.*, 33:1404–1406, Dec 1974.
- [44] J. E. et al. Augustin. Discovery of a narrow resonance in e^+e^- annihilation. *Phys. Rev. Lett.*, 33:1406–1408, Dec 1974.
- [45] G. Goldhaber et al. D and d meson production near 4 gev in $e+e$ annihilation. *Physics Letters B*, 69(4):503–507, 1977.
- [46] Peruzzi et al. Study of d mesons produced in the decay of the $\psi(3772)$. *Phys. Rev. Lett.*, 39:1301–1304, Nov 1977.
- [47] F.J. Hasert et al. Search for elastic muon-neutrino electron scattering. *Physics Letters B*, 46(1):121–124, 1973.
- [48] F.J. Hasert et al. Observation of neutrino-like interactions without muon or electron in the gargamelle neutrino experiment. *Physics Letters B*, 46(1):138–140, 1973.
- [49] G. Arnison et al. Experimental observation of isolated large transverse energy electrons with associated missing energy at $s=540$ gev. *Physics Letters B*, 122(1):103–116, 1983.
- [50] M. Banner et al. Observation of single isolated electrons of high transverse momentum in events with missing transverse energy at the cern pp collider. *Physics Letters B*, 122(5):476–485, 1983.
- [51] J. H. Christenson, J. W. Cronin, V. L. Fitch, and R. Turlay. Evidence for the 2π decay of the k_2^0 meson. *Phys. Rev. Lett.*, 13:138–140, Jul 1964.
- [52] Makoto Kobayashi and Toshihide Maskawa. CP-Violation in the Renormalizable Theory of Weak Interaction. *Progress of Theoretical Physics*, 49(2):652–657, 02 1973.
- [53] M. L. et al. Perl. Evidence for anomalous lepton production in $e^+ - e^-$ annihilation. *Phys. Rev. Lett.*, 35:1489–1492, Dec 1975.

-
- [54] Observation of tau neutrino interactions. *Physics Letters B*, 504.
- [55] S. W. Herb et al. Observation of a Dimuon Resonance at 9.5-GeV in 400-GeV Proton-Nucleus Collisions. *Phys. Rev. Lett.*, 39:252–255, 1977.
- [56] Observation of b_0 - \bar{b}_0 mixing. *Physics Letters B*, 192(1).
- [57] D. Buskulic et al. Observation of the time dependence of b_0 - \bar{b}_0 mixing. *Physics Letters B*, 313(3):498–508, 1993.
- [58] B. et al. Aubert. Observation of CP violation in the b^0 meson system. *Phys. Rev. Lett.*, 87:091801, Aug 2001.
- [59] K. et al. Abe. Observation of large CP violation in the neutral B meson system. *Phys. Rev. Lett.*, 87:091802, Aug 2001.
- [60] Bernard Aubert et al. Observation of direct CP violation in $B^0 \rightarrow K^+\pi^-$ decays. *Phys. Rev. Lett.*, 93:131801, 2004.
- [61] Y. Chao et al. Evidence for direct CP violation in $B^0 \rightarrow K^+\pi^-$ decays. *Phys. Rev. Lett.*, 93:191802, 2004.
- [62] F. et al. Abe. Observation of top quark production in $\bar{p}p$ collisions with the collider detector at fermilab. *Phys. Rev. Lett.*, 74:2626–2631, Apr 1995.
- [63] S. et al. Abachi. Observation of the top quark. *Phys. Rev. Lett.*, 74:2632–2637, Apr 1995.
- [64] Georges Aad et al. Observation of a new particle in the search for the Standard Model Higgs boson with the ATLAS detector at the LHC. *Phys. Lett. B*, 716:1–29, 2012.
- [65] Serguei Chatrchyan et al. Observation of a New Boson at a Mass of 125 GeV with the CMS Experiment at the LHC. *Phys. Lett. B*, 716:30–61, 2012.
- [66] Observation of vector-boson-fusion production of Higgs bosons in the $H \rightarrow WW^* \rightarrow e\nu\mu\nu$ decay channel in pp collisions at $\sqrt{s} = 13$ TeV with the ATLAS detector. 8 2020.
- [67] Albert M. Sirunyan et al. Measurements of properties of the Higgs boson decaying to a W boson pair in pp collisions at $\sqrt{s} = 13$ TeV. *Phys. Lett. B*, 791:96, 2019.

- [68] M. Aaboud et al. Observation of higgs boson production in association with a top quark pair at the lhc with the atlas detector. *Physics Letters B*, 784:173–191, 2018.
- [69] A. M. et al. Sirunyan. Observation of $t\bar{t}h$ production. *Phys. Rev. Lett.*, 120:231801, Jun 2018.
- [70] Morad Aaboud et al. Observation of $H \rightarrow b\bar{b}$ decays and VH production with the ATLAS detector. *Phys. Lett. B*, 786:59–86, 2018.
- [71] A. M. Sirunyan et al. Observation of Higgs boson decay to bottom quarks. *Phys. Rev. Lett.*, 121(12):121801, 2018.
- [72] Georges Aad et al. Evidence for the Higgs-boson Yukawa coupling to tau leptons with the ATLAS detector. *JHEP*, 04:117, 2015.
- [73] Albert M Sirunyan et al. Observation of the Higgs boson decay to a pair of τ leptons with the CMS detector. *Phys. Lett. B*, 779:283–316, 2018.
- [74] T. Rostami and S. Jalalzadeh. Why the measured cosmological constant is small. *Phys. Dark Univ.*, 9-10:31–36, 10 2015.
- [75] Massimo Cerdonio. About the measure of the bare cosmological constant. *Foundations of Physics*, 49(8):830–836, 2019.
- [76] P. A. R. Ade et al. Planck 2015 results. XIII. Cosmological parameters. *Astron. Astrophys.*, 594:A13, 2016.
- [77] Sidney van den Bergh. The early history of dark matter. *Publications of the Astronomical Society of the Pacific*, 111(760):657–660, jun 1999.
- [78] Vardan Khachatryan et al. Search for dark matter, extra dimensions, and unparticles in monojet events in proton–proton collisions at $\sqrt{s} = 8$ TeV. *Eur. Phys. J. C*, 75(5):235, 2015.
- [79] E. Aprile et al. Dark Matter Search Results from a One Ton-Year Exposure of XENON1T. *Phys. Rev. Lett.*, 121(11):111302, 2018.
- [80] Leszek Roszkowski, Enrico Maria Sessolo, and Sebastian Trojanowski. WIMP dark matter candidates and searches—current status and future prospects. *Rept. Prog. Phys.*, 81(6):066201, 2018.

- [81] Bernd A. Kniehl. Higgs phenomenology at one loop in the standard model. *Physics Reports*, 240(4):211–300, 1994.
- [82] Boris Kayser. Neutrino Oscillation Phenomenology. In *61st Scottish Universities Summer School in Physics: Neutrinos in Particle Physics, Astrophysics and Cosmology (SUSSP61)*, pages 51–64, 4 2008.
- [83] M.C. Gonzalez-Garcia and Michele Maltoni. Phenomenology with massive neutrinos. *Physics Reports*, 460(1):1–129, 2008.
- [84] Ivan Esteban, M. C. Gonzalez-Garcia, Michele Maltoni, Thomas Schwetz, and Albert Zhou. The fate of hints: updated global analysis of three-flavor neutrino oscillations. *Journal of High Energy Physics*, 2020(9):178, 2020.
- [85] Global analysis of neutrino oscillation measurements in the sm framework with 3 massive neutrinos and some of its extension, 2022.
- [86] Michelle J. Dolinski, Alan W. P. Poon, and Werner Rodejohann. Neutrinoless Double-Beta Decay: Status and Prospects. *Ann. Rev. Nucl. Part. Sci.*, 69:219–251, 2019.
- [87] A. Blondel et al. Research Proposal for an Experiment to Search for the Decay $\mu \rightarrow eee$. 1 2013.
- [88] Cristina Martin Perez and Luigi Vigani. Searching for the Muon Decay to Three Electrons with the Mu3e Experiment. *Universe*, 7(11):420, 2021.
- [89] Gino Isidori (University of Zurich Switzerland) Marina Artuso (Syracuse University, USA) and USA) Sheldon Stone (Syracuse University. *New Physics in b Decays*. World Scientific, 2022.
- [90] Steven Weinberg. Baryon- and lepton-nonconserving processes. *Phys. Rev. Lett.*, 43:1566–1570, Nov 1979.
- [91] Gerhard Buchalla, Andrzej J. Buras, and Markus E. Lautenbacher. Weak decays beyond leading logarithms. *Rev. Mod. Phys.*, 68:1125–1144, 1996.
- [92] Thomas Blake, Gaia Lanfranchi, and David M. Straub. Rare B Decays as Tests of the Standard Model. *Prog. Part. Nucl. Phys.*, 92:50–91, 2017.

-
- [93] Wolfgang Altmannshofer, Patricia Ball, Aoife Bharucha, Andrzej J. Buras, David M. Straub, and Michael Wick. Symmetries and Asymmetries of $B \rightarrow K^* \mu^+ \mu^-$ Decays in the Standard Model and Beyond. *JHEP*, 01:019, 2009.
- [94] Aoife Bharucha, David M. Straub, and Roman Zwicky. $B \rightarrow V \ell^+ \ell^-$ in the Standard Model from light-cone sum rules. *JHEP*, 08:098, 2016.
- [95] Nico Gubernari, Ahmet Kokulu, and Danny van Dyk. $B \rightarrow P$ and $B \rightarrow V$ Form Factors from B -Meson Light-Cone Sum Rules beyond Leading Twist. *JHEP*, 01:150, 2019.
- [96] R. R. Horgan, Z. Liu, S. Meinel, and M. Wingate. Rare B decays using lattice QCD form factors. *PoS, LATTICE2014*:372, 2015.
- [97] A. Khodjamirian, Th. Mannel, A. A. Pivovarov, and Y. M. Wang. Charm-loop effect in $B \rightarrow K^{(*)} \ell^+ \ell^-$ and $B \rightarrow K^* \gamma$. *JHEP*, 09:089, 2010.
- [98] Christoph Bobeth, Marcin Chrzaszcz, Danny van Dyk, and Javier Virto. Long-distance effects in $B \rightarrow K^* \ell \ell$ from analyticity. *Eur. Phys. J. C*, 78(6):451, 2018.
- [99] Christiane Lefèvre. The CERN accelerator complex. Complexe des accélérateurs du CERN. 2008.
- [100] K Aamodt et al. The ALICE experiment at the CERN LHC. *Journal of Instrumentation*, 3(08):S08002–S08002, aug 2008.
- [101] G Aad et al. The ATLAS experiment at the CERN large hadron collider. *Journal of Instrumentation*, 3(08):S08003–S08003, aug 2008.
- [102] S Chatrchyan et al. The CMS experiment at the CERN LHC. *Journal of Instrumentation*, 3(08):S08004–S08004, aug 2008.
- [103] A Augusto Alves et al. The LHCb detector at the LHC. *Journal of Instrumentation*, 3(08):S08005–S08005, aug 2008.
- [104] Christian Elsässer. $\bar{b}b$ production angle plots.
- [105] Michelangelo L. Mangano. Two lectures on heavy quark production in hadronic collisions. *Proc. Int. Sch. Phys. Fermi*, 137:95–137, 1998.

- [106] Nicolò Cartiglia. Measurement of the proton-proton total cross section at 2, 7, 8 and 57 TeV. In *32nd International Symposium on Physics in Collision*, pages 55–64, 3 2013.
- [107] Roel Aaij et al. Measurement of the b -quark production cross-section in 7 and 13 TeV pp collisions. *Phys. Rev. Lett.*, 118(5):052002, 2017. [Erratum: *Phys.Rev.Lett.* 119, 169901 (2017)].
- [108] Irina Machikhiliyan and. Current status and performance of the LHCb electromagnetic and hadron calorimeters. *Journal of Physics: Conference Series*, 293:012052, apr 2011.
- [109] R. Aaij et al. Differential branching fractions and isospin asymmetries of $B \rightarrow K^{(*)}\mu^+\mu^-$ decays. *JHEP*, 06:133, 2014.
- [110] Roel Aaij et al. Measurements of the S-wave fraction in $B^0 \rightarrow K^+\pi^-\mu^+\mu^-$ decays and the $B^0 \rightarrow K^*(892)^0\mu^+\mu^-$ differential branching fraction. *JHEP*, 11:047, 2016. [Erratum: *JHEP* 04, 142 (2017)].
- [111] Roel Aaij et al. Branching Fraction Measurements of the Rare $B_s^0 \rightarrow \phi\mu^+\mu^-$ and $B_s^0 \rightarrow f_2'(1525)\mu^+\mu^-$ Decays. *Phys. Rev. Lett.*, 127(15):151801, 2021.
- [112] Roel Aaij et al. Differential branching fraction and angular analysis of $\Lambda_b^0 \rightarrow \Lambda\mu^+\mu^-$ decays. *JHEP*, 06:115, 2015. [Erratum: *JHEP* 09, 145 (2018)].
- [113] William Detmold, C. J. David Lin, Stefan Meinel, and Matthew Wingate. $\Lambda_b \rightarrow \Lambda\ell^+\ell^-$ form factors and differential branching fraction from lattice QCD. *Phys. Rev. D*, 87(7):074502, 2013.
- [114] William Detmold and Stefan Meinel. $\Lambda_b \rightarrow \Lambda\ell^+\ell^-$ form factors, differential branching fraction, and angular observables from lattice QCD with relativistic b quarks. *Phys. Rev. D*, 93(7):074501, 2016.
- [115] Thomas Blake, Stefan Meinel, and Danny van Dyk. Bayesian Analysis of $b \rightarrow s\mu^+\mu^-$ Wilson Coefficients using the Full Angular Distribution of $\Lambda_b \rightarrow \Lambda(\rightarrow p\pi^-)\mu^+\mu^-$ Decays. *Phys. Rev. D*, 101(3):035023, 2020.
- [116] U. Egede, T. Hurth, J. Matias, M. Ramon, and W. Reece. New observables in the decay mode $\bar{B}_d \rightarrow \bar{K}^{*0}l^+l^-$. *JHEP*, 11:032, 2008.

- [117] Sebastien Descotes-Genon, Joaquim Matias, Marc Ramon, and Javier Virto. Implications from clean observables for the binned analysis of $B^- \rightarrow K^* \mu^+ \mu^-$ at large recoil. *JHEP*, 01:048, 2013.
- [118] Joaquim Matias, Federico Mescia, Marc Ramon, and Javier Virto. Complete Anatomy of $\bar{B}_d^- \rightarrow \bar{K}^{*0}(- \rightarrow K\pi)l^+l^-$ and its angular distribution. *JHEP*, 04:104, 2012.
- [119] R Aaij et al. Measurement of Form-Factor-Independent Observables in the Decay $B^0 \rightarrow K^{*0} \mu^+ \mu^-$. *Phys. Rev. Lett.*, 111:191801, 2013.
- [120] Roel Aaij et al. Angular analysis of the $B^0 \rightarrow K^{*0} \mu^+ \mu^-$ decay using 3 fb^{-1} of integrated luminosity. *JHEP*, 02:104, 2016.
- [121] Roel Aaij et al. Measurement of CP -Averaged Observables in the $B^0 \rightarrow K^{*0} \mu^+ \mu^-$ Decay. *Phys. Rev. Lett.*, 125(1):011802, 2020.
- [122] Roel Aaij et al. Angular Analysis of the $B^+ \rightarrow K^{*+} \mu^+ \mu^-$ Decay. *Phys. Rev. Lett.*, 126(16):161802, 2021.
- [123] Roel Aaij et al. Angular analysis of the $B^0 \rightarrow K^{*0} e^+ e^-$ decay in the low- q^2 region. *JHEP*, 04:064, 2015.
- [124] Roel Aaij et al. Angular analysis of the rare decay $B_s^0 \rightarrow \phi \mu^+ \mu^-$. *JHEP*, 11:043, 2021.
- [125] Nico Gubernari, Danny van Dyk, and Javier Virto. Non-local matrix elements in $B_{(s)} \rightarrow \{K^{(*)}, \phi\} \ell^+ \ell^-$. *JHEP*, 02:088, 2021.
- [126] Andrea Mauri, Nicola Serra, and Rafael Silva Coutinho. Towards establishing lepton flavor universality violation in $\bar{B} \rightarrow \bar{K}^* \ell^+ \ell^-$ decays. *Phys. Rev. D*, 99(1):013007, 2019.
- [127] Wolfgang Altmannshofer, Christoph Niehoff, and David M. Straub. $B_s \rightarrow \mu^+ \mu^-$ as current and future probe of new physics. *JHEP*, 05:076, 2017.
- [128] Martin Beneke, Christoph Bobeth, and Robert Szafron. Power-enhanced leading-logarithmic QED corrections to $B_q \rightarrow \mu^+ \mu^-$. *JHEP*, 10:232, 2019.
- [129] Morad Aaboud et al. Study of the rare decays of B_s^0 and B^0 mesons into muon pairs using data collected during 2015 and 2016 with the ATLAS detector. *JHEP*, 04:098, 2019.

- [130] Albert M Sirunyan et al. Measurement of properties of $B_s^0 \rightarrow \mu^+\mu^-$ decays and search for $B^0 \rightarrow \mu^+\mu^-$ with the CMS experiment. *JHEP*, 04:188, 2020.
- [131] Roel Aaij et al. Measurement of the $B_s^0 \rightarrow \mu^+\mu^-$ decay properties and search for the $B^0 \rightarrow \mu^+\mu^-$ and $B_s^0 \rightarrow \mu^+\mu^-\gamma$ decays. *Phys. Rev. D*, 105(1):012010, 2022.
- [132] Measurement of $B_s^0 \rightarrow \mu^+\mu^-$ decay properties and search for the $B^0 \rightarrow \mu\mu$ decay in proton-proton collisions at $\sqrt{s} = 13$ TeV. Technical report, CERN, Geneva, 2022.
- [133] Wolfgang Altmannshofer and Peter Stangl. New physics in rare b decays after moriond 2021. *The European Physical Journal C*, 81(10):952, 2021.
- [134] D. Lancierini and R. D. Moise. Anomalous measurements: recent results deepen flavour puzzle. 7 2021.
- [135] Roel Aaij et al. Physics case for an LHCb Upgrade II - Opportunities in flavour physics, and beyond, in the HL-LHC era. 8 2018.
- [136] Gudrun Hiller and Frank Krüger. More model-independent analysis of $b \rightarrow s$ processes. *Phys. Rev.*, D69:074020, 2004.
- [137] Yili Wang and David Atwood. Rate difference between $b \rightarrow s\mu^+\mu^-$ and $b \rightarrow se^+e^-$ in supersymmetry with large $\tan \beta$. *Phys. Rev.*, D68:094016, 2003.
- [138] Marzia Bordone, Gino Isidori, and Andrea Pattori. On the Standard Model predictions for R_K and R_{K^*} . *Eur. Phys. J. C*, 76(8):440, 2016.
- [139] Gino Isidori, Saad Nabeebaccus, and Roman Zwicky. QED corrections in $\bar{B} \rightarrow \bar{K}\ell^+\ell^-$ at the double-differential level. *JHEP*, 12:104, 2020.
- [140] R. Aaij et al. Test of lepton universality with $B^0 \rightarrow K^{*0}\ell^+\ell^-$ decays. *JHEP*, 08:055, 2017.
- [141] Roel Aaij et al. Search for lepton-universality violation in $B^+ \rightarrow K^+\ell^+\ell^-$ decays. *Phys. Rev. Lett.*, 122(19):191801, 2019.
- [142] Roel Aaij et al. Tests of lepton universality using $B^0 \rightarrow K_s^0\ell^+\ell^-$ and $B^+ \rightarrow K^{*+}\ell^+\ell^-$ decays. *Phys. Rev. Lett.*, 128(19):191802, 2022.
- [143] S. Choudhury et al. Test of lepton flavor universality and search for lepton flavor violation in $B \rightarrow K\ell\ell$ decays. *JHEP*, 03:105, 2021.

-
- [144] S. Wehle et al. Test of lepton-flavor universality in $B \rightarrow K^* \ell^+ \ell^-$ decays at Belle. *Phys. Rev. Lett.*, 126:161801, Apr 2021.
- [145] S. et al. Wehle. Test of lepton-flavor universality in $b \rightarrow K^* \ell^+ \ell^-$ decays at belle. *Phys. Rev. Lett.*, 126:161801, Apr 2021.
- [146] S. et al. Choudhury. Test of lepton flavor universality and search for lepton flavor violation in $b \rightarrow k$ decays. *Journal of High Energy Physics*, 2021(3):105, 2021.
- [147] J. P. Lees et al. Measurement of branching fractions and rate asymmetries in the rare decays $B \rightarrow K^{(*)} \ell^+ \ell^-$. *Phys. Rev.*, D86:032012, Aug 2012.
- [148] Roel Aaij et al. Test of lepton universality with $\Lambda_b^0 \rightarrow p K^- \ell^+ \ell^-$ decays. *JHEP*, 05:040, 2020.
- [149] Gino Isidori, Davide Lancierini, Saad Nabeebaccus, and Roman Zwicky. QED in $\bar{B} \rightarrow \bar{K} \ell^+ \ell^-$ LFU ratios: Theory versus Experiment, a Monte Carlo Study. 5 2022.
- [150] R. et al Aaij. Test of lepton universality in beauty-quark decays. *Nature Physics*, 18(3):277–282, 2022.
- [151] Gino Isidori, Davide Lancierini, Patrick Owen, and Nicola Serra. On the significance of new physics in $b \rightarrow s \ell^+ \ell^-$ decays. *Phys. Lett. B*, 822:136644, 2021.
- [152] Gino Isidori, Davide Lancierini, Abhijit Mathad, Patrick Owen, Nicola Serra, and Rafael Silva Coutinho. A general effective field theory description of $b \rightarrow s \ell^+ \ell^-$ lepton universality ratios. *Phys. Lett. B*, 830:137151, 2022.

Appendix 1.A Appendix to Chapter 1

1.A.1 The optical theorem

The Standard Model of particle physics (SM) is a relativistic quantum field theory (QFT) that describes the fundamental constituents of matter and their interactions. Starting from symmetries of the Lagrangian and the representations of the particles under such symmetries, QFT allows to derive predictions for observables such as properties of bound states, cross sections and branching fractions. In QFT the probabilities are calculated via the scattering matrix \mathcal{S} , its (i, j) -th element encodes the transition probability from an initial state $|i\rangle$ to a final state $|f\rangle$

$$\mathcal{S}_{ij} = {}_{\text{in}}\langle i|f\rangle_{\text{out}} \quad (1.101)$$

The requirement that the sum of all the probabilities related to every outcome is one implies the unitarity of the scattering matrix \mathcal{S} . By decomposing the matrix \mathcal{S} in a trivial, non-interacting part proportional to the identity matrix (for which $i = f$), and an interaction part \mathcal{T} (for which $i \neq f$)

$$\mathcal{S} = \mathbb{1} + i\mathcal{T} \quad (1.102)$$

the unitarity of \mathcal{S} implies:

$$\mathcal{T}\mathcal{T}^\dagger = -i(\mathcal{T} - \mathcal{T}^\dagger) \quad (1.103)$$

which can be inserted in the bra-ket product of states a and b to obtain:

$$\langle a|\mathcal{T}\mathcal{T}^\dagger|b\rangle = -i(\langle a|\mathcal{T}|b\rangle - \langle a|\mathcal{T}^\dagger|b\rangle) \quad (1.104)$$

The matrix element \mathcal{S}_{ij} is related to the transition amplitude via Fermi's golden rule:

$$\langle f|\mathcal{T}|b\rangle = \mathcal{M}_{af}(2\pi)^4\delta(p_a - p_f) \quad (1.105)$$

The Lorentz invariant completeness relation reads

$$\mathbb{1} = \sum_f \left(\prod_j \int \frac{d^3p_j^f}{(2\pi)^3 2E_j^f} \right) |f\rangle\langle f| \quad (1.106)$$

Which, when inserted in (1.104), and by making use of Fermi's golden rule (1.105) yields the relation:

$$\sum_f \left(\prod_j \int \frac{d^3 p_j^f}{(2\pi)^3 2E_j^f} \right) (2\pi)^4 \delta(p_a - \sum_j p_j^f) \delta(p_b - \sum_j p_j^f) \mathcal{M}_{bf} \mathcal{M}_{af}^* = -i (\mathcal{M}_{ba} - \mathcal{M}_{ab}^*) \delta(p_a - p_b) \quad (1.107)$$

This expression can be simplified by making use of the Dirac δ to fix $p_a = p_b = \sum_j p_j^f$

$$\sum_f \left(\prod_j \int \frac{d^3 p_j^f}{(2\pi)^3 2E_j^f} \right) (2\pi)^4 \delta(p_a - \sum_j p_j^f) \mathcal{M}_{bf} \mathcal{M}_{af}^* = -i (\mathcal{M}_{ba} - \mathcal{M}_{ab}^*) \quad (1.108)$$

In case $a = b$, (1.108) connects the imaginary part of the amplitude for elastic scattering to the sum of all possible cross sections of $a \rightarrow$ anything.

$$2\mathcal{I}m(\mathcal{M}_{aa}) = \sum_f \left(\prod_j \int \frac{d^3 p_j^f}{(2\pi)^3 2E_j^f} \right) (2\pi)^4 \delta(p_a - \sum_j p_j^f) |\mathcal{M}_{af}|^2 \quad (1.109)$$

Using very general arguments of unitarity of the scattering matrix, Lorentz invariance of the completeness relation and Fermi's golden rule, the optical theorem Eq.(1.109), connects the imaginary part of an elastic scattering amplitude \mathcal{M}_{aa} with the sum of the square moduli of all possible final states f , $|\mathcal{M}_{af}|^2$.

1.A.2 Applications of the optical theorem

1.A.2.1 Decay widths and unstable particles

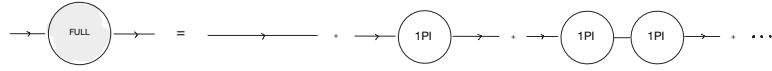
An important application of the optical theorem can be found in the definition of the total decay width, which for a particle of mass m reads:

$$\Gamma_{\text{tot}} = \sum_f \Gamma_f = \frac{1}{2m} \sum_f \left[\left(\prod_j \int \frac{d^3 p_j^f}{(2\pi)^3 2E_j^f} \right) (2\pi)^4 \delta(p_a - \sum_j p_j^f) |\mathcal{M}_{af}|^2 \right] \quad (1.110)$$

Using (1.109) we can connect the total decay width of a particle with the elastic scattering amplitude

$$m\Gamma_{\text{tot}} = \mathcal{I}m(\mathcal{M}_{aa}) \quad (1.111)$$

The elastic scattering amplitude \mathcal{M}_{aa} is decomposed as a sum of one particle irreducible diagrams, which is resummed as a geometric series:



$$= 1 + \Pi(q^2) + (\Pi(q^2))^2 + \dots = \frac{1}{1 - \Pi(q^2)} \quad (1.112)$$

Fig. 1.19 Decomposition of the full elastic scattering amplitude as sum of powers of 1PI transition amplitudes. This is resummed as a geometric series leading to the propagator term in Eq. (1.113)

The resummed term in (1.112) is nothing but the full propagator:

$$\frac{i}{q^2 - m_0^2 - \mathcal{R}e(\Pi(q^2)) - i\mathcal{I}m(\Pi(q^2))} \quad (1.113)$$

With m_0^2 being the pole mass. By proceeding to its renormalisation we can assign a physical (measurable) mass to the term that satisfies the following equation:

$$m^2 - m_0^2 - \mathcal{R}e(\Pi(q^2)) = 0 \quad (1.114)$$

Substituting the definition of physical mass Eq.(1.114) and the optical theorem as declined in Eq.(1.111) in the propagator of Eq.(1.113) we obtain:

$$\frac{i}{q^2 - m^2 - im\Gamma_{\text{tot}}} \quad (1.115)$$

The imaginary part of the elastic scattering amplitude dresses the bare propagator and shifts the pole from the physical mass, eliminating the divergences at denominator. Example with $e^+e^- \rightarrow Z \rightarrow f\bar{f}$.

$$\sigma(e^+e^- \rightarrow Z \rightarrow f\bar{f})(q^2) \propto \frac{1}{(q^2 - m_Z^2)^2 + \Gamma_{\text{tot}}m_Z^2}$$

1.A.2.2 Unitarity bound

If we shift our focus to processes involving two particles in the initial state as well as in the final state, the optical theorem places an upper bound on the cross section. Let's consider the case of two massless particles colliding head to head, $p_1 + p_2 = k_1 + k_2$ and pick the center of mass frame to explicit the momenta:

$$\begin{aligned} p_1 &= E(+1, 0, 0, +1), & k_1 &= E(1, +\sin\theta, 0, +\cos\theta), \\ p_2 &= E(+1, 0, 0, -1), & k_2 &= E(1, -\sin\theta, 0, -\cos\theta), \end{aligned} \quad (1.116)$$

Here we have set the azimuthal angle $\varphi = 0$ exploiting the rotational invariance of the system. There are two independent Mandelstam variables for this system, s and t :

$$s = (p_1 + p_2)^2 = 4E^2, \quad t = (p_1 - k_1)^2 = -\frac{s}{2}(1 - \cos\theta), \quad u = -s - t \quad (1.117)$$

Hence the matrix element describing this process can be described by two independent kinematic variables

$$\mathcal{M}(2 \rightarrow 2) = f(s, t) = f(s, z) \quad (1.118)$$

With $z = \cos\theta$ and $|z| \leq 1$. Since the matrix element $\mathcal{M}(2 \rightarrow 2)$ depends on the bounded variable z , it can be projected onto the Legendre polynomial basis:

$$\mathcal{M}(2 \rightarrow 2)(s, z) = 16\pi \sum_j (2j + 1) a_j(s) P_j(z) \quad (1.119)$$

Where $P_j(z)$ is the j – th Legendre polynomial, satisfying the orthonormality relation:

$$\int_{-\infty}^{+\infty} dz P_j(z) P_k(z) = \frac{2}{2j+1} \delta_{jk} \quad (1.120)$$

The energy dependent coefficient $a_j(s)$ is recovered by projecting the matrix element $\mathcal{M}(2 \rightarrow 2)(s, z)$ onto the Legendre polynomial basis:

$$a_j(s) = \frac{1}{32\pi} \int_{-\infty}^{+\infty} dz P_j(z) \mathcal{M}(s, z) \quad (1.121)$$

If we recover the formulation of the optical theorem of (1.109), we can split the RHS into elastic and inelastic processes as:

$$\begin{aligned} \frac{1}{s} \mathcal{I}m(\mathcal{M}_{aa}) &= \underbrace{\sigma(2 \rightarrow 2)}_{\text{elastic}} + \underbrace{\sigma(2 \rightarrow \text{anything})}_{\text{inelastic}} \\ &\geq \underbrace{\sigma(2 \rightarrow 2)}_{\text{elastic}} \end{aligned} \quad (1.122)$$

If we decompose the RHS (1.122) in partial waves:

$$\begin{aligned} \sigma(2 \rightarrow 2)(s) &= \frac{1}{2s} \int \frac{d^3 k_1}{(2\pi)^2 2E_1} \frac{d^3 k_2}{(2\pi)^2 2E_2} (2\pi)^2 \delta^4(p_1 + p_2 - k_1 - k_2) |\mathcal{M}(s, z)|^2 \\ &= \frac{1}{32\pi s} \int_{-1}^1 dz \left[16\pi \sum_j (2j+1) a_j(s) P_j(z) \right] \left[16\pi \sum_k (2k+1) a_k^*(s) P_k(z) \right] \\ &= \frac{16\pi}{s} \sum_j (2j+1) |a_j(s)|^2 \end{aligned} \quad (1.123)$$

Doing the same on the LHS of (1.122) we obtain:

$$2\mathcal{I}m[\mathcal{M}_{aa}(s, z)] \stackrel{k_1 \parallel p_1}{=} 2[\mathcal{M}_{aa}(s, 1)] \stackrel{P_j(1)=1}{=} 32\pi \sum_j (2j+1) \mathcal{I}m[a_j(s)] \quad (1.124)$$

Recovering the inequality of (1.122) and substituting (1.123) and (1.124) we can see that for any j , the coefficients (1.121) partial wave decomposition of $\mathcal{M}(2 \rightarrow 2)$ need to satisfy

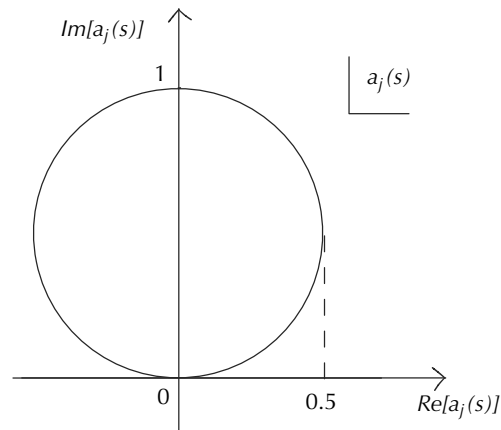


Fig. 1.20 Argand diagram for the partial wave decomposition coefficients $a_j(s)$. The area delimited by the circumference is the one allowed by the optical theorem

$$\mathcal{I}m[a_j(s)] \geq |a_j(s)|^2 \quad (1.125)$$

Hence, the optical theorem imposes an upper boundary on the coefficients of the partial wave decomposition of $\mathcal{M}(2 \rightarrow 2)$. In order for it to be satisfied,

$$\mathcal{R}e[a_j(s)] < \frac{1}{2}, \quad \text{and} \quad |a_j(s)| \leq 1 \quad (1.126)$$

This has an important consequence on the validity of the contact interaction model in the Fermi theory, as well as of the gauge vector boson model in the electroweak theory.

1.A.3 General facts about $SU(N)$

$SU(N)$ is the group of complex unitary matrices with unit determinant:

$$SU(N) = \{U(n \times n) \ / \ UU^\dagger = U^\dagger U = \mathbb{1}, \quad \det(U) = 1\} \quad (1.127)$$

Out of the $2n^2$ real parameters defining a generic complex $n \times n$ matrix, $n^2 - 1$ are free if $U \in SU(N)$. If we express the matrix U using the exponential parametrisation:

$$U = \exp[i\alpha_K t_K] \quad (1.128)$$

where the α_K are real parameters, and expand U around the identity, we find:

$$U \xrightarrow{\alpha_K \rightarrow 0} \mathbb{1} + i\alpha_K t_K + \mathcal{O}(\alpha^2) \quad (1.129)$$

The t_K are the $n^2 - 1$ generators of the Lie algebra associated to the group and form a vector space which has the same dimensionality as $SU(N)$.

To identify the characteristics that the generators must have, we make use of the conditions of unitarity of U :

$$UU^\dagger = (\mathbb{1} + i\alpha_K t_K)(\mathbb{1} - i\alpha_K t_K^\dagger) = \mathbb{1} \implies t = t^\dagger \quad (1.130)$$

And the unity of its determinant:

$$\det(U) = e^{\text{Tr}[i\alpha_K t_K]} = 1 \implies \text{Tr}[t_K] = 0 \quad (1.131)$$

Where we made use that for a diagonalisable matrix M

$$\det(M) = \det(\Lambda) = \prod_i^N \lambda_i$$

with $\Lambda = S M S^{-1}$ eigenvalue matrix, then:

$$\exp[\text{Tr}(\log M)] = \exp\left[\text{Tr}\left(S \log \Lambda S^{-1}\right)\right] = \exp\left[\sum_{i=1}^N \log \lambda_i\right] = \prod_i^N \lambda_i = \det(M)$$

The t_K form a basis of the vector space of traceless hermitian matrices, the commutator of this Lie algebra is a linear combination of elements of the basis. In fact

$$i[t_k, t_j] = i(t_j t_k - t_k t_j) \quad (1.132)$$

is hermitian

$$[i(t_j t_k - t_k t_j)]^\dagger = -i[(t_k t_j - t_j t_k)] = i(t_j t_k - t_k t_j) \quad (1.133)$$

and traceless:

$$i\text{Tr}[(t_j t_k - t_k t_j)] = \text{Tr}[t_j t_k] - \text{Tr}[t_k t_j] = 0 \quad (1.134)$$

Hence we define the structure constants f_{ijk}

$$[t_k, t_j] = i f_{jk}^\ell t_\ell \quad (1.135)$$

1.A.4 Symmetries and interactions

1.A.4.1 *global vs. local gauge invariance*

As extensively discussed in the previous sub-section, symmetries play an important role in the definition of the Standard Model. The Lagrangian density:

$$\mathcal{L}_0 = \bar{\psi}(x)(i\not{\partial} - m)\psi(x) \quad (1.136)$$

for a free particle exhibits a *global* $U(1)$ symmetry, since the transformation

$$\begin{aligned} \psi(x) &\rightarrow e^{i\theta q}\psi(x) \\ \partial_\mu\psi(x) &\rightarrow e^{i\theta q}\partial_\mu\psi(x) \end{aligned} \quad (1.137)$$

with θ and q constant parameters, leaves it invariant. According to Noether's theorem, there exist a conserved current $J_\mu(x) = q\bar{\psi}(x)\gamma_\mu\psi(x)$ and an associated conserved charge q .

The interactions between matter and forces arise naturally by requiring that the Lagrangian is *locally* gauge invariant. In fact, if we gauge this symmetry, and promote the $U(1)$ symmetry to a local symmetry (*i.e.* $\theta \rightarrow \theta(x)$), we obtain QED.

The local $U(1)$ gauge transformation reads:

$$\begin{aligned} \psi(x) &\rightarrow e^{i\theta(x)q}\psi(x) \\ \partial_\mu\psi(x) &\rightarrow e^{i\theta(x)q}\partial_\mu\psi(x) + iqe^{i\theta(x)q}\psi(x)\partial_\mu\theta(x) \end{aligned} \quad (1.138)$$

Clearly, the gauge invariance of Eq. (1.136) is now broken due to the extra term generated by the space-time dependence of the transformation. In other words, gauge invariance is violated since fields and derivatives of fields transform differently under a *local* gauge transformation.

By redefining the derivative $\partial_\mu \rightarrow D_\mu$ as:

$$D_\mu \equiv \partial_\mu + iqA_\mu \quad (1.139)$$

the requirement that both $\psi(x)$ and D_μ now transform in the same way under a *local* $U(1)$ transformation

$$\begin{aligned}\psi(x) &\rightarrow e^{i\theta q(x)}\psi(x) = U(x)\psi(x) \\ D_\mu\psi(x) &\rightarrow e^{i\theta q(x)}D_\mu\psi(x) = U(x)D_\mu\psi(x)\end{aligned}\quad (1.140)$$

is enforced by the fact that a redefinition of the field

$$A_\mu \rightarrow A'_\mu = A_\mu - \partial_\mu\theta(x) \quad (1.141)$$

leaves the Maxwell equations unchanged. The covariant derivative of Eq. (1.141), plugged in the Lagrangian of Eq.(1.136)

$$\begin{aligned}\mathcal{L}_1 &= \bar{\psi}(x)(i\not{D} - m)\psi(x) \\ &= \bar{\psi}(x)(i\not{\partial} - m)\psi(x) - q\bar{\psi}(x)\gamma_\mu\psi(x)A^\mu\end{aligned}\quad (1.142)$$

generates a term that can be interpreted as the coupling between the electromagnetic current $J^\mu = q\bar{\psi}(x)\gamma_\mu\psi(x)$ and the photon field A^μ . A peculiar feature of abelian field theories (such as QED) is given by the fact that the field strength tensor $F^{\mu\nu}(x)$ is gauge invariant:

$$F^{\mu\nu}(x) = \frac{1}{iq}[D^\mu, D^\nu] = \frac{1}{iq}[\partial^\mu + iqA^\mu, \partial^\nu + iqA^\nu] = \partial^\mu A^\nu(x) - \partial^\nu A^\mu(x) \quad (1.143)$$

The last missing ingredient to have \mathcal{L}_{QED} is a kinetic term for the photon field $\mathcal{L}_{\text{kin}} = \frac{1}{2}(|\vec{E}(x)|^2 - |\vec{B}(x)|^2)$, which in manifestly covariant form reads:

$$\mathcal{L}_{\text{kin}} = -\frac{1}{4}F^{\mu\nu}(x)F_{\mu\nu}(x)$$

hence:

$$\mathcal{L}_{\text{QED}} = \bar{\psi}(x)(i\not{D} - m)\psi(x) - \frac{1}{4}F^{\mu\nu}(x)F_{\mu\nu}(x) \quad (1.144)$$

Which is *local* $U(1)$ gauge invariant. Including a mass term for the gauge boson, proportional to $A^\mu(x)A^\nu(x)$, would violate such invariance:

$$m_\gamma^2 A^\mu(x)A^\nu(x) \xrightarrow{\text{LGT}} m_\gamma^2 [A^\mu(x) + \partial^\mu\theta(x)][A^\nu(x) + \partial^\nu\theta(x)] \neq m_\gamma^2 A^\mu(x)A^\nu(x) \quad (1.145)$$

1.A.4.2 Non-abelian (Yang-Mills) gauge theories

The procedure outlined for $U(1)$ can be extended to the more general case of $SU(N)$ gauge invariance. We start from a Lagrangian of free fields which is invariant under a global symmetry:

$$\mathcal{L}_\psi(\psi, \partial_\mu \psi) \quad (1.146)$$

where ψ is a N -tuple of a compact Lie group G . The *global* gauge invariance of \mathcal{L}_ψ implies that the transformation:

$$\psi \rightarrow \psi' = U(\theta)\psi \quad (1.147)$$

with $U(\theta) \in SU(N)$, leaves the Lagrangian invariant. If we express the matrix U in exponential parametrisation $U = \exp[ig t_a \theta^a]$ and expand around the identity, we see that the generators of this symmetry group are $N^2 - 1$ traceless hermitian matrices t_a which generate infinitesimal transformations around the identity (1.A.3):

$$U = \mathbb{1} + ig t_a \theta^a + \mathcal{O}(\theta^2) \quad (1.148)$$

In order to gauge this symmetry and allow the parameters θ^a to be function of the space-time coordinates, hence promoting this symmetry to a *local* symmetry of the Lagrangian, the derivative in (1.146) has to be made covariant:

$$\mathcal{L}_\psi(\psi, \partial_\mu \psi) \rightarrow \mathcal{L}_\psi(\psi, D_\mu \psi) \quad (1.149)$$

With

$$D_\mu = \partial_\mu + ig t^a A_\mu^a \quad (1.150)$$

From the requirement that both fields and field derivatives transform homogeneously under a local transformation

$$\begin{aligned} \psi(x) &\rightarrow \psi'(x) = U(\theta(x))\psi(x) \\ D_\mu \psi(x) &\rightarrow (D_\mu \psi(x))' = U(\theta(x))D_\mu \psi(x) \end{aligned} \quad (1.151)$$

We obtain the transformation rule for the covariant derivative, *i.e.* $D'_\mu = UD_\mu U^\dagger$. Which, once substituting the definition of covariant derivative (1.150) yields the transformation law for the fields A_μ^a

$$A_\mu^a \rightarrow A'^a_\mu = A_\mu^a - \partial_\mu \theta^a(x) - gf^{abc} A_\mu^b \theta^c(x) + \mathcal{O}(\theta^2) \quad (1.152)$$

The $t^a A_\mu^a$ are $(n \times n)$ matrices which result from the sum of the $N^2 - 1$ t^a multiplied by a vector of dimension N . In complete analogy to the abelian case, the kinetic term for the A_μ^a fields are obtained from the commutator of the covariant derivative:

$$\frac{1}{ig} [D_\mu, D_\nu] = t^a F_{\mu\nu}^a, \quad \text{with} \quad F_{\mu\nu}^a = \partial_\mu A_\nu^a - \partial_\nu A_\mu^a - gf^{abc} A_\mu^b A_\nu^c \quad (1.153)$$

Having defined $A_\mu = t^a A_\mu^a$ and $F_{\mu\nu} = t^a F_{\mu\nu}^a$ the field strength tensor can be expressed as:

$$F_{\mu\nu} = \partial_\nu A_\mu - \partial_\mu A_\nu + ig [A_\mu, A_\nu] \quad (1.154)$$

As opposed to non-abelian gauge theories, the newly defined field strength tensor $F_{\mu\nu}^a$ is not gauge invariant by itself

$$F'_{\mu\nu} = UF'_{\mu\nu}U^\dagger$$

However, it can be shown that the kinetic term $F_{\mu\nu}^a F^{a,\mu\nu}$ is gauge invariant:

$$\begin{aligned} \mathcal{L}_{\text{kin}} &= -\frac{1}{4} F_{\mu\nu}^a F^{a,\mu\nu} \\ &= -\frac{1}{4} \delta^{ab} F_{\mu\nu}^a F^{b,\mu\nu} \\ &= -\frac{1}{2} \text{Tr}[t^a t^b] F_{\mu\nu}^a F^{b,\mu\nu} \\ &= -\frac{1}{2} \text{Tr}[F_{\mu\nu} F^{\mu\nu}] \end{aligned} \quad (1.155)$$

And the gauge transformed Lagrangian would read:

$$\begin{aligned}
\mathcal{L}'_{\text{kin}} &= -\frac{1}{2}\text{Tr}[F'_{\mu\nu}F'^{\mu\nu}] \\
&= -\frac{1}{2}\text{Tr}[UF'_{\mu\nu}\underbrace{U^\dagger U}_{\mathbb{1}}F'^{\mu\nu}U^\dagger] = \mathcal{L}_{\text{kin}}
\end{aligned}
\tag{1.156}$$

Putting the pieces back together we obtain the Yang-Mills Lagrangian:

$$\mathcal{L}_{\text{YM}} = -\frac{1}{4}F_{\mu\nu}^a F^{a,\mu\nu} + \mathcal{L}_\psi(\psi, \partial_\mu\psi)
\tag{1.157}$$

Where \mathcal{L}_ψ is the Lagrangian describing matter fields. Much as Eq. (1.144), Eq. (1.157) describes forces mediated by massless bosons since a mass term $A_\mu^a A^{a,\mu}$ would violate gauge invariance. This indicates that gauge bosons like W^\pm/Z must acquire mass via a different mechanism. Moreover an interesting feature arises from the kinetic term for $SU(N)$ gauge theories:

$$F_{\mu\nu}^a F^{a,\mu\nu} = (\partial_\mu A_\nu^a - \partial_\nu A_\mu^a - gf^{abc}A_\mu^b A_\nu^c)(\partial^\mu A^{a,\nu} - \partial^\nu A^{a,\mu} - gf^{abc}A^{b,\mu} A^{c,\nu})
\tag{1.158}$$

the requirement of gauge invariance has determined the appearance in the Lagrangian of cubic and quartic self-interaction terms between bosons. These were not appearing in QED since $f^{abc} = 0$ for an abelian group such as $U(1)$. Moreover, if $N = 3$ we obtain the QCD Lagrangian, where the fermions are triplet of colour and there are $N^2 - 1 = 8$ massless gauge bosons which are identified as the gluons.

Chapter 2

QED in $\bar{B} \rightarrow \bar{K} \ell^+ \ell^-$ LFU ratios: Theory versus Experiment, a Monte Carlo Study

2.1 Introduction

Within the Standard Model (SM), the Yukawa coupling is the only interaction that distinguishes the different fermion families. In the lepton sector, all the Yukawa couplings are small compared to the SM gauge couplings, giving rise to an approximate accidental symmetry known as Lepton Flavour Universality (LFU). This symmetry holds to a very good accuracy within the SM, especially for the two lightest families (e and μ), and it can be tested to high accuracy in B meson decays, where the kinematic effects due to light lepton masses are small (see e.g. Ref. [1,2] for a review).

Particularly interesting in this respect are the μ/e LFU ratios in flavour changing neutral currents (FCNC) transitions [3], such as

$$R_K|_{q_0^2 \in [q_1^2, q_2^2]} \text{GeV}^2 = \frac{\Gamma[\bar{B} \rightarrow \bar{K} \mu^+ \mu^-]}{\Gamma[\bar{B} \rightarrow \bar{K} e^+ e^-]} \Big|_{q_0^2 \in [q_1^2, q_2^2]} \text{GeV}^2, \quad (2.1)$$

where $q_0^2 \equiv (p_B - p_K)^2$. In the SM, $R_K^{\text{SM}} \approx 1$ up to QED corrections [4,5]. The current experimental determination is [6–8]

$$R_K|_{q_0^2 \in [1.1, 6]} \text{GeV}^2 = 0.846_{-0.039-0.012}^{+0.042+0.016}, \quad (2.2)$$

and exhibits a statistically significant deviation from the theory prediction. Similar tensions between data and SM predictions, albeit with smaller statistical significance, have been reported in the analogous quantities R_{K^*0} [9], $R_{K^{**}}$ and R_{K_S} [10].

In this paper, we assess the robustness of the theoretical determination of R_K with respect to QED corrections, which provide the dominant source of LFU violation within the SM. While QED corrections are tiny for fully inclusive observables (when differential in collinear-safe variables), they induce non-universal corrections of the type $(\alpha/\pi) \ln(m_\ell/m_B)$ which can reach the 10% level in the electron mode, when accompanied by tight cuts on the photon energy [4,5]. These effects are corrected for by the experimental collaborations: the value in Eq. ((2.2)), as well as the results for the LFU ratios reported in [9,10], correspond to photon-inclusive observables (in the collinear safe differential variable q_0^2 , cf. Sec. 2.2.1.) However, what is really measured are not photon-inclusive observables: tight cuts on reconstructed B mass are employed to reduce, amongst the different background contributions, events originated from resonant modes, e.g. $\bar{B} \rightarrow \bar{K}(J/\Psi \rightarrow \ell^+ \ell^-)$ that leak into the signal region. The photon-inclusive results are obtained by comparing with appropriate Monte Carlo (MC) simulations. The purpose of this paper is to check this procedure using a dedicated MC-framework developed on grounds on our earlier work [5]. The latter consists of a complete differential description of $O(\alpha)$ QED corrections in $\bar{B} \rightarrow \bar{K} \ell^+ \ell^- (\gamma)$ based on an effective meson theory.

In the experimental analyses, QED corrections are implemented via photon shower algorithms such as PHOTOS [11–14], or the PHOTONS++ module [15] of SHERPA [?], where mesons are treated as point-like particles. In [5], using gauge invariance, it was shown that no further lepton non-universal collinear logs (i.e. $\ln(m_\ell)$ terms) are generated by structure dependent corrections, i.e. that the point-like approximation for the mesons is a very good approximation, especially when considering LFU ratios. The photon shower algorithms used by the experiments therefore do provide a very good starting point to describe data. In practice, QED corrections in $\bar{B} \rightarrow \bar{K} \ell^+ \ell^- (\gamma)$ are not treated perfectly due to the resonant mode being simulated separately from the rare mode, therefore neglecting the respective interference. The latter is a potentially dangerous effect due to the *migration* towards lower q^2 -values of events with on-shell charmonium resonances and sizeable photon-energy emission: an effect which is particularly pronounced for the electron mode [4,5]. We note that in the inclusive case these effects have been investigated in the factorisation approximation in [?], whereas we can go beyond since the $\bar{B} \rightarrow \bar{K} \Psi$ branching fractions are known from experiment.

This paper consists of two parts. Firstly, the description of our MC-framework based on [5], and its comparison with PHOTOS at the fully differential level, considering the rare mode only (i.e. the short-distance (SD) part of the decay amplitude) is discussed. Second, going beyond the PHOTOS analysis, we assess the impact of the charmonium resonances (or the long-distance (LD) contribution to the decay amplitude), which is particularly relevant in the electron mode [6–8]. This second part is addressed in a twofold manner: i) by means of our MC-framework, assessing the impact of the SD–LD interference effects (not included in PHOTOS), focusing on the region $q^2 \in [1.1, 6] \text{ GeV}^2$; ii) by means of a semi-analytic approach, using the splitting function, assessing the complete impact of the resonant modes beyond interference terms (and resumming the leading collinear logs).

We limit our analysis to the neutral mode $\bar{B}^0 \rightarrow \bar{K}^0 \ell^+ \ell^-$. This choice does not limit the validity of our conclusions on SD–LD interference effects due to charmonium resonances, whilst it has an important simplification for the numerical study. In this case, we can analyse in full generality the impact of the hadronic form factor, without resorting to a derivative expansion in the underlying meson effective theory [5].

It is noted that a first comparison of analytical estimates of QED corrections and PHOTOS has been presented in Ref. [4]. The present study provides significant improvements compared to [4] on various aspects: i) building a dedicated MC to simulate $\bar{B} \rightarrow \bar{K} \ell^+ \ell^- (\gamma)$ events, we are able to perform an extensive study of the tool used to interpret data at a fully differential level; ii) our MC is valid for generic photon kinematics, while the analysis of [4] implicitly assumed tight cuts on the photon-angle emission (cf. App. A.2 [5]); iii) we perform a detailed study of the effects of the resonances, taking into account also the variation of the strong phase between SD and LD contributions.¹

The paper is organised as follows. In Sec. 2.2, we introduce the the basic kinematics of the process and the principles of our MC-approach. In the following Sec. 2.3, we compare kinematic distributions obtained with our MC-simulation with those obtained with PHOTOS. The impact of charmonium resonances is discussed in Sec. 2.4. Finally, in Sec. 5.5, we summarise our results and present a brief outlook. Technical details are deferred to Apps. 2.A.1, 2.A.2 to 2.A.4 and supplementary plots are collected in App. 2.A.3.

¹ Some other studies related to Monte Carlo are for semileptonic modes $B \rightarrow \pi \ell \nu$ [16] and $B \rightarrow D \ell \nu$ [17] and are different in that they do not contain resonances from the phenomenological viewpoint alone.

2.2 Monte Carlo Framework

2.2.1 Generalities

The process of interest is

$$\bar{B}(p_B) \rightarrow \bar{K}(p_K)\ell_1(\ell_1)\bar{\ell}_2(\ell_2) + g_A(k) . \quad (2.3)$$

In the absence of photon emission, it is a 3-body process, while in the presence of real photon emission, it corresponds to a 4-body process. The latter is characterised by five independent kinematic variables, cf. App. 2.A.1. The two kinematic variables adopted to describe the 3-body kinematics, or even the 4-body one if the photon is not detected, are

$$q^2 = (\ell_1 + \ell_2)^2 \quad \text{and} \quad c_\ell \equiv \cos \theta_\ell = - \left(\frac{\vec{\ell}_1 \cdot \vec{p}_K}{|\vec{\ell}_1| |\vec{p}_K|} \right)_{q\text{-RF}} , \quad (2.4)$$

where q -RF denotes the dilepton rest frame (RF). If the B momentum is known (e.g. at the generator level, or in a B -factory type experimental setup) the following the kinematic variables

$$q_0^2 = (p_B - p_K)^2 \quad \text{and} \quad c_0 \equiv \cos \theta_0 = - \left(\frac{\vec{\ell}_1 \cdot \vec{p}_K}{|\vec{\ell}_1| |\vec{p}_K|} \right)_{q_0\text{-RF}} , \quad (2.5)$$

are more useful [5]. Furthermore we define

$$\bar{p}_B \equiv p_B - k = \ell_1 + \ell_2 + p_K , \quad \bar{p}_B^2 = (m_B^{\text{rec}})^2 , \quad (2.6)$$

which corresponds to the reconstructed B -meson mass from its visible decay products, and the variable δ_{ex} ,

$$(m_B^{\text{rec}})^2 = m_B^2(1 - \delta_{\text{ex}}) , \quad 0 < \delta_{\text{ex}} < 1 , \quad (2.7)$$

which provides a natural choice for the physical cut-off regulating soft divergences of real photons emission. Soft and soft-collinear logs then manifest as $\ln \delta_{\text{ex}}$ and $\ln \delta_{\text{ex}} \ln m_\ell$ terms. Single $\ln m_\ell$ terms are referred to (hard)-collinear logs throughout; a terminology which differs at times from the ones used in soft-collinear effective theories [?].

As stated in many textbooks, a photon energy cut-off, m_B^{rec} or δ_{ex} in our case, is sufficient to define IR-safe observables (for massive charged particles). However, this is not the procedure applied in many of today's experiments, especially at hadron colliders. In this case the event distributions are *fitted* in a given window of $m_B^{\text{rec}} > m_B^{\text{rec},\ell}$ and m_B^{rec} becomes a key differential variable. Using the simulated shape in m_B^{rec} , by a MC-tool (e.g. PHOTOS), the theoretical non-radiative rate in the IR-safe differential variable q_0^2 is reconstructed.² Checking the validity of this procedure requires the comparison of the MC-tool used in the data analysis with one based on a QED calculation defined in a full theoretical framework, such as the one presented in [5]. The validation of the procedure ensures that, within the SM, the measured R_K is then $R_K|_{\text{reconstr.}}^{\text{SM}} = 1 + \mathcal{O}(\frac{\alpha}{\pi})$, where $\alpha = e^2/(4\pi) \approx 1/137$ is the fine structure constant.

2.2.2 Basic strategy of the Monte Carlo approach

The strategy of our MC-framework is based on the following steps:

- We introduce a technical cut-off $E_{\gamma,\text{cut}}^{(i)}$ on the photon energy in a given RF (indicated by the superscript i). This cut-off is chosen well below the experimental resolution on the missing energy, such that events with $E_{\gamma}^{(i)} < E_{\gamma,\text{cut}}^{(i)}$ can be simulated according to 3-body kinematics, while events with $E_{\gamma}^{(i)} > E_{\gamma,\text{cut}}^{(i)}$ are simulated according to 4-body kinematics.
- The 3-body and 4-body events are simulated according to the corresponding (Born-level) distributions reported in Ref. [5], which depends on the $f_{\pm}(q^2)$ hadronic form factors for $B \rightarrow K$. The relative normalisation between 3-body events (N_3) and 4-body events (N_4), namely the ratio

$$f^{\text{th}} \equiv \frac{N_3}{N_4} \equiv \frac{\Gamma_3}{\Gamma_4} = f(E_{\gamma,\text{cut}}^{(i)}) , \quad (2.8)$$

is the key theory input for the numerical simulation.

- The 3-body rate is computed at $\mathcal{O}(\alpha)$, taking into account both virtual and real corrections. By construction, Γ_3 is free from soft divergences, but it depends logarithmically on the (artificial) photon energy cut-off $E_{\gamma,\text{cut}}^{(i)}$. It can be decomposed as

$$\Gamma_3 = \Gamma_{\text{soft-log}} \ln E_{\gamma,\text{cut}}^{(i)} + \Gamma_{\text{rest}}^{(i)} . \quad (2.9)$$

²In terms of the q_0^2 -variable, the single-differential non-radiative rate is equivalent to the fully photon-inclusive rate up to $\mathcal{O}(\frac{\alpha}{\pi})$ corrections.

Here, $\Gamma_{\text{soft-log}}$ is the well-known universal (Lorentz-invariant) coefficient of the soft singularities [18], while $\Gamma_{\text{rest}}^{(i)}$ is a frame-dependent quantity, indicated by the superscript [5].

- A key simplification for the determination of f^{th} is the observation that the total rate Γ_{tot} is equal to the tree-level rate, Γ_{tree} , up to finite (non-log enhanced) corrections of $\mathcal{O}(\alpha)$:

$$\Gamma_{\text{tot}} \equiv \Gamma_3 + \Gamma_4 = \Gamma_{\text{tree}} \times [1 + \mathcal{O}(\alpha)] . \quad (2.10)$$

Neglecting the tiny $\mathcal{O}(\alpha)$ terms, this allows us to extract f^{th} simply by the ratio $\Gamma_{\text{tree}}/\Gamma_3$, via the relation

$$f^{\text{th}} = \left(\frac{\Gamma_{\text{tree}}}{\Gamma_3} - 1 \right)^{-1} . \quad (2.11)$$

- As demonstrated in [5], the q_0^2 single-differential spectrum is also free from soft and collinear divergences. This implies that the relation ((2.10)) holds not only for the total rate, but also for the q_0^2 single-differential rate (or partial rates defined on a given q_0^2 interval). Using Eq. (2.11) simplifies the numerical analysis considerably, since $\Gamma_{\text{tree}}/\Gamma_3$ can be determined using only 3-body phase-space integrations. The values of $\Gamma_{\text{tree}}/\Gamma_3$ computed using the analytic code from [5] relevant to the present study are reported in Tab. 2.3 in App. 2.A.4.

2.2.3 Numerical procedure

The 3- and 4-body decay rates are implemented in a numerical framework by means of the zfit package [19]. They are interpreted as (non-negative) probability distribution functions (PDFs) with an a priori unknown normalisation. This allows us to generate the MC samples by means of the hit-or-miss algorithm. The concrete sampling procedure, for both 3- and 4-body decays, is outlined as follows:

1. A single point in phase space, denoted by \vec{x} , is uniformly sampled in the kinematically allowed region of (q^2, c_ℓ) or $(q^2, \vec{p}_B^2, c_\ell, c_\gamma, \phi_\gamma)$ for simulated 3- or 4-body events, respectively.
2. Using the kinematic decomposition reported in App. 2.A.1, the sampled variables are translated to the corresponding momenta of the B decay products. The scalar

products that enter the decay widths, as well as the decay width $\Gamma(\vec{x})$ itself, are evaluated at the sampled point in phase space.

3. A random number r is extracted uniformly in the range $r \in [0, m]$, where m is the maximum value of the decay width in the allowed kinematic range. If $r > \Gamma(\vec{x})$ ("miss") points 1. and 2. are repeated until for one sampled r , $r < \Gamma(\vec{x})$ ("hit") and the point \vec{x} is kept.

The standard hit-or-miss algorithm can suffer from very low sampling efficiency in the case where the decay width exhibits pronounced peaks since it only accepts a fraction of extractions equal to the ratio of the volume under $\Gamma(\vec{x})$ and the volume of the hypercube containing $\Gamma(\vec{x})$ itself. This is valid in particular for the 4-body decay width $\Gamma_4(\vec{x})$ which is peaked close to collinear and soft regions. In order to increase the sampling efficiency, the "importance sampling" technique is employed. This technique consists in dividing the support, over which \vec{x} is sampled, such that in each subinterval, $\Gamma(\vec{x})$ has a smaller variation than in the overall range, hence allowing to increase the sampling efficiency by one to two orders of magnitude.

2.2.3.0.1 We compare our MC-approach against the EvtGen [20] + PHOTOS [11,12] which are the simulation software packages used by the LHCb collaboration. The former is an event generator specifically designed for B -physics in which the decay amplitudes (models), instead of PDFs, are used for the simulation of heavy meson decays. PHOTOS encodes the QED radiative corrections to such decays and uses a splitting function approach iteratively. In principle, this achieves the inclusion of the leading logs and thus, remaining discrepancies can be expected to be of $\mathcal{O}(\frac{\alpha}{\pi})$. Since 2005, when multi-photon radiation was introduced [13], there were no further public upgrades of the program until 2010, when PHOTOS was moved to a C++ environment allowing the use of event records such as HepMC [21]. We employ version 3.64 which enables the use of PHOTOS in the case where there are no parent particle(s) or incoming beams generating the decaying particle, which, paired with the EvtGen package, allows us for a direct comparison with our MC simulation. In order to match the EvtGen model with our description of the decay, $\mathcal{O}(\alpha_s)$ two-loop virtual corrections [22] to the decay width are switched off from the default EvtGen configuration.

Moreover, since our MC accounts for QED corrections up to $\mathcal{O}(\alpha)$, for each B decay in which more than a real photon is emitted, only the hardest emission is considered and all the softer emissions' momenta are summed and saved into one "particle" for further cross-checks.

2.3 Direct Comparison with PHOTOS at the Short Distance Level

2.3.1 Parameterisation of the short distance amplitude

In this section, we compare our MC-method, as described in Sec. 2.2.3, with the PHOTOS framework at the level of the SD contribution. Since both frameworks are expected to capture the leading logs one should expect differences to be of order of $\mathcal{O}(\frac{\alpha}{\pi})$ only. Let us first define the SD amplitude. Following our previous conventions [5], we write

$$\mathcal{A}_{\bar{B} \rightarrow \bar{K} \ell^+ \ell^-} \equiv \langle \bar{K} \ell^+ \ell^- | (-\mathcal{L}_{\text{int}}) | \bar{B} \rangle = \frac{G_F}{\sqrt{2}} V_{\text{ts}}^* V_{\text{tb}} L_0 \cdot H_0 + \mathcal{O}(\alpha), \quad (2.12)$$

where L_0 and H_0 correspond to the leptonic and hadronic parts which read

$$\begin{aligned} L_0^\mu(q^2) &= \bar{u}(\ell^-) g_A^\mu (C_V + C_{A g_{A5}}) v(\ell^+), \\ H_0^\mu(q^2) &= f_+(q^2) (p_B + p_K)^\mu + f_-(q^2) (p_B - p_K)^\mu, \end{aligned} \quad (2.13)$$

with $C_{V(A)} = -\alpha C_{9(10)}/(2\pi)$, thereby neglecting the dipole operator O_7 as justified for a scalar meson final state.³ The SD contribution consists of the standard form factors f_\pm . Note that when f_- is traded for the scalar form factor $f_0 = f_+ + \frac{q^2}{m_B^2 - m_K^2} f_-$ only f_+ enters the vector part $C_V \propto C_9$. The specific form factors are taken from [23] (with set 2), which is a light-cone sum rules computation up to NLO twist-3 and $\mathcal{O}(\alpha_s)$, and is also used by the LHCb collaboration.

2.3.2 Comparison of our Monte Carlo with PHOTOS

The main results of this section consist of the plots in Fig. 2.1 and Fig. 2.2, for the kinematic variables q_0^2 (2.5) and q^2 (2.4), respectively. In each of these figures, the top plots display the impact of the radiative corrections on the q_0^2 - and q^2 -spectra when considering either muons (left) and electrons (right), in our MC. The normalisation per se of the MC-plots is not meaningful as both LO and NLO are separately normalised to 1 when integrated over q_0^2 or q^2 (compare with the normalised plots in Fig. 4 in [5]). This ambiguity can be removed by taking double ratios between our MC-approach and

³ In the relation of $C_{V(A)}$ and $C_{9(10)}$ we correct a factor minus two w.r.t. the published version of [5] which, however, has no impact on the result of that paper as all results are relative.

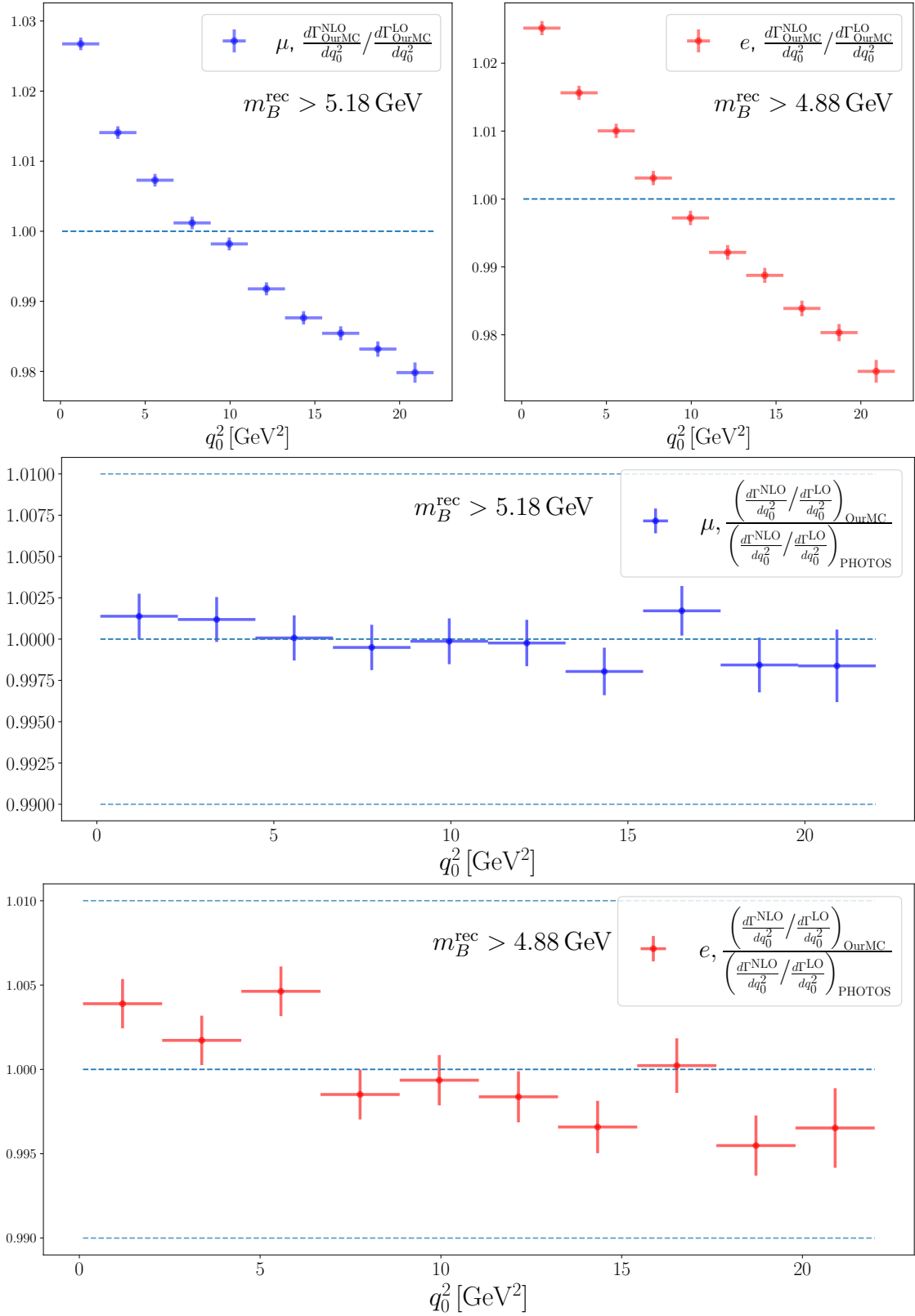


Fig. 2.1 Differential distributions in q_0^2 for the short distance transition only: NLO over LO for muons in blue (top left) and for electrons in red (top right) in our MC, with appropriate cuts as in Tab. 2.1. The normalisation of these upper plots is arbitrary (cf. main text). The double ratios of our MC versus the PHOTOS framework, shown in the middle and bottom plots, are free of ambiguities.

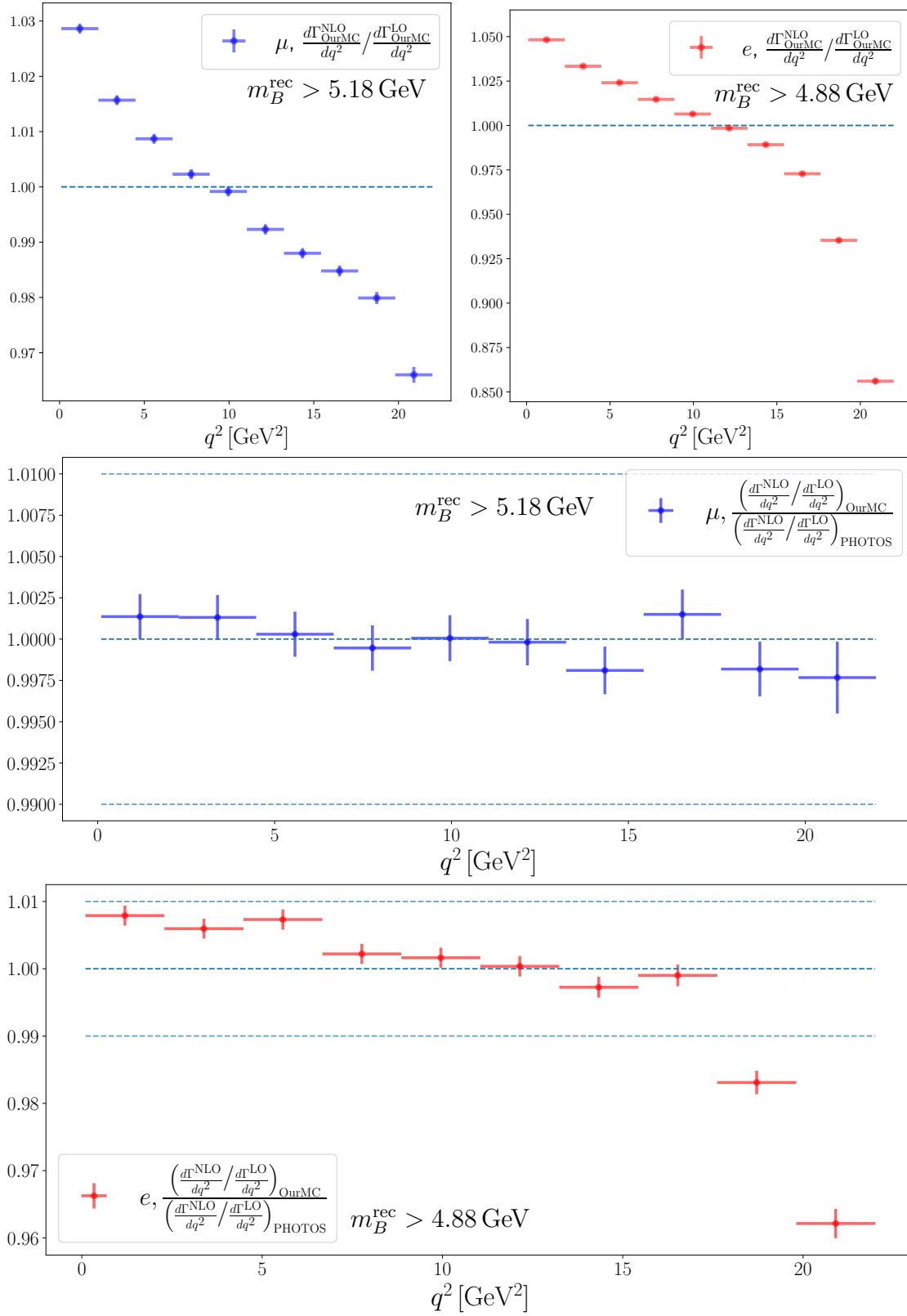


Fig. 2.2 Differential distributions in q^2 for the short distance transition only: The notation is the same as in Fig. 2.1.

the PHOTOS software as shown in the middle and bottom of these figures for muons and electrons respectively.

Let us discuss the q_0^2 -variable first. Even though the hard-collinear logs cancel in this variable, the introduction of a photon energy cut-off, via $m_B^{\text{rec}} = (4.88, 5.18)$ GeV, leads to sizeable QED contributions. The agreement between the two approaches is excellent as shown by the good compatibility of these distributions with unity across the q_0^2 -spectrum, for both lepton flavours (bottom plot).

The distributions in the q^2 -variable, shown in Fig. 2.2, are more delicate as hard collinear logs do not cancel. In addition, events can migrate in the q^2 -spectrum due to radiation which will be important when discussing the impact of the resonances. Hence, even without placing a photon-energy cut-off, the corrections are sizeable, cf. Fig. 4 in [5].

Again, the agreement between the two approaches is excellent, as expected, except for electrons at high q^2 where deviations up to $\mathcal{O}(4\%)$ are found. This originates from large corrections that go beyond the fixed $\mathcal{O}(\alpha)$ accuracy of our MC. In fact, at the kinematic endpoint, the corrections are roughly 20% (cf. Fig. 8 in [5]) at NLO, indicating the need of NNLO accuracy to reach % level precision, and explaining qualitatively the residual difference with PHOTOS (where the resummation of the leading-log corrections is implemented). Using the splitting function formalism in Sec. 2.4.3, in its resummed form, we were able to reproduce quantitatively the $\mathcal{O}(4\%)$ -effect between our MC and PHOTOS (cf. footnote 8).

It is worthwhile to elaborate on why the corrections are large at the kinematic endpoint in q^2 . This happens because, at the endpoint, the leptons carry all the energy and there is effectively no phase space for the real radiation. As a result, near the endpoint in q^2 , virtual corrections dominate and the cancellation between real and virtual corrections is maximally out of balance. In other words, requiring large q^2 is equivalent to a tight cut on the photon emission energy. In the splitting function approach, this can be seen from the lower boundary of the real emission integral (over the momentum fraction carried by the lepton, z) approaching the upper boundary.

In summary, the cross checks we have performed allow us to validate that the approximations adopted by PHOTOS in describing (real and virtual) QED corrections in $\bar{B}^0 \rightarrow \bar{K}^0 \ell^+ \ell^-$ decays are accurate to sub-percent level. Additional plots displaying comparisons of the impact of radiative corrections on the kinematic variable $\cos \theta_\ell$ between our MC and PHOTOS can be found in App. 2.A.3.

ℓ	$m_B^{\text{rec}} [\text{GeV}]$	δ_{ex}	$(q_0^2)_{\text{max}}$
μ	5.18	0.0486	$q^2 + 1.36 \text{ GeV}^2$
e	4.88	0.146	$q^2 + 4.07 \text{ GeV}^2$

Table 2.1 Relation between the cut on the reconstructed mass m_B^{rec} and the maximal value of q_0^2 affecting the spectrum at a given q^2 -value, after photon radiation, according to ((2.14)). The specific values of m_B^{rec} are fixed to the same values used in the LHCb analysis of R_K [24].

2.4 Adding Long Distance (Charmonium Resonances)

In this section, we assess the impact of the charmonium resonances on the lower part of the spectrum, specifically on the $1.1 \text{ GeV}^2 < q^2 < 6 \text{ GeV}^2$ region currently used to measure the LFU ratios. While the main contribution (peak) of the resonances is cut in the experimental analyses, a residual effect from the radiative tail of the resonances is potentially present at hadron colliders, where the q_0^2 variable is not accessible. As previously mentioned, the migration in q^2 , due to QED radiation, implies that events generated at high q_0^2 (e.g. close to the resonance region) necessarily move down toward low q^2 -values, possibly affecting the *signal* region for the rare mode. The migration is controlled by the m_B^{rec} cut: only events with

$$q^2 \leq q_0^2 \leq (q_0^2)_{\text{max}} \equiv q^2 + \delta_{\text{ex}} m_B^2, \quad (2.14)$$

are relevant to determine radiative corrections at a given q^2 -value.⁴

The m_B^{rec} cuts used to define the signal windows for electron and muon modes in the LHCb analyses are reported in Tab. 2.1. Note that the cut on the electrons is looser than the one on the muons: a measure implemented to decrease the loss of events in the electron case where radiation effect is stronger. As can easily be checked, in the electron case, events at $q^2 = 6 \text{ GeV}^2$ probe (via photon radiation) the non-radiative spectrum above the J/Ψ -resonance ($m_{J/\Psi}^2 \approx 9.58 \text{ GeV}^2$), but do not probe the $\Psi(2S)$ peak.

This effect is well known and the residual contribution of radiation from the J/Ψ in the signal region is taken into account in the experimental analyses. However, this is simulated as a completely incoherent process, while in reality interference effects between the SD amplitude and LD one are present. The purpose of this section is to estimate the possible impact of these effects. In Sec. 2.4.1, we discuss how the amplitude of the rare mode can be adapted to describe SD-LD interference terms. Using this modified parametrisation of the amplitude, in Sec. 2.4.2, we analyse the

⁴ The value $(q_0^2)_{\text{max}}$ is reached for photons emitted backward with respect to \vec{q} in the B RF [5].

Ψ	m_Ψ [MeV]	$\mathcal{B}(\Psi \rightarrow e^+e^-)$	$\mathcal{B}(\Psi \rightarrow \mu^+\mu^-)$	Γ_Ψ [MeV]
$J/\Psi(1S)$	3097	$5.971(32) \cdot 10^{-2}$	$5.961(33) \cdot 10^{-2}$	92.6(17)
$\Psi(2S)$	3686.1(6)	$7.93(17) \cdot 10^{-3}$	$8.0(6) \cdot 10^{-3}$	294(8)

Table 2.2 Data of charmonium resonances included in our analysis as taken from [25]. The J/Ψ mass uncertainty is negligibly small.

numerical impact of the interference terms in our MC-framework. Finally, in Sec. 2.4.3 we analyse the effect of interference terms, as well as the whole modulus square of the LD amplitude, via a semi-analytic approach.

2.4.1 Parameterisation of the charm amplitude

We extend the parameterisation of the amplitude in Sec. 2.3 for the SD form factor by including the effects of the charmonium resonances which we label as long distance (LD)

$$\mathcal{A}_{\bar{B} \rightarrow \bar{K} \ell^+ \ell^-}^{\text{tot}} = \mathcal{A}_{\bar{B} \rightarrow \bar{K} \ell^+ \ell^-}^{\text{SD}} + \mathcal{A}_{\bar{B} \rightarrow \bar{K} \ell^+ \ell^-}^{\text{LD}} . \quad (2.15)$$

The LD contribution can be absorbed into,

$$C_9^{\text{eff}}(q^2) = C_9 + \Delta C_9(q^2) , \quad (2.16)$$

a q^2 -dependent Wilson coefficient $\Delta C_9(q^2)$ (recall $C_V \propto C_9$). Its q^2 -dependence is parameterised by an n -times subtracted dispersion relation

$$\Delta C_9(q^2) = \sum_{k \geq 0}^{n-1} \frac{(q^2 - s_0)^k}{k!} \Delta C_9^{(k)}(s_0) + \frac{(q^2 - s_0)^n}{2\pi i} \int_{\text{cut}}^{\infty} \frac{ds}{(s - s_0)^n} \frac{\text{disc}[\Delta C_9](s)}{s - q^2 - i0} , \quad (2.17)$$

with a cut starting just below $m_{J/\Psi}^2$. Above, ‘‘disc’’ stands for the discontinuity, the k -superscript denotes the k^{th} derivative, and ‘‘cut’’ stands for the branch cut. Formally, $n \geq 1$ as otherwise, the dispersion integral is not convergent. In this form, (2.17) is valid in full generality and one can equally write it for the amplitude. For the representation (2.17), the main idea is to evaluate the Taylor series in ΔC_9 for some $q^2 = s_0$, where perturbative methods can be trusted. The discontinuity, $\text{disc}[\Delta C_9]$, which enters the dispersion integral, is approximated by the Breit-Wigner form for the resonances. This is sufficient for the purposes of estimating the contamination of the resonances on $\bar{B} \rightarrow \bar{K} \ell^+ \ell^-$ due to QED-corrections.⁵ The final form of ΔC_9 used is

⁵ Refinements include the interference of broad resonances [?] and the inclusion of two-particle thresholds assuming strong constant phases [26].

the one corresponding to one subtraction

$$\Delta C_9(q^2) = \Delta C_9(s_0) - \sum_{r \in \Psi} \left(\frac{q^2 - s_0}{m_r^2 - s_0} \right) \frac{\eta_r e^{i\delta_r} m_r \Gamma_r}{q^2 - m_r^2 + im_r \Gamma_r}. \quad (2.18)$$

The values of the phenomenological coefficients η_r and δ_r for the first two narrow resonances are reported in Sec. 2.4.2 and Sec. 2.4.3 respectively (cf. (2.33) on how η_r relates to underlying parameters). The value used for the subtraction term is $\Delta C_9(0 \text{ GeV}^2) \approx 0.27 + 0.073i$. More details on the charm parameterisation are deferred to App. 2.A.2.

2.4.2 Study of the J/Ψ -resonance interference term in our Monte Carlo

In the MC-study, we include the J/Ψ -resonance in the sampling method outlined in Sec. 2.2.3, by extending the definition of $C_9^{\text{eff}}(q^2)$ as detailed in the previous section. The modulus squared of the resonant mode, $\mathcal{A}_{\bar{B} \rightarrow \bar{K}(J/\Psi \rightarrow \ell^+ \ell^-)} \subset \mathcal{A}_{\bar{B} \rightarrow \bar{K} \ell^+ \ell^-}^{\text{LD}}$ in Eq. (2.15), is not included in our simulation since its sharp pole at $q^2 \approx m_{J/\Psi}^2$ renders the MC sampling efficiency too low. In turn, this requires to place a cut on $q_0^2 \leq 9.59 \text{ GeV}^2$ (cf. App. 2.A.4 for details) since the remaining terms become negative above that threshold, invalidating their interpretation as a PDF (cf. Sec. 2.2.3). Another factor limiting the sampling efficiency is the lepton mass, which in the electron case has to be increased to 10 times its physical value (c.f. App. 2.A.4) to allow for efficient sampling.⁶

Our approach is well justified since the modulus squared of the J/Ψ -resonance is well simulated by PHOTOS (see [8]), and the component describing its leakage in the signal region is included in the fit used to extract the rare mode yield. With our simulation, we aim to analyse the effect on the q^2 bin migration of the J/Ψ interference term, that has so far not been considered in the experimental analyses.

The resonance data is given by the normalisation $\eta_{J/\Psi} = 8180$ in the notation of (2.18) (or $\rho_{J/\Psi} = 1.38$, in the notation of (2.33)), with mass and width in Tab. 2.2, and the interference phase $\delta_{J/\Psi}$. For the latter, we choose two representative values: $\delta_{J/\Psi} = (1.47, 0)$ where the former is deduced by the LHCb analysis of the dilepton spectrum [27], and the latter is a conservative choice aimed at maximising the J/Ψ interference effect.

⁶ We have checked that the $\ln m_\ell$ -behaviour is consistent with what is obtained using the the semi-analytic method described in Sec. 2.4.3.

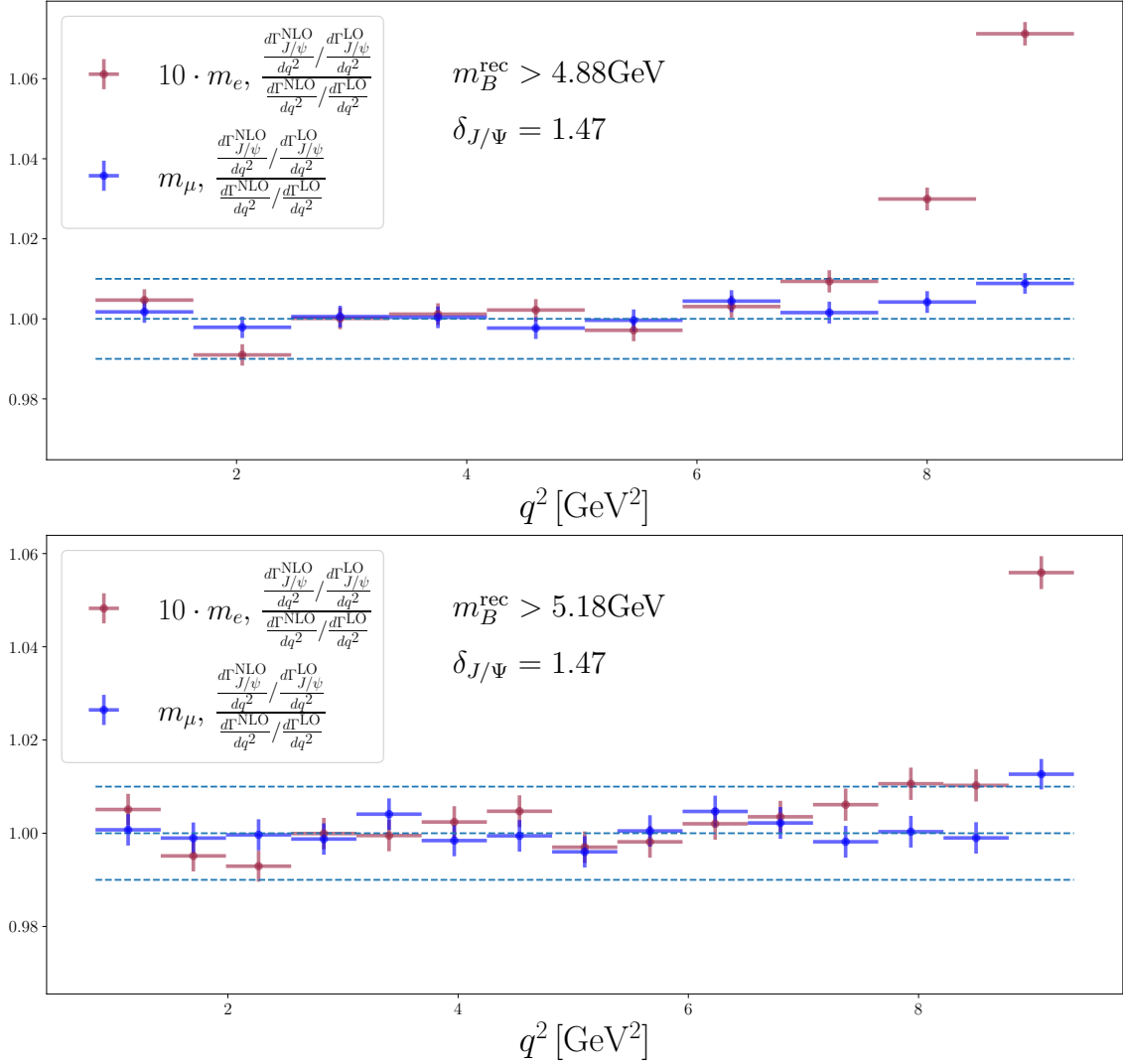


Fig. 2.3 Double ratio of the q^2 -spectrum, with and without the inclusion of interference effects induced by the J/Ψ -resonance, for electron and muons, using the respective reference m_B^{rec} cuts in Tab. 2.1. For numerical stability we use $m_e \rightarrow 10m_e$ (as indicated by the darker shade in red). The phase of the J/Ψ amplitude, relative to the SD term, is set to $\delta_{J/\Psi} = 1.47$.

The plots in Figs. 2.3 and 2.4 show the effect, as a function of q^2 , on the radiative corrections when including the J/Ψ interference term in the decay width, for interference phases of $\delta_{J/\Psi} = (1.47, 0)$ respectively. More specifically, they represent the double ratio of NLO over LO differential decay widths including charm over the same ratio without charm.

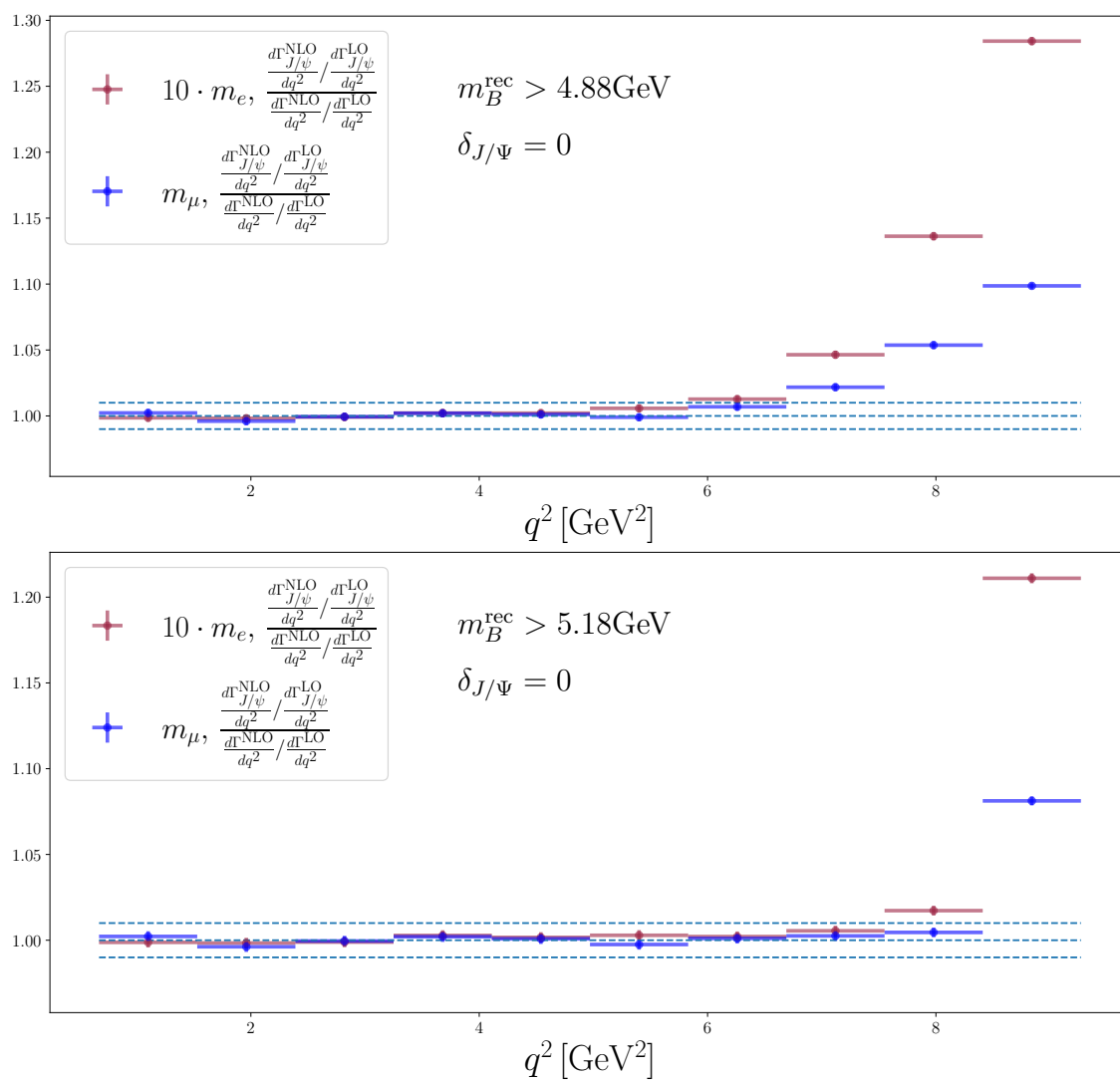


Fig. 2.4 Same plots as in Fig. 2.3 with the relative phase of the J/Ψ amplitude set to $\delta_{J/\Psi} = 0$.

Both figures include electron-like (red) and muon (blue) distributions, with appropriate $m_B^{\text{rec}} = (4.88, 5.18)$ GeV cuts (cf. Tab. 2.1). As can be seen from these plots, the impact of the SD–LD interference term is well below the 1%-level in the $q^2 < 6 \text{ GeV}^2$ region, for the (realistic) phase choice $\delta_{J/\Psi} = 1.47$. Even, in the conservative case $\delta_{J/\Psi} = 0$, it remains just below 1%. We thus conclude that when applying the aforementioned cuts, the experimental approach of neglecting the *interference* effect of charmonium resonances, when fitting for the rare mode in the $q^2 < 6 \text{ GeV}^2$ region, is well-justified.

2.4.3 J/Ψ and $\Psi(2S)$, including the resonant mode via a semi-analytic approach

Here, we follow a semi-analytic approach, using the splitting function, which reproduces the relevant collinear logarithms. There are a few advantages to this approach: it is numerically less demanding, there is no normalisation ambiguity, no issues with positivity, further resonances are easily incorporated, we can simulate for the actual electron mass and we may assess the impact of the full resonant amplitude. While it is not a MC-based approach, and therefore not directly of use for an event simulation, it may serve as a reweighting tool for our MC-framework.

Evaluating the impact of the full resonant amplitude is of interest since its rate is sizeable $\mathcal{B}(\bar{B}^0 \rightarrow \bar{K}^0 J/\psi) = 8.91(21) \cdot 10^{-4}$ compared to the rare mode itself which is $\mathcal{O}(10^{-6})$, and with a cut set at $m_B^{\text{rec}} = 4.88 \text{ GeV}$ the electron mode does probe the first resonant peak for $q^2 \approx 6 \text{ GeV}^2$, as previously stated. In fact, in a decay like $\bar{B} \rightarrow \bar{K} \ell^+ \ell^-$ the (hard)-collinear and soft-collinear logs in the lepton mass can be reproduced from the lepton to lepton-photon splitting function.^{7,8}

It is convenient to parameterise the relative QED correction $d^2\Gamma \propto (1 + \Delta^{(\ell)}(\hat{q}^2, c_\ell)) d\hat{q}^2 dc_\ell$, following our earlier work, as

$$\Delta_{\text{hc}}^{(\ell)}(\hat{q}^2, c_\ell) = \frac{\alpha}{\pi} \left(\frac{1}{\Gamma^{\text{LO}}} \frac{d^2\Gamma^{\text{LO}}(\hat{q}^2)}{d\hat{q}^2 dc_\ell^2} \right)^{-1} \left(\hat{Q}_{\ell_1}^2 \tilde{\Delta}_{\text{hc}, \ell_1}^{(\ell)} + \hat{Q}_{\ell_2}^2 \tilde{\Delta}_{\text{hc}, \ell_2}^{(\ell)} \right). \quad (2.19)$$

⁷ The specific details are postponed to a future publication [?] and for more generic remarks we refer the reader to [?]. Although, note that the kinematic relations, to follow below, can be found in our previous work [5] (cf. ancillary notebook for the expression with $m_K \neq 0$). Eq. (A.5) in [5] corresponds to the single-differential and photon-inclusive version of (2.20).

⁸ This formalism can be extended to resum all the collinear logs using the electron structure function. Taking the last bin $[20.9 \text{ GeV}^2, (m_B - m_K)^2]$, used in Fig. 2.2, and weighing by the rate, we produce an effect of ≈ 0.96 which agrees very well with the central value in that figure.

where $\hat{q}^2 \equiv q^2/m_B^2$ for brevity and the subscript ‘‘hc’’ stands for the (hard) collinear contribution. This quantity reads

$$\tilde{\Delta}_{\text{hc}, \ell_1}^{(\ell)}(\hat{q}^2, c_\ell) = \ln \frac{\mu_{\text{hc}}}{m_{\ell_1}} \left(\frac{1}{\Gamma^{\text{LO}}} \int_{\max(\hat{q}^2, z_{\ell_1}^\delta)}^1 dz P_{f \rightarrow f g_A}(z) \frac{d^2 \Gamma^{\text{LO}}(\hat{q}_0^2, c_0)}{d\hat{q}_0^2 dc_0} \right) J_{\ell_1}(c_\ell, z), \quad (2.20)$$

where $P_{f \rightarrow f g_A}(z) = \lim_{z^* \rightarrow 0} \left[\frac{1+z^2}{(1-z)} \theta((1-z^*) - z) + \left(\frac{3}{2} + 2 \ln z^*\right) \delta(1-z) \right]$ is the splitting function where $\mu_{\text{hc}} = \mathcal{O}(m_B)$ is an a priori undetermined scale (to be commented further below). The variable relations and the Jacobian ($dq_0^2 dc_0 = J_{\ell_1}(c_\ell, z) dq^2 dc_\ell$) are given by

$$q^2 = z q_0^2, \quad c_0|_{m_K=0} = \frac{c_\ell(1+z) + \bar{z}}{c_\ell \bar{z} + 1 + z}, \quad J_{\ell_1}(c_\ell, z)|_{m_K=0} = \frac{4}{(c_\ell \bar{z} + 1 + z)^2}, \quad (2.21)$$

with $\bar{z} \equiv 1 - z$. The lower integration boundary is set by the maximum of the photon inclusive limit \hat{q}^2 and the photon-cut off dependent

$$z_{\ell_1}^\delta|_{m_K=0} = \frac{1 + \hat{q}^2 - \delta + c_\ell(1 - \hat{q}^2 - \delta)}{1 + \hat{q}^2 + \delta + c_\ell(1 - \hat{q}^2 - \delta)}. \quad (2.22)$$

The corresponding expression for $\tilde{\Delta}_{\text{hc}, \ell_2}^{(\ell)}$ can be obtained by changing the signs on all the cosines in the lepton angles in Eqs. (2.21) and (2.22).

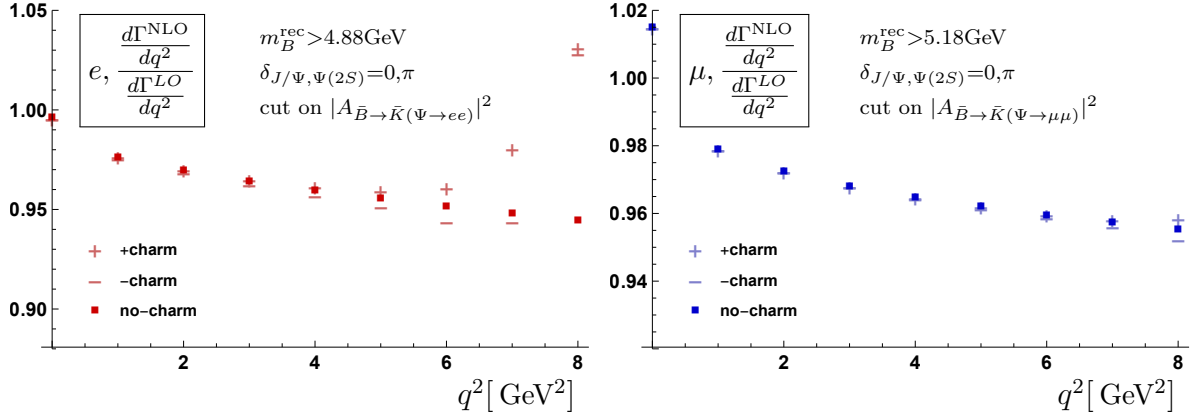


Fig. 2.5 Plots with the resonant mode cut out (cf. main text for explanation). For $q^2 < 6 \text{ GeV}^2$ the interference effects are small, even in the electron case (confirming the plot in Fig. 2.4), and do not indicate any contamination to R_K in particular. The corresponding plot without the LO normalisation can be found in App. 2.A.3 in Fig. 2.8.

We turn to the practical implementation. As compared to the previous section, we include the second resonance $\Psi(2S)$, cf. Tab. 2.2 for the basic inputs. In this case $\eta_{\Psi(2S)} = 1160$ (or $\rho_{\Psi(2S)} = 1.56$, in the notation of (2.33)) describes its residue up

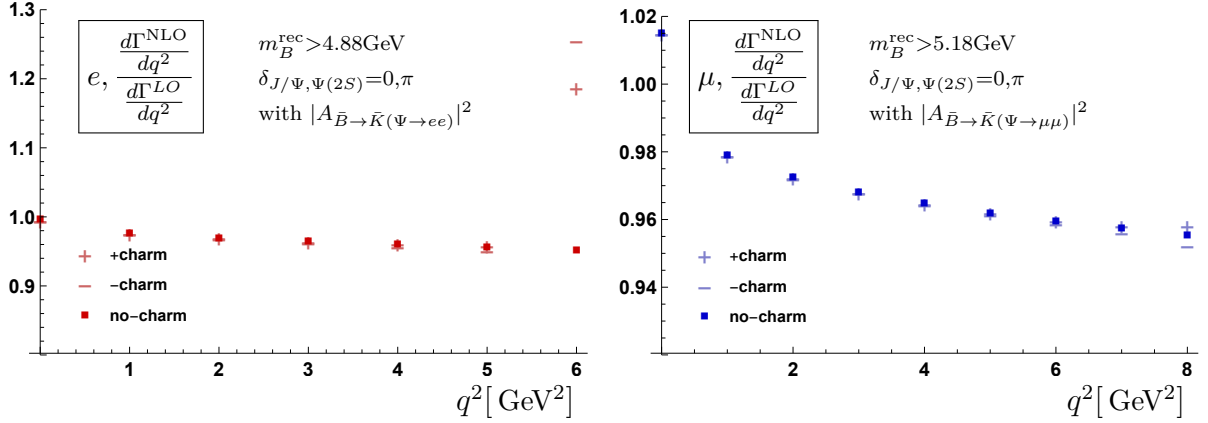


Fig. 2.6 Same plots as in Fig. 2.5 including resonant modes: (left) for electrons and (right) for muons respectively. It is noted that at $q^2 = 6 \text{ GeV}^2$, the effect is noticeable for electrons and care has to be taken (cf. main text). For the electrons, the plot ends at $q^2 = 6 \text{ GeV}^2$ since beyond this value the effects are too large (at $q^2 = (7, 8) \text{ GeV}^2$ we find, approximately, (6.5, 40) and (8.4, 73) for +charm and -charm respectively). We have checked that resummation slightly tames the effect but qualitatively, it remains the same. The muon plot looks deceptively similar to the one in Fig. 2.5 for $q^2 < 8 \text{ GeV}^2$ but differences arise thereafter. The corresponding plot without the LO normalisation can be found in App. 2.A.3 in Fig. 2.9.

the free phase $\delta_{\Psi(2S)}$. In order to emulate the LHCb procedure in eliminating the J/Ψ mode, we cut out the amplitude squared of the resonant mode in the following q_0^2 -window: $m_{\Psi}^2 - \Delta\omega^2 < q_0^2 < m_{\Psi}^2 + \Delta\omega^2$ with $\Delta\omega^2 = 0.1 \text{ GeV}^2$. Empirically, we find that choosing the undetermined scale to be $\mu_{\text{hc}}^2 \approx 6q^2$, does reproduce our short distance results in [5] rather well. It is not surprising that the scale is proportional to q^2 since this is the relevant scale “seen” by the lepton pair.

In order to assess the possible uncertainty of the charm contribution, we choose the phases to give rise to maximal interference i.e. $\delta_{J/\Psi, \Psi(2S)} = 0$ and plot the three graphs: one without any charm, one as described above and one with the sign reversed (i.e. $\delta_{J/\Psi, \Psi(2S)} = \pi$). The maximal difference can then be seen as a conservative estimate for the error of not including the charm.

Plots for the electron and the muon cases with the resonances cut out are shown in Fig. 2.5. This situation mimics the interference of the rare and resonant mode and it is seen from the plots that, for $q^2 < 6 \text{ GeV}^2$, this contribution is small. At $q^2 = 6 \text{ GeV}^2$ the difference between the two charm contributions with opposite sign is 2% and when this effect is averaged over the entire $[1.1, 6] \text{ GeV}^2$ bin it is clear that the effect does not exceed $\mathcal{O}(1\%)$ which would be comparable to structure dependent corrections. This is fortunate since, as previously mentioned, resonant versus rare-mode interference are not included in the LHCb analysis. These results can be seen as a validation of the

double ratio plots in Fig. 2.4 obtained in the MC-framework (with meaningful absolute normalisation).

We turn to the case where we include the full resonant mode. Crucially, the squared resonant amplitude is independent of the $\delta_{J/\Psi}$ -phase and dominates over the interference. This can be seen from the electron plot shown in Fig. 2.6, by comparing it to the corresponding one in Fig. 2.5. Furthermore, it can be seen that for the electron cut-off, QED effects begin to be sizeable below the $q^2 < 6 \text{ GeV}^2$ and thus care has to be taken. The effect is coming from the J/Ψ resonance and the effect of the $\Psi(2S)$ resonance is moderate for the given electron cut.

This is further reflected in the LHCb mass fit projections to the signal mode (cf. Fig. 2 in [8]) where the leakage of the resonant mode is included in the total fit model, together with the other backgrounds components, to extract the electron signal yield. Amongst the cross-checks performed in the measurement of R_K are the integrated and differential ratios $r_{J/\Psi}$, which directly compare electron and muon detection efficiencies, and thus constitute a stringent validation of their analysis. The value of $r_{J/\Psi}$ is known in the SM to be unity to a very high degree of accuracy, since it originates from the tree level mediated resonant mode, and was measured in the R_K analysis, $r_{J/\Psi} = 0.981 \pm 0.020$. This result is one sigma compatible the SM prediction and with the previous measurements of this quantity [25]. Moreover, as can be seen from Fig. 9-10 of [8], $r_{J/\Psi}$ is also performed differentially as a function of variables which are used in the determination of the dilepton invariant mass, such as the opening angle of the lepton pair and their transverse momentum. The flatness of $r_{J/\Psi}$ in those variables reflects an excellent description of the efficiency-related effects in muons and electrons. Not only are these crucial cross-checks per se, but they also validate the double ratio method used to minimise the efficiency-related systematic error in the R_K measurement [8], and the accuracy in the description of the QED corrections from the absolute square of the J/Ψ -mode.

Despite all these positive cross-checks, since the overall impact of the resonance modes is large (cf. Fig. 2.5), it would be of great relevance if the LHCb collaboration could perform a q^2 -binned analysis of R_K . This would provide a further important test of the robustness of R_K .

Related to that, we have investigated the robustness of the results with respect to non-perturbative aspects which are difficult to control: the extrapolation of the Breit-Wigner form and neglecting higher resonances. The Breit-Wigner resonance gives a good approximation close to its pole only and its extension away from the pole is not thoroughly known. When using (2.18) an implicit assumption on its form

was made; it is dictated by the short distance form factors (cf. App. 2.A.2 for further comments). We may therefore assess the effect by choosing flat form factors multiplying the Breit-Wigner resonances and adjusting the residue to reproduce the $B \rightarrow \Psi e^+ e^-$ rate. Specifically, we replace the form factor by its value at the subtraction point. It is found that this effect leads to changes which do not exceed the 2%-level for $q^2 < 6 \text{ GeV}^2$ and is thus fortunately moderate. The effect of changing the number of subtractions in (2.17) can be seen as a way to estimate neglecting higher resonances since many of them are needed to reproduce the precise asymptotics of perturbative QCD. However, one versus no subtraction leads to small $\mathcal{O}(1\%)$ changes only and might be seen as an indication of the consistency of the subtraction value with the resonance data. In summary the extension of the J/Ψ -resonance has a much larger effect than neglecting higher states.

All in all, this underlines the importance of a refined q^2 -binning from a different viewpoint. Another way to look at it is that it emphasises the importance of knowing the LO amplitude (i.e. the idealised amplitude in the absence of QED) since its precise form affects the detailed form (size and magnitude) of QED corrections. In this respect, given the smaller impact of QED effects and the better experimental resolution, the muon case can serve as a tool for a precise determination of the LO spectrum in a data-driven approach.

2.5 Outlook and Conclusions

In this article, we investigated numerical aspects of QED corrections on the $\bar{B}^0 \rightarrow \bar{K}^0 \ell^+ \ell^-$ decay, which is of particular relevance in view of LFU tests. We constructed a dedicated Monte Carlo framework based on the computation in [5] (cf. Sec. 2.2), and further analysed QED effects by means of a semi-analytic (splitting-function based) approach (cf. Sec. 2.4.3) which captures the numerically dominant collinear logs.

In Sec. 2.3, we compared our Monte Carlo framework with PHOTOS at the level of the short distance matrix element (rare mode) and found good agreement at the differential level in all relevant variables (in particular q^2 , c_ℓ and q_0^2 , c_0). Particularly relevant is the comparison in the q^2 -distribution, illustrated in Fig. 2.2, which plays a key role in the LFU tests at hadron colliders. Since PHOTOS and our approach are supposed to capture all the leading logs, agreement was to be expected. Indeed, a partial cross-check of PHOTOS, in the q_0^2 - and with an effective cut-off in the q^2 -distribution were already reported in [4]. Our double differential comparison thus provides a solid cross-validation of both our Monte Carlo framework and PHOTOS.

In addition to the short distance contribution, our Monte Carlo and semi-analytic framework has allowed us to assess the impact of the resonant mode $\bar{B} \rightarrow \bar{K}(J/\Psi \rightarrow \ell^+ \ell^-)$ on the extraction of R_K (in Secs. 2.4.2 and 2.4.3 respectively). Both the Monte Carlo and the semi-analytic approach confirm that the interference effects between resonant and rare mode (not included in PHOTOS) are below 1% for $q^2 < 6 \text{ GeV}^2$. This justifies not simulating these effects in the experimental setup, as currently done. On the other hand, the resonant mode, as known and expected, has a significant effect in the electron mode below 6 GeV^2 as the plot in Fig. 2.6 quantifies. This is taken care of in the present experimental analyses. As pointed out, a useful validation of this procedure could be obtained with an extraction of R_K in different q^2 -bins (in the $q^2 < 6 \text{ GeV}^2$ region). A further independent cross-check could be obtained varying m_B^{rec} (in particular setting a tighter cut on the electron mode). Last but not least, we stress that a precise description of the q^2 -dependence of the non-radiative amplitude, including short- and long- distance terms, is a key ingredient to obtain the $\mathcal{O}(\alpha)$ corrections at the sub-percent level (cf. remarks at the end of Sec. 2.4.3).

In this paper, we have specifically focused on the case of neutral hadrons, which has facilitated the implementation of an arbitrary q^2 -dependence in the form factor. As discussed, we expect the conclusions for the charged modes to be qualitatively similar, especially as far as the interference effects between resonant and rare modes are concerned. Moreover, the same outcomes ought to hold for the $\bar{B} \rightarrow \bar{K}^* \ell^+ \ell^-$ and the $\Lambda_b \rightarrow \Lambda \ell^+ \ell^-$ modes.

A decisive aspect is that the remaining QED corrections, due to structure dependence, which are not incorporated in PHOTOS, have been shown to be free of $\ln m_\ell$ enhanced factors (cf. Sec. 3.4 [5]). When going to the structure dependent level, which necessitates the introduction of new gauge invariant interpolating operators [?] and or new gauge invariant distribution amplitudes [?], new sizeable $\ln m_{K(\pi)}$ -effects can be expected to be present for $K(\pi)$ final states. However, they would cancel in LFU ratios [4,5], along with (other) structure dependent effects, for the reasons mentioned above.

Putting all these ingredients together, the present analysis provides an important further validation that the LFU tests so far performed by the LHCb collaboration are robust with respect to LFU violations induced by QED corrections.

References

- [1] Marina Artuso, Gino Isidori, and Sheldon Stone. *Searching for New Physics in b decays*. World Scientific, 2022.
- [2] Simone Bifani, Sébastien Descotes-Genon, Antonio Romero Vidal, and Marie-Hélène Schune. Review of Lepton Universality tests in B decays. *J. Phys. G*, 46(2):023001, 2019.
- [3] Gudrun Hiller and Frank Kruger. More model-independent analysis of $b \rightarrow s$ processes. *Phys. Rev. D*, 69:074020, 2004.
- [4] Marzia Bordone, Gino Isidori, and Andrea Pattori. On the SM predictions for R_K and R_{K^*} . *Eur. Phys. J.*, C76(8):440, 2016.
- [5] Gino Isidori, Saad Nabeebaccus, and Roman Zwicky. QED corrections in $\bar{B} \rightarrow \bar{K} \ell^+ \ell^-$ at the double-differential level. *JHEP*, 12:104, 2020.
- [6] Roel Aaij et al. Test of lepton universality using $B^+ \rightarrow K^+ \ell^+ \ell^-$ decays. *Phys. Rev. Lett.*, 113:151601, 2014.
- [7] Roel Aaij et al. Search for lepton-universality violation in $B^+ \rightarrow K^+ \ell^+ \ell^-$ decays. *Phys. Rev. Lett.*, 122(19):191801, 2019.
- [8] Roel Aaij et al. Test of lepton universality in beauty-quark decays. *Nature Phys.*, 18(3):277–282, 2022.
- [9] R. Aaij et al. Test of lepton universality with $B^0 \rightarrow K^{*0} \ell^+ \ell^-$ decays. *JHEP*, 08:055, 2017.
- [10] Roel Aaij et al. Tests of lepton universality using $B^0 \rightarrow K_s^0 \ell^+ \ell^-$ and $B^+ \rightarrow K^{*+} \ell^+ \ell^-$ decays. 10 2021.

-
- [11] Elisabetta Barberio, Bob van Eijk, and Zbigniew Was. PHOTOS: A Universal Monte Carlo for QED radiative corrections in decays. *Comput. Phys. Commun.*, 66:115–128, 1991.
- [12] Elisabetta Barberio and Zbigniew Was. PHOTOS: A Universal Monte Carlo for QED radiative corrections. Version 2.0. *Comput. Phys. Commun.*, 79:291–308, 1994.
- [13] Piotr Golonka and Zbigniew Was. PHOTOS Monte Carlo: A Precision tool for QED corrections in Z and W decays. *Eur. Phys. J. C*, 45:97–107, 2006.
- [14] N. Davidson, T. Przedzinski, and Z. Was. PHOTOS interface in C++: Technical and Physics Documentation. *Comput. Phys. Commun.*, 199:86–101, 2016.
- [15] Marek Schonherr and Frank Krauss. Soft Photon Radiation in Particle Decays in SHERPA. *JHEP*, 12:018, 2008.
- [16] Florian U. Bernlochner and Marek Schonherr. Comparing different ansatzes to describe electroweak radiative corrections to exclusive semileptonic B meson decays into (pseudo)scalar final state mesons using Monte-Carlo techniques. 10 2010.
- [17] Stefano Calí, Suzanne Klaver, Marcello Rotondo, and Barbara Sciascia. Impacts of radiative corrections on measurements of lepton flavour universality in $B \rightarrow D\ell\nu_\ell$ decays. *Eur. Phys. J. C*, 79(9):744, 2019.
- [18] Steven Weinberg. Infrared photons and gravitons. *Phys. Rev.*, 140:B516–B524, 1965.
- [19] Jonas Eschle, Albert Puig Navarro, Rafael Silva Coutinho, and Nicola Serra. zfit: scalable pythonic fitting. 10 2019.
- [20] Anders Ryd, David Lange, Natalia Kuznetsova, Sophie Versille, Marcello Rotondo, David P. Kirkby, Frank K. Wuerthwein, and Akimasa Ishikawa. EvtGen: A Monte Carlo Generator for B-Physics. 5 2005.
- [21] Matt Dobbs and Jorgen Beck Hansen. The HepMC C++ Monte Carlo event record for High Energy Physics. *Comput. Phys. Commun.*, 134:41–46, 2001.
- [22] H. H. Asatrian, H. M. Asatrian, C. Greub, and M. Walker. Two loop virtual corrections to $B \rightarrow X_s l^+ l^-$ in the SM. *Phys. Lett. B*, 507:162–172, 2001.

-
- [23] Patricia Ball and Roman Zwicky. New results on $B \rightarrow \pi, K, \eta$ decay formfactors from light-cone sum rules. *Phys. Rev. D*, 71:014015, 2005.
- [24] Roel Aaij et al. Test of lepton universality using $B^+ \rightarrow K^+ \ell^+ \ell^-$ decays. *Phys. Rev. Lett.*, 113:151601, 2014.
- [25] P.A. Zyla et al. Review of Particle Physics. *PTEP*, 2020(8):083C01, 2020.
- [26] Claudia Cornella, Gino Isidori, Matthias König, Sascha Liechti, Patrick Owen, and Nicola Serra. Hunting for $B^+ \rightarrow K^+ \tau^+ \tau^-$ imprints on the $B^+ \rightarrow K^+ \mu^+ \mu^-$ dimuon spectrum. *Eur. Phys. J. C*, 80(12):1095, 2020.
- [27] Roel Aaij et al. Measurement of the phase difference between short- and long-distance amplitudes in the $B^+ \rightarrow K^+ \mu^+ \mu^-$ decay. *Eur. Phys. J. C*, 77(3):161, 2017.
- [28] James Gratrex, Markus Hopfer, and Roman Zwicky. Generalised helicity formalism, higher moments and the $B \rightarrow K_{JK}(\rightarrow K\pi)\bar{\ell}_1\ell_2$ angular distributions. *Phys. Rev.*, D93(5):054008, 2016.

Appendix 2.A Appendix to Chapter 2

2.A.1 Kinematics

Following Ref. [5], we reproduce the relevant kinematic paramterisation for the 4-body decay kinematics in terms the five independent variables $(q^2, \bar{p}_B^2, c_\ell, c_\gamma, \phi_\gamma)$, where $c_i \equiv \cos \theta_i$. We start by defining the photon and the meson momenta in the \bar{p}_B -RF (indicated by an upper index (2)):

$$\begin{aligned} k^{(2)} &= (E_{g_A}^{(2)}, -\cos \theta_{g_A} |\vec{k}_{g_A}^{(2)}|, -\sin \theta_{g_A} \cos \phi_{g_A} |\vec{k}_{g_A}^{(2)}|, -\sin \theta_{g_A} \sin \phi_{g_A} |\vec{k}_{g_A}^{(2)}|), \\ \bar{p}_B^{(2)} &= (\bar{p}_B, 0, 0, 0), \quad q^{(2)} = (\bar{p}_B - p_K)^{(2)} = (\bar{p}_B - E_K^{(2)}, |\vec{p}_K^{(2)}|, 0, 0) = (E_q^{(2)}, |\vec{p}_K^{(2)}|, 0, 0), \\ p_K^{(2)} &= (E_K^{(2)}, -|\vec{p}_K^{(2)}|, 0, 0). \end{aligned} \quad (2.23)$$

Here,

$$\begin{aligned} E_K^{(2)} &= \sqrt{|\vec{p}_K^{(2)}|^2 + m_K^2} = \frac{1}{2\bar{p}_B} (\bar{p}_B^2 - q^2 + m_K^2), \quad |\vec{p}_K^{(2)}| = \frac{\lambda^{1/2}(\bar{p}_B^2, q^2, m_K^2)}{2\bar{p}_B}, \\ E_{g_A}^{(2)} &= \sqrt{|\vec{k}_{g_A}^{(2)}|^2 + m_\gamma^2} = \frac{1}{2\bar{p}_B} (m_B^2 - \bar{p}_B^2 - m_\gamma^2), \quad |\vec{k}_{g_A}^{(2)}| = \frac{\lambda^{1/2}(\bar{p}_B^2, m_B^2, m_\gamma^2)}{2\bar{p}_B}, \\ E_q^{(2)} &= \sqrt{|\vec{p}_K^{(2)}|^2 + q^2} = \frac{1}{2\bar{p}_B} (\bar{p}_B^2 + q^2 - m_K^2), \end{aligned} \quad (2.24)$$

and

$$\lambda(s, m_1^2, m_2^2) = (s - (m_1 - m_2)^2)(s - (m_1 + m_2)^2). \quad (2.25)$$

The lepton momenta $\ell_{1,2}$ depend on the angle of the leptons w.r.t to the decay axis in the q -RF,

$$\begin{aligned} \ell_1^{(2)} &= (g_A(E_{\ell_1}^{(3)} + \beta \cos \theta_\ell |\vec{\ell}_1^{(3)}|), g_A(\beta E_{\ell_1}^{(3)} + \cos \theta_\ell |\vec{\ell}_1^{(3)}|), -|\vec{\ell}_1^{(3)}| \sin \theta_\ell, 0), \\ \ell_2^{(2)} &= (g_A(E_{\ell_2}^{(3)} - \beta \cos \theta_\ell |\vec{\ell}_1^{(3)}|), g_A(\beta E_{\ell_2}^{(3)} - \cos \theta_\ell |\vec{\ell}_1^{(3)}|), +|\vec{\ell}_1^{(3)}| \sin \theta_\ell, 0), \end{aligned} \quad (2.26)$$

where $E_{\ell_{1,2}}^{(3)}$ and $|\vec{\ell}_1^{(3)}|$ are quantities defined in the q -RF:

$$E_{\ell_{1,2}}^{(3)} = \sqrt{|\vec{\ell}_1^{(3)}|^2 + m_{\ell_{1,2}}^2} = \frac{1}{2q} (q^2 + m_{\ell_{1,2}}^2 - m_{\ell_{2,1}}^2), \quad |\vec{\ell}_1^{(3)}| = \frac{\lambda^{1/2}(q^2, m_{\ell_1}^2, m_{\ell_2}^2)}{2q}. \quad (2.27)$$

The boost velocity β and g_A -factor are given by

$$\beta = \frac{|\vec{p}_K^{(2)}|}{E_q^{(2)}}, \quad g_A = \frac{1}{\sqrt{1-\beta^2}} = \frac{E_q^{(2)}}{q}. \quad (2.28)$$

2.A.2 More Detail on the Charm Parameterisation

Here we give some more detail on the charm parameterisation (2.18) used in this paper. The perturbative evaluation of $\Delta C_9(q^2)$ reads

$$\Delta C_9(q^2) = (C_2 + 3C_1)h_c(q^2) - \frac{\alpha_s}{4\pi} \sum_{i=1,2} C_i F_i^{(9)}(q^2) + \mathcal{O}(\alpha_s^2, C_{3,6}), \quad (2.29)$$

where h_c is vacuum polarisation ($\text{Im}[h_c(s)] = \frac{\pi}{3}R(s)$ with $R(s) \equiv \frac{\sigma(e^+e^- \rightarrow \text{hadrons})}{\sigma(e^+e^- \rightarrow \mu^+\mu^-)}$ an experimentally well-studied ratio of cross sections [25]), reproduced in [?] for example, and the second term includes *b*scc-vertex corrections not captured by the first term. For the latter, we have adapted the notation and results from the inclusive mode $b \rightarrow s\ell\ell$ [22]. This treatment falls short of effects specific to the structure of the \bar{B} - and \bar{K} -mesons. The Wilson coefficients $C_{3,6}$ correspond to the penguin induced four quark operators and can be neglected for our purposes. The $C_2 \approx 1$ Wilson coefficient arises at tree level and $C_1 \approx -0.15$ is generated by renormalisation group running (specifically we employ $(C_1, C_2, C_9)(m_b) = (-0.15, 1, 4.035)$ as reference values). The combination $C_2 + 3C_1 \approx 0.6$ is referred to as the colour suppressed contribution whereas the radiative corrections are colour enhanced and reduce the LO corrections considerably. In our numerical analysis we use a single subtracted point at $\Delta C_9(0 \text{ GeV}^2) \approx 0.27 + 0.073i$.

We turn to the input into the dispersion integral which is the discontinuity. Let us clarify the approximations used. In the case of infinitely narrow resonances and further assuming naïve factorisation (NF) one has, $(2\pi i)^{-1} \text{disc}[\Delta C_9]_{\text{NF}}(s) = \frac{3\pi}{\alpha^2} (C_2 + 3C_1) m_\Psi \Gamma_{\Psi \rightarrow \ell^+\ell^-} \delta(s - m_\Psi^2)$. In this limit, one can correct for NF by multiplying the amplitude by a complex number $\rho_\Psi e^{i\delta_\Psi}$ ($\rho_\Psi \geq 0$),

$$\frac{1}{2\pi i} \text{disc}[\Delta C_9](s) \Big|_{\frac{\Gamma_\Psi}{m_\Psi} \rightarrow 0} = \frac{3\pi}{\alpha^2} (C_2 + 3C_1) \rho_\Psi e^{i\delta_\Psi} m_\Psi \Gamma_{\Psi \rightarrow \ell^+\ell^-} \delta(s - m_\Psi^2) + \dots, \quad (2.30)$$

which parameterises its deviation. Turning to the more realistic case of finite widths, the dispersion integral in (2.17) assumes the form

$$\begin{aligned} \frac{(q^2 - s_0)^n}{2\pi i} \int_{\text{cut}}^{\infty} \frac{ds}{(s - s_0)^n} \frac{\text{disc}[\Delta C_9](s)}{s - q^2 - i0} = \\ -\frac{3\pi}{\alpha^2} (C_2 + 3C_1) \sum_{r \in \Psi} \left(\frac{q^2 - s_0}{m_r^2 - s_0} \right)^n \frac{\rho_r e^{i\delta_r} m_r \Gamma_{r \rightarrow \ell^+ \ell^-}}{q^2 - m_r^2 + i m_r \Gamma_r} + \dots \end{aligned} \quad (2.31)$$

As previously mentioned the dots stand for neglected multi-hadron contributions which start at $q^2 = 4m_D^2$. At last, let us comment on the status of the resonance data, the significance of writing the dispersion relation in ΔC_9 rather than the amplitude and parameterising without reference to the SM.

- From the branching fractions, it has been known for a long time that $\rho_{J/\Psi} \approx 1.38$ and $\rho_{\Psi(2S)} \approx 1.56$ and that there are sizeable corrections to NF. By fitting the interference of the (broad) charm resonances with the short distance contributions, the corresponding correction factors were found to be even larger and come with opposite phase $\delta_{\Psi} \approx \pi$ as compared to NF [?] (cf. plots and tables therein). Later, the LHCb collaboration [27] fitted the phases of the J/Ψ - and $\Psi(2S)$ -resonances which are more challenging as they are narrow. Qualitatively, a four fold degeneracy ($\delta_{J/\Psi}, \delta_{\Psi(2S)} \approx (\pm \frac{\pi}{2}, \pm \frac{\pi}{2})$) (cf. Tab. 3 in [27]) emerges which indicates a rather small interference effect since the short distance contribution is real.
- In principle, one could have directly written a dispersion relation for the full amplitude. However, the amplitude and ΔC_9 essentially differ by the form factor $f_+(q^2)$ which is an analytic function with a pole and branch points above the physical region. They are thus both legitimate functions for a dispersion relation. Differences comes into play when approximations are made. In our case, they differ on how we extend from the narrow resonance limit, which is not-known from first principles, and thus, a priori, any of the two seems as good as the other. Perhaps, the one for ΔC_9 is preferable as we know that the extension is at least correct in the case of NF, which might be seen as a reasonable qualitative starting point (cf. end of Sec. 2.4.3 for comments on the actual numerical relevance.)
- One may parameterise without reference to NF (cf. Eq. (3) in [27])

$$\frac{1}{2\pi i} \text{disc}[\Delta C_9](s) = \eta_r e^{i\delta_r} m_r \Gamma_r \delta(s - m_r^2), \quad (2.32)$$

thereby avoiding reference to the SM. Comparison with (2.30) reveals the relation between the parameters

$$\eta_r \Gamma_r = \rho_r \frac{3\pi}{\alpha^2} (C_2 + 3C_1) \Gamma_{r \rightarrow \ell^+ \ell^-} . \quad (2.33)$$

2.A.3 Supplementary plots

In this appendix, we provide a few supplementary plots which might be of interest to certain readers of the paper. This includes the MC-plots in Figs. 2.7 about angular distributions. The fact that QED gives rise to qualitatively different angular distribution (or higher moments) was pointed out in [28] (cf. Sec. 5) and advertised as a way to measure pure QED effects. Auxiliary plots for the semi-analytic approach are shown in Figs. 2.8 and 2.9 which can help to better understand the normalised figures since the normalisation depends on the charm input.

2.A.4 Values of f^{th} used in the Monte Carlo Simulations

Tab. 2.3 gives the values of $\frac{\Gamma_3}{\Gamma_{\text{tree}}}$ for various cases, which are used to calculate f^{th} , needed for the normalisation of the Monte Carlo.

When the resonance is “off”, only the contribution from the rare mode is considered, and the integration for the total rates is performed over the full range of q_0^2 . In this case, we consider two possible frames (\bar{p}_B and q_0) for imposing the spurious cut on the photon energy $E_\gamma^{(i)}$ in order to separate 3- and 4-body events. We note that the coefficient of the soft log ($\ln E_\gamma^{(i)}$) is the same for each case, as expected. The results are given for 3 different leptons (μ , $10e$ and e) for each photon energy cut. The shorthand $10e$ denotes an “intermediate” lepton which has a mass of $m_{10e} = 10 m_e$, which is roughly in between the muon and electron mass.

When the resonance is “on”, the contribution from the interference of the rare mode with the Breit-Wigner term of the J/ψ is included, but not the square of the Breit-Wigner term itself. In this case, we consider two possible values for the phase of the J/ψ : $\delta_{J/\psi} = 0$ (maximum interference) and $\delta_{J/\psi} = 1.47$ (LHCb value from [27]). The corresponding restrictions on the range of the q_0^2 integration are $q_0^2 \leq 9.5905 \text{ GeV}^2$ and $q_0^2 \leq 9.585 \text{ GeV}^2$ respectively. This is done in order to capture the maximum effect from the interference term in each case. Only results for photon energy cuts in the q_0 -RF are given, since in the \bar{p}_B -RF, the MC has extremely low efficiency. This is because for a photon energy cut-off in the \bar{p}_B -RF, the sampling for the MC also has to be performed in \bar{p}_B . Then, applying a cut in q_0^2 (which is now a function

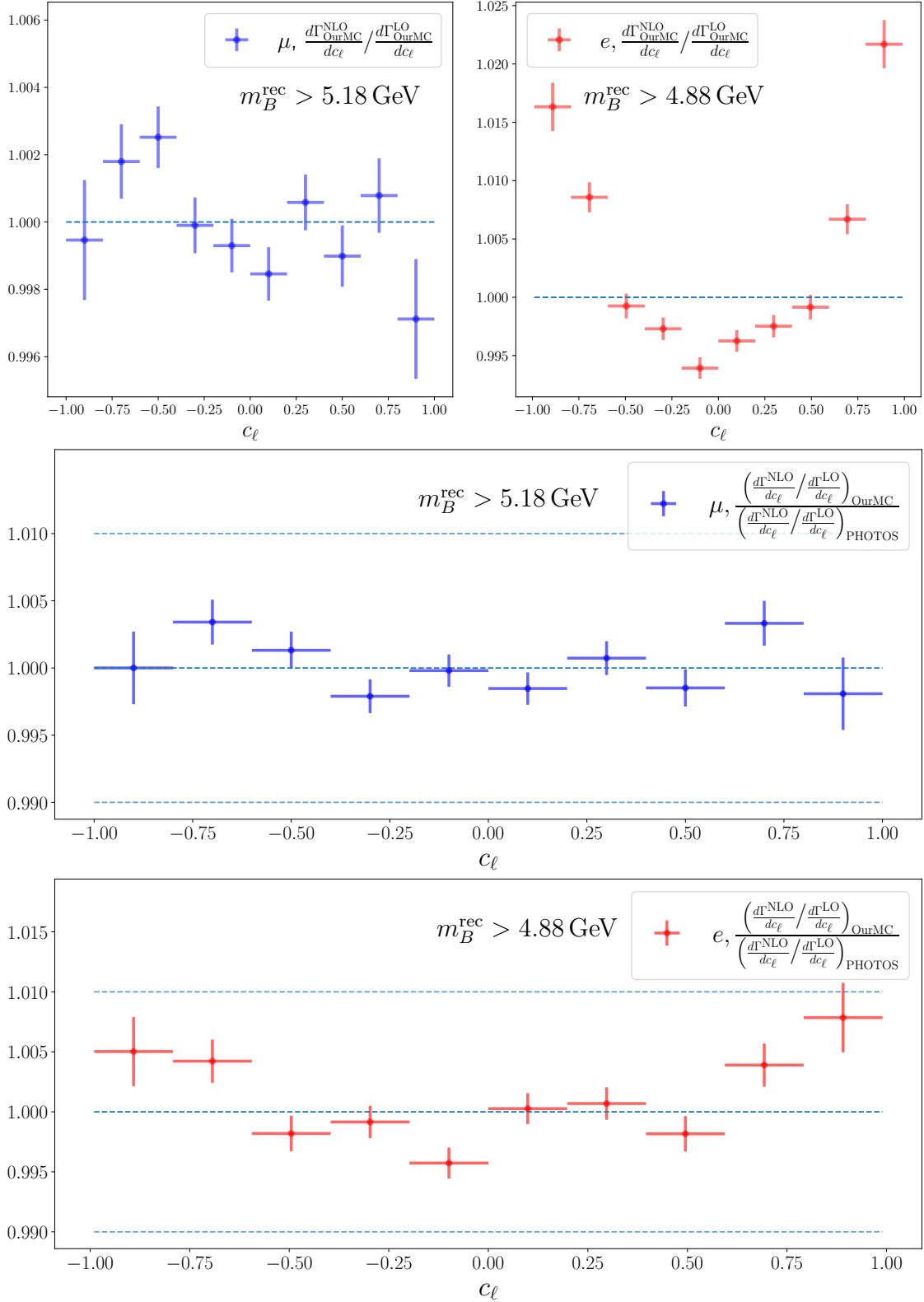


Fig. 2.7 Short distance (form factor) plots, in the $\cos\theta_\ell$ -variable, NLO over LO for muons in blue (top left) and for electrons in red (top right) in our MC, with appropriate cuts as in Tab. 2.1. The normalisation of these plots is not meaningful (cf. main text). However, double ratios, shown in the middle and bottom, of our Monte Carlo versus the PHOTOS framework are free of ambiguities.

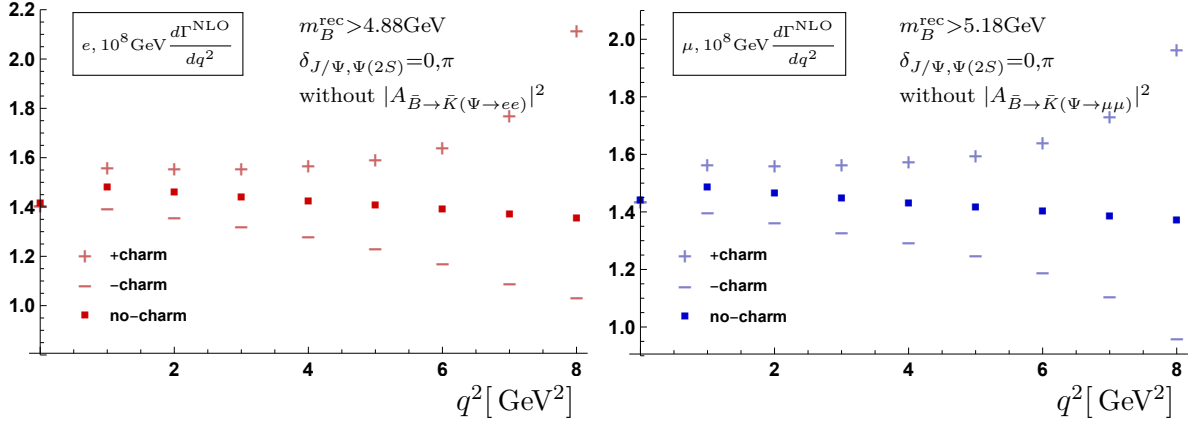


Fig. 2.8 Same plots as in Fig. 2.5 without LO-normalisation.

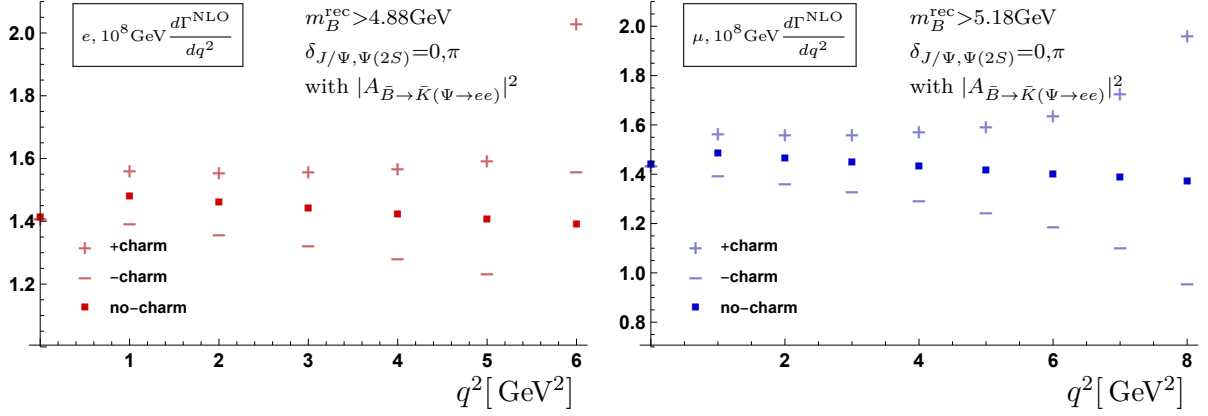


Fig. 2.9 Same plots as in Fig. 2.6 without LO-normalisation.

of several sampling variables) becomes problematic, and significantly decreases the sampling efficiency. Furthermore, having an electron mass also significantly decreases the efficiency of the Monte Carlo, so we restrict ourselves to a muon mass m_μ and an "intermediate" mass $m_{10e}(=10m_e)$ when interference effects are considered.

Resonance	Frame for $E_{\gamma,\text{cut}}^{(i)}$	Lepton	$\frac{\Gamma_3}{\Gamma_{\text{tree}}}$
Off	\bar{p}_B	μ	$1 + \frac{\alpha}{\pi} \left(5.1479 + 10.924 \ln E_{\gamma,\text{cut}}^{(\bar{p}_B)} \right)$
		$10e$	$1 + \frac{\alpha}{\pi} \left(7.8551 + 23.012 \ln E_{\gamma,\text{cut}}^{(\bar{p}_B)} \right)$
		e	$1 + \frac{\alpha}{\pi} \left(9.9605 + 32.222 \ln E_{\gamma,\text{cut}}^{(\bar{p}_B)} \right)$
	q_0	μ	$1 + \frac{\alpha}{\pi} \left(6.8903 + 10.924 \ln E_{\gamma,\text{cut}}^{(q_0)} \right)$
		$10e$	$1 + \frac{\alpha}{\pi} \left(12.473 + 23.012 \ln E_{\gamma,\text{cut}}^{(q_0)} \right)$
		e	$1 + \frac{\alpha}{\pi} \left(16.772 + 32.222 \ln E_{\gamma,\text{cut}}^{(q_0)} \right)$
On, $\delta_{J/\psi} = 0$	q_0	μ	$1 + \frac{\alpha}{\pi} \left(8.7111 + 10.140 \ln E_{\gamma,\text{cut}}^{(q_0)} \right)$
		$10e$	$1 + \frac{\alpha}{\pi} \left(16.658 + 22.223 \ln E_{\gamma,\text{cut}}^{(q_0)} \right)$
On, $\delta_{J/\psi} = 1.47$	q_0	μ	$1 + \frac{\alpha}{\pi} \left(9.6159 + 9.5767 \ln E_{\gamma,\text{cut}}^{(q_0)} \right)$
		$10e$	$1 + \frac{\alpha}{\pi} \left(19.271 + 21.647 \ln E_{\gamma,\text{cut}}^{(q_0)} \right)$

Table 2.3 f^{th} for different cases. When the resonance is ‘‘on’’, the interference of the Breit-Wigner term of the J/ψ and the rare mode is included (but not the square of the Breit-Wigner term). $10e$ is a ‘fake’ lepton that has an ‘intermediate’ mass (between the muon and the electron), and we take $m_{10e} = 10 m_e$. When the resonance is ‘‘off’’ (ie. only rare mode), the full range of q_0^2 is integrated over. When $\delta_{J/\psi} = 0$, the q_0^2 integration is restricted in the region $q_0^2 \leq 9.5905 \text{ GeV}^2$, whereas when $\delta_{J/\psi} = 1.47$, the q_0^2 integration is restricted in the region $q_0^2 \leq 9.585 \text{ GeV}^2$. $E_{\gamma,\text{cut}}^{(i)}$ is given in GeV units.

Chapter 3

Test of lepton flavour universality in beauty quark-decays

The Standard Model (SM) of particle physics provides precise predictions for the properties and interactions of fundamental particles, which have been confirmed by numerous experiments since the inception of the model in the 1960's. However, it is clear that the model is incomplete. The SM is unable to explain cosmological observations of the dominance of matter over antimatter, the apparent dark-matter content of the Universe, or explain the patterns seen in the interaction strengths of the particles. Particle physicists have therefore been searching for ‘new physics’ — the new particles and interactions that can explain the SM's shortcomings.

One method to search for new physics is to compare measurements of the properties of hadron decays, where hadrons are bound states of quarks, with their SM predictions. Measurable quantities can be predicted precisely in the decays of a charged beauty hadron, B^+ , into a charged kaon, K^+ , and two charged leptons, $\ell^+\ell^-$. The B^+ hadron contains a beauty antiquark, \bar{b} , and the K^+ a strange antiquark, \bar{s} , such that at the quark level the decay involves a $\bar{b} \rightarrow \bar{s}$ transition. Quantum field theory allows such a process to be mediated by virtual particles that can have a physical mass larger than the energy available in the interaction. In the SM description of such processes, these virtual particles include the electroweak-force carriers, the γ , W^\pm and Z^0 bosons, and the top quark (see Fig. 3.1, left). Such decays are highly suppressed [1] and the fraction of B^+ hadrons that decay into this final state (the branching fraction, \mathcal{B}) is of the order of 10^{-6} [2].

A distinctive feature of the SM is that the different leptons, electron (e^-), muon (μ^-) and tau (τ^-), have the same interaction strengths. This is known as ‘lepton universality’. The only exception to this is due to the Higgs field, since the lepton-Higgs

interaction strength gives rise to the differing lepton masses $m_\tau > m_\mu > m_e$. The suppression of $\bar{b} \rightarrow \bar{s}$ transitions is understood in terms of the fundamental symmetries on which the SM is built. Conversely, lepton universality is an accidental symmetry of the SM, which is not a consequence of any axiom of the theory. Extensions to the SM that aim to address many of its shortfalls predict new virtual particles that could contribute to $\bar{b} \rightarrow \bar{s}$ transitions (see Fig. 3.1, right) and could have nonuniversal interactions, hence giving branching fractions of $B^+ \rightarrow K^+ \ell^+ \ell^-$ decays with different leptons that differ from the SM predictions. Whenever a process is specified in this article, the inclusion of the charge-conjugate mode is implied.

Calculation of the SM predictions for the branching fractions of $B^+ \rightarrow K^+ \mu^+ \mu^-$ and $B^+ \rightarrow K^+ e^+ e^-$ decays is complicated by the strong nuclear force that binds together the quarks into hadrons, as described by quantum chromodynamics (QCD). The large interaction strengths preclude predictions of QCD effects with the perturbation techniques used to compute the electroweak force amplitudes and only approximate calculations are presently possible. However, the strong force does not couple directly to leptons and hence its effect on the $B^+ \rightarrow K^+ \mu^+ \mu^-$ and $B^+ \rightarrow K^+ e^+ e^-$ decays is identical. The ratio between the branching fractions of these decays is therefore predicted with $\mathcal{O}(1\%)$ precision [3–8]. Due to the small masses of both electrons and muons compared to that of b quarks, this ratio is predicted to be close to unity, except where the value of the dilepton invariant mass-squared (q^2) significantly restricts the phase space available to form the two leptons. Similar considerations apply to decays with other B hadrons, $B \rightarrow H \mu^+ \mu^-$ and $B \rightarrow H e^+ e^-$, where $B = B^+, B^0, B_s^0$ or Λ_b^0 ; and H can be *e.g.* an excited kaon, K^{*0} , or a combination of particles such as a proton

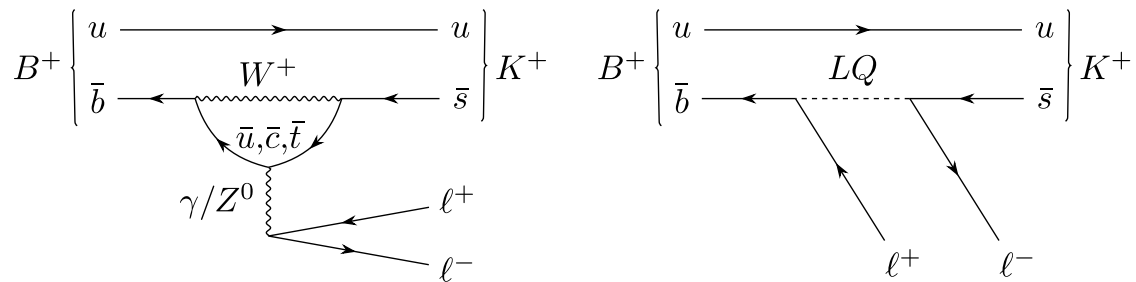


Fig. 3.1 Contributions to $B^+ \rightarrow K^+ \ell^+ \ell^-$ decays in the SM and possible new physics models. A B^+ meson, consisting of \bar{b} and u quarks, decays into a K^+ , containing \bar{s} and u quarks, and two charged leptons, $\ell^+ \ell^-$. (Left) The SM contribution involves the electroweak bosons γ , W^+ and Z^0 , and the up-type quarks \bar{u} , \bar{c} and \bar{t} . (Right) A possible new physics contribution to the decay with a hypothetical leptoquark (LQ) which, unlike the electroweak bosons, could have different interaction strengths with the different types of leptons.

and charged kaon, pK^- . The ratio of branching fractions, R_H [9,10], is defined in the dilepton mass-squared range $q_{\min}^2 < q^2 < q_{\max}^2$ as

$$R_H \equiv \frac{\int_{q_{\min}^2}^{q_{\max}^2} \frac{d\mathcal{B}(B \rightarrow H\mu^+\mu^-)}{dq^2} dq^2}{\int_{q_{\min}^2}^{q_{\max}^2} \frac{d\mathcal{B}(B \rightarrow He^+e^-)}{dq^2} dq^2}. \quad (3.1)$$

For decays with $H = K^+$ and $H = K^{*0}$ such ratios, denoted R_K and $R_{K^{*0}}$, respectively, have previously been measured by the LHCb [11,12], Belle [13,14] and BaBar [15] collaborations. For R_K the LHCb measurements are in the region $1.1 < q^2 < 6.0 \text{ GeV}^2/c^4$, whereas for $R_{K^{*0}}$ the regions are $0.045 < q^2 < 1.1 \text{ GeV}^2/c^4$ and $1.1 < q^2 < 6.0 \text{ GeV}^2/c^4$. These ratios have been determined to be 2.1–2.5 standard deviations below their respective SM expectations [3–5,16–18,6,19,7,20–22]. The analogous ratio has also been measured for Λ_b^0 decays with $H = pK^-$ and is compatible with unity at the level of one standard deviation [23].

These decays all proceed via the same $\bar{b} \rightarrow \bar{s}$ quark transition and the results have therefore further increased interest in measurements of angular observables [24–34] and branching fractions [35–38] of decays mediated by $\bar{b} \rightarrow \bar{s}\mu^+\mu^-$ transitions. Such decays also exhibit some tension with the SM predictions but the extent of residual QCD effects is still the subject of debate [21,3,39–47]. A consistent model-independent interpretation of all these data is possible via a modification of the $\bar{b} \rightarrow \bar{s}$ coupling strength [48–54]. Such a modification can be realised in new physics models with an additional heavy neutral boson [55–78] or with leptoquarks [79–108]. Other explanations of the data involve a variety of extensions to the SM, such as supersymmetry, extended Higgs-boson sectors and models with extra dimensions [109–120]. Tension with the SM is also seen in the combination of several ratios that test lepton-universality in $\bar{b} \rightarrow \bar{c}\ell^+\nu_\ell$ transitions [121–129].

In this article, a measurement of the R_K ratio is presented based on proton-proton collision data collected with the LHCb detector at CERN’s Large Hadron Collider (see Methods). The data were recorded during the years 2011, 2012 and 2015–2018, in which the centre-of-mass energy of the collisions was 7, 8 and 13 TeV, and correspond to an integrated luminosity of 9 fb^{-1} . Compared to the previous LHCb R_K result [11], the experimental method is essentially identical but the analysis uses an additional 4 fb^{-1} of data collected in 2017 and 2018. The results supersede those of the previous LHCb analysis.

The analysis strategy aims to reduce systematic uncertainties induced in modelling the markedly different reconstruction of decays with muons in the final state, compared to decays with electrons. These differences arise due to the significant bremsstrahlung radiation emitted by the electrons and the different detector subsystems that are used to identify electron and muon candidates (see Methods). The major challenge of the measurement is then correcting for the efficiency of the selection requirements used to isolate signal candidates and reduce background. In order to avoid unconscious bias, the analysis procedure was developed and the cross-checks described below performed before the result for R_K was examined.

In addition to the process discussed above, the $K^+\ell^+\ell^-$ final state is produced via a $B^+ \rightarrow X_{q\bar{q}}K^+$ decay, where $X_{q\bar{q}}$ is a bound state (meson) such as the J/ψ . The J/ψ meson consists of a charm quark and antiquark, $c\bar{c}$, and is produced resonantly at $q^2 = 9.59 \text{ GeV}^2/c^4$. This ‘charmonium’ resonance subsequently decays into two leptons, $J/\psi \rightarrow \ell^+\ell^-$. The $B^+ \rightarrow J/\psi(\rightarrow \ell^+\ell^-)K^+$ decays are not suppressed and hence have a branching fraction orders of magnitude larger than that of $B^+ \rightarrow K^+\ell^+\ell^-$ decays. These two processes are separated by applying a requirement on q^2 . The $1.1 < q^2 < 6.0 \text{ GeV}^2/c^4$ region used to select $B^+ \rightarrow K^+\ell^+\ell^-$ decays is chosen to reduce the pollution from the J/ψ resonance and the high- q^2 region that contains contributions from further excited charmonium resonances, such as the $\psi(2S)$ and $\psi(3770)$ states, and from lighter $s\bar{s}$ resonances, such as the $\phi(1020)$ meson. In the remainder of this article, the notation $B^+ \rightarrow K^+\ell^+\ell^-$ is used to denote only decays with $1.1 < q^2 < 6.0 \text{ GeV}^2/c^4$, which are referred to as nonresonant, whereas $B^+ \rightarrow J/\psi(\rightarrow \ell^+\ell^-)K^+$ decays are denoted resonant.

To help overcome the challenge of modelling precisely the different electron and muon reconstruction efficiencies, the branching fractions of $B^+ \rightarrow K^+\ell^+\ell^-$ decays are measured relative to those of $B^+ \rightarrow J/\psi K^+$ decays [130]. Since the $J/\psi \rightarrow \ell^+\ell^-$ branching fractions are known to respect lepton universality to within 0.4% [131,2], the R_K ratio is determined via the double ratio of branching fractions

$$R_K = \frac{\mathcal{B}(B^+ \rightarrow K^+\mu^+\mu^-)}{\mathcal{B}(B^+ \rightarrow J/\psi(\rightarrow \mu^+\mu^-)K^+)} \bigg/ \frac{\mathcal{B}(B^+ \rightarrow K^+e^+e^-)}{\mathcal{B}(B^+ \rightarrow J/\psi(\rightarrow e^+e^-)K^+)}. \quad (3.2)$$

In this equation, each branching fraction can be replaced by the corresponding event yield divided by the appropriate overall detection efficiency (see Methods), as all other factors needed to determine each branching fraction individually cancel out. The efficiency of the nonresonant $B^+ \rightarrow K^+e^+e^-$ decay therefore needs to be known only relative to that of the resonant $B^+ \rightarrow J/\psi(\rightarrow e^+e^-)K^+$ decay, rather than relative to the

$B^+ \rightarrow K^+ \mu^+ \mu^-$ decay. As the detector signature of each resonant decay is similar to that of its corresponding nonresonant decay, systematic uncertainties that would otherwise dominate the calculation of these efficiencies are suppressed. The yields observed in these four decay modes and the ratios of efficiencies determined from simulated events then enable an R_K measurement with statistically dominated uncertainties. As detailed below, percent-level control of the efficiencies is verified with a direct comparison of the $B^+ \rightarrow J/\psi(\rightarrow e^+e^-)K^+$ and $B^+ \rightarrow J/\psi(\rightarrow \mu^+\mu^-)K^+$ branching fractions in the ratio $r_{J/\psi} = \mathcal{B}(B^+ \rightarrow J/\psi(\rightarrow \mu^+\mu^-)K^+)/\mathcal{B}(B^+ \rightarrow J/\psi(\rightarrow e^+e^-)K^+)$, which does not benefit from the same cancellation of systematic effects.

Candidate $B^+ \rightarrow K^+ \ell^+ \ell^-$ decays are found by combining the reconstructed trajectory (track) of a particle identified as a charged kaon, together with the tracks from a pair of well-reconstructed oppositely charged particles identified as either electrons or muons. The particles are required to originate from a common vertex, displaced from the proton-proton interaction point, with good vertex-fit quality. The techniques used to identify the different particles and to form B^+ candidates are described in Methods.

The invariant mass of the final state particles, $m(K^+ \ell^+ \ell^-)$, is used to discriminate between signal and background contributions, with the signal expected to accumulate around the known mass of the B^+ meson. Background originates from particles selected from multiple hadron decays, referred to as combinatorial background, and from specific decays of B hadrons. The latter also tend to accumulate around specific values of $m(K^+ \ell^+ \ell^-)$. For the muon modes, the residual background is combinatorial and, for the resonant mode, there is an additional contribution from $B^+ \rightarrow J/\psi \pi^+$ decays with a pion misidentified as a kaon. For the electron modes, in addition to combinatorial background, other specific background decays contribute significantly in the signal region. The dominant such background for the nonresonant and resonant modes comes from partially reconstructed $B^{(0,+)} \rightarrow K^+ \pi^{(-,0)} e^+ e^-$ and $B^{(0,+)} \rightarrow J/\psi(\rightarrow e^+ e^-) K^+ \pi^{(-,0)}$ decays, respectively, where the pion is not included in the B^+ candidate. Decays of the form $B^+ \rightarrow \bar{D}^0(\rightarrow K^+ e^- \bar{\nu}_e) e^+ \nu_e$ also contribute at the level of $\mathcal{O}(1\%)$ of the $B^+ \rightarrow K^+ e^+ e^-$ signal; and there is also a contribution from $B^+ \rightarrow J/\psi(\rightarrow e^+ e^-) K^+$ decays, where a photon is emitted but not reconstructed. The kinematic correlation between $m(K^+ e^+ e^-)$ and q^2 means that, irrespective of misreconstruction effects, the latter background can only populate the $m(K^+ e^+ e^-)$ region well below the signal peak.

After the application of the selection requirements, the resonant and nonresonant decays are clearly visible in the mass distributions (see Fig. 3.2). The yields in the two $B^+ \rightarrow K^+ \ell^+ \ell^-$ and two $B^+ \rightarrow J/\psi(\rightarrow \ell^+ \ell^-) K^+$ decay modes are determined by performing unbinned extended maximum-likelihood fits to these distributions

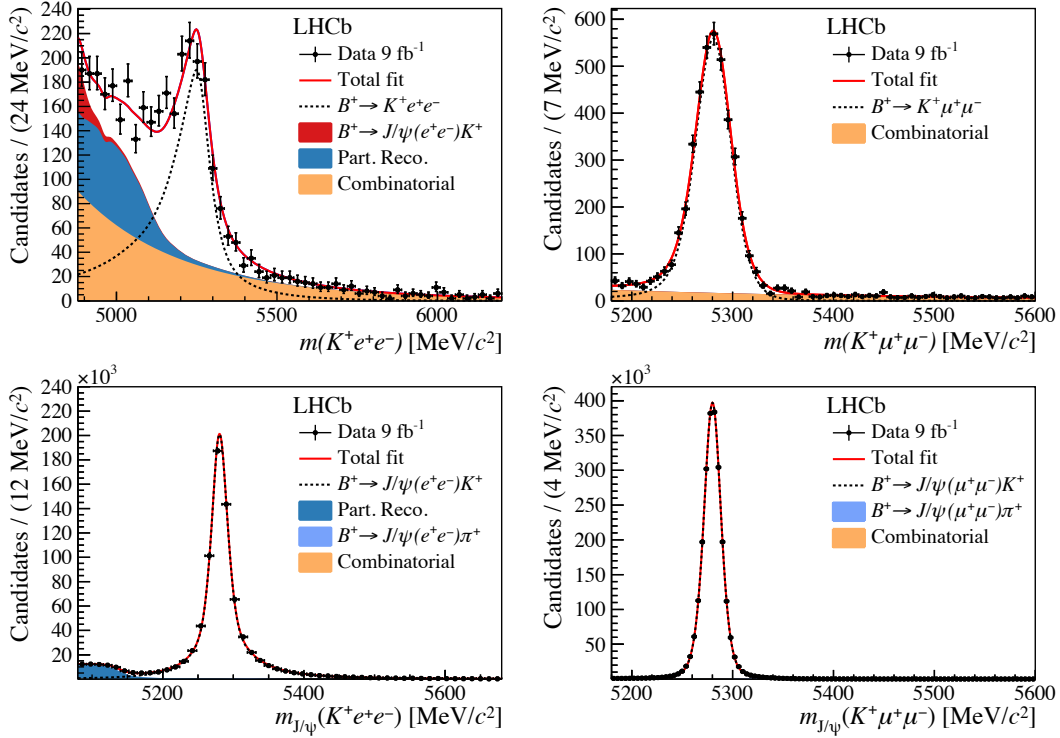


Fig. 3.2 Candidate invariant mass distributions. Distribution of the invariant mass $m_{(J/\psi)}(K^+\ell^+\ell^-)$ for candidates with (left) electron and (right) muon pairs in the final state for the (top) nonresonant $B^+ \rightarrow K^+\ell^+\ell^-$ signal channels and (bottom) resonant $B^+ \rightarrow J/\psi(\rightarrow \ell^+\ell^-)K^+$ decays. The fit projection is superimposed, with dotted lines describing the signal contribution and solid areas representing each of the background components described in the text and listed in the legend. In the resonant-mode distributions, some fit components are too small to be visible.

(see Methods). For the nonresonant candidates, the $m(K^+e^+e^-)$ and $m(K^+\mu^+\mu^-)$ distributions are fitted with a likelihood function that has the $B^+ \rightarrow K^+\mu^+\mu^-$ yield and R_K as fit parameters and the resonant decay-mode yields incorporated as Gaussian-constraint terms. The resonant yields are determined from separate fits to the mass, $m_{J/\psi}(K^+\ell^+\ell^-)$, formed by kinematically constraining the dilepton system to the known J/ψ mass [2] and thereby improving the mass resolution.

Simulated events are used to derive the two ratios of efficiencies needed to form R_K using Eq. (3.2). Control channels are used to calibrate the simulation in order to correct for the imperfect modelling of the B^+ production kinematics and various aspects of the detector response. The overall effect of these corrections on the measured value of R_K is a relative shift of $(+3 \pm 1)\%$. When compared with the 20% shift that these corrections induce in the measurement of $r_{J/\psi}$, this demonstrates the robustness

of the double-ratio method in suppressing systematic biases that affect the resonant and nonresonant decay modes similarly.

The systematic uncertainty (see Methods) from the choice of signal and background mass-shape models in the fits is estimated by fitting pseudoexperiments with alternative models that still describe the data well. The effect on R_K is at the 1% level. A comparable uncertainty arises from the limited size of the calibration samples, with negligible contributions from the calibration of the B^+ production kinematics and modelling of the selection and particle-identification efficiencies. Systematic uncertainties that affect the ratios of efficiencies influence the measured value of R_K and are taken into account using constraints on the efficiency values. Correlations between different categories of selected events and data-taking periods are taken into account in these constraints. The combined statistical and systematic uncertainty is then determined by scanning the profile-likelihood and the statistical contribution to the uncertainty is isolated by repeating the scan with the efficiencies fixed to their fitted values.

The determination of the $r_{J/\psi}$ ratio requires control of the relative selection efficiencies for the resonant electron and muon modes, and does not therefore benefit from the cancellation of systematic effects in the double ratio used to measure R_K . Given the scale of the corrections required, comparison of $r_{J/\psi}$ with unity is a stringent cross check of the experimental procedure. In addition, if the simulation is correctly calibrated, the measured $r_{J/\psi}$ value will not depend on any variable. The $r_{J/\psi}$ ratio is therefore also computed as a function of different kinematic variables. Even though the nonresonant and resonant samples are mutually exclusive as a function of q^2 , there is significant overlap between them in the quantities on which the efficiency depends, such as the laboratory-frame momenta of the final-state particles, or the opening angle between the two leptons. This is because a given set of values for the final-state particles' momenta and angles in the B^+ rest frame will result in a distribution of such values when transformed to the laboratory frame.

The value of $r_{J/\psi}$ is measured to be 0.981 ± 0.020 . This uncertainty includes both statistical and systematic effects, where the latter dominate. The consistency of this ratio with unity demonstrates control of the efficiencies well in excess of that needed for the determination of R_K . In the measurement of the $r_{J/\psi}$ ratio, the systematic uncertainty is dominated by the imperfect modelling of the B^+ production kinematics and the modelling of selection requirements, which have a negligible impact on the R_K measurement. No significant trend is observed in the differential determination of $r_{J/\psi}$ as a function of any considered variable. An example distribution, with $r_{J/\psi}$ determined as a function of B^+ momentum component transverse to the beam direction,

p_T , is shown in Fig. 3.3. Assuming the observed $r_{J/\psi}$ variation in such distributions reflects genuine mismodelling of the efficiencies, rather than statistical fluctuations, and taking into account the spectrum of the relevant variables in the nonresonant decay modes, a total shift on R_K is computed for each of the variables examined. The resulting variations are typically at the permille level and hence well within the estimated systematic uncertainty on R_K . Similarly, computations of the $r_{J/\psi}$ ratio in bins of two kinematic variables also do not show any trend and are consistent with the systematic uncertainties assigned on the R_K measurement.

In addition to $B^+ \rightarrow J/\psi K^+$ decays, clear signals are observed from $B^+ \rightarrow \psi(2S)K^+$ decays. The double ratio of branching fractions, $R_{\psi(2S)}$, defined by

$$R_{\psi(2S)} = \frac{\mathcal{B}(B^+ \rightarrow \psi(2S)(\rightarrow \mu^+\mu^-)K^+)}{\mathcal{B}(B^+ \rightarrow J/\psi(\rightarrow \mu^+\mu^-)K^+)} \bigg/ \frac{\mathcal{B}(B^+ \rightarrow \psi(2S)(\rightarrow e^+e^-)K^+)}{\mathcal{B}(B^+ \rightarrow J/\psi(\rightarrow e^+e^-)K^+)}, \quad (3.3)$$

provides an independent validation of the double-ratio analysis procedure and further tests the control of the efficiencies. This double ratio is expected to be close to unity [2] and is determined to be 0.997 ± 0.011 , where the uncertainty includes both statistical and systematic effects, the former of which dominates. This can be interpreted as a world-leading test of lepton flavour universality in $\psi(2S) \rightarrow \ell^+\ell^-$ decays.

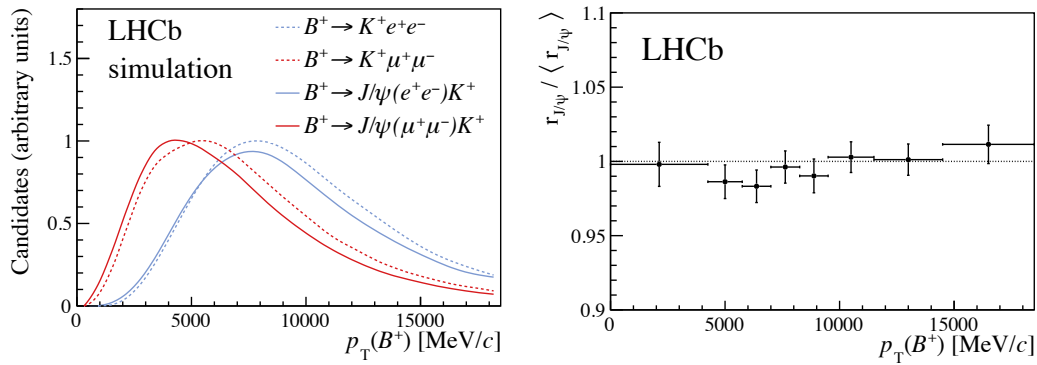


Fig. 3.3 Differential $r_{J/\psi}$ measurement. The distributions of (left) the B^+ transverse momentum, p_T , and (right) the ratio $r_{J/\psi}$ relative to its average value $\langle r_{J/\psi} \rangle$ as a function of p_T . The p_T spectrum of the $B^+ \rightarrow J/\psi K^+$ decays is similar to that of the corresponding $B^+ \rightarrow K^+ \ell^+ \ell^-$ decays such that the measurement of $r_{J/\psi}$ tests the kinematic region relevant for the R_K measurement. The lack of any dependence of the value of $r_{J/\psi} / \langle r_{J/\psi} \rangle$ as a function of B^+ p_T demonstrates control of the efficiencies. Uncertainties on the data points are statistical only.

The fit projections for the $m(K^+\ell^+\ell^-)$ and $m_{J/\psi}(K^+\ell^+\ell^-)$ distributions are shown in Fig. 3.2. The fit is of good quality and the value of R_K is measured to be

$$R_K(1.1 < q^2 < 6.0 \text{ GeV}^2/c^4) = 0.846_{-0.039}^{+0.042} {}_{-0.012}^{+0.013},$$

where the first uncertainty is statistical and the second systematic. Combining the uncertainties gives $R_K = 0.846_{-0.041}^{+0.044}$. This is the most precise measurement to date and is consistent with the SM expectation, 1.00 ± 0.01 [3–7], at the level of 0.10% (3.1 standard deviations), giving evidence for the violation of lepton universality in these decays. The value of R_K is found to be consistent in subsets of the data divided on the basis of data-taking period, different selection categories and magnet polarity (see Methods). The profile-likelihood is given in Methods. A comparison with previous measurements is shown in Fig. 3.4.

The 3850 ± 70 $B^+ \rightarrow K^+\mu^+\mu^-$ decay candidates that are observed are used to compute the $B^+ \rightarrow K^+\mu^+\mu^-$ branching fraction as a function of q^2 . The results are consistent between the different data-taking periods and with previous LHCb measurements [37]. The $B^+ \rightarrow K^+e^+e^-$ branching fraction is determined by combining the value of R_K with the value of $d\mathcal{B}(B^+ \rightarrow K^+\mu^+\mu^-)/dq^2$ in the region ($1.1 < q^2 < 6.0 \text{ GeV}^2/c^4$) [37], taking into account correlated systematic uncertainties. This gives

$$\frac{d\mathcal{B}(B^+ \rightarrow K^+e^+e^-)}{dq^2}(1.1 < q^2 < 6.0 \text{ GeV}^2/c^4) = (28.6_{-1.4}^{+1.5} \pm 1.3) \times 10^{-9} \text{ c}^4/\text{GeV}^2.$$

The 1.9% uncertainty on the $B^+ \rightarrow J/\psi K^+$ branching fraction [2] gives rise to the dominant systematic uncertainty. This is the most precise measurement of this quantity to date and, given the large ($\mathcal{O}(10\%)$) theoretical uncertainty on the predictions [132,7], is consistent with the SM.

A breaking of lepton universality would require an extension of the gauge structure of the SM that gives rise to the known fundamental forces. It would therefore constitute a significant evolution in our understanding and would challenge an inference based on a wealth of experimental data in other processes. Confirmation of any beyond the SM effect will clearly require independent evidence from a wide range of sources.

Measurements of other R_H observables with the full LHCb data set will provide further information on the quark-level processes measured. In addition to affecting the decay rates, new physics can also alter how the decay products are distributed in phase space. An angular analysis of the electron mode, where SM-like behaviour might be expected in the light of the present results and those from $\bar{b} \rightarrow \bar{s}\mu^+\mu^-$ decays,

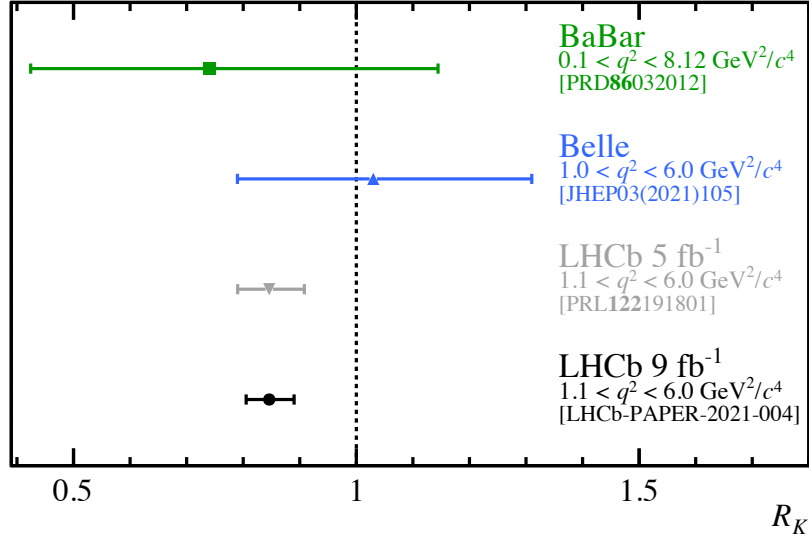


Fig. 3.4 Comparison between R_K measurements. In addition to the LHCb result, the measurements by the BaBar [15] and Belle [13] collaborations, which combine $B^+ \rightarrow K^+ \ell^+ \ell^-$ and $B^0 \rightarrow K_S^0 \ell^+ \ell^-$ decays, are also shown. The vertical dashed line indicates the SM prediction.

would allow the formation of ratios between observable quantities other than branching fractions, enabling further precise tests of lepton universality [133,16,31,134,18]. The hierarchical effect needed to explain the existing $\bar{b} \rightarrow \bar{s} \ell^+ \ell^-$ and $\bar{b} \rightarrow \bar{c} \ell^+ \nu_\ell$ data, with the largest effects observed in tau modes, then muon modes, and little or no effects in electron modes, suggests that studies of $\bar{b} \rightarrow \bar{s} \tau^+ \tau^-$ transitions are also of great interest [135,136]. There are excellent prospects for all of the above and further measurements with the much larger samples that will be collected with the upgraded LHCb detector from 2022 and, in the longer term, with the LHCb Upgrade II [137]. Other experiments should also be able to determine R_H ratios, with the Belle II experiment in particular expected to have competitive sensitivity [138]. The ATLAS and CMS experiments may also be able to contribute [139,140].

In summary, in the dilepton mass-squared region $1.1 < q^2 < 6.0 \text{ GeV}^2/c^4$, the ratio of branching fractions for $B^+ \rightarrow K^+ \mu^+ \mu^-$ and $B^+ \rightarrow K^+ e^+ e^-$ decays is measured to be $R_K = 0.846_{-0.041}^{+0.044}$. This is the most precise measurement of this ratio to date and is compatible with the SM prediction with a p-value of 0.10%. The significance of this discrepancy is 3.1 standard deviations, giving evidence for the violation of lepton universality in these decays.

Methods

3.0.1 Experimental setup

The Large Hadron Collider (LHC) is the world's highest-energy particle accelerator and is situated approximately 100 m underground, close to Geneva, Switzerland. The collider accelerates two counter-rotating beams of protons, guided by superconducting magnets located around a 27 km circular tunnel, and brings them into collision at four interaction points that house large detectors. The LHCb experiment [141,142] is instrumented in the region covering the polar angles between 10 and 250 mrad around the proton beam axis, in which the products from B -hadron decays can be efficiently captured and identified. The detector includes a high-precision tracking system with a dipole magnet, providing measurements of momentum and impact parameter (IP), defined for charged particles as the minimum distance of a track to a primary proton-proton interaction vertex (PV). Different types of charged particles are distinguished using information from two ring-imaging Cherenkov (RICH) detectors, a calorimeter and a muon system [142–147].

Since the associated data storage and analysis costs would be prohibitive, the experiment does not record all collisions. Only potentially interesting events, selected using real-time event filters referred to as triggers, are recorded. The LHCb trigger system has a hardware stage, based on information from the calorimeter and muon systems; followed by a software stage that uses all the information from the detector, including the tracking, to make the final selection of events to be recorded for subsequent analysis. The trigger selection algorithms are based on identifying key characteristics of B hadrons and their decay products, such as high p_T final state particles, and a decay vertex that is significantly displaced from any of the PVs in the event.

For the R_K measurement, candidate events are required to have passed a hardware trigger algorithm that selects either a high p_T muon; or an electron, hadron or photon with high transverse energy deposited in the calorimeters. The $B^+ \rightarrow K^+ \mu^+ \mu^-$ and $B^+ \rightarrow J/\psi (\rightarrow \mu^+ \mu^-) K^+$ candidates must be triggered by one of the muons, whereas $B^+ \rightarrow K^+ e^+ e^-$ and $B^+ \rightarrow J/\psi (\rightarrow e^+ e^-) K^+$ candidates must be triggered in one of three ways: by either one of the electrons; by the kaon from the B^+ decay; or by particles in the event that are not decay products of the B^+ candidate. In the software trigger, the tracks of the final-state particles are required to form a displaced vertex with good fit quality. A multivariate algorithm is used for the identification of displaced vertices consistent with the decay of a B hadron [148,149].

3.0.2 Analysis description

The analysis technique used to obtain the results presented in this article is essentially identical to that used to obtain the previous LHCb R_K measurement, described in Ref. [11] and only the main analysis steps are reviewed here.

3.0.2.1 Event selection

Kaon and muon candidates are identified using the output of multivariate classifiers that exploit information from the tracking system, the RICH detectors, the calorimeters and the muon chambers. Electrons are identified by matching tracks to particle showers in the electromagnetic calorimeter (ECAL) and using the ratio of the energy detected in the ECAL to the momentum measured by the tracking system. An electron that emits a bremsstrahlung photon due to interactions with the material of the detector downstream of the dipole magnet results in the photon and electron depositing their energy in the same ECAL cells, and therefore in a correct measurement of the original energy of the electron in the ECAL. However, a bremsstrahlung photon emitted upstream of the magnet will deposit energy in a different part of the ECAL than the electron, which is deflected in the magnetic field. For each electron track, a search is therefore made in the ECAL for energy deposits around the extrapolated track direction before the magnet that are not associated with any other charged tracks. The energy of any such deposit is added to the electron energy that is derived from the measurements made in the tracker. Bremsstrahlung photons can be added to none, either, or both of the final-state e^+ and e^- candidates.

In order to suppress background, each final-state particle is required to have sizeable p_T and to be inconsistent with coming from a PV. The particles are required to originate from a common vertex, with good vertex-fit quality, that is displaced significantly from all of the PVs in the event. The PVs are reconstructed by searching for space points where an accumulation of track trajectories is observed. A weighted least-squares method is then employed to find the precise vertex position. The B^+ momentum vector is required to be aligned with the vector connecting one of the PVs in the event (below referred to as the associated PV) and the B^+ decay vertex. The value of q^2 is calculated using only the lepton momenta, without imposing any constraint on the $m(K^+\ell^+\ell^-)$ mass.

The $m(K^+\ell^+\ell^-)$ mass ranges and the q^2 regions used to select the different decay modes are shown in Table 3.1. The selection requirements applied to the nonresonant and resonant decays are otherwise identical. For the muon modes, the superior mass

Table 3.1 Nonresonant and resonant mode q^2 and $m(K^+\ell^+\ell^-)$ ranges. The variables $m(K^+\ell^+\ell^-)$ and $m_{J/\psi}(K^+\ell^+\ell^-)$ are used for nonresonant and resonant decays, respectively.

Decay mode	q^2 [GeV ² /c ⁴]	$m_{(J/\psi)}(K^+\ell^+\ell^-)$ [GeV/c ²]
nonresonant e^+e^-	1.1 – 6.0	4.88 – 6.20
resonant e^+e^-	6.00 – 12.96	5.08 – 5.70
nonresonant $\mu^+\mu^-$	1.1 – 6.0	5.18 – 5.60
resonant $\mu^+\mu^-$	8.68 – 10.09	5.18 – 5.60

resolution allows a fit in a reduced $m(K^+\ell^+\ell^-)$ mass range compared to the electron modes. For the electron modes, a wider mass region is needed to perform an accurate fit, but the range chosen suppresses any significant contribution from decays with two or more additional pions that are not reconstructed. The residual contribution from such decays is considered as a source of systematic uncertainty. Resolution effects similarly motivate the choice of nonresonant q^2 regions, with a lower limit that excludes contributions from ϕ -meson decays and an upper limit that reduces the tail from $B^+ \rightarrow J/\psi(\rightarrow e^+e^-)K^+$ decays. The proportion of signal candidates that migrate in and out of the q^2 region of interest is of the order of 10%. This effect is accounted for using simulation.

Cascade background of the form $B \rightarrow H_c(\rightarrow K^+\ell^-\bar{\nu}_\ell X)\ell^+\nu_\ell Y$, where H_c is a hadron containing a c quark (D^0 , D^+ , D_s^+ , Λ_c^+), and X , Y are particles that are not included in the B^+ candidate, are suppressed by requiring that the kaon-lepton invariant mass is in the region $m(K^+\ell^-) > m_{D^0}$, where m_{D^0} is the known D^0 mass [2]. For the electron mode, this requirement is illustrated in Fig. 3.5 (left). Analogous background sources with a misidentified particle are reduced by applying a similar veto, but with the lepton-mass hypothesis changed to that of a pion (denoted $\ell_{[\rightarrow\pi]}$). In the muon case, $K\mu_{[\rightarrow\pi]}$ combinations with a mass smaller than m_{D^0} are rejected. In the electron case, a ± 40 MeV/c² window around the D^0 mass is used to reject candidates where the veto is applied without the bremsstrahlung recovery, *i.e.* based on only the measured track momenta. The mass distributions are shown in Fig. 3.5. The electron and muon veto cuts differ given the relative helicity suppression of $\pi^+ \rightarrow \ell^+\nu_\ell$ decays. This causes misidentification backgrounds to populate a range of $K\mu$ masses but only a peak in the Ke mass. The veto requirements retain 97% of $B^+ \rightarrow K^+\mu^+\mu^-$ and 95% of $B^+ \rightarrow K^+e^+e^-$ decays passing all other selection requirements.

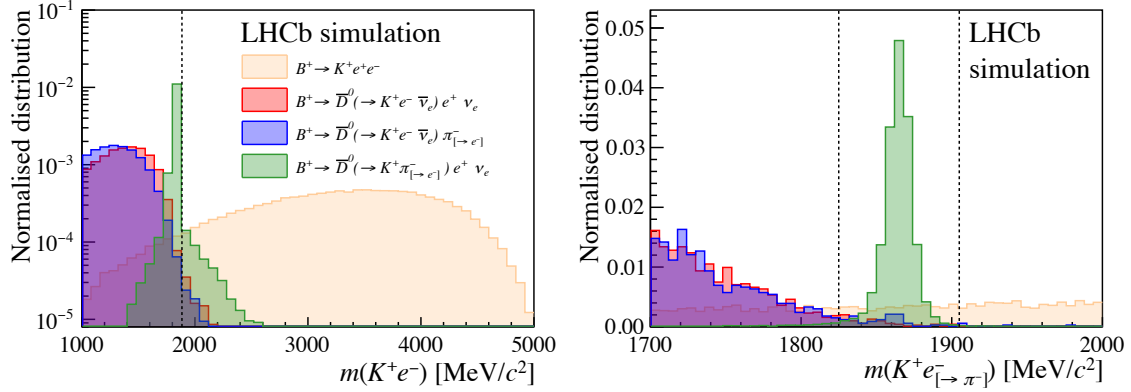


Fig. 3.5 Simulated K^+e^- mass distributions for signal and various cascade background samples. The signal is represented by the orange shaded region and the various cascade background contributions by red, dark blue and light blue shaded regions. The distributions are all normalised to unity. (Left, with log y -scale) the bremsstrahlung correction to the momentum of the electron is applied, resulting in a tail to the right. The region to the left of the vertical dashed line is rejected. (Right, with linear y -scale) the mass is computed only from the track information. The notation $\pi^-_{[\rightarrow e^-]}$ ($e^-_{[\rightarrow \pi^-]}$) is used to denote a pion (electron) that is reconstructed as an electron (pion). The region between the dashed vertical lines is rejected.

Background from other exclusive B -hadron decays requires at least two particles to be misidentified. These include the decays $B^+ \rightarrow K^+\pi^+\pi^-$, and misreconstructed $B^+ \rightarrow J/\psi(\rightarrow \ell^+\ell^-)K^+$ and $B^+ \rightarrow \psi(2S)(\rightarrow \ell^+\ell^-)K^+$ decays. In the latter two decays the kaon is misidentified as a lepton and the lepton (of the same electric charge) as a kaon. Such background is reduced to a negligible level by particle-identification criteria. Background from decays with a photon converted into an e^+e^- pair are also negligible due to the q^2 selection.

3.0.2.2 Multivariate selection

A Boosted Decision Tree (BDT) algorithm [150] with gradient boosting [151] is used to reduce combinatorial background. For the nonresonant muon mode and for each of the three different trigger categories of the nonresonant electron mode, a single BDT classifier is trained for the 7 and 8 TeV data, and an additional classifier is trained for the 13 TeV data. The BDT output is not strongly correlated with q^2 and the same classifiers are used to select the respective resonant decays. In order to train the classifier, simulated nonresonant $B^+ \rightarrow K^+\ell^+\ell^-$ decays are used as a proxy for the signal and nonresonant $K^+\ell^+\ell^-$ candidates selected from the data with $m(K^+\ell^+\ell^-) > 5.4 \text{ GeV}/c^2$ are used as a background sample. The k -folding technique

is used in the training and testing [152]. The classifier includes the following variables: the p_T of the B^+ , K^+ and dilepton candidates, and the minimum and maximum p_T of the leptons; the B^+ , dilepton and K^+ χ_{IP}^2 with respect to the associated PV, where χ_{IP}^2 is defined as the difference in the vertex-fit χ^2 of the PV reconstructed with and without the considered particle; the minimum and maximum χ_{IP}^2 of the leptons; the B^+ vertex-fit quality; the statistical significance of the B^+ flight distance; and the angle between the B^+ candidate momentum vector and the direction between the associated PV and the B^+ decay vertex. The p_T of the final state particles, the vertex-fit χ^2 and the significance of the flight distance have the most discriminating power. For each of the classifiers, a requirement is placed on the output variable in order to maximise the predicted significance of the nonresonant signal yield. For the electron modes that dictate the R_K precision, this requirement reduces the combinatorial background by approximately 99%, while retaining 85% of the signal mode. The muon BDT classifier has similar performance. In both cases, for both signal and background, the efficiency of the BDT selection has negligible dependence on $m(K^+\ell^+\ell^-)$ and q^2 in the regions used to determine the event yields.

3.0.2.3 Calibration of simulation

The simulated data used in this analysis are produced using the software described in Refs. [153,155–157,159]. Bremsstrahlung emission in the decay of particles is simulated using the PHOTOS software in the default configuration [160], which is observed to agree with an independent quantum electrodynamics calculation at the level of 1% [5].

Simulated events are weighted to correct for the imperfect modelling using control channels. The B^+ production kinematics are corrected using $B^+ \rightarrow J/\psi(\rightarrow \ell^+\ell^-)K^+$ events. The particle-identification performance is calibrated using data, where the species of particles in the final state can be unambiguously determined purely on the basis of the kinematics. The calibration samples consist of $D^{*+} \rightarrow D^0(\rightarrow K^-\pi^+)\pi^+$, $J/\psi \rightarrow \mu^+\mu^-$, and $B^+ \rightarrow J/\psi(\rightarrow e^+e^-)K^+$ decays, from which kaons, muons, and electrons, respectively, can be selected without applying particle-identification requirements. The performance of the particle-identification requirements is then evaluated from the proportion of events in these samples which fulfil the particle-identification selection criteria. The trigger response is corrected using weights applied to simulation as a function of variables relevant to the trigger algorithms. The weights are calculated by requiring that simulated $B^+ \rightarrow J/\psi(\rightarrow \ell^+\ell^-)K^+$ events exhibit the same trigger performance as the control data. The $B^+ \rightarrow J/\psi(\rightarrow \ell^+\ell^-)K^+$ events selected from the data have also been used to demonstrate control of the electron track-reconstruction

efficiency at the percent level [161]. Whenever $B^+ \rightarrow J/\psi(\rightarrow \ell^+\ell^-)K^+$ events are used to correct the simulation, the correlations between calibration and measurement samples are taken into account in the results and cross-checks presented in the article. The correlation is evaluated using a bootstrapping method to recompute the yields and efficiencies many times with different subsets of the data.

3.0.2.4 Likelihood fit

An unbinned extended maximum-likelihood fit is made to the $m(K^+e^+e^-)$ and $m(K^+\mu^+\mu^-)$ distributions of nonresonant candidates. The value of R_K is a fit parameter, which is related to the signal yields and efficiencies according to

$$R_K = \frac{N(B^+ \rightarrow K^+\mu^+\mu^-)}{\varepsilon(B^+ \rightarrow K^+\mu^+\mu^-)} \cdot \frac{\varepsilon(B^+ \rightarrow K^+e^+e^-)}{N(B^+ \rightarrow K^+e^+e^-)} \times \frac{\varepsilon(B^+ \rightarrow J/\psi(\rightarrow \mu^+\mu^-)K^+)}{N(B^+ \rightarrow J/\psi(\rightarrow \mu^+\mu^-)K^+)} \cdot \frac{N(B^+ \rightarrow J/\psi(\rightarrow e^+e^-)K^+)}{\varepsilon(B^+ \rightarrow J/\psi(\rightarrow e^+e^-)K^+)}, \quad (3.4)$$

where $N(X)$ indicates the yield of decay mode X and $\varepsilon(X)$ is the efficiency for selecting decay mode X . The resonant yields are determined from separate fits to $m_{J/\psi}(K^+\ell^+\ell^-)$. In the fit for R_K these yields, together with the efficiencies, are incorporated as Gaussian-constraint terms.

In order to take into account the correlation between the selection efficiencies, the $m(K^+e^+e^-)$ and $m(K^+\mu^+\mu^-)$ distributions of nonresonant candidates in each of the different trigger categories and data-taking periods are fitted simultaneously, with a common value of R_K . The relative fraction of partially reconstructed background in each trigger category is also shared across the different data-taking periods.

The mass-shape parameters are derived from the calibrated simulation. The four signal modes are modelled by multiple Gaussian functions with power-law tails on both sides of the peak [162,163], although the differing detector response gives different shapes for the electron and muon modes. The signal mass shapes of the electron modes are described with the sum of three distributions, which model whether the ECAL energy deposit from a bremsstrahlung photon was added to both, either, or neither of the e^\pm candidates. The expected values from simulated events are used to constrain the fraction of signal decays in each of these categories. These fractions are observed to agree well with those observed in resonant events selected from the data. In order to take into account residual differences in the signal shape between data and simulation, an offset in the peak position and a scaling of the resolution are allowed to vary in the fits to the resonant modes. The corresponding parameters are then fixed in the fits

to the relevant nonresonant modes. This resolution scaling changes the migration of candidates into the q^2 region of interest by less than 1%.

For the modelling of nonresonant and resonant partially reconstructed backgrounds, data are used to correct the simulated $K\pi$ mass spectrum for $B^{(0,+)} \rightarrow K^+\pi^{(-,0)}e^+e^-$ and $B^{(0,+)} \rightarrow J/\psi(\rightarrow e^+e^-)K^+\pi^{(-,0)}$ decays [164]. The calibrated simulation is used subsequently to obtain the $m(K^+\ell^+\ell^-)$ mass shape and relative fractions of these background components. In order to accommodate possible lepton-universality violation in these partially reconstructed processes, which are underpinned by the same $\bar{b} \rightarrow \bar{s}$ quark-level transitions as those of interest, the overall yield of such decays is left to vary freely in the fit. The shape of the $B^+ \rightarrow J/\psi \pi^+$ background contribution is taken from simulation but the size with respect to the $B^+ \rightarrow J/\psi K^+$ mode is constrained using the known ratio of the relevant branching fractions [165,2] and efficiencies.

In the fits to nonresonant $B^+ \rightarrow K^+e^+e^-$ candidates, the mass shape of the background from $B^+ \rightarrow J/\psi(\rightarrow e^+e^-)K^+$ decays with an emitted photon that is not reconstructed is also taken from simulation and, adjusting for the relevant selection efficiency, its yield is constrained to the value from the fit to the resonant mode within its uncertainty. In all fits, the combinatorial background is modelled with an exponential function with a freely varying yield and shape.

The fits to the nonresonant (resonant) decay modes in different data-taking periods and trigger categories are shown in Fig. 3.6 (Fig. 3.7). For the resonant modes the results from independent fits to each period/category are shown. Conversely, the nonresonant distributions show the projections from the simultaneous fit across data taking periods and trigger categories that is used to obtain R_K . The fitted yields for the resonant and nonresonant decays are given in Table 3.2.

The profile likelihood for the fit to the nonresonant decays is shown in Fig. 3.8. The likelihood is non-Gaussian in the region $R_K > 0.95$ due to the comparatively low yield of $B^+ \rightarrow K^+e^+e^-$ events. Following the procedure described in Refs. [11,12], the

Table 3.2 Yields of the nonresonant and resonant decay modes obtained from the fits to the data. The quoted uncertainty is the combination of statistical and systematic effects.

Decay mode	Yield
$B^+ \rightarrow K^+e^+e^-$	$1\,640 \pm 70$
$B^+ \rightarrow K^+\mu^+\mu^-$	$3\,850 \pm 70$
$B^+ \rightarrow J/\psi(\rightarrow e^+e^-)K^+$	$743\,300 \pm 900$
$B^+ \rightarrow J/\psi(\rightarrow \mu^+\mu^-)K^+$	$2\,288\,500 \pm 1\,500$

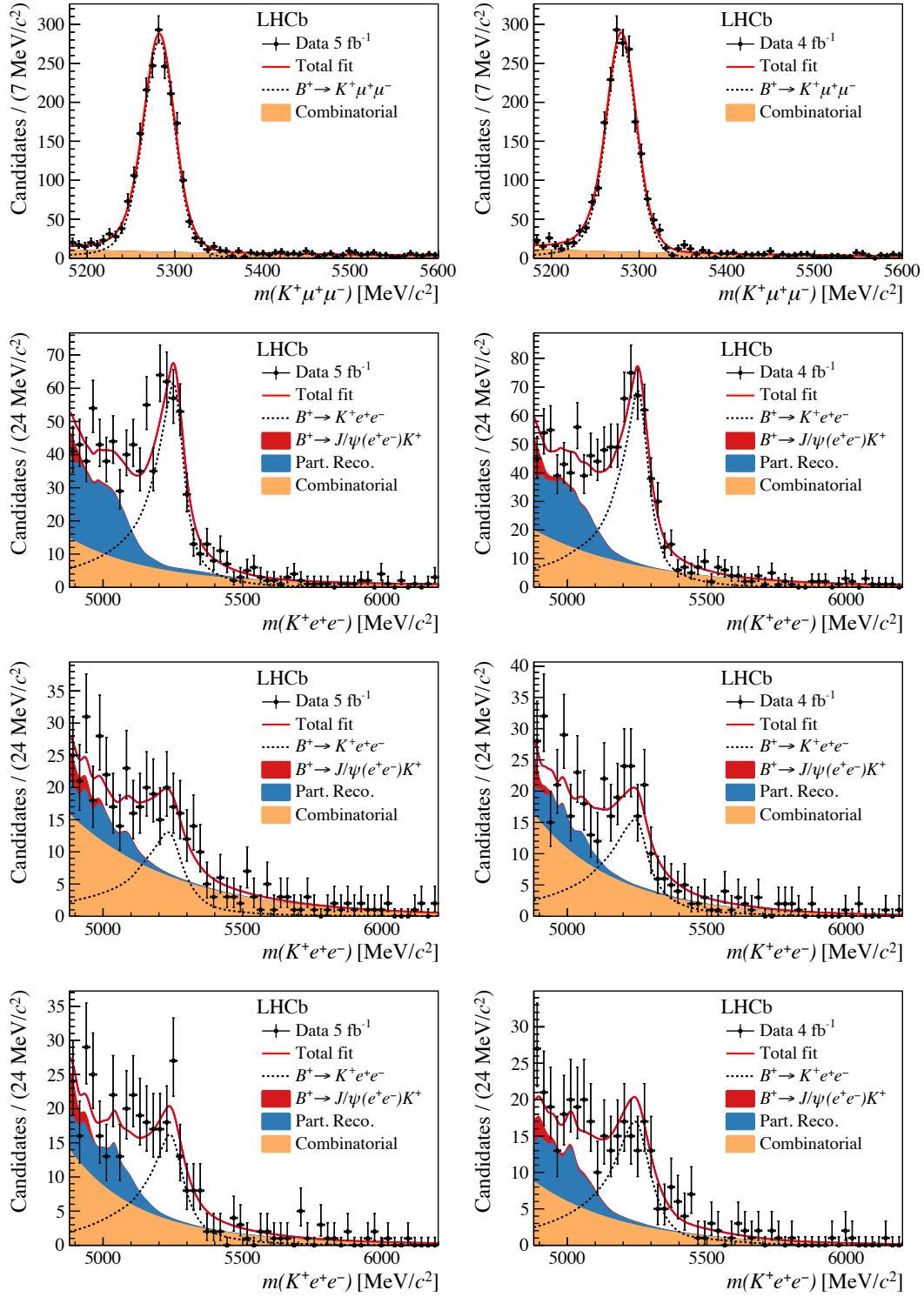


Fig. 3.6 Candidate invariant mass distributions. Distribution of the invariant mass $m(K^+\ell^+\ell^-)$ for nonresonant candidates in the (left) sample previously analysed [11] and (right) the new data sample. The top row shows the fit to the muon modes and the subsequent rows the fits to the electron modes triggered by (second row) one of the electrons, (third row) the kaon and (last row) by other particles in the event. The fit projections are superimposed, with dotted lines describing the signal contribution and solid areas representing each of the background components described in the text and listed in the legend.

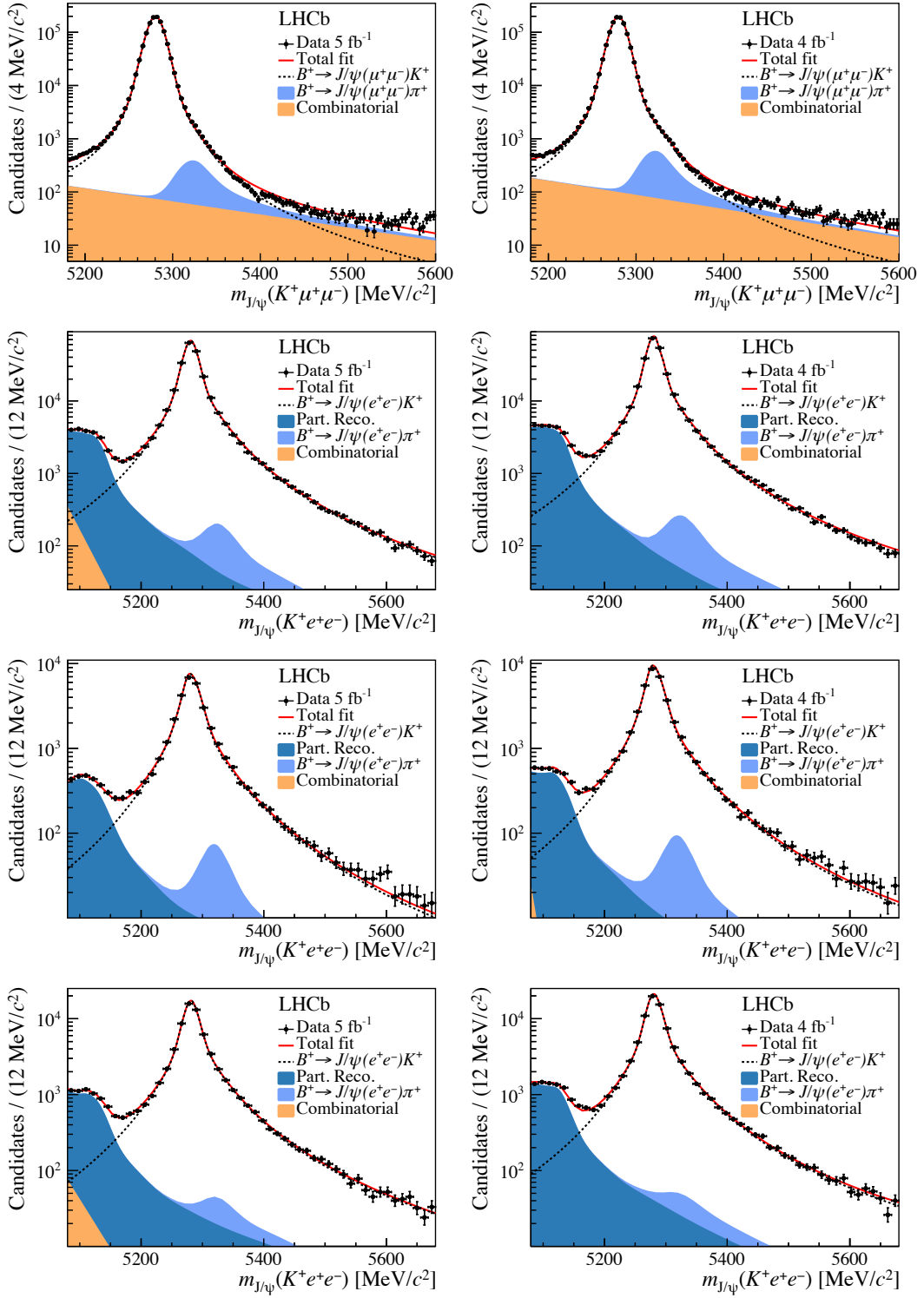


Fig. 3.7 Candidate invariant mass distributions. Distribution of the invariant mass $m_{J/\psi}(K^+\ell^+\ell^-)$ for resonant candidates in the (left) sample previously analysed [11] and (right) the new data sample. The top row shows the fit to the muon modes and the subsequent rows the fits to the electron modes triggered by (second row) one of the electrons, (third row) the kaon and (last row) by other particles in the event. The fit projections are superimposed, with dotted lines describing the signal contribution and solid areas representing each of the background components described in the text and listed in the legend.

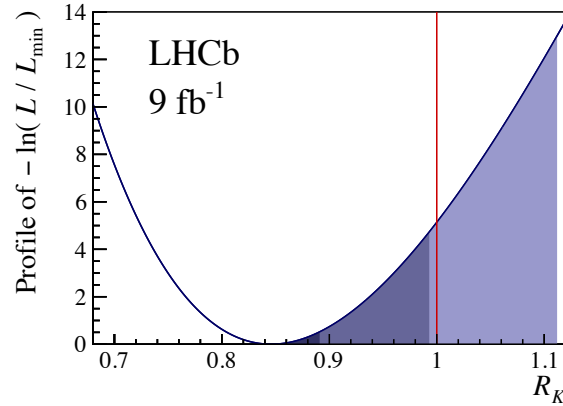


Fig. 3.8 Likelihood function from the fit to the nonresonant $B^+ \rightarrow K^+ \ell^+ \ell^-$ candidates in terms of the ratio between the likelihood value (L) and that found by the fit (L_{\max}) as a function of R_K . The extent of the dark, medium and light blue regions shows the values allowed for R_K at 1σ , 3σ and 5σ levels. The red line indicates the prediction from the SM.

p-value is computed by integrating the posterior probability density function for R_K , having folded in the theory uncertainty on the SM prediction, for R_K values larger than the SM expectation. The corresponding significance in terms of standard deviations is computed using the inverse Gaussian cumulative distribution function for a one-sided conversion.

A test statistic is constructed that is based on the likelihood ratio between two hypotheses with common (null) or different (test) R_K values for the part of the sample analysed previously (7, 8 and part of the 13 TeV data) and for the new portion of the 13 TeV data. Using pseudoexperiments based on the null hypothesis, the data suggest that the R_K value from the new portion of the data is compatible with that from the previous sample with a p-value of 95%. Further tests give good compatibility for subsamples of the data corresponding to different trigger categories and magnet polarities.

The departure of the profile likelihood shown in Fig. 3.8 from a normal distribution stems from the definition of R_K . In particular, in the R_K ratio the denominator is affected by larger statistical uncertainties than the numerator, owing to the larger number of nonresonant muonic signal candidates. However, the intervals of the likelihood distribution are found to be the same when estimated with $1/R_K$ as the fit parameter.

3.0.2.5 Additional cross-checks

The $r_{J/\psi}$ single ratio is used to perform a number of additional cross-checks. The distribution of this ratio as a function of the angle between the leptons and the minimum p_T of the leptons is shown in Fig. 3.9, together with the spectra expected for the resonant and nonresonant decays. No significant trend is observed in either $r_{J/\psi}$ distribution. Assuming the deviations observed are genuine mismodelling of the efficiencies, rather than statistical fluctuations, a total shift of R_K at a level less than 0.001 would be expected due to these effects. This estimate takes into account the spectrum of the relevant variables in the nonresonant decay modes of interest and is compatible with the estimated systematic uncertainties on R_K . Similarly, the variations seen in $r_{J/\psi}$ as a function of all other reconstructed quantities examined are compatible with the systematic uncertainties assigned. In addition, $r_{J/\psi}$ is computed in two-dimensional intervals of reconstructed quantities, as shown in Fig. 3.10. Again, no significant trend is seen.

3.0.2.6 Systematic uncertainties

The majority of the sources of systematic uncertainty affect the relative efficiencies between nonresonant and resonant decays. These are included in the fit to R_K by allowing the relative efficiency to vary within Gaussian constraints. The width of the constraint is determined by adding the contributions from the different sources in quadrature. Correlations in the systematic uncertainties between different trigger categories and run periods are taken into account. Systematic uncertainties affecting the determination of the signal yield are assessed using pseudoexperiments generated with variations of the fit model. Pseudoexperiments are also used to assess the degree of bias originating from the fitting procedure. The bias is found to be 1% of the statistical precision, *i.e.* negligible with respect to other sources of systematic uncertainty.

For the nonresonant $B^+ \rightarrow K^+ e^+ e^-$ decays, the systematic uncertainties are dominated by the modelling of the signal and background components used in the fit. The effect on R_K is at the 1% level. A significant proportion (0.7%) of this uncertainty comes from the limited knowledge of the $K\pi$ spectrum in $B^{(0,+)} \rightarrow K^+ \pi^{(-,0)} e^+ e^-$ decays. In addition, a 0.2% systematic uncertainty is assigned for the potential contribution from partially reconstructed decays with two additional pions. A comparable uncertainty to that from the modelling of the signal and background components is induced by the limited sizes of calibration samples. Other sources of systematic uncertainty, such as the calibration of B^+ production kinematics, the trigger calibration and the determination

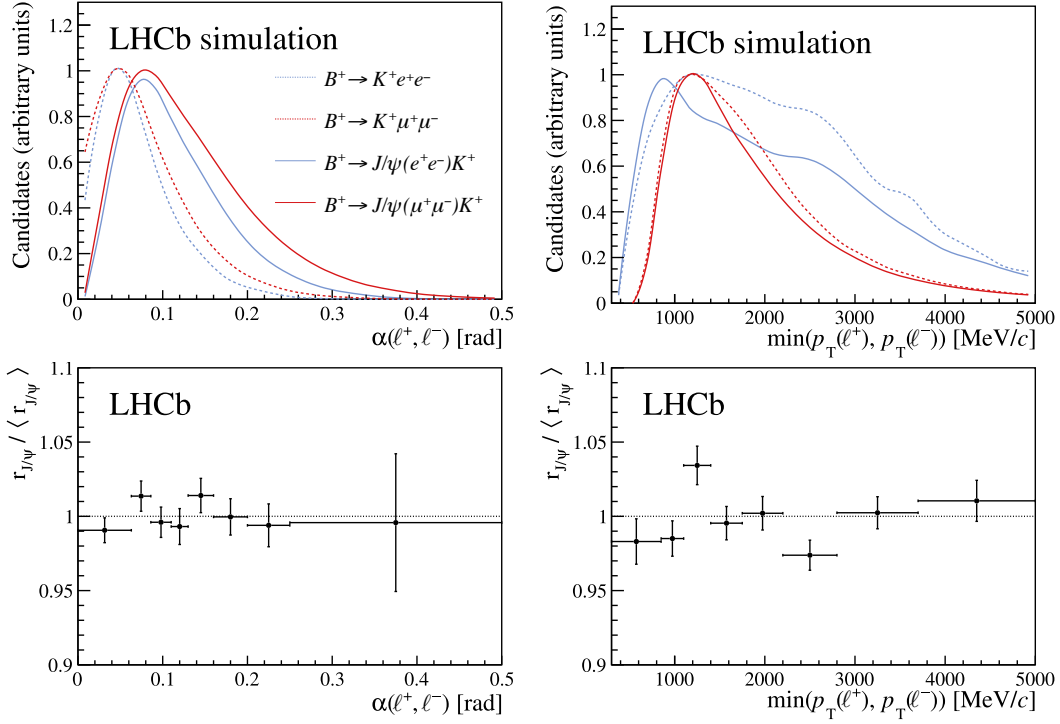


Fig. 3.9 Differential $r_{J/\psi}$ measurement. (Top) distributions of the reconstructed spectra of (left) the angle between the leptons, $\alpha(\ell^+, \ell^-)$, and (right) the minimum p_T of the leptons for $B^+ \rightarrow K^+ \ell^+ \ell^-$ and $B^+ \rightarrow J/\psi (\rightarrow \ell^+ \ell^-) K^+$ decays. (Bottom) the single ratio $r_{J/\psi}$ relative to its average value $\langle r_{J/\psi} \rangle$ as a function of these variables. In the electron minimum p_T spectra, the structure at 2800 MeV/c is related to the trigger threshold. Uncertainties on the data points are statistical only.

of the particle identification efficiencies, contribute at the few-permille or permille level, depending strongly on the data-taking period and the trigger category.

The uncertainties on parameters used in the simulation model of the signal decays affect the q^2 distribution and hence the selection efficiency. These uncertainties are propagated to an uncertainty on R_K using predictions from the FLAVIO software package [7] but give rise to a negligible effect. Similarly, the differing q^2 resolution between data and simulation, which alters estimates of the q^2 migration, has negligible impact on the result.

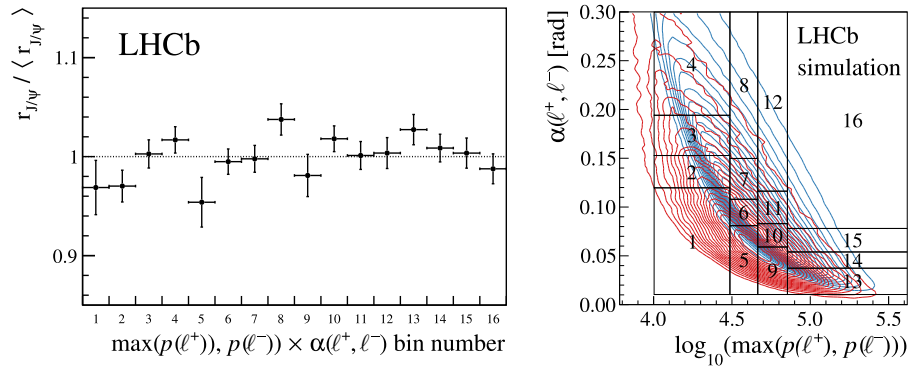


Fig. 3.10 Double differential $r_{J/\psi}$ measurement. (Left) the value of $r_{J/\psi}$, relative to the average value of $r_{J/\psi}$, measured in two-dimensional bins of the maximum lepton momentum, $p(\ell)$, and the opening angle between the two leptons, $\alpha(\ell^+, \ell^-)$. (Right) the bin definition in this two-dimensional space together with the distribution for $B^+ \rightarrow K^+ e^+ e^-$ ($B^+ \rightarrow J/\psi(\rightarrow e^+ e^-) K^+$) decays depicted as red (blue) contours. Uncertainties on the data points are statistical only.

References

- [1] S. L. Glashow, J. Iliopoulos, and L. Maiani. Weak interactions with lepton-hadron symmetry. *Phys. Rev.*, D2:1285–1292, 1970.
- [2] P. A. Zyla et al. Review of particle physics. *Prog. Theor. Exp. Phys.*, 2020(8):083C01, 2020.
- [3] Sébastien Descotes-Genon, Lars Hofer, Joaquim Matias, and Javier Virto. Global analysis of $b \rightarrow s\ell\ell$ anomalies. *JHEP*, 06:092, 2016.
- [4] Christoph Bobeth, Gudrun Hiller, and Giorgi Piranishvili. Angular distributions of $\bar{B} \rightarrow K\bar{\ell}\ell$ decays. *JHEP*, 12:040, 2007.
- [5] Marzia Bordone, Gino Isidori, and Andrea Pattori. On the Standard Model predictions for R_K and R_{K^*} . *Eur. Phys. J.*, C76(8):440, 2016.
- [6] Danny van Dyk, Nico Gubernari, DomLeljask, MÉRil Reboud, elgicse, Christoph Bobeth, Martin Ritter, Stephan Kürten, Thomas Blake, Marzia Bordone, Ahmet Kokulu, Eduardo Romero, Ismo Toijala, KKVos, Philip Lüghausen, and Eike Eberhard. Eos version 0.3.3, March (2021).
- [7] David M. Straub. flavio: a python package for flavour and precision phenomenology in the Standard Model and beyond. 2018.
- [8] Gino Isidori, Saad Nabeebaccus, and Roman Zwicky. QED corrections in $\bar{B} \rightarrow \bar{K}\ell^+\ell^-$ at the double-differential level. *JHEP*, 12:104, 2020.
- [9] Gudrun Hiller and Frank Krüger. More model-independent analysis of $b \rightarrow s$ processes. *Phys. Rev.*, D69:074020, 2004.
- [10] Yili Wang and David Atwood. Rate difference between $b \rightarrow s\mu^+\mu^-$ and $b \rightarrow se^+e^-$ in supersymmetry with large $\tan\beta$. *Phys. Rev.*, D68:094016, 2003.

-
- [11] R. Aaij et al. Search for lepton-universality violation in $B^+ \rightarrow K^+ \ell^+ \ell^-$ decays. *Phys. Rev. Lett.*, 122:191801, 2019.
- [12] R. Aaij et al. Test of lepton universality with $B^0 \rightarrow K^{*0} \ell^+ \ell^-$ decays. *JHEP*, 08:055, 2017.
- [13] S. Choudhury et al. Test of lepton flavor universality and search for lepton flavor violation in $B \rightarrow K \ell \ell$ decays. *JHEP*, 03:105, 2021.
- [14] S. Wehle et al. Test of lepton-flavor universality in $B \rightarrow K^* \ell^+ \ell^-$ decays at Belle. *Phys. Rev. Lett.*, 126:161801, Apr 2021.
- [15] J. P. Lees et al. Measurement of branching fractions and rate asymmetries in the rare decays $B \rightarrow K^{(*)} \ell^+ \ell^-$. *Phys. Rev.*, D86:032012, Aug 2012.
- [16] Bernat Capdevila, Sebastien Descotes-Genon, Joaquim Matias, and Javier Virto. Assessing lepton-flavour non-universality from $B \rightarrow K^* \ell \ell$ angular analyses. *JHEP*, 10:075, 2016.
- [17] Bernat Capdevila, Sebastien Descotes-Genon, Lars Hofer, and Joaquim Matias. Hadronic uncertainties in $B \rightarrow K^* \mu^+ \mu^-$: a state-of-the-art analysis. *JHEP*, 04:016, 2017.
- [18] Nicola Serra, Rafael Silva Coutinho, and Danny van Dyk. Measuring the breaking of lepton flavor universality in $B \rightarrow K^* \ell^+ \ell^-$. *Phys. Rev.*, D95(3):035029, 2017.
- [19] Aoife Bharucha, David M. Straub, and Roman Zwicky. $B \rightarrow V \ell^+ \ell^-$ in the Standard Model from light-cone sum rules. *JHEP*, 08:098, 2016.
- [20] Wolfgang Altmannshofer, Christoph Niehoff, Peter Stangl, and David M. Straub. Status of the $B \rightarrow K^* \mu^+ \mu^-$ anomaly after Moriond 2017. *Eur. Phys. J.*, C77(6):377, 2017.
- [21] Sebastian Jäger and Jorge Martin Camalich. Reassessing the discovery potential of the $B \rightarrow K^* \ell^+ \ell^-$ decays in the large-recoil region: SM challenges and BSM opportunities. *Phys. Rev.*, D93(1):014028, 2016.
- [22] Diptimoy Ghosh, Marco Nardecchia, and S. A. Renner. Hint of lepton flavour non-universality in B meson decays. *JHEP*, 12:131, 2014.
- [23] R. Aaij et al. Test of lepton universality using $\Lambda_b^0 \rightarrow p K^- \ell^+ \ell^-$ decays. *JHEP*, 05:040, 2020.

- [24] R. Aaij et al. Angular analysis of the $B^+ \rightarrow K^{*+} \mu^+ \mu^-$ decay. *Phys. Rev. Lett.*, 126:161802, Apr 2021.
- [25] R. Aaij et al. Measurement of CP -averaged observables in the $B^0 \rightarrow K^{*0} \mu^+ \mu^-$ decay. *Phys. Rev. Lett.*, 125:011802, 2020.
- [26] R. Aaij et al. Angular analysis of the $B^0 \rightarrow K^{*0} \mu^+ \mu^-$ decay using 3 fb^{-1} of integrated luminosity. *JHEP*, 02:104, 2016.
- [27] Morad Aaboud et al. Angular analysis of $B_d^0 \rightarrow K^* \mu^+ \mu^-$ decays in pp collisions at $\sqrt{s} = 8 \text{ TeV}$ with the ATLAS detector. *JHEP*, 10:047, 2018.
- [28] Bernard Aubert et al. Measurements of branching fractions, rate asymmetries, and angular distributions in the rare decays $B \rightarrow K \ell^+ \ell^-$ and $B \rightarrow K^* \ell^+ \ell^-$. *Phys. Rev.*, D73:092001, 2006.
- [29] J. P. Lees et al. Measurement of angular asymmetries in the decays $B \rightarrow K^* \ell^+ \ell^-$. *Phys. Rev.*, D93(5):052015, 2016.
- [30] J. T. Wei et al. Measurement of the differential branching fraction and forward-backward asymmetry for $B \rightarrow K^{(*)} \ell^+ \ell^-$. *Phys. Rev. Lett.*, 103:171801, 2009.
- [31] S. Wehle et al. Lepton-flavor-dependent angular analysis of $B \rightarrow K^* \ell^+ \ell^-$. *Phys. Rev. Lett.*, 118:111801, 2017.
- [32] T. Aaltonen et al. Measurements of the angular distributions in the decays $B \rightarrow K^{(*)} \mu^+ \mu^-$ at CDF. *Phys. Rev. Lett.*, 108:081807, 2012.
- [33] Vardan Khachatryan et al. Angular analysis of the decay $B^0 \rightarrow K^{*0} \mu^+ \mu^-$ from pp collisions at $\sqrt{s} = 8 \text{ TeV}$. *Phys. Lett.*, B753:424–448, 2016.
- [34] Albert M Sirunyan et al. Measurement of angular parameters from the decay $B^0 \rightarrow K^{*0} \mu^+ \mu^-$ in proton-proton collisions at $\sqrt{s} = 8 \text{ TeV}$. *Phys. Lett.*, B781:517–541, 2018.
- [35] R. Aaij et al. Measurements of the S-wave fraction in $B^0 \rightarrow K^+ \pi^- \mu^+ \mu^-$ decays and the $B^0 \rightarrow K^*(892)^0 \mu^+ \mu^-$ differential branching fraction. *JHEP*, 11:047, 2016.
- [36] R. Aaij et al. Angular analysis and differential branching fraction of the decay $B_s^0 \rightarrow \phi \mu^+ \mu^-$. *JHEP*, 09:179, 2015.
- [37] R. Aaij et al. Differential branching fractions and isospin asymmetries of $B \rightarrow K^{(*)} \mu^+ \mu^-$ decays. *JHEP*, 06:133, 2014.

- [38] R. Aaij et al. Differential branching fraction and angular analysis of $A_b^0 \rightarrow A\mu^+\mu^-$ decays. *JHEP*, 06:115, 2015.
- [39] James Lyon and Roman Zwicky. Resonances gone topsy turvy – the charm of QCD or new physics in $b \rightarrow s\ell^+\ell^-$? 2014.
- [40] A. Khodjamirian, Th. Mannel, and Y. M. Wang. $B \rightarrow K\ell^+\ell^-$ decay at large hadronic recoil. *JHEP*, 02:010, 2013.
- [41] A. Khodjamirian, Th. Mannel, A. A. Pivovarov, and Y. M. Wang. Charm-loop effect in $B \rightarrow K^{(*)}\ell^+\ell^-$ and $B \rightarrow K^*\gamma$. *JHEP*, 09:089, 2010.
- [42] Sébastien Descotes-Genon, Lars Hofer, Joaquim Matias, and Javier Virto. On the impact of power corrections in the prediction of $B \rightarrow K^*\mu^+\mu^-$ observables. *JHEP*, 12:125, 2014.
- [43] Ronald R. Horgan, Zhaofeng Liu, Stefan Meinel, and Matthew Wingate. Calculation of $B^0 \rightarrow K^{*0}\mu^+\mu^-$ and $B_s^0 \rightarrow \phi\mu^+\mu^-$ observables using form factors from lattice QCD. *Phys. Rev. Lett.*, 112:212003, 2014.
- [44] Frederik Beaujean, Christoph Bobeth, and Danny van Dyk. Comprehensive Bayesian analysis of rare (semi)leptonic and radiative B decays. *Eur. Phys. J.*, C74:2897, 2014.
- [45] Christian Hambrock, Gudrun Hiller, Stefan Schacht, and Roman Zwicky. $B \rightarrow K^*$ form factors from flavor data to QCD and back. *Phys. Rev.*, D89(7):074014, 2014.
- [46] Wolfgang Altmannshofer and David M. Straub. New physics in $B \rightarrow K^*\mu\mu$? *Eur. Phys. J.*, C73:2646, 2013.
- [47] Christoph Bobeth, Marcin Chrzaszcz, Danny van Dyk, and Javier Virto. Long-distance effects in $B \rightarrow K^*\ell\ell$ from analyticity. *Eur. Phys. J.*, C78(6):451, 2018.
- [48] Marco Ciuchini, Marco Fedele, Enrico Franco, Ayan Paul, Luca Silvestrini, and Mauro Valli. Lessons from the $B^{0,+} \rightarrow K^{*0,+}\mu^+\mu^-$ angular analyses. *Phys. Rev.*, D103(1):015030, 2021.
- [49] Kamila Kowalska, Dinesh Kumar, and Enrico Maria Sessolo. Implications for new physics in $b \rightarrow s\mu\mu$ transitions after recent measurements by Belle and LHCb. *Eur. Phys. J.*, C79(10):840, 2019.

- [50] Marcel Algueró, Bernat Capdevila, Andreas Crivellin, Sébastien Descotes-Genon, Pere Masjuan, Joaquim Matias, Martín Novoa Brunet, and Javier Virto. Emerging patterns of new physics with and without lepton flavour universal contributions. *Eur. Phys. J.*, C79(8):714, 2019. [Addendum: *Eur.Phys.J.C* 80, 511 (2020)].
- [51] T. Hurth, F. Mahmoudi, and S. Neshatpour. Implications of the new LHCb angular analysis of $B \rightarrow K^* \mu^+ \mu^-$: Hadronic effects or new physics? *Phys. Rev.*, D102(5):055001, 2020.
- [52] Marco Ciuchini, António M. Coutinho, Marco Fedele, Enrico Franco, Ayan Paul, Luca Silvestrini, and Mauro Valli. New Physics in $b \rightarrow s \ell^+ \ell^-$ confronts new data on lepton universality. *Eur. Phys. J.*, C79(8):719, 2019.
- [53] Jason Aebischer, Wolfgang Altmannshofer, Diego Guadagnoli, MÉRIL Reboud, Peter Stangl, and David M. Straub. B -decay discrepancies after Moriond 2019. *Eur. Phys. J.*, C80(3):252, 2020.
- [54] Ashutosh Kumar Alok, Amol Dighe, Shireen Gangal, and Dinesh Kumar. Continuing search for new physics in $b \rightarrow s \mu \mu$ decays: two operators at a time. *JHEP*, 06:089, 2019.
- [55] Bhubanjyoti Bhattacharya, Alakabha Datta, David London, and Shanmuka Shivashankara. Simultaneous explanation of the R_K and $R(D^{(*)})$ puzzles. *Phys. Lett.*, B742:370–374, 2015.
- [56] Wolfgang Altmannshofer, Stefania Gori, Maxim Pospelov, and Itay Yavin. Quark flavor transitions in $L_\mu - L_\tau$ models. *Phys. Rev.*, D89:095033, 2014.
- [57] Andreas Crivellin, Giancarlo D’Ambrosio, and Julian Heeck. Explaining $h \rightarrow \mu^\pm \tau^\mp$, $B \rightarrow K^* \mu^+ \mu^-$ and $B \rightarrow K \mu^+ \mu^- / B \rightarrow K e^+ e^-$ in a two-Higgs-doublet model with gauged $L_\mu - L_\tau$. *Phys. Rev. Lett.*, 114:151801, 2015.
- [58] Alejandro Celis, Javier Fuentes-Martín, Martín Jung, and Hugo Serôdio. Family nonuniversal Z' models with protected flavor-changing interactions. *Phys. Rev.*, D92(1):015007, 2015.
- [59] Adam Falkowski, Marco Nardecchia, and Robert Ziegler. Lepton flavor non-universality in B-meson decays from a $U(2)$ flavor model. *JHEP*, 11:173, 2015.
- [60] Geneviève Bélanger, Cédric Delaunay, and Susanne Westhoff. A dark matter relic from muon anomalies. *Phys. Rev. D*, 92:055021, 2015.

- [61] Andreas Crivellin, Giancarlo D'Ambrosio, and Julian Heeck. Addressing the LHC flavor anomalies with horizontal gauge symmetries. *Phys. Rev. D*, 91(7):075006, 2015.
- [62] Bhubanjyoti Bhattacharya, Alakabha Datta, Jean-Pascal Guévin, David London, and Ryoutaro Watanabe. Simultaneous explanation of the R_K and $R_{D^{(*)}}$ puzzles: A model analysis. *JHEP*, 01:015, 2017.
- [63] Stephen F. King. Flavourful Z' models for $R_{K^{(*)}}$. *JHEP*, 08:019, 2017.
- [64] Cheng-Wei Chiang, Xiao-Gang He, Jusak Tandean, and Xing-Bo Yuan. $R_{K^{(*)}}$ and related $b \rightarrow s\ell\bar{\ell}$ anomalies in minimal flavor violation framework with Z' boson. *Phys. Rev. D*, 96(11):115022, 2017.
- [65] Adam Falkowski, Stephen F. King, Elena Perdomo, and Mathias Pierre. Flavourful Z' portal for vector-like neutrino dark matter and $R_{K^{(*)}}$. *JHEP*, 08:061, 2018.
- [66] B. C. Allanach, J. M. Butterworth, and Tyler Corbett. Collider constraints on Z' models for neutral current B-anomalies. *JHEP*, 08:106, 2019.
- [67] B. C. Allanach and Joe Davighi. Naturalising the third family hypercharge model for neutral current B -anomalies. *Eur. Phys. J.*, C79(11):908, 2019.
- [68] Junichiro Kawamura, Stuart Raby, and Andreas Trautner. Complete vectorlike fourth family and new $U(1)'$ for muon anomalies. *Phys. Rev.*, D100(5):055030, 2019.
- [69] Siddharth Dwivedi, Dilip Kumar Ghosh, Adam Falkowski, and Nivedita Ghosh. Associated Z' production in the flavorful $U(1)$ scenario for $R_{K^{(*)}}$. *Eur. Phys. J.*, C80(3):263, 2020.
- [70] Zhi-Long Han, Ran Ding, Su-Jie Lin, and Bin Zhu. Gauged $U(1)_{L_\mu-L_\tau}$ scotogenic model in light of $R_{K^{(*)}}$ anomaly and AMS-02 positron excess. *Eur. Phys. J.*, C79(12):1007, 2019.
- [71] Bernat Capdevila, Andreas Crivellin, Claudio Andrea Manzari, and Marc Montull. Explaining $b \rightarrow s\ell^+\ell^-$ and the Cabibbo angle anomaly with a vector triplet. *Phys. Rev.*, D103(1):015032, 2021.

- [72] Wolfgang Altmannshofer, Joe Davighi, and Marco Nardecchia. Gauging the accidental symmetries of the Standard Model, and implications for the flavor anomalies. *Phys. Rev.*, D101(1):015004, 2020.
- [73] Shao-Long Chen, Amit Dutta Banik, Zhaofeng Kang, Qin Qin, and Yoshihiro Shigekami. Signatures of a flavor changing Z' boson in $B_q \rightarrow \gamma Z'$. *Nucl. Phys.*, B962:115237, 2021.
- [74] Alexandre Carvunis, Diego Guadagnoli, M eril Reboud, and Peter Stangl. Composite dark matter and a horizontal symmetry. *JHEP*, 02:056, 2021.
- [75] A. Karozas, G. K. Leontaris, I. Tavellaris, and N. D. Vlachos. On the LHC signatures of $SU(5) \times U(1)'$ F-theory motivated models. *Eur. Phys. J.*, C81(1):35, 2021.
- [76] Debasish Borah, Lopamudra Mukherjee, and Soumitra Nandi. Low scale $U(1)_X$ gauge symmetry as an origin of dark matter, neutrino mass and flavour anomalies. *JHEP*, 12:052, 2020.
- [77] B. C. Allanach. $U(1)_{B_3-L_2}$ explanation of the neutral current B -anomalies. *Eur. Phys. J.*, C81(1):56, 2021.
- [78] Jin-Huan Sheng. The analysis of $b \rightarrow s\ell^+\ell^-$ in the family non-universal Z' Model. *Int. J. Theor. Phys.*, 60(1):26–46, 2021.
- [79] Gudrun Hiller and Martin Schmaltz. R_K and future $b \rightarrow s\ell\ell$ physics beyond the Standard Model opportunities. *Phys. Rev.*, D90:054014, 2014.
- [80] Ben Gripaios, Marco Nardecchia, and S. A. Renner. Composite leptoquarks and anomalies in B -meson decays. *JHEP*, 05:006, 2015.
- [81] Ivo de Medeiros Varzielas and Gudrun Hiller. Clues for flavor from rare lepton and quark decays. *JHEP*, 06:072, 2015.
- [82] Riccardo Barbieri, Christopher W. Murphy, and Fabrizio Senia. B-decay anomalies in a composite leptoquark model. *Eur. Phys. J.*, C77(1):8, 2017.
- [83] Luca Di Luzio, Admir Greljo, and Marco Nardecchia. Gauge leptoquark as the origin of B-physics anomalies. *Phys. Rev. D*, 96(11):115011, 2017.

- [84] Andreas Crivellin, Dario Müller, and Toshihiko Ota. Simultaneous explanation of $R(D^{(*)})$ and $b \rightarrow s\mu^+\mu^-$: the last scalar leptoquarks standing. *JHEP*, 09:040, 2017.
- [85] Damir Bečirević and Olcyr Sumensari. A leptoquark model to accommodate $R_K^{\text{exp}} < R_K^{\text{SM}}$ and $R_{K^*}^{\text{exp}} < R_{K^*}^{\text{SM}}$. *JHEP*, 08:104, 2017.
- [86] Admir Greljo and Ben A. Stefanek. Third family quark–lepton unification at the TeV scale. *Phys. Lett. B*, 782:131–138, 2018.
- [87] Marzia Bordone, Claudia Cornella, Javier Fuentes-Martín, and Gino Isidori. Low-energy signatures of the PS3 model: from B-physics anomalies to LFV. *JHEP*, 10:148, 2018.
- [88] Bartosz Fornal, Sri Aditya Gadam, and Benjamin Grinstein. Left-right SU(4) vector leptoquark model for flavor anomalies. *Phys. Rev.*, D99(5):055025, 2019.
- [89] A. Angelescu, Damir Bečirević, D. A. Faroughy, and O. Sumensari. Closing the window on single leptoquark solutions to the B -physics anomalies. *JHEP*, 10:183, 2018.
- [90] Damir Bečirević, Ilja Doršner, Svjetlana Fajfer, Nejc Košnik, Darius A. Faroughy, and Olcyr Sumensari. Scalar leptoquarks from grand unified theories to accommodate the B -physics anomalies. *Phys. Rev. D*, 98(5):055003, 2018.
- [91] Shyam Balaji and Michael A. Schmidt. Unified SU(4) theory for the $R_{D^{(*)}}$ and $R_{K^{(*)}}$ anomalies. *Phys. Rev.*, D101(1):015026, 2020.
- [92] Claudia Cornella, Javier Fuentes-Martin, and Gino Isidori. Revisiting the vector leptoquark explanation of the B-physics anomalies. *JHEP*, 07:168, 2019.
- [93] Alakabha Datta, Divya Sachdeva, and John Waite. Unified explanation of $b \rightarrow s\mu^+\mu^-$ anomalies, neutrino masses, and $B \rightarrow \pi K$ puzzle. *Phys. Rev.*, D100(5):055015, 2019.
- [94] Oleg Popov, Michael A. Schmidt, and Graham White. R_2 as a single leptoquark solution to $R_{D^{(*)}}$ and $R_{K^{(*)}}$. *Phys. Rev.*, D100(3):035028, 2019.
- [95] Innes Bigaran, John Gargalionis, and Raymond R. Volkas. A near-minimal leptoquark model for reconciling flavour anomalies and generating radiative neutrino masses. *JHEP*, 10:106, 2019.

-
- [96] Jordan Bernigaud, Ivo de Medeiros Varzielas, and Jim Talbert. Finite family groups for fermionic and leptoquark mixing patterns. *JHEP*, 01:194, 2020.
- [97] Leandro Da Rold and Federico Lamagna. A vector leptoquark for the B -physics anomalies from a composite GUT. *JHEP*, 12:112, 2019.
- [98] Javier Fuentes-Martín, Mario Reig, and Avelino Vicente. Strong CP problem with low-energy emergent QCD: The 4321 case. *Phys. Rev.*, D100(11):115028, 2019.
- [99] C. Hati, J. Kriewald, J. Orloff, and A. M. Teixeira. A non-unitary interpretation for a single vector leptoquark combined explanation to the B -decay anomalies. *JHEP*, 12:006, 2019.
- [100] Alakabha Datta, Jonathan L. Feng, Saeed Kamali, and Jacky Kumar. Resolving the $(g - 2)_\mu$ and B anomalies with leptoquarks and a dark Higgs boson. *Phys. Rev.*, D101(3):035010, 2020.
- [101] Andreas Crivellin, Dario Müller, and Francesco Saturnino. Flavor phenomenology of the leptoquark singlet-triplet model. *JHEP*, 06:020, 2020.
- [102] Christoph Borschensky, Benjamin Fuks, Anna Kulesza, and Daniel Schwartzländer. Scalar leptoquark pair production at hadron colliders. *Phys. Rev.*, D101(11):115017, 2020.
- [103] Shaikh Saad. Combined explanations of $(g - 2)_\mu$, $R_{D^{(*)}}$, $R_{K^{(*)}}$ anomalies in a two-loop radiative neutrino mass model. *Phys. Rev.*, D102(1):015019, 2020.
- [104] Javier Fuentes-Martín and Peter Stangl. Third-family quark-lepton unification with a fundamental composite Higgs. *Phys. Lett.*, B811:135953, 2020.
- [105] P. S. Bhupal Dev, Rukmani Mohanta, Sudhanwa Patra, and Suchismita Sahoo. Unified explanation of flavor anomalies, radiative neutrino masses, and ANITA anomalous events in a vector leptoquark model. *Phys. Rev.*, D102(9):095012, 2020.
- [106] Bartosz Fornal. Gravitational wave signatures of lepton universality violation. *Phys. Rev.*, D103(1):015018, 2021.
- [107] Joe Davighi, Matthew Kirk, and Marco Nardecchia. Anomalies and accidental symmetries: charging the scalar leptoquark under $L_\mu - L_\tau$. *JHEP*, 12:111, 2020.

- [108] K. S. Babu, P. S. Bhupal Dev, Sudip Jana, and Anil Thapa. Unified framework for B -anomalies, muon $g - 2$ and neutrino masses. *JHEP*, 03:179, 2021.
- [109] Basabendu Barman, Debasish Borah, Lopamudra Mukherjee, and Soumitra Nandi. Correlating the anomalous results in $b \rightarrow s$ decays with inert Higgs doublet dark matter and muon ($g - 2$). *Phys. Rev.*, D100(11):115010, 2019.
- [110] Monika Blanke and Andreas Crivellin. B meson anomalies in a Pati-Salam model within the Randall-Sundrum background. *Phys. Rev. Lett.*, 121(1):011801, 2018.
- [111] Shao-Ping Li, Xin-Qiang Li, Ya-Dong Yang, and Xin Zhang. $R_{D^{(*)}}, R_{K^{(*)}}$ and neutrino mass in the 2HDM-III with right-handed neutrinos. *JHEP*, 09:149, 2018.
- [112] Avirup Shaw. Looking for $B \rightarrow X_s \ell^+ \ell^-$ in a nonminimal universal extra dimensional model. *Phys. Rev.*, D99(11):115030, 2019.
- [113] Pere Arnau, Andreas Crivellin, Marco Fedele, and Federico Mescia. Generic loop effects of new scalars and fermions in $b \rightarrow s \ell^+ \ell^-$ and a vector-like 4th generation. *JHEP*, 06:118, 2019.
- [114] Sokratis Trifinopoulos. B-physics anomalies: The bridge between R-parity violating supersymmetry and flavored dark matter. *Phys. Rev.*, D100(11):115022, 2019.
- [115] Luigi Delle Rose, Shaaban Khalil, Simon J. D. King, and Stefano Moretti. R_K and R_{K^*} in an aligned 2HDM with right-handed neutrinos. *Phys. Rev.*, D101(11):115009, 2020.
- [116] Astrid Ordell, Roman Pasechnik, Hugo Serôdio, and Franz Nottensteiner. Classification of anomaly-free 2HDMs with a gauged $U(1)'$ symmetry. *Phys. Rev.*, D100(11):115038, 2019.
- [117] Carlo Marzo, Luca Marzola, and Martti Raidal. Common explanation to the $R_{K^{(*)}}, R_{D^{(*)}}$ and ϵ'/ϵ anomalies in a 3HDM $+\nu_R$ and connections to neutrino physics. *Phys. Rev.*, D100(5):055031, 2019.
- [118] Luc Darmé, Marco Fedele, Kamila Kowalska, and Enrico Maria Sessolo. Flavour anomalies from a split dark sector. *JHEP*, 08:148, 2020.
- [119] Quan-Yi Hu and Lin-Lin Huang. Explaining $b \rightarrow s \ell^+ \ell^-$ data by sneutrinos in the R -parity violating MSSM. *Phys. Rev.*, D101(3):035030, 2020.

- [120] Quan-Yi Hu, Ya-Dong Yang, and Min-Di Zheng. Revisiting the B -physics anomalies in R -parity violating MSSM. *Eur. Phys. J.*, C80(5):365, 2020.
- [121] J. P. Lees et al. Evidence for an excess of $\bar{B} \rightarrow D^{(*)}\tau^-\bar{\nu}_\tau$ decays. *Phys. Rev. Lett.*, 109:101802, 2012.
- [122] R. Aaij et al. Measurement of the ratio of branching fractions $\mathcal{B}(B_c^+ \rightarrow J/\psi \tau^+ \nu_\tau)/\mathcal{B}(B_c^+ \rightarrow J/\psi \mu^+ \nu_\mu)$. *Phys. Rev. Lett.*, 120:121801, 2018.
- [123] J. P. Lees et al. Measurement of an excess of $\bar{B} \rightarrow D^{(*)}\tau^-\bar{\nu}_\tau$ decays and implications for charged Higgs bosons. *Phys. Rev.*, D88(7):072012, 2013.
- [124] Y. Sato et al. Measurement of the branching ratio of $\bar{B}^0 \rightarrow D^{*+}\tau^-\bar{\nu}_\tau$ relative to $\bar{B}^0 \rightarrow D^{*+}\ell^-\bar{\nu}_\ell$ decays with a semileptonic tagging method. *Phys. Rev.*, D94(7):072007, 2016.
- [125] R. Aaij et al. Measurement of the ratio of branching fractions $\mathcal{B}(\bar{B}^0 \rightarrow D^{*+}\tau^-\bar{\nu}_\tau)/\mathcal{B}(\bar{B}^0 \rightarrow D^{*+}\mu^-\bar{\nu}_\mu)$. *Phys. Rev. Lett.*, 115:111803, 2015.
- [126] M. Huschle et al. Measurement of the branching ratio of $\bar{B} \rightarrow D^{(*)}\tau^-\bar{\nu}_\tau$ relative to $\bar{B} \rightarrow D^{(*)}\ell^-\bar{\nu}_\ell$ decays with hadronic tagging at Belle. *Phys. Rev.*, D92(7):072014, 2015.
- [127] R. Aaij et al. Test of lepton flavor universality by the measurement of the $B^0 \rightarrow D^{*-}\tau^+\nu_\tau$ branching fraction using three-prong τ decays. *Phys. Rev.*, D97:072013, 2018.
- [128] G. Caria et al. Measurement of $\mathcal{R}(D)$ and $\mathcal{R}(D^*)$ with a semileptonic tagging method. *Phys. Rev. Lett.*, 124(16):161803, 2020.
- [129] S. Hirose et al. Measurement of the τ lepton polarization and $R(D^*)$ in the decay $\bar{B} \rightarrow D^*\tau^-\bar{\nu}_\tau$ with one-prong hadronic τ decays at Belle. *Phys. Rev.*, D97(1):012004, 2018.
- [130] R. Aaij et al. Test of lepton universality using $B^+ \rightarrow K^+\ell^+\ell^-$ decays. *Phys. Rev. Lett.*, 113:151601, 2014.
- [131] M. Ablikim et al. Precision measurements of $\mathcal{B}[\psi(3686) \rightarrow \pi^+\pi^-J/\psi]$ and $\mathcal{B}[J/\psi \rightarrow \ell^+\ell^-]$. *Phys. Rev.*, D88(3):032007, 2013.

- [132] Alexander Khodjamirian and Aleksey V. Rusov. $B_s \rightarrow K\ell\nu_\ell$ and $B_{(s)} \rightarrow \pi(K)\ell^+\ell^-$ decays at large recoil and CKM matrix elements. *JHEP*, 08:112, 2017.
- [133] Wolfgang Altmannshofer and Itay Yavin. Predictions for lepton flavor universality violation in rare B decays in models with gauged $L_\mu - L_\tau$. *Phys. Rev.*, D92(7):075022, 2015.
- [134] Li-Sheng Geng, Benjamín Grinstein, Sebastian Jäger, Jorge Martin Camalich, Xiu-Lei Ren, and Rui-Xiang Shi. Towards the discovery of new physics with lepton-universality ratios of $b \rightarrow s\ell\ell$ decays. *Phys. Rev.*, D96(9):093006, 2017.
- [135] R. Aaij et al. Search for the decays $B_s^0 \rightarrow \tau^+\tau^-$ and $B^0 \rightarrow \tau^+\tau^-$. *Phys. Rev. Lett.*, 118:251802, 2017.
- [136] J. P. Lees et al. Search for $B^+ \rightarrow K^+\tau^+\tau^-$ at the BaBar experiment. *Phys. Rev. Lett.*, 118(3):031802, 2017.
- [137] Physics case for an LHCb Upgrade II — Opportunities in flavour physics, and beyond, in the HL-LHC era. (CERN-LHCC-2018-027 LHCb-PUB-2018-009), 2018.
- [138] W. Altmannshofer et al. The Belle II physics book. *PTEP*, 2019(12):123C01, 2019.
- [139] R. Bainbridge, on behalf of the CMS collaboration. Recording and reconstructing 10 billion unbiased b hadron decays in CMS. *EPJ Web Conf.*, 245:01025, 2020.
- [140] G. Aad et al. Performance of the ATLAS Level-1 topological trigger in Run 2. 2021.
- [141] A. A. Alves Jr. et al. The LHCb detector at the LHC. *JINST*, 3:S08005, 2008.
- [142] R. Aaij et al. LHCb detector performance. *Int. J. Mod. Phys.*, A30:1530022, 2015.
- [143] R. Aaij et al. Performance of the LHCb Vertex Locator. *JINST*, 9:P09007, 2014.
- [144] R. Arink et al. Performance of the LHCb Outer Tracker. *JINST*, 9:P01002, 2014.
- [145] F. Archilli et al. Performance of the muon identification at LHCb. *JINST*, 8:P10020, 2013.

-
- [146] M. Adinolfi et al. Performance of the LHCb RICH detector at the LHC. *Eur. Phys. J.*, C73:2431, 2013.
- [147] A A Alves Jr. et al. Performance of the LHCb muon system. *JINST*, 8:P02022, 2013.
- [148] V. V. Gligorov and M. Williams. Efficient, reliable and fast high-level triggering using a bonsai boosted decision tree. *JINST*, 8:P02013, 2013.
- [149] T. Likhomanenko et al. LHCb topological trigger reoptimization. *J. Phys. Conf. Ser.*, 664:082025, Oct 2015.
- [150] L. Breiman, J. H. Friedman, R. A. Olshen, and C. J. Stone. *Classification and regression trees*. Wadsworth international group, Belmont, California, USA, 1984.
- [151] Peter J. Huber. *Robust estimation of a location parameter*, page 492. Springer New York, New York, NY, 1992.
- [152] Avrim Blum, Adam Kalai, and John Langford. Beating the hold-out: bounds for k-fold and progressive cross-validation. In *Proceedings of the twelfth annual conference on computational learning theory*, COLT '99, page 203, New York, NY, USA, 1999. ACM.
- [153] Torbjörn Sjöstrand, Stephen Mrenna, and Peter" Skands. PYTHIA 6.4 physics and manual. *JHEP*, 05:026, 2006.
- [154] Torbjörn Sjöstrand, Stephen Mrenna, and Peter" Skands. A brief introduction to PYTHIA 8.1. *Comput. Phys. Commun.*, 178:852–867, 2008.
- [155] I. Belyaev et al. Handling of the generation of primary events in Gauss, the LHCb simulation framework. *J. Phys. Conf. Ser.*, 331:032047, 2011.
- [156] D. J. Lange. The EvtGen particle decay simulation package. *Nucl. Instrum. Meth.*, A462:152–155, 2001.
- [157] John Allison, K. Amako, J. Apostolakis, H. Araujo, P.A. Dubois, et al. Geant4 developments and applications. *IEEE Trans.Nucl.Sci.*, 53:270, 2006.
- [158] S. Agostinelli et al. Geant4: A simulation toolkit. *Nucl. Instrum. Meth.*, A506:250, 2003.
- [159] M Clemencic et al. The LHCb simulation application, Gauss: Design, evolution and experience. *J. Phys. Conf. Ser.*, 331:032023, 2011.

-
- [160] N. Davidson, T. Przedzinski, and Z. Was. PHOTOS interface in C++: Technical and physics documentation. *Comput. Phys. Commun.*, 199:86–101, 2016.
- [161] Roel Aaij et al. Measurement of the electron reconstruction efficiency at LHCb. *JINST*, 14:P11023, 2019.
- [162] Tomasz Skwarnicki. *A study of the radiative cascade transitions between the Upsilon-prime and Upsilon resonances*. PhD thesis, Institute of Nuclear Physics, Krakow, 1986. DESY-F31-86-02.
- [163] Diego Martínez Santos and Frédéric Dupertuis. Mass distributions marginalized over per-event errors. *Nucl. Instrum. Meth.*, A764:150–155, 2014.
- [164] R. Aaij et al. Differential branching fraction and angular analysis of the decay $B^0 \rightarrow K^+ \pi^- \mu^+ \mu^-$ in the $K_{0,2}^*(1430)^0$ region. *JHEP*, 12:065, 2016.
- [165] R. Aaij et al. Measurement of the ratio of branching fractions and difference in CP asymmetries of the decays $B^+ \rightarrow J/\psi \pi^+$ and $B^+ \rightarrow J/\psi K^+$. *JHEP*, 03:036, 2017.
- [166] Jon A. Bailey et al. $B \rightarrow Kl^+l^-$ decay form factors from three-flavor lattice QCD. *Phys. Rev.*, D93:025026, 2016.
- [167] Daping Du, A. X. El-Khadra, Steven Gottlieb, A. S. Kronfeld, J. Laiho, E. Lunghi, R. S. Van de Water, and Ran Zhou. Phenomenology of semileptonic B-meson decays with form factors from lattice QCD. *Phys. Rev.*, D93(3):034005, 2016.

Appendix 3.A Appendix to Chapter 3

Appendix 3.B Branching fraction measurements

The comparison of the $B^+ \rightarrow K^+ \mu^+ \mu^-$ branching fraction from Ref. [37] to the $B^+ \rightarrow K^+ e^+ e^-$ branching fraction resulting from the measurement of R_K presented in this paper is shown in Fig. 3.11. The uncertainty stemming from the branching fractions of the corresponding normalisation channels is folded into the total uncertainty of each measurement.

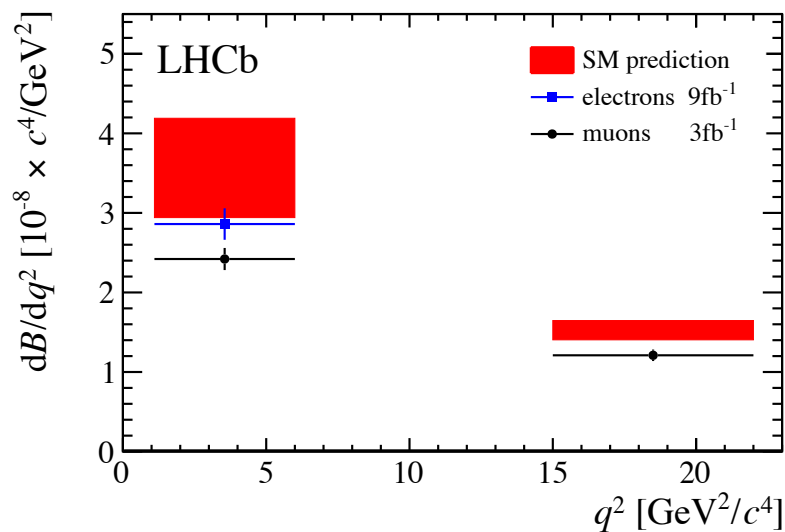


Fig. 3.11 Branching fractions of (blue) $B^+ \rightarrow K^+ e^+ e^-$ from this paper and (black) $B^+ \rightarrow K^+ \mu^+ \mu^-$ from Ref. [37] including the q^2 bin $15.0 < q^2 < 22.0 \text{ GeV}^2/c^4$. The SM predictions (red area) from Refs. [166,167] are also shown.

Appendix 3.C Fits to the $B^+ \rightarrow \psi(2S)K^+$ resonant mode

The fits to the resonant $B^+ \rightarrow \psi(2S)K^+$ decay mode in different data-taking periods and trigger categories are shown in Fig. 3.12. The strong correlation between the combinatorial background and the partially reconstructed decays from higher charmonium resonances causes the variation of the fitted mass shapes across data-taking periods and trigger categories. However, this has a negligible effect on the signal yield extraction as the sum of the two contributions is constant across data-taking periods and trigger categories.

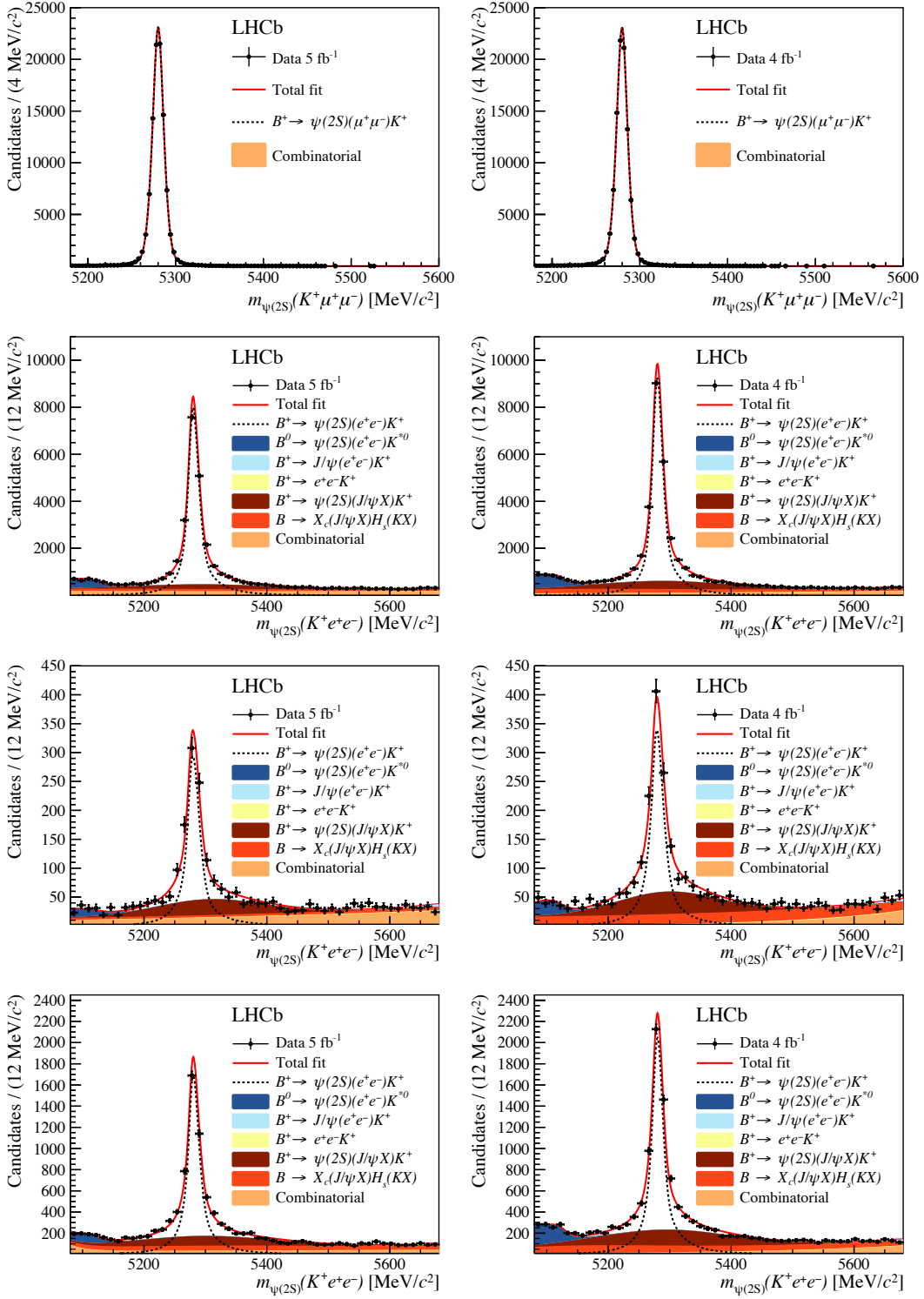


Fig. 3.12 Candidate invariant mass distributions. Distribution of the invariant mass $m_{\psi(2S)}(K^+ \ell^+ \ell^-)$ for $B^+ \rightarrow \psi(2S)K^+$ resonant candidates in the (left) sample previously analysed [11] and (right) the new data sample. The top row shows the fit to the muon modes, the combinatorial component is included in the fit but is too small to be seen. The subsequent rows show the fits to the electron modes triggered by (second row) one of the electrons, (third row) the kaon and (last row) by other particles in the event. The fit projections are superimposed.

Appendix 3.D Effect of q^2 migration

Due to the finite resolution in q^2 , signal candidates with a true q^2 (q_{true}^2) outside the interval of interest can be reconstructed with $1.1 < q^2 < 6.0 \text{ GeV}^2/c^4$. The contribution from $B^+ \rightarrow K^+e^+e^-$ candidates that undergo this q^2 migration is shown in Fig. 3.13 for simulation and Fig. 3.14 for data.

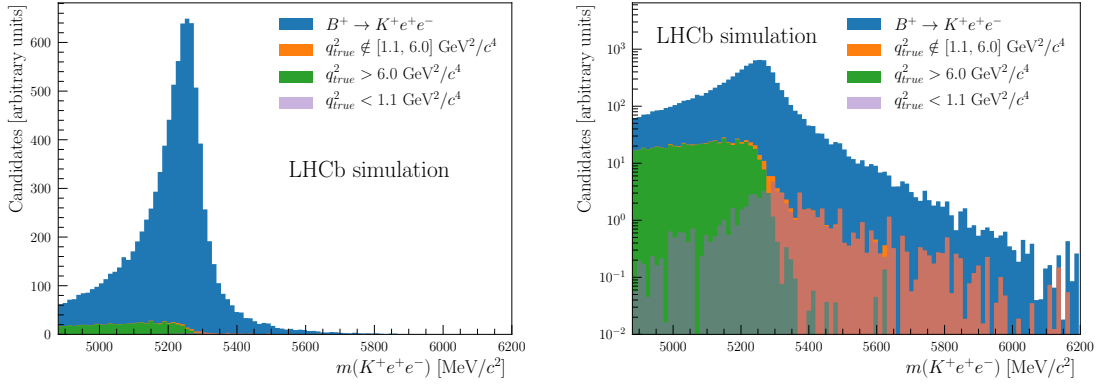


Fig. 3.13 Distribution of $m(K^+e^+e^-)$ in simulated $B^+ \rightarrow K^+e^+e^-$ decays. The orange shaded area corresponds to $B^+ \rightarrow K^+e^+e^-$ candidates with true q^2 outside the interval of interest. The green and purple components correspond to candidates with $q_{\text{true}}^2 > 6.0 \text{ GeV}^2/c^4$ and $q_{\text{true}}^2 < 1.1 \text{ GeV}^2/c^4$, respectively. (Left) linear and (right) logarithmic scales are shown.

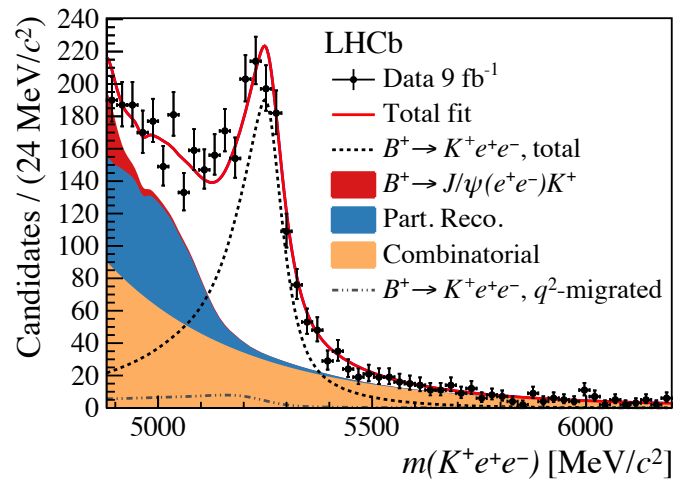


Fig. 3.14 Distribution of the invariant mass $m(K^+e^+e^-)$ for $B^+ \rightarrow K^+e^+e^-$ candidates. The fit projection is superimposed, with a black dotted line describing the signal contribution and solid areas representing each of the background components described in the text and listed in the legend. For illustration, the expected distribution of signal candidates with $q_{\text{true}}^2 < 1.1 \text{ GeV}^2/c^4$ or $q_{\text{true}}^2 > 6.0 \text{ GeV}^2/c^4$ is shown as a grey dashed and dotted line.

Appendix 3.E Overview of R_K measurements

An overview of available measurements of R_K in different q^2 regions is given in Fig 3.15. Previous LHCb measurements are also included for comparison in Fig 3.16 and Fig 3.17.

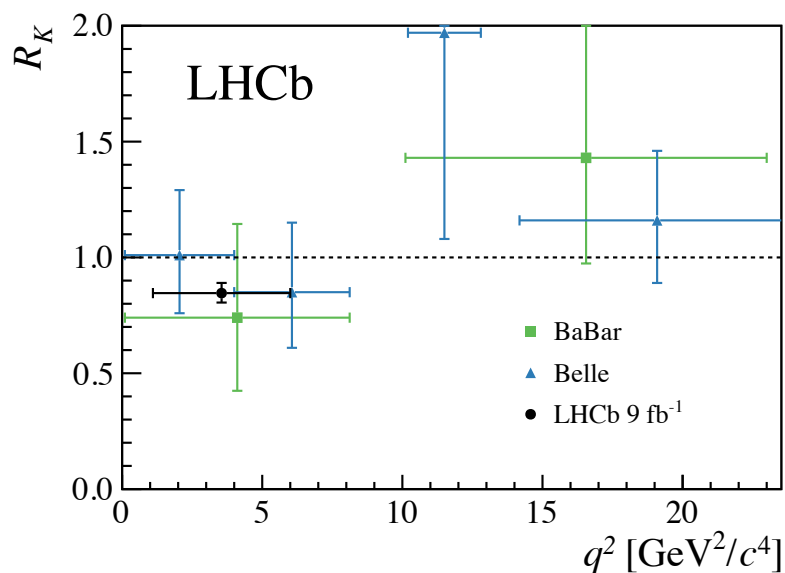


Fig. 3.15 Comparison between R_K measurements. The measurements by the BaBar [15] and Belle [13] collaborations combine $B^+ \rightarrow K^+ \ell^+ \ell^-$ and $B^0 \rightarrow K_s^0 \ell^+ \ell^-$ decays.

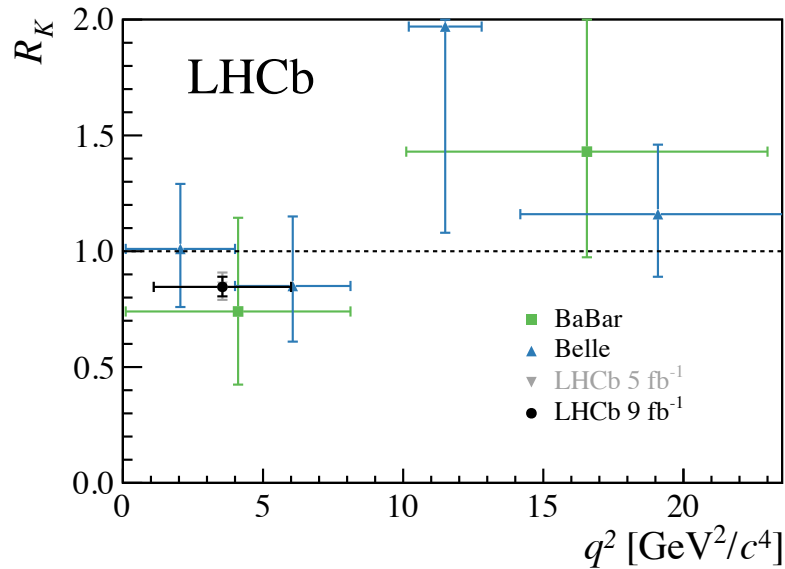


Fig. 3.16 Comparison between R_K measurements. The measurements by the BaBar [15] and Belle [13] collaborations combine $B^+ \rightarrow K^+ \ell^+ \ell^-$ and $B^0 \rightarrow K_S^0 \ell^+ \ell^-$ decays. The previous LHCb measurement [11], superseded by the present result, is also shown.

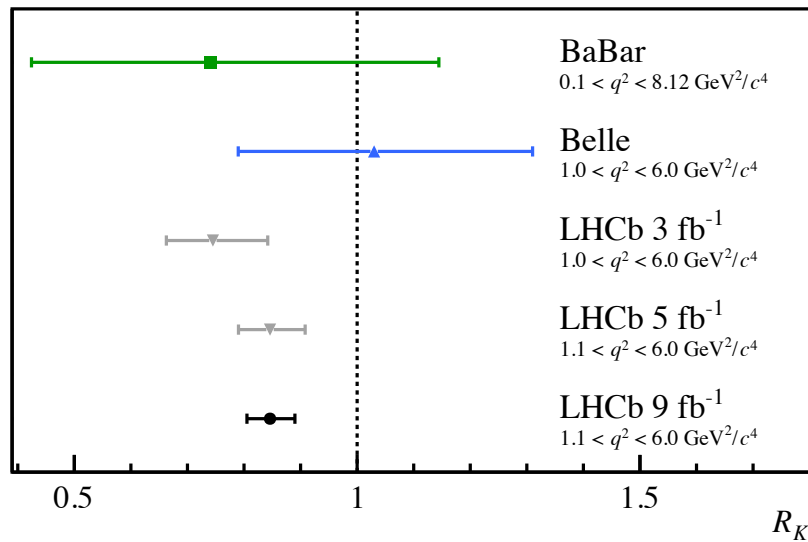


Fig. 3.17 Comparison between R_K measurements. The measurements by the BaBar [15] and Belle [13] collaborations combine $B^+ \rightarrow K^+ \ell^+ \ell^-$ and $B^0 \rightarrow K_S^0 \ell^+ \ell^-$ decays. The previous LHCb measurements [11] and [130], superseded by the present result, are also shown.

Chapter 4

On the significance of new physics in $b \rightarrow s\ell^+\ell^-$ decays

4.1 Introduction

Since 2013, several measurements have shown deviations from Standard Model (SM) predictions in rare b -hadron decays controlled by the underlying quark-level transition $b \rightarrow s\ell^+\ell^-$ ($\ell = e, \mu$) [1–10]. The latest of these measurements provides the first evidence of a violation of Lepton Flavor Universality (LFU) in a single process [11].

While there is no single result exhibiting a 5σ deviation from the SM, the pattern of deviations, collectively denoted as the $b \rightarrow s\ell^+\ell^-$ *anomalies*, is striking. In order to guide future activities in this field, and possibly claim a discovery, it is essential to determine the combined statistical significance of these anomalies in a robust way. This is the purpose of this paper.

The first point to clarify is the alternative hypothesis that we aim to test with respect to the SM. The scope of this paper is to test in general terms the hypothesis of a new *short-distance* interaction connecting the b and s quarks with a dilepton pair. By short-distance we mean a NP interaction which appears as a local interaction in b -hadron decays. This general hypothesis, which is well justified by the absence of non-SM particles observed so far at colliders, allows us to describe $b \rightarrow s\ell^+\ell^-$ transitions using the general formalism of effective Lagrangians, encoding a hypothetical NP contribution via appropriate four-fermion operators. This description, which is conceptually similar to Fermi's theory of beta decays [12], allows to consider each specific b -hadron decay of interest as a different way to probe the same underlying $b \rightarrow s\ell^+\ell^-$ short-distance interaction.

The hypothesis of NP effects in $b \rightarrow s\ell^+\ell^-$ transitions of short-distance origin was formulated first in Ref. [13]. Later on several theory groups have analysed these processes within the framework of effective Lagrangians (see e.g. Ref. [14–27]). These analyses provided fits of the coefficients of well-defined sets of four-fermion operators, the so-called Wilson Coefficients (WCs), obtaining significances that in the last few years largely exceed the 5σ level [25–27]. While these results are interesting and highly valuable, they do not provide the robust and general estimate of the significance we aim for. Our goal is not obtaining the best fit values of the WCs, which is the main goal of these previous studies, but rather estimating the significance of the NP hypothesis irrespective of its specific structure.

Most of the WC fits quoted in the literature are obtained by varying a small number of WCs, typically one or two. While this approach is well suited to test specific (often well motivated) NP hypotheses, and to determine the values of the WCs in these frameworks, it does not provide an unbiased estimate of the significance of the NP hypothesis. As we clarify below, the significance thus obtained resembles the *local significance* in resonance searches. The concern lies in the fact that several measurements are performed but only a few exhibit deviations with respect to the SM, corresponding to well-defined sets of WCs. It should also be stressed that the WC basis is a purely conventional choice: if a given correlation emerges from data in a two-parameter fit, one can change the basis and perform a fit with apparently higher significance enforcing such correlation via the basis choice and using a single parameter.

Overestimating the significance of a subset of measurements is equivalent to the *look-elsewhere effect* (LEE) in searches for new resonances [28–30]. While there is a small probability to observe a $n\sigma$ statistical fluctuation in a given bin of a distribution where the resonance could appear (local p-value), when several bins are measured the probability that at least one of them deviates by $n\sigma$ is larger (global p-value). When searching for a new resonance with unknown mass, the LEE can be addressed by calculating a trial-factor with an ensemble of pseudo-experiments [30–32], which is the ratio of the global and local p-values. Conceptually, this is the same approach we adopt in this paper: We estimate the significance of the NP hypothesis in real data via pseudo-experiments. The trial-factor is then due to alternative deviations which could have emerged in a hypothetical dataset with the same experimental precision.

There are fits in the literature that use a large number of WCs and a rather general NP hypothesis [14,25,33]. In particular, Ref. [33] fits all possible WC directions and therefore does not suffer from the LEE. The issue in this case is not the number of WCs

but the effective number of degrees of freedom in the system, which depends on the correlations between WCs and the observables that are accessible to the experiments. Using pseudo-experiments is an efficient method to eliminate flat directions in the space of WCs and can easily account for many experimental details such as non-Gaussian uncertainties and correlated systematics.

As far as theoretical uncertainties are concerned, the main concern are non-local contributions due to intermediate charm states. This subject has been widely discussed in the literature [34–38,37,39–45]. As a conservative choice, we simply disregard the extraction of short-distance information on amplitudes which might receive such non-local contributions.

Summarizing, the approach we propose to determine the statistical significance of NP in $b \rightarrow s\ell^+\ell^-$ transitions is based on the following points:

- We consider the short-distance $b \rightarrow s\ell^+\ell^-$ transition as a unique process constrained by different decay channels.
- We describe NP effects in $b \rightarrow s\ell^+\ell^-$ transitions using the most general effective Lagrangian compatible with the hypothesis of an effective local interaction.
- We estimate the trial-factor via an ensemble of pseudo-experiments generated according to the SM hypothesis and using the likelihood ratio as the test statistic.
- We adopt a highly-conservative attitude towards theory uncertainties, particularly in the case of non-local charm contributions.

This method allows us to evaluate the probability to observe the numerical coherence that is seen in data by chance. Only coherent deviations with respect to the SM can give a large value of the test statistic. All possible deviations in both the measurements and Wilson coefficients are considered. Therefore, this method evaluates the *global significance* of the $b \rightarrow s\ell^+\ell^-$ anomalies for the first time.

4.2 Effective Lagrangian and selection of the observables

In the limit where we assume no new particles below the electroweak scale, we can describe $b \rightarrow s\ell^+\ell^-$ transitions by means of an effective Lagrangian containing only light SM fields. The only difference between SM and effective Lagrangians, renormalized at a scale $\mu \sim m_b$, is the number of effective operators, which can be larger in the NP

case. To describe all the relevant non-standard local contributions, we add to the SM effective Lagrangian

$$\Delta\mathcal{L}_{\text{NP}}^{b \rightarrow s\ell\ell} = \frac{4G_F}{\sqrt{2}} \sum_i C_i \mathcal{O}_i + \text{h.c.}, \quad (4.1)$$

where G_F denotes the Fermi constant, and where the index i indicates the following set of dimension-six operators (treated independently for $\ell = e$ and μ):

$$\begin{aligned} \mathcal{O}_9^\ell &= (\bar{s}_L \gamma_\mu b_L)(\bar{\ell} \gamma^\mu \ell), & \mathcal{O}_{10}^\ell &= (\bar{s}_L \gamma_\mu b_L)(\bar{\ell} \gamma^\mu \gamma_5 \ell), \\ \mathcal{O}_9^{\ell'} &= (\bar{s}_R \gamma_\mu b_R)(\bar{\ell} \gamma^\mu \ell), & \mathcal{O}_{10}^{\ell'} &= (\bar{s}_R \gamma_\mu b_R)(\bar{\ell} \gamma^\mu \gamma_5 \ell), \\ \mathcal{O}_{\hat{S}}^\ell &= (\bar{s}_L b_R)(\bar{\ell}_R \ell_L), & \mathcal{O}_{\hat{S}}^{\ell'} &= (\bar{s}_R b_L)(\bar{\ell}_L \ell_R). \end{aligned} \quad (4.2)$$

As shown in [46], these operators are in one-to-one correspondence with the independent combinations of dimension-six operators involving b , s and lepton fields in the complete basis of dimension-six operators invariant under the SM gauge group.

We do not include in the list (5.4) the dipole operators, $\mathcal{O}_7^{(\prime)}$, for two reasons: these do not describe a $b \rightarrow s\ell^+\ell^-$ local interaction and they are well constrained by $\Gamma(B \rightarrow X_s \gamma)$ and $\Gamma(B \rightarrow K^* \gamma)$.¹

The four scalar operators in (5.4) lead to $b \rightarrow s\ell^+\ell^-$ amplitudes which are helicity suppressed. We thus restrict the attention to the single effective combination which contributes to the $B_s^0 \rightarrow \mu^+\mu^-$ helicity-suppressed rate. Finally, in the absence of stringent experimental constraints on CP-violating observables, we treat the NP WCs as real parameters.² According to these general hypotheses, NP effects in $b \rightarrow s\ell^+\ell^-$ transitions are described in full generality by nine real parameters. As far as $C_{9,10}^{e,\mu}$ are concerned, it is convenient to separate universal and non-universal corrections in lepton flavor, defining

$$\begin{aligned} C_i^e &= C_i^{\text{SM}} + \Delta C_i^U, \\ C_i^\mu &= C_i^{\text{SM}} + \Delta C_i^U + \Delta C_i^\mu. \end{aligned} \quad (4.3)$$

Adopting a conservative attitude toward theoretical uncertainties, we restrict the attention to the following three sets of observables: i) the LFU ratios R_K [11] and R_{K^*} [5], ii) the branching ratio for the rare dilepton mode $B_s^0 \rightarrow \mu^+\mu^-$ [3,6,7,47] and, iii) the normalized angular distribution in $B^0 \rightarrow K^{*0}\mu^+\mu^-$ decays [9,10]. As

¹An explicit quantification of the change of the significance when $C_7^{(\prime)}$ are also varied, taking into account their *a priori* knowledge before any LHCb measurements, is presented in Section IV.

²This statement refers to the standard quark-phase convention, where the WCs are approximately real also in the SM. Imaginary contributions to the WCs would not interfere with the SM amplitude and cannot induce large deviations from the SM in CP-conserving observables.

the measurements in class i) and ii) are statistically dominated, they are treated as uncorrelated whereas the full experimental correlation matrix given in Ref [9] is used for the $B \rightarrow K^* \mu^+ \mu^-$ angular observables.

By construction, the observables in class i) and ii) are insensitive to form-factor and decay constant uncertainties (except for f_{B_0} in class ii) as well as non-local charm contributions. The latter induce contributions to the decay amplitudes that can effectively be described via the shift

$$\Delta C_9^U \rightarrow \Delta C_9^U + f_{B \rightarrow f}^{c\bar{c}}(q^2) \quad (4.4)$$

where q^2 denotes the squared dilepton invariant mass. The absence of a completely reliable estimate of the theoretical uncertainty on the function $f_{B \rightarrow f}^{c\bar{c}}$, in particular on its normalization at $q^2 = 0$, forces us to treat the determination of ΔC_9^U as SM nuisance parameter³ and ignore the information from exclusive decay rates or dilepton spectra. This way we automatically remove most of the uncertainties associated to the hadronic form factors: a choice that maybe seen as too conservative, but that certainly does not lead to overestimate the NP significance.

The only observable with a residual form-factor uncertainty we retain is the $B^0 \rightarrow K^{*0} \mu^+ \mu^-$ angular distribution. We keep it since this distribution is sensitive to non-standard effects in short-distance operators other than \mathcal{O}_9^μ , even if we marginalise over ΔC_9^U . To reduce the form-factor uncertainty we make use of the P_i observables [48]. We explicitly checked that consistent results are obtained using the S_i observables [49], employing the form-factor parameterization in [50].

The set of nine parameters discussed above provides an unbiased description of heavy NP contributions to $b \rightarrow s \ell^+ \ell^-$ transitions. In order to evaluate the impact of motivated, but more specific theoretical assumptions, we also define a reduced set of WCs based on the hypotheses of small flavor-violating effects in the right-handed sector. According to this hypothesis, $C_i^{\ell\ell} \approx 0$ and the set of independent WCs is reduced to five operators. This hypothesis follows from the general assumption of a minimally broken $U(2)^3$ flavor symmetry: A general property of SM extensions which was proposed in [51] well before the observation of the $b \rightarrow s \ell^+ \ell^-$ anomalies, motivated by the stringent constraints on right-handed quark flavor mixing especially in the kaon system (see e.g. [52]).

³If we were to include more channels potentially affected by non-local charm contributions, we would need to treat the determination of ΔC_9^U from each channel as an independent nuisance parameter.

4.3 Statistical Method

To evaluate the significance of the NP hypothesis in the $b \rightarrow s\ell^+\ell^-$ system we use

$$\Delta\chi^2 = -2 \log \frac{\mathcal{L}(X|\Delta\hat{C}_9^U, C_i^{\text{SM}})}{\mathcal{L}(X|\hat{C}_i)} \quad (4.5)$$

as the test statistic. The trial-factor is calculated with a similar technique as described in Ref. [30–32]. Starting from SM predictions, a large number of pseudo-experiments are generated, varying the measurements according to the experimental uncertainty. For each simulated experiment, the full set of WCs (C_i) is fitted and the $\Delta\chi^2$ between the best fit (\hat{C}_i) and the SM prediction ($\Delta\hat{C}_9^U, C_i^{\text{SM}}$) is calculated. Data are fitted in the same way as pseudo-experiments and the distribution of $\Delta\chi^2$ is used to calculate the p-value. The software package *Flavio* [53] is used to fit WCs.

One of the interesting features of the $b \rightarrow s\ell^+\ell^-$ anomalies is that they can be easily explained with only one WC: $C_{LL}^\mu = \Delta C_9^\mu - \Delta C_{10}^\mu$. While this makes the NP hypothesis easy to interpret from the theory point of view, it is not the best way to assess the sensitivity with respect to the SM. To illustrate this point we apply our method to the fit of one or two WCs. In Fig. 4.1, the $\Delta\chi^2$ distribution under the SM hypothesis is shown when the one/two WCs which maximise the likelihood are chosen to fit the data: For each pseudo-experiment, we fit every single possible one/two WC combination and choose the largest test statistic. The blue curve is an empirical function that best describes the distribution. The comparison with a χ^2 distribution with one/two degrees of freedom demonstrates that a sizeable trial-factor is present. Taking for instance a hypothetical 4σ discrepancy when fitting the best one/two WCs, it would be diluted down to $3.7/3.5\sigma$ with a trial-factor equal to $4.1/7.0$, respectively. Since the current best scenarios to explain the anomalies with NP in C_{LL}^ℓ or in C_9 and C_{10} have emerged from the data, using this hypotheses to evaluate the NP significance can lead to overestimates.

As discussed in Sec. 4.2, we advocate the full set of nine WCs to be used if we would like to have an agnostic approach to NP. However, the full set of WCs contains redundancy, which makes the fit unstable. For instance, the deviations in R_K and R_K^* can be explained with non zero values of C_{LL}^μ or non-zero values of $C_{RL}^\mu = C_9^\mu - C_{10}^\mu$. Here we are not interested in interpreting the best NP direction and we therefore treat all of these in the same way. In total, the maximum number of WCs that can be fitted is seven, with the full basis of muonic operators, the single effective combination of scalar operators, and two electronic operators. Each pseudo-experiment is fitted

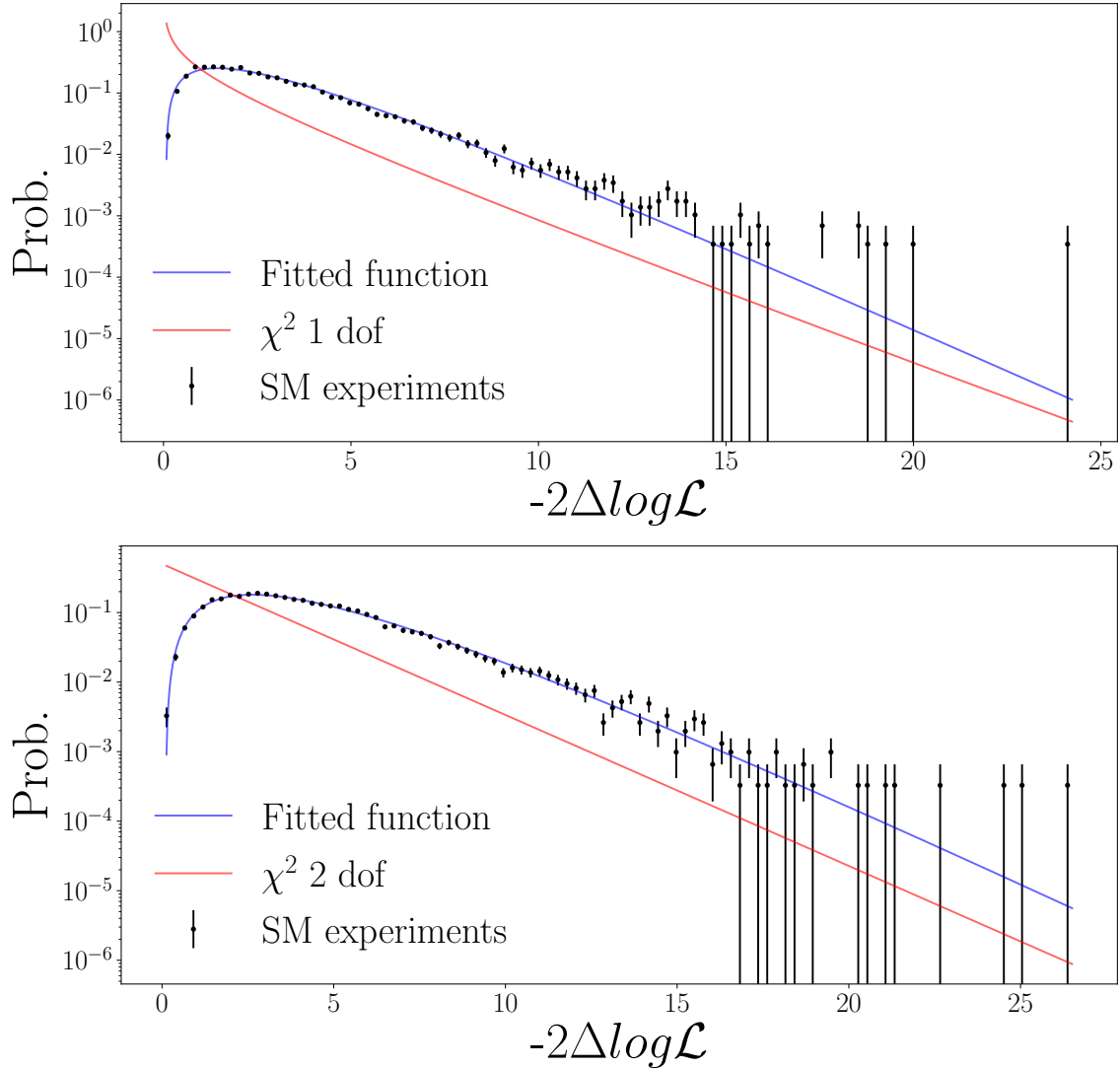


Fig. 4.1 $\Delta\chi^2$ distribution extracted from pseudo-experiments (blue) for fitting the best one/two WCs varying the SM, compared to the theoretical χ^2 distribution with one/two degrees of freedom (red).

six times, with all possible combinations of seven WCs. For each experiment, the largest test-statistic value is used. Adding redundant directions will not improve the χ^2 of a given pseudo-experiment, since there are not enough sensitive measurements to constrain simultaneously all nine WCs.

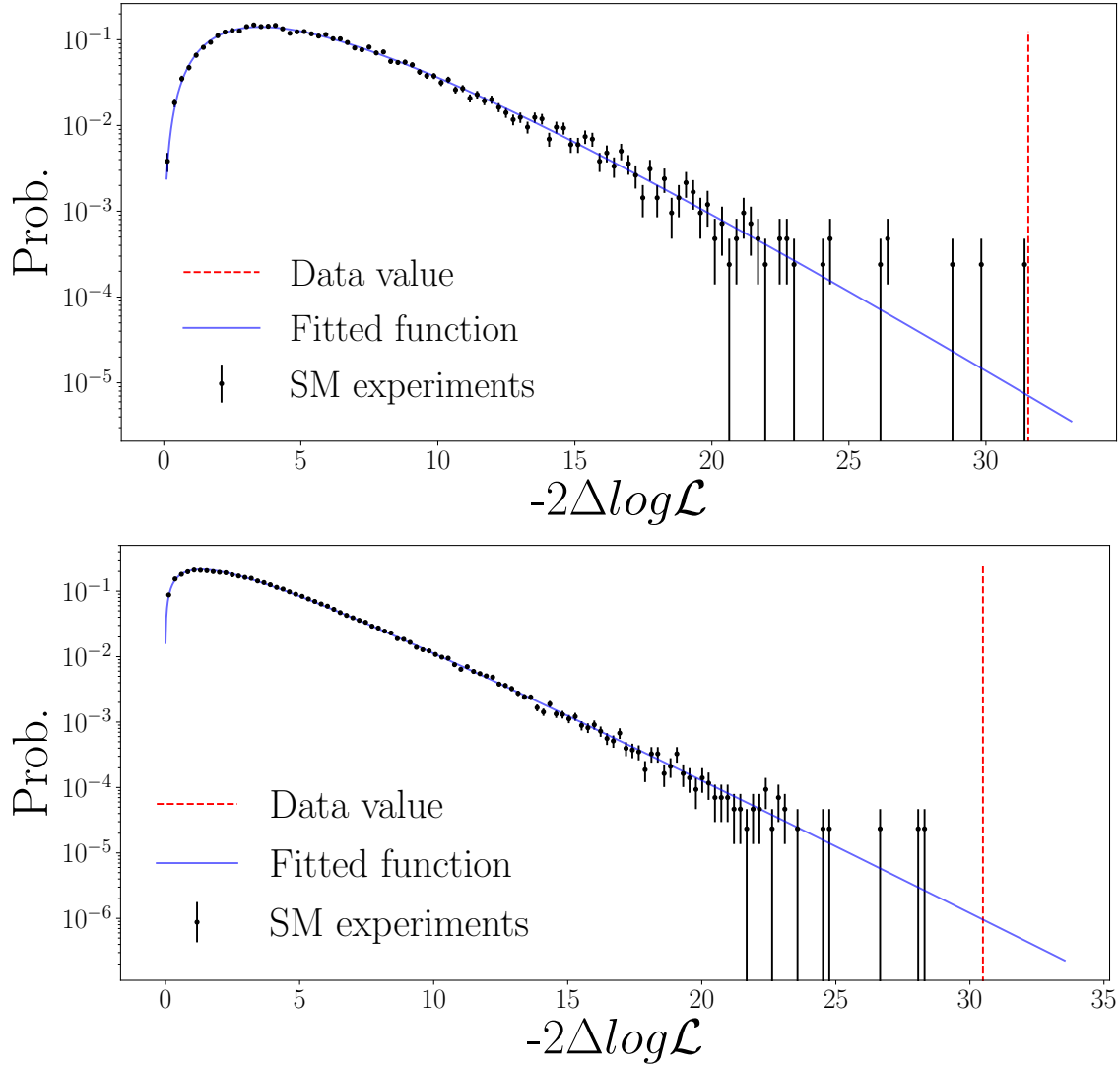


Fig. 4.2 $\Delta\chi^2$ distribution (blue) for SM pseudo-experiments in the general 9 WC fit basis (top) and the reduced 5 WC basis (bottom). The data is shown as a vertical red line on the plot.

4.4 Results

The $\Delta\chi^2$ distribution for the fit to the full set of Wilson coefficients is shown in Fig. 4.2 (top). The same procedure is then used in data, obtaining a $\Delta\chi^2 = 31.4$, which corresponds to a global significance of 4.3σ . As expected, the large $\Delta\chi$ value arises mostly due to the discrepancies with respect to the SM in the LFU ratios, R_K and R_K^* . The goodness of fit to data can be computed by calculating the p-value of the absolute χ^2 of the best fit. This results in a 11% p-value, which is acceptable. The largest pulls of the best fit with respect to the measurements come from the lowest q^2 bins of the

angular observables in the $B^0 \rightarrow K^{*0} \mu^+ \mu^-$ decays. This is a known issue [54] and has a small impact on the significance. Eliminating the lowest q^2 bin of all the angular observables decreases the $\Delta\chi^2$ by only one unit and the fit quality of the fit improves, leading to a p-value associated to the absolute χ^2 of 24%.

While the $C_7^{(\prime)}$ WCs do not describe $b \rightarrow s\ell\ell$ contact interactions and are not included in the default analysis, we investigated the impact of adding them to the set of WCs we allow to be affected by NP. Imposing constraints on $C_7^{(\prime)}$ prior to the flavour anomalies from Ref [55] and including the angular analysis of $B^0 \rightarrow K^* e^+ e^-$ from Ref [56], the total significance marginally decreases, as expected, from 4.3σ to 4.2σ .

Here we advocate that for claiming a discovery, the NP significance should be calculated using an agnostic approach. However, as discussed in Sec. 4.2, there were good *a-priori* theoretical reasons to assume no NP in $C_{9,10}^{\ell\prime}$. To evaluate the significance of this hypothesis we apply our method to the reduced set of five WCs. The $\Delta\chi^2$ distribution is shown in Fig. 4.2 (bottom)⁴. Applying the same fit to data we obtain a $\Delta\chi^2 = 30.5$, which integrating the distribution corresponds to a significance of 4.7σ . Interestingly, this is similar to the values quoted in the recent literature [57–59] for single-parameter fits of theoretically clean observables only. Having a larger number of free parameters, one could have expected a lower significance in our case. However, in this specific case the LEE effect is compensated by two facts: i) the inclusion of the angular distribution of the $B \rightarrow K^* \mu^+ \mu^-$ decay which, even after marginalizing over ΔC_9^U , retains some sensitivity to the other WCs; ii) the overall higher $\Delta\chi^2$ obtained with more parameters. This observation reinforces the high significance of the $b \rightarrow s\ell^+\ell^-$ anomalies in motivated NP models.

4.5 Conclusion and discussion

In conclusion, we have presented a method to evaluate the global significance for the NP interpretation of the $b \rightarrow s\ell^+\ell^-$ anomalies. This method transposes the known criteria used for discovering new resonances, such as the Higgs boson, into searching for NP in $b \rightarrow s\ell^+\ell^-$ transitions. It is worth emphasizing that, while it is remarkable that all data can be explained by fitting one or two WCs and that this observation can be used to investigate what are the interesting theoretical directions, this hypothesis has been made after having seen the data. Using the same hypothesis to evaluate the

⁴The 5 WCs fit has the same goodness of fit as the 9 WCs fit, since data can be well described with a smaller number of Wilson Coefficients.

global significance of NP would be the Bayesian-inference equivalent of choosing the prior after having calculated the likelihood. Therefore, we advocate a more agnostic method to calculate the global NP significance with respect to the SM in $b \rightarrow s\ell^+\ell^-$ processes. To this end, we have calculated the LEE for the first time and shown that the trial-factor cannot be neglected.

We stress that the approach proposed in this paper should not be interpreted as a criticism towards existing attempts made so far of combining and interpreting the anomalies in motivated theoretical frameworks. We are simply addressing a different question. While current fits of selected WC sets in the $b \rightarrow s\ell^+\ell^-$ system only evaluate a local significance, these approaches are fundamental to obtain theory insights on the flavor anomalies. Similarly, there is a strong theoretical interest in trying to combine the $b \rightarrow s\ell^+\ell^-$ anomalies with other hints of deviations from the SM, such as the $b \rightarrow c\ell\nu$ anomalies [60–68] or the recent $(g-2)_\mu$ result [69,70] (see also [71]). However, this combination is not appropriate to establish a global significance, given the hypothesis of a connection between different processes is made a posteriori, after having observed data.

We also recognise that our approach of treating ΔC_9^U as a nuisance SM parameter can be viewed as an overly conservative choice. Nevertheless, in the absence of a widely accepted estimate for the theory uncertainty of the non-local $c\bar{c}$ contributions, this is mandatory for a conservative estimate of the significance.

While the uncertainty of all the measurements used here are statistically dominated, the results of our analysis can be improved by adding correlations of experimental systematic uncertainties and taking into account that they can follow non-Gaussian PDFs. Additional potential improvements concern the observables to be included. To simplify the numerical analysis we have only included the observables that are most sensitive.

For instance, observables such as Q_5 [54] measured by Belle [72], were not included in this work since these measurements are still not precise enough to have a sizeable impact. For the same reason, angular observables in $B_s^0 \rightarrow \phi\mu^+\mu^-$ [73,74] decays are not considered. While the decay $B_s^0 \rightarrow \phi\mu^+\mu^-$ is analogous to $B^0 \rightarrow K^{*0}\mu^+\mu^-$ from theory point of view, it is limited statistically due to the value of the fragmentation fraction f_s/f_d [75] and that it is not self-tagged decay.

While beyond the scope of this paper, a more rigorous approach of including all observables and treat all correlated systematics is desirable in view of future combinations.

With current data, all these effects are expected to have a small impact and will not change the main conclusions presented here.

The global significance of 4.3 standard deviations we obtain for the NP hypothesis in the $b \rightarrow s\ell^+\ell^-$ system clearly demonstrates the potential of combining different measurements in this system, even when adopting an agnostic alternative hypothesis and an highly conservative theory approach. In view of future measurements, we advocate that experimental collaborations adopt this method to calculate the global significance of the new physics hypothesis in a conservative and unbiased way.

References

- [1] R Aaij et al. Measurement of Form-Factor-Independent Observables in the Decay $B^0 \rightarrow K^{*0} \mu^+ \mu^-$. *Phys. Rev. Lett.*, 111:191801, 2013.
- [2] Roel Aaij et al. Test of lepton universality using $B^+ \rightarrow K^+ \ell^+ \ell^-$ decays. *Phys. Rev. Lett.*, 113:151601, 2014.
- [3] Vardan Khachatryan et al. Observation of the rare $B_s^0 \rightarrow \mu^+ \mu^-$ decay from the combined analysis of CMS and LHCb data. *Nature*, 522:68–72, 2015.
- [4] Roel Aaij et al. Angular analysis of the $B^0 \rightarrow K^{*0} \mu^+ \mu^-$ decay using 3 fb^{-1} of integrated luminosity. *JHEP*, 02:104, 2016.
- [5] R. Aaij et al. Test of lepton universality with $B^0 \rightarrow K^{*0} \ell^+ \ell^-$ decays. *JHEP*, 08:055, 2017.
- [6] Morad Aaboud et al. Study of the rare decays of B_s^0 and B^0 mesons into muon pairs using data collected during 2015 and 2016 with the ATLAS detector. *JHEP*, 04:098, 2019.
- [7] Albert M Sirunyan et al. Measurement of properties of $B_s^0 \rightarrow \mu^+ \mu^-$ decays and search for $B^0 \rightarrow \mu^+ \mu^-$ with the CMS experiment. *JHEP*, 04:188, 2020.
- [8] Roel Aaij et al. Search for lepton-universality violation in $B^+ \rightarrow K^+ \ell^+ \ell^-$ decays. *Phys. Rev. Lett.*, 122(19):191801, 2019.
- [9] Roel Aaij et al. Measurement of CP -Averaged Observables in the $B^0 \rightarrow K^{*0} \mu^+ \mu^-$ Decay. *Phys. Rev. Lett.*, 125(1):011802, 2020.
- [10] Roel Aaij et al. Angular analysis of the $B^+ \rightarrow K^{*+} \mu^+ \mu^-$ decay. 12 2020.
- [11] Roel Aaij et al. Test of lepton universality in beauty-quark decays. 3 2021.
- [12] E. Fermi. An attempt of a theory of beta radiation. 1. *Z. Phys.*, 88:161–177, 1934.

-
- [13] Sebastien Descotes-Genon, Joaquim Matias, and Javier Virto. Understanding the $B \rightarrow K^* \mu^+ \mu^-$ Anomaly. *Phys. Rev. D*, 88:074002, 2013.
- [14] Wolfgang Altmannshofer and David M. Straub. New Physics in $B \rightarrow K^* \mu \mu$? *Eur. Phys. J. C*, 73:2646, 2013.
- [15] Tobias Hurth and Farvah Mahmoudi. On the LHCb anomaly in $B \rightarrow K^* \ell^+ \ell^-$. *JHEP*, 04:097, 2014.
- [16] Gudrun Hiller and Martin Schmaltz. R_K and future $b \rightarrow s \ell \ell$ physics beyond the SM opportunities. *Phys. Rev. D*, 90:054014, 2014.
- [17] Rodrigo Alonso, Benjamin Grinstein, and Jorge Martin Camalich. $SU(2) \times U(1)$ gauge invariance and the shape of new physics in rare B decays. *Phys. Rev. Lett.*, 113:241802, 2014.
- [18] T. Hurth, F. Mahmoudi, and S. Neshatpour. Global fits to $b \rightarrow s \ell \ell$ data and signs for lepton non-universality. *JHEP*, 12:053, 2014.
- [19] Wolfgang Altmannshofer and David M. Straub. New physics in $b \rightarrow s$ transitions after LHC run 1. *Eur. Phys. J. C*, 75(8):382, 2015.
- [20] Sébastien Descotes-Genon, Lars Hofer, Joaquim Matias, and Javier Virto. Global analysis of $b \rightarrow s \ell \ell$ anomalies. *JHEP*, 06:092, 2016.
- [21] Marco Ciuchini, Antonio M. Coutinho, Marco Fedele, Enrico Franco, Ayan Paul, Luca Silvestrini, and Mauro Valli. On Flavourful Easter eggs for New Physics hunger and Lepton Flavour Universality violation. *Eur. Phys. J. C*, 77(10):688, 2017.
- [22] Guido D'Amico, Marco Nardecchia, Paolo Panci, Francesco Sannino, Alessandro Strumia, Riccardo Torre, and Alfredo Urbano. Flavour anomalies after the R_{K^*} measurement. *JHEP*, 09:010, 2017.
- [23] Bernat Capdevila, Andreas Crivellin, Sébastien Descotes-Genon, Joaquim Matias, and Javier Virto. Patterns of New Physics in $b \rightarrow s \ell^+ \ell^-$ transitions in the light of recent data. *JHEP*, 01:093, 2018.
- [24] Wolfgang Altmannshofer, Christoph Niehoff, Peter Stangl, and David M. Straub. Status of the $B \rightarrow K^* \mu^+ \mu^-$ anomaly after Moriond 2017. *Eur. Phys. J. C*, 77(6):377, 2017.

- [25] Marcel Algueró et al. Emerging patterns of New Physics with and without Lepton Flavour Universal contributions. *Eur. Phys. J. C*, 79(8):714, 2019. [Addendum: *Eur.Phys.J.C* 80, 511 (2020)].
- [26] Jason Aebischer, Wolfgang Altmannshofer, Diego Guadagnoli, MÉRIL Reboud, Peter Stangl, and David M. Straub. B -decay discrepancies after Moriond 2019. *Eur. Phys. J. C*, 80(3):252, 2020.
- [27] Marco Ciuchini, Marco Fedele, Enrico Franco, Ayan Paul, Luca Silvestrini, and Mauro Valli. Lessons from the $B^{0,+} \rightarrow K^{*0,+} \mu^+ \mu^-$ angular analyses. *Phys. Rev. D*, 103(1):015030, 2021.
- [28] Louis Lyons. Open statistical issues in particle physics. *The Annals of Applied Statistics*, 2(3), Sep 2008.
- [29] Eilam Gross and Ofer Vitells. Trial factors for the look elsewhere effect in high energy physics. *Eur. Phys. J. C*, 70:525–530, 2010.
- [30] Luv Demortier. P Values and Nuisance Parameters. 2008.
- [31] P Bock et al. Technical Report CERN-EP-98-046. CERN-L3-146. CERN-OPAL-TN-503. OPAL-TN-503, Apr 1998.
- [32] G. L. Bayatian et al. CMS technical design report, volume II: Physics performance. *J. Phys. G*, 34(6):995–1579, 2007.
- [33] T. Hurth, F. Mahmoudi, D. Martínez Santos, and S. Neshatpour. More Indications for Lepton Nonuniversality in $b \rightarrow s \ell^+ \ell^-$. 4 2021.
- [34] James Lyon and Roman Zwicky. Resonances gone topsy turvy - the charm of QCD or new physics in $b \rightarrow s \ell^+ \ell^-$? 6 2014.
- [35] Aoife Bharucha, Diogo Boito, and Cédric Méaux. Disentangling QCD and New Physics in $D^+ \rightarrow \pi^+ \ell^+ \ell^-$. 11 2020.
- [36] Nico Gubernari, Danny Van Dyk, and Javier Virto. Non-local matrix elements in $B_{(s)} \rightarrow \{K^{(*)}, \phi\} \ell^+ \ell^-$. *JHEP*, 02:088, 2021.
- [37] Tobias Huber, Tobias Hurth, Jack Jenkins, Enrico Lunghi, Qin Qin, and K. Keri Vos. Long distance effects in inclusive rare B decays and phenomenology of $\bar{B} \rightarrow X_d \ell^+ \ell^-$. *JHEP*, 10:228, 2019.

- [38] Sebastian Jäger, Matthew Kirk, Alexander Lenz, and Kirsten Leslie. Charming New B -Physics. *JHEP*, 03:122, 2020.
- [39] Katsumasa Nakayama and Shoji Hashimoto. Test of factorization for the long-distance effects from charmonium on $B \rightarrow K\ell^+\ell^-$. *PoS, LATTICE2018:221*, 2019.
- [40] A. Arbey, T. Hurth, F. Mahmoudi, and S. Neshatpour. Hadronic and New Physics Contributions to $b \rightarrow s$ Transitions. *Phys. Rev. D*, 98(9):095027, 2018.
- [41] Marcin Chrzaszcz, Andrea Mauri, Nicola Serra, Rafael Silva Coutinho, and Danny van Dyk. Prospects for disentangling long- and short-distance effects in the decays $B \rightarrow K^*\mu^+\mu^-$. *JHEP*, 10:236, 2019.
- [42] Thomas Blake, Ulrik Egede, Patrick Owen, Konstantinos Alexandros Petridis, and Gabriela Pomery. An empirical model to determine the hadronic resonance contributions to $\bar{B}^0 \rightarrow \bar{K}^{*0}\mu^+\mu^-$ transitions. *Eur. Phys. J. C*, 78(6):453, 2018.
- [43] Mohammad Ahmady, Dan Hatfield, Sébastien Lord, and Ruben Sandapen. Effect of $c\bar{c}$ resonances in the branching ratio and forward-backward asymmetry of the decay $B \rightarrow K^*\mu^+\mu^-$. *Phys. Rev. D*, 92(11):114028, 2015.
- [44] Sebastien Descotes-Genon, Lars Hofer, Joaquim Matias, and Javier Virto. Theoretical status of $B \rightarrow K^*\mu^+\mu^-$: The path towards New Physics. *J. Phys. Conf. Ser.*, 631(1):012027, 2015.
- [45] Marco Ciuchini, Marco Fedele, Enrico Franco, Satoshi Mishima, Ayan Paul, Luca Silvestrini, and Mauro Valli. $B \rightarrow K^*\ell^+\ell^-$ decays at large recoil in the SM: a theoretical reappraisal. *JHEP*, 06:116, 2016.
- [46] Rodrigo Alonso, Benjamín Grinstein, and Jorge Martin Camalich. Lepton universality violation and lepton flavor conservation in B -meson decays. *JHEP*, 10:184, 2015.
- [47] Martin Beneke, Christoph Bobeth, and Robert Szafron. Power-enhanced leading-logarithmic QED corrections to $B_q \rightarrow \mu^+\mu^-$. *JHEP*, 10:232, 2019.
- [48] Joaquim Matias, Federico Mescia, Marc Ramon, and Javier Virto. Complete Anatomy of $\bar{B}_d \rightarrow \bar{K}^{*0}(- \rightarrow K\pi)l^+l^-$ and its angular distribution. *JHEP*, 04:104, 2012.

-
- [49] Wolfgang Altmannshofer, Patricia Ball, Aoife Bharucha, Andrzej J. Buras, David M. Straub, and Michael Wick. Symmetries and Asymmetries of $B \rightarrow K^* \mu^+ \mu^-$ Decays in the SM and Beyond. *JHEP*, 01:019, 2009.
- [50] Aoife Bharucha, David M. Straub, and Roman Zwicky. $B \rightarrow V \ell^+ \ell^-$ in the SM from light-cone sum rules. *JHEP*, 08:098, 2016.
- [51] Riccardo Barbieri, Gino Isidori, Joel Jones-Perez, Paolo Lodone, and David M. Straub. $U(2)$ and Minimal Flavour Violation in Supersymmetry. *Eur. Phys. J. C*, 71:1725, 2011.
- [52] Sacha Davidson, Gino Isidori, and Selma Uhlig. Solving the flavour problem with hierarchical fermion wave functions. *Phys. Lett. B*, 663:73–79, 2008.
- [53] David M. Straub. flavio: a Python package for flavour and precision phenomenology in the SM and beyond. 10 2018.
- [54] Marcel Algueró, Bernat Capdevila, Sébastien Descotes-Genon, Pere Masjuan, and Joaquim Matias. What R_K and Q_5 can tell us about New Physics in $b \rightarrow s \ell \ell$ transitions? *JHEP*, 07:096, 2019.
- [55] HFLAV Collaboration. World average branching fraction for $b \rightarrow x_s \gamma$. HFLAV Web site.
- [56] Roel Aaij et al. Strong constraints on the $b \rightarrow s \gamma$ photon polarisation from $B^0 \rightarrow K^{*0} e^+ e^-$ decays. *JHEP*, 12:081, 2020.
- [57] Li-Sheng Geng, Benjamín Grinstein, Sebastian Jäger, Shuang-Yi Li, Jorge Martin Camalich, and Rui-Xiang Shi. Implications of new evidence for lepton-universality violation in $b \rightarrow s \ell^+ \ell^-$ decays. 3 2021.
- [58] Wolfgang Altmannshofer and Peter Stangl. New Physics in Rare B Decays after Moriond 2021. 3 2021.
- [59] Claudia Cornella, Darius A. Faroughy, Javier Fuentes-Martín, Gino Isidori, and Matthias Neubert. Reading the footprints of the B-meson flavor anomalies. 3 2021.
- [60] J. P. Lees et al. Evidence for an excess of $\bar{B} \rightarrow D^{(*)} \tau^- \bar{\nu}_\tau$ decays. *Phys. Rev. Lett.*, 109:101802, 2012.

- [61] R. Aaij et al. Test of lepton flavor universality by the measurement of the $B^0 \rightarrow D^{*-}\tau^+\nu_\tau$ branching fraction using three-prong τ decays. *Phys. Rev.*, D97(7):072013, 2018.
- [62] J. P. Lees et al. Measurement of an excess of $\bar{B} \rightarrow D^{(*)}\tau^-\bar{\nu}_\tau$ decays and implications for charged Higgs bosons. *Phys. Rev.*, D88(7):072012, 2013.
- [63] Y. Sato et al. Measurement of the branching ratio of $\bar{B}^0 \rightarrow D^{*+}\tau^-\bar{\nu}_\tau$ relative to $\bar{B}^0 \rightarrow D^{*+}\ell^-\bar{\nu}_\ell$ decays with a semileptonic tagging method. *Phys. Rev.*, D94(7):072007, 2016.
- [64] Roel Aaij et al. Measurement of the ratio of branching fractions $\mathcal{B}(\bar{B}^0 \rightarrow D^{*+}\tau^-\bar{\nu}_\tau)/\mathcal{B}(\bar{B}^0 \rightarrow D^{*+}\mu^-\bar{\nu}_\mu)$. *Phys. Rev. Lett.*, 115(11):111803, 2015. [Erratum: *Phys.Rev.Lett.* 115, 159901 (2015)].
- [65] M. Huschle et al. Measurement of the branching ratio of $\bar{B} \rightarrow D^{(*)}\tau^-\bar{\nu}_\tau$ relative to $\bar{B} \rightarrow D^{(*)}\ell^-\bar{\nu}_\ell$ decays with hadronic tagging at Belle. *Phys. Rev.*, D92(7):072014, 2015.
- [66] R. Aaij et al. Measurement of the ratio of branching fractions $\mathcal{B}(B_c^+ \rightarrow J/\psi\tau^+\nu_\tau)/\mathcal{B}(B_c^+ \rightarrow J/\psi\mu^+\nu_\mu)$. *Phys. Rev. Lett.*, 120(12):121801, 2018.
- [67] G. Caria et al. Measurement of $\mathcal{R}(D)$ and $\mathcal{R}(D^*)$ with a semileptonic tagging method. *Phys. Rev. Lett.*, 124(16):161803, 2020.
- [68] S. Hirose et al. Measurement of the τ lepton polarization and $R(D^*)$ in the decay $\bar{B} \rightarrow D^*\tau^-\bar{\nu}_\tau$ with one-prong hadronic τ decays at Belle. *Phys. Rev.*, D97(1):012004, 2018.
- [69] B. Abi et al. Measurement of the Positive Muon Anomalous Magnetic Moment to 0.46 ppm. *Phys. Rev. Lett.*, 126:141801, 2021.
- [70] T. Albahri et al. Measurement of the anomalous precession frequency of the muon in the Fermilab Muon g-2 experiment. *Phys. Rev. D*, 103:072002, 2021.
- [71] Sz. Borsanyi et al. Leading hadronic contribution to the muon 2 magnetic moment from lattice QCD. 2 2020.
- [72] S. Wehle et al. Lepton-Flavor-Dependent Angular Analysis of $B \rightarrow K^*\ell^+\ell^-$. *Phys. Rev. Lett.*, 118(11):111801, 2017.
- [73] Roel Aaij et al. Angular analysis of the rare decay $B_s^0 \rightarrow \phi\mu^+\mu^-$. 7 2021.

-
- [74] Roel Aaij et al. Angular analysis and differential branching fraction of the decay $B_s^0 \rightarrow \phi\mu^+\mu^-$. *JHEP*, 09:179, 2015.
- [75] Roel Aaij et al. Precise measurement of the f_s/f_d ratio of fragmentation fractions and of B_s^0 decay branching fractions. 3 2021.

Chapter 5

A general effective field theory description of $b \rightarrow s\ell^+\ell^-$ lepton universality ratios

5.1 Introduction

In recent years, a pattern of deviations with respect to Standard Model (SM) predictions has manifested in measurements of $b \rightarrow s\ell^+\ell^-$ processes. These include deviations in the angular distribution of the decay $B^0 \rightarrow K^{*0}\mu^+\mu^-$ [2,6,14,13], a deficit in the decay rates [38,1,3,8,18,19,17] and deviations in lepton flavour universality (LFU) ratios [5,10,12,20]. Within the framework of effective field theories, these deviations are numerically consistent with each other, pointing to a well-defined hypothesis of new physics of short-distance origin [25,21,22,29,32,26]. Even under highly conservative theoretical assumptions, the global significance of the new physics hypothesis is as large as 4.3σ [33].

Among these deviations, the LFU ratios are particularly interesting as their SM uncertainty is very precise [30,24,34]. They are defined within a region of squared dilepton invariant mass (q^2) as

$$R_X \equiv \frac{\int_{q_{\min}^2}^{q_{\max}^2} \frac{d\Gamma(H_b \rightarrow X_s \mu^+ \mu^-)}{dq^2} dq^2}{\int_{q_{\min}^2}^{q_{\max}^2} \frac{d\Gamma(H_b \rightarrow X_s e^+ e^-)}{dq^2} dq^2}. \quad (5.1)$$

where H_b represents a b -hadron (meson or baryon) and X_s represents a well-defined hadronic system with strangeness, such that the transition satisfies $\Delta B = \Delta S$.

While the SM prediction $R_X^{\text{SM}} = 1$ is very robust,¹ the precise cancellation of hadronic uncertainties can be broken in presence of new physics (NP) [21]. Namely, the interpretation of a new physics structure affecting these LFU ratios relies on the knowledge of the hadronic structure of the decays involved. This is why the LFU ratio R_{pK} [12] has not been included yet in $b \rightarrow s\ell^+\ell^-$ global fits, despite its clean SM prediction [24,34,31]. The same problem holds for any LFU ratio which contains a mixture of overlapping/interfering hadronic resonances where the underlying structure is unknown, referred to in the following as non-exclusive R_X ratios. Examples of this type are the LFU ratios $R_{K\pi\pi}$ and $R_{K\pi}$, where for the latter the $K\pi$ system has an invariant mass larger than the $K^*(892)^0$ resonance. The experimental prospects for these ratios are promising but their interpretation in terms of $b \rightarrow s\ell^+\ell^-$ short-distance dynamics is not obvious.

Here, we propose a new method that allows to interpret any LFU ratio within the framework of effective Lagrangians for the first time, even if the detailed structure of the hadronic matrix elements is unknown. The key observation that allows us to reduce the number of unknown hadronic quantities is the fact that the SM amplitude is both lepton flavour universal and approximately left-handed. These two properties imply that only a very limited set of NP amplitudes can yield sizeable non-standard contributions to R_X . Their contribution can be described in terms of very few combinations of hadronic parameters, which can in turn be treated as nuisance parameters.

The theoretical decomposition of R_X following this logic is presented in Sect. 5.2. Using this decomposition we perform a global $b \rightarrow s\ell^+\ell^-$ combination including the measurement of R_{pK} for the first time, improving upon the global estimate of the significance presented in Ref. [33]. Using this method we also explore the potential impact of the expected measurements of R_{pK} , $R_{K\pi\pi}$, and $R_{K\pi}$ with the full dataset collected so far by LHCb (Sec. 5.4). The conclusions of our analysis are summarised in Sect. 5.5.

¹We assume the q^2 range extends well above the dilepton mass threshold.

5.2 General expression of R_X in terms of Wilson coefficients

In the limit of heavy new physics, we can describe both SM and NP effects in $b \rightarrow s\ell^+\ell^-$ decays by means of an effective Lagrangian containing only light SM fields. We normalise it as

$$\Delta\mathcal{L}_{\text{eff}}^{b \rightarrow s\ell\ell} = \frac{4G_F}{\sqrt{2}} \frac{\alpha}{4\pi} V_{ts}^* V_{tb} \sum_i C_i \mathcal{O}_i + \text{h.c.}, \quad (5.2)$$

where G_F and α denote the Fermi constant and the electromagnetic coupling, respectively, and V_{ij} denotes the elements of the Cabibbo-Kobayashi-Maskawa matrix. The only difference between the SM and NP cases lies in the number of effective operators, which is larger in a generic NP framework. In full generality the dimension-six operators with a non-vanishing tree-level matrix element in $b \rightarrow s\ell^+\ell^-$ decays can be composed into three sets: i) dipole operators,

$$\mathcal{O}_7 = \frac{m_b}{e} (\bar{s}_L \sigma_{\mu\nu} b_R) F^{\mu\nu}, \quad \mathcal{O}'_7 = \frac{m_b}{e} (\bar{s}_R \sigma_{\mu\nu} b_L) F^{\mu\nu}, \quad (5.3)$$

ii) vector operators,

$$\begin{aligned} \mathcal{O}_9^\ell &= (\bar{s}_L \gamma_\mu b_L) (\bar{\ell} \gamma^\mu \ell), & \mathcal{O}_{10}^\ell &= (\bar{s}_L \gamma_\mu b_L) (\bar{\ell} \gamma^\mu \gamma_5 \ell), \\ \mathcal{O}'_9 &= (\bar{s}_R \gamma_\mu b_R) (\bar{\ell} \gamma^\mu \ell), & \mathcal{O}'_{10} &= (\bar{s}_R \gamma_\mu b_R) (\bar{\ell} \gamma^\mu \gamma_5 \ell), \end{aligned} \quad (5.4)$$

and ii) scalar operators,

$$\mathcal{O}_S^\ell = (\bar{s}_L b_R) (\bar{\ell}_R \ell_L), \quad \mathcal{O}'_S = (\bar{s}_R b_L) (\bar{\ell}_L \ell_R). \quad (5.5)$$

In the NP case the $\ell = e$ and $\ell = \mu$ terms should be treated separately. The scalar operators lead to $b \rightarrow s\ell^+\ell^-$ amplitudes which are helicity suppressed and can be safely neglected in most of the observables we are interested in. The only exception being the (single) effective combination which contributes to the $B_s \rightarrow \mu^+\mu^-$ helicity-suppressed rate. The dipole operator \mathcal{O}'_7 is negligible in the SM and is severely constrained by $\Gamma(B \rightarrow K^*\gamma)$ and $\Gamma(B \rightarrow K^*\ell^+\ell^-)$ at low q^2 [15]. To describe SM and NP effects in the R_X ratios, we can thus limit our attention to the SM dipole operator (\mathcal{O}_7) and the four vector operators in Eq. (5.4).

As pointed in [31], to elucidate general properties of the LFU ratios beyond the SM, irrespective of the detailed structure of the hadronic matrix elements, it is convenient to write the decay amplitudes in a basis of chirally projected operators. To do so, we introduce the combinations

$$\begin{aligned} C_L^\ell &= C_9^\ell - C_{10}^\ell, & C_L^{\ell'} &= C_9^{\ell'} - C_{10}^{\ell'}, \\ C_R^\ell &= C_9^\ell + C_{10}^\ell, & C_R^{\ell'} &= C_9^{\ell'} + C_{10}^{\ell'}. \end{aligned} \quad (5.6)$$

With this notation, the generic $H_b \rightarrow X_s\ell^+\ell^-$ transition amplitude can be decomposed as

$$\mathcal{A}(H_b \rightarrow X_s\ell^+\ell^-) \propto (\mathcal{M}_{X,L}^\ell)^\alpha (J_L^\ell)_\alpha + (\mathcal{M}_{X,R}^\ell)^\alpha (J_R^\ell)_\alpha \quad (5.7)$$

where

$$(J_L^\ell)_\alpha = \bar{\ell}_L \gamma^\alpha \ell_L, \quad (J_R^\ell)_\alpha = \bar{\ell}_R \gamma^\alpha \ell_R, \quad (5.8)$$

and

$$\begin{aligned} (\mathcal{M}_{X,L}^\ell)^\alpha &= C_L^\ell J_X^\alpha + C_L^{\ell'} J_X'^\alpha + C_7 J_X^{7\alpha} \\ (\mathcal{M}_{X,R}^\ell)^\alpha &= C_R^\ell J_X^\alpha + C_R^{\ell'} J_X'^\alpha + C_7 J_X^{7\alpha} \end{aligned} \quad (5.9)$$

with

$$\begin{aligned} J_X^\alpha &= \langle X_s | \bar{s}_L \gamma^\alpha b_L | H_b \rangle, & J_X'^\alpha &= \langle X_s | \bar{s}_R \gamma^\alpha b_R | H_b \rangle, \\ J_X^{7\alpha} &\propto \frac{1}{q^2} q_\nu \langle X_s | \bar{s}_L \sigma^{\alpha\nu} b_R | H_b \rangle. \end{aligned} \quad (5.10)$$

In the limit where we neglect small lepton mass effects, the terms in Eq. (5.7) proportional to the left-handed and right-handed leptonic currents do not interfere. Moreover, the following relation holds

$$|\mathcal{M}_{X,R}^\ell|^2 = |\mathcal{M}_{X,L}^\ell|^2_{\{C_L^\ell \rightarrow C_R^\ell, C_L^{\ell'} \rightarrow C_R^{\ell'}\}}. \quad (5.11)$$

Integrating over all kinematic variables but for q^2 , we can thus decompose the decay rate as

$$\frac{d\Gamma_X^\ell}{dq^2} = \frac{d\Gamma_{X,L}^\ell}{dq^2} + \frac{d\Gamma_{X,R}^\ell}{dq^2}, \quad (5.12)$$

with

$$\frac{d\Gamma_{X,R}^\ell}{dq^2} = \frac{d\Gamma_{X,L}^\ell}{dq^2} \Big|_{\{C_L^\ell \rightarrow C_R^\ell, C_L^{\ell'} \rightarrow C_R^{\ell'}\}}. \quad (5.13)$$

The explicit expression of $d\Gamma_{X,L}^\ell/dq^2$ in terms of Wilson coefficients is

$$\begin{aligned} \frac{d\Gamma_{X,L}^\ell}{dq^2} = f_X^\ell(q^2) & \left\{ |C_L^\ell|^2 + |C_L^{\ell'}|^2 + \text{Re} \left[\eta_X^0(q^2) C_L^{\ell*} C_L^{\ell'} \right] \right. \\ & \left. + \eta_X^{77}(q^2) |C_7|^2 + \text{Re} \left[\eta_X^{79}(q^2) C_7^* C_L^\ell + \eta_X^{79'}(q^2) C_7^* C_L^{\ell'} \right] \right\}, \end{aligned} \quad (5.14)$$

where $f_X^\ell(q^2)$ and the four $\eta_X^i(q^2)$ are channel-dependent hadronic parameters. The hadronic matrix elements J_X^α and J_X^α are transformed into each other under the action of parity, which is a unitary operator. As a result, integrating over the phase space of $|X_s\rangle$ for any q^2 value, and summing (averaging) over the spin configurations of both $|X_s\rangle$ and $|H_b\rangle$, leads to the same coefficients in Eq. (5.14) for $|C_L^\ell|^2$ and $|C_L^{\ell'}|^2$. Moreover, the positivity of the squared matrix element implies

$$|\eta_X^0(q^2)| \leq 2, \quad \eta_X^{77}(q^2) > 0. \quad (5.15)$$

Given the definition of R_X in Eq. (5.1), it is convenient to define the following q^2 -integrated hadronic parameters:

$$\begin{aligned} F_X^\ell &= \int_{q_{\min}^2}^{q_{\max}^2} f_X^\ell(q^2) dq^2, \\ \langle \eta_X^{i,\ell} \rangle &= \frac{1}{F_X^\ell} \int_{q_{\min}^2}^{q_{\max}^2} f_X^\ell(q^2) \eta_X^i(q^2) dq^2. \end{aligned} \quad (5.16)$$

The normalization factor $f_X^\ell(q^2)$ depends on the lepton mass via kinematic effects, which are sizeable only close to the endpoint (i.e. for $q^2 \rightarrow 4m_\ell^2$). If the q^2 range of the measurement extends well above the di-lepton mass threshold, the lepton mass dependence is safely neglected and we can set

$$F_X^\mu = F_X^e \equiv F_X, \quad \langle \eta_X^{i,\ell} \rangle \equiv \langle \eta_X^i \rangle. \quad (5.17)$$

In this limit the overall normalization factor drops out in R_X and the same hadronic parameters appear in both numerator and denominator:

$$R_X = \frac{\left\{ |C_L^\mu|^2 + |C_L^{\mu'}|^2 + \text{Re} \left[\langle \eta_X^0 \rangle C_L^{\mu*} C_L^{\mu'} + C_7^* \left(\langle \eta_X^{77} \rangle C_7 + \langle \eta_X^{79} \rangle C_L^\mu + \langle \eta_X^{79'} \rangle C_L^{\mu'} \right) \right] \right\} + \left\{ L \rightarrow R \right\}}{\left\{ |C_L^e|^2 + |C_L^{e'}|^2 + \text{Re} \left[\langle \eta_X^0 \rangle C_L^{e*} C_L^{e'} + C_7^* \left(\langle \eta_X^{77} \rangle C_7 + \langle \eta_X^{79} \rangle C_L^e + \langle \eta_X^{79'} \rangle C_L^{e'} \right) \right] \right\} + \left\{ L \rightarrow R \right\}}. \quad (5.18)$$

This implies that in the SM, and in all models where the Wilson coefficients are lepton universal, $R_X \approx 1$ up to corrections due to QED and/or residual kinematic effects which are at most of $O(1\%)$ [24,34].

The key observation of the present work is that R_X retains a significant discriminating power with respect to NP models even in the absence of a precise knowledge of the hadronic parameters, i.e. even when treating the $\langle\eta_X^i\rangle$ as nuisance parameters. This statement emerges quite clearly by the following two observations:

- Sizeable deviations of R_X from unity can only be attributed to non-universal Wilson coefficients, i.e. $|R_X - 1| \neq 0$ only if $|\Delta C_i| \neq 0$ for some i , where

$$\Delta C_i = C_i^\mu - C_i^e, \quad i = L, L', R, R'. \quad (5.19)$$

- Other observables constrain NP effects to be a small perturbation over the SM: this implies that large NP effects in R_X can arise only by non-vanishing ΔC_i interfering with the SM amplitude. The latter has a peculiar structure,

$$\begin{aligned} |C_L^{\text{SM}}| &= O(10) \gg |C_7^{\text{SM}}|, |C_R^{\text{SM}}|, \\ |C_{L,R}^{\ell'}|^{\text{SM}} &= 0, \end{aligned} \quad (5.20)$$

hence only a very limited set of NP amplitudes can lead to $|R_X - 1| \gg 0$.

These two observations become evident when linearising the theoretical expression of R_X with respect to the ΔC_i and neglecting the interference of ΔC_i with suppressed SM amplitudes. In this limit we obtain

$$R_X - 1 \approx \frac{\text{Re} \left(2 \frac{\Delta C_L}{C_L^{\text{SM}}} + \langle\eta_X^0\rangle \frac{\Delta C_L'}{C_L^{\text{SM}}} \right)}{1 + \langle\eta_X^{77}\rangle \left| \frac{C_L^{\text{SM}}}{C_L^{\text{SM}}} \right|^2 + \text{Re} \left[\langle\eta_X^{79}\rangle \frac{C_L^{\text{SM}}}{C_L^{\text{SM}}} \right]}. \quad (5.21)$$

As can be seen, only two types of NP effects can lead to a sizeable deviation of R_X from one: a lepton non-universal shift in either C_L^ℓ or $C_L^{\ell'}$. Note also that the only hadronic parameter with direct impact on the extraction of NP constraints from R_X is η_X^0 , which is bounded by Eq. (5.15). The η_X^{77} and η_X^{79} parameters have a minor role: they control the *dilution* of the LFU violation in the rate due to the lepton-universal contribution by \mathcal{O}_7 . Finally, the effect of $\eta_X^{79'}$ is always subleading.

5.2.0.0.1 Numerical estimate of the $\langle\eta_X^i\rangle$. The approximate expression in Eq. (5.21) is shown for illustrative purposes only, in the following numerical analysis we

Parameter	Limits	
	default	4q-ops
$\langle \eta_X^0 \rangle$		[-2,2]
$\langle \eta_X^{79} \rangle$	[-12,12]	[-20,20]
$\langle \eta_X^{79'} \rangle$	[-4,4]	[-10,10]
$\langle \eta_{pK}^{77} \rangle$	[0,120]	[0, 160]
$\langle \eta_{K\pi, K\pi\pi}^{77} \rangle$	[0,60]	[0,100]

Table 5.1 Limits placed on the hadronic nuisance parameters. The default values are determined by a conservative extrapolation from $B^0 \rightarrow K^*(892)^0$ matrix elements (see section 5.2.a). The larger interval for $\langle \eta_{pK}^{77} \rangle$ compared to $\langle \eta_{K\pi, K\pi\pi}^{77} \rangle$ takes into account the different q^2 ranges in the experimental measurements [12]. The values in the last column correspond to an extremely conservative extrapolation assuming large non-local matrix elements of four-quark operators (see section 5.2.b).

use the complete expression in Eq. (5.18), treating all the $\langle \eta_X^i \rangle$ as nuisance parameters. In order to define a range for the $\langle \eta_X^{7i} \rangle$, we use a channel where we are able to compute the values of the $\langle \eta_X^i \rangle$ parameters explicitly and where the impact of the dipole operator is maximal, namely the $B^0 \rightarrow K^*(892)^0 \ell^+ \ell^-$ decay. In this mode, characterised by a spin-one final state, the dipole operator is maximally enhanced by the $q^2 \rightarrow 0$ pole. In multi-body channels, such as $B^0 \rightarrow K^+ \pi^- \ell^+ \ell^-$ and $B^+ \rightarrow K^+ \pi^- \pi^+ \ell^+ \ell^-$, with a sizeable S -wave component of the hadronic final state, we expect a significantly smaller contribution of \mathcal{O}_7 to the total decay rate.

The values for the $\langle \eta_{K^*}^i \rangle$ as a function of q_{\min}^2 , setting $q_{\max}^2 = 6 \text{ GeV}^2$, are shown Fig. 5.1.² These parameters are determined numerically as a function of q_{\min}^2 by means of Eq. (5.16), using the $B \rightarrow K^*$ form-factors and non-local charm contributions from the Flavio software package [39]. The ranges derived from these figures, used in the numerical analysis for the other observables, are shown in Table 5.1 (default column). These range are calculated for the cut on q_{\min}^2 used in the corresponding existing analyses.

5.2.0.0.2 Impact of four-fermion operators. In Eq. (5.14) we have neglected the contribution to the rate of four-quark operators. Via non-local hadronic matrix elements, the latter produce non-vanishing corrections to the decay amplitudes of dilepton modes. These are responsible for an irreducible theoretical uncertainty in

²Note that the large value of $\langle \eta_X^{77} \rangle$ is largely compensated by the smallness of C_7 : even if $\langle \eta_X^{77} \rangle = O(100)$, $\langle \eta_X^{77} \rangle |C_7|^2 = O(10) \ll |C_L^{\text{SM}}|^2 = O(100)$.

LFU conserving observables. However, four-quark operators *cannot* induce a violation of LFU and modify only the vector-part of the amplitude, i.e. they can be described as an effective q^2 -dependent (and channel-dependent) modification of C_9 with respect to its short-distance value. In turn, this implies that the effect of four-quark operators in R_X can still be described in full generality by Eq. (5.18) simply re-defining the $\langle\eta_X^i\rangle$.

To understand the last statement, consider the following modification in Eq. (5.14): $C_9^\ell \rightarrow C_9^\ell + Y_X(q^2)$, where $Y_X(q^2)$ is a lepton-independent function of q^2 that describes the effect of the four-quark operators in a given hadronic transition. Then the expression of R_X in Eq. (5.18) remains valid provided we shift the $\langle\eta_X^i\rangle$ as follows

$$\langle\eta_X^{79}\rangle \rightarrow \langle\eta_X^{79}\rangle + \frac{\langle\zeta_X^1\rangle}{C_7}, \quad (5.22)$$

$$\langle\eta_X^{79'}\rangle \rightarrow \langle\eta_X^{79'}\rangle + \frac{\langle\zeta_X^2\rangle}{C_7}, \quad (5.23)$$

$$\langle\eta_X^{77}\rangle \rightarrow \langle\eta_X^{77}\rangle + \frac{\langle\zeta_X^3\rangle}{C_7} + \frac{\langle\zeta_X^4\rangle}{C_7^2}, \quad (5.24)$$

where

$$\langle\zeta_X^1\rangle = \frac{2}{F_X} \int f_X(q^2) Y_X(q^2) dq^2, \quad (5.25)$$

$$\langle\zeta_X^2\rangle = \frac{1}{F_X} \int f_X(q^2) Y_X(q^2) \eta_X^0(q^2) dq^2, \quad (5.26)$$

$$\langle\zeta_X^3\rangle = \frac{1}{F_X} \int f_X(q^2) Y_X(q^2) \eta_X^{79}(q^2) dq^2, \quad (5.27)$$

$$\langle\zeta_X^4\rangle = \frac{1}{F_X} \int f_X(q^2) |Y_X(q^2)|^2 dq^2. \quad (5.28)$$

Assuming $|Y_X(q^2)| \leq 1$, i.e. up to 25% corrections to C_9 from four-quark operators, which is a very conservative assumption, the previously determined ranges for $\langle\eta_X^i\rangle$ are enlarged as shown in the last column in Table 5.1. As we shall discuss in the following, this modification has an almost irrelevant impact in the numerical analysis of the significance of the NP hypothesis. This provides a clear demonstration of the marginal role played by the four-quark operators in R_X .

We conclude this section two additional observations:

- The parameter η_X^0 weights the relative contribution of vector and axial currents in the hadronic transition, and is maximal for hadronic final states with well-defined parity. In the $B \rightarrow K$ case, where only the vector current contributes, $\eta_K^0 = 2$;

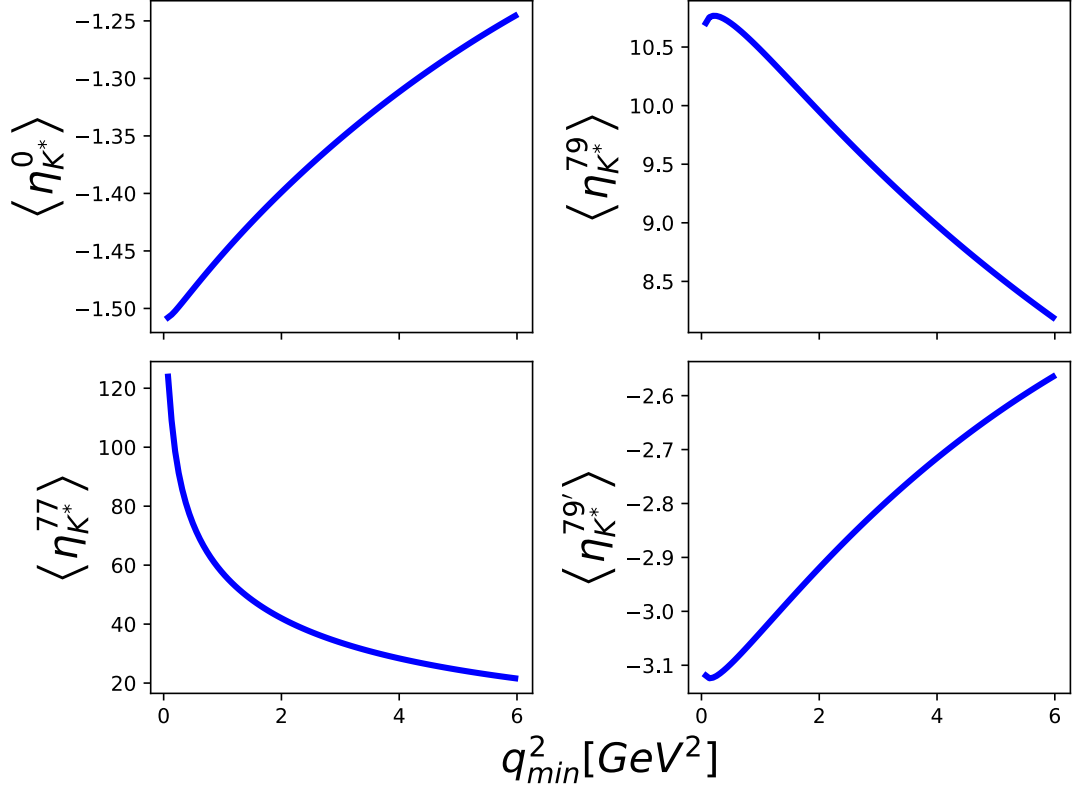


Fig. 5.1 Integrated hadronic parameters $\langle \eta_X^i \rangle$, defined in Eq. (5.16), extracted from $B^0 \rightarrow K^{*0}(\rightarrow K\pi)\mu^+\mu^-$ as a function of q_{min}^2 , setting $q_{max}^2 = 6 \text{ GeV}^2$.

in the $B \rightarrow K^*$ case, which is dominated by the axial-current contribution, $-2 < \eta_{K^*}^0 < -1$; in the fully inclusive case $\eta_{K^*}^0 \approx 0$.

- As pointed first in [31] (see also [28]), in the motivated class of NP models where the lepton non-universal amplitudes have a pure left-handed structure, the value of R_X is expected to be the same for any $H_b \rightarrow X_s \ell^+ \ell^-$ transition:

$$(R_X - 1)|_{\Delta_{CL} \neq 0} \approx (R_K - 1)|_{\Delta_{CL} \neq 0} . \quad (5.29)$$

5.3 Global combination of current measurements

In this section we present a combination of $b \rightarrow s \ell^+ \ell^-$ measurements following the procedure described in Ref. [33]. We include the following three sets of observables: i) the LFU ratios R_K [20], R_{K^*} [10] and R_{pK} [16], ii) the branching ratio for the rare dilepton mode $B_s^0 \rightarrow \mu^+ \mu^-$ [35,1,38,23] and, iii) the normalised angular distribution in

$B^0 \rightarrow K^{*0}\mu^+\mu^-$ decays [14,13]. In the case of R_K and R_{K^*} , where the structure of the hadronic matrix elements is well understood, we use the standard theoretical expressions in terms of Wilson coefficients and form factors using the Flavio package [39]. The ratio R_{pK} is described by means of Eq. (5.18).

As discussed in Ref. [33], we employ a highly generic NP hypothesis and a highly conservative approach towards hadronic uncertainties. We generate pseudo-experiments according to the SM, fluctuating the measurements according to their experimental uncertainties, and calculate the likelihood ratio between the NP and SM hypotheses. The distribution of the likelihood ratio is then used to calculate the p-value of a fit to data. Long-distance charm contributions are treated by allowing for a lepton universal shift of \mathcal{O}_9^ℓ in the SM definition.

The lepton universality ratio R_{pK} has been measured by the LHCb collaboration to be consistent with unity in the q^2 region $0.1 < q^2 < 6.0 \text{ GeV}^2/c^4$ [16]. We include it in the combination by means of Eq. (5.18), using the limits reported in Table 5.1 (default values) for the hadronic parameters. In fact, preliminary results on the differential branching fraction intervals of the dimuon invariant mass further confirms the smaller contribution of \mathcal{O}_7 to the total rate [36], if compared to the benchmark $B^0 \rightarrow K^*(892)^0\mu^+\mu^-$ decay [9]. As four nuisance parameters are included with only one measurement, degeneracies in the likelihood can occur due to multiple solutions. To counteract this, loose Gaussian constraints, whose width is set to be the same as the ranges given in table 5.1, are placed on each parameter to ensure the likelihood has a well-defined minimum. The exact value of these ranges has a very small effect on the numerical results.

The distribution of the likelihood ratio for the SM pseudoexperiments is shown in Fig 5.2, along with the value obtained from data. The inclusion of the measurement of R_{pK} increases the effective degrees of freedom by 0.6 units. This increase represents the uncertainty on the $\langle\eta_X^i\rangle$ which allows for potentially different NP sensitivity compared to the existing R_K and R_{K^*} ratios. Compared with the results from Ref. [33], we observe a small reduction in significance, from 4.3σ to 4.2σ when including the observable R_{pK} . This is due to the fact that the value of R_{pK} is not perfectly consistent with the other LFU ratios and the hadronic uncertainties allow to accommodate deviations from the SM amplitude in other directions, within a general NP hypothesis.

Using the same approach we test the specific hypothesis of a violation of lepton universality, considering all R_X ratios measured so far, i.e. including R_K , R_{K^*} and R_{pK} , and ignoring all other observables. This results in a local significance of 4.1σ for the hypothesis of a LFU violation, which is very close to the global significance of

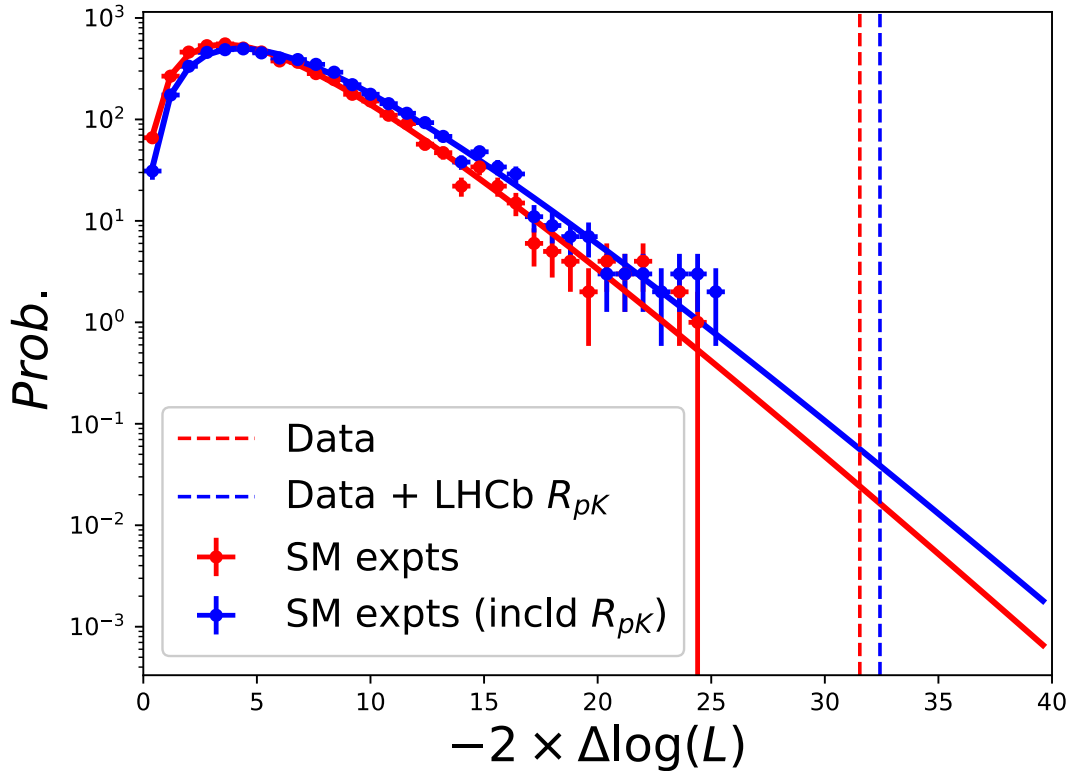


Fig. 5.2 Distribution of the likelihood ratio for pseudo-experiments under the SM hypothesis along with the value obtained from data. Results are shown under the same conditions as in Ref. [33] and also when the measurements of $R_{\rho K}$ is included.

NP in $b \rightarrow s\ell^+\ell^-$ decays. This small variation in the significance can be understood as follows: the analysis of LFU observables has a smaller trial factor compared to the generic NP analysis; however, with present data, this effect is compensated by the lack of inclusion in the fit of $\mathcal{B}(B_s \rightarrow \mu^+\mu^-)$ [38,1,35,19,17], which enhances the significance in the generic NP case.

5.4 Impact of future measurements

In addition to assessing the significance with the current measurements, we calculate the expected gain in discovery potential by using this approach with other non-exclusive R_X measurements that can be performed at LHCb in the near future. To this end, we estimate the experimental sensitivity of these ratios and include the hypothetical measurements in a fit with the current measurements.

We estimate the experimental sensitivity of three modes with the full run I and run II dataset of 9fb^{-1} for the following ratios:

$$\begin{aligned} R_{pK} &= \frac{\mathcal{B}(\Lambda_b^0 \rightarrow pK^- \mu^+ \mu^-)}{\mathcal{B}(\Lambda_b^0 \rightarrow pK^- e^+ e^-)}, \\ R_{K\pi\pi} &= \frac{\mathcal{B}(B^+ \rightarrow K^+ \pi^- \pi^+ \mu^+ \mu^-)}{\mathcal{B}(B^+ \rightarrow K^+ \pi^- \pi^+ e^+ e^-)}, \\ R_{K\pi} &= \frac{\mathcal{B}(B^0 \rightarrow K^+ \pi^+ \mu^+ \mu^-)}{\mathcal{B}(B^0 \rightarrow K^+ \pi^+ e^+ e^-)}, \end{aligned}$$

where for the $R_{K\pi}$ case, the $K^+\pi^-$ invariant mass is required to be above 1 GeV to separate it from the comparatively well understood $K^*(892)^0$ resonance.

The sensitivity for non-exclusive R_X measurements depends primarily on the precision of the electron mode. Given the ratio R_{pK} has already been measured, the precision can easily be predicted assuming it scales with luminosity, resulting in a precision of 12.2%. As the decays $B^+ \rightarrow K^+\pi^-\pi^+e^+e^-$ and $B^0 \rightarrow K^+\pi^-e^+e^-$ have yet to be observed, their yields are extrapolated from the corresponding muonic decay modes from Refs. [7,4], by scaling with luminosity and the centre-of-mass energy. These muon yields are compared to the corresponding yield in the R_{K^*} measurement [11] to scale the resulting precision of the LFU ratio. A statistical uncertainty on $R_{K\pi}$ and $R_{K\pi\pi}$ of 7.7% and 13.5% is expected for the full run I-II datasets in the range of $1.1 < q^2 < 6.0 \text{ GeV}^2/c^4$. The estimated uncertainty on $R_{K\pi}$ turns out to be comparable with that of R_{K^*} , as can be expected given there are many significant contributions above the $K^*(892)^0$ resonance [7,37].

Information on the differential branching fraction in intervals of the dimuon invariant mass can provide insights on the underlying dynamics of the non-exclusive hadronic system, which allows us to check the limits of the $\langle \eta_X^i \rangle$ parameters. For instance, for the $B^0 \rightarrow K^{*0} \mu^+ \mu^-$ decay a relative increase of the differential branching fraction between the $0.1 < q^2 < 0.98$ and $1.1 < q^2 < 6.0 \text{ GeV}^2/c^4$ regions by a factor of three is reported in Ref. [9]. Similar inspection can be performed for the non-exclusive channels and are found to be at the order of 2.0 and 2.6 for the $K\pi$ and $K\pi\pi$ hadronic systems, respectively [7,4]. As a result, this confirms the conclusion of Sec 5.2 that the limits obtained for the $\langle \eta_X^i \rangle$ parameters involving the $K^*(892)^0$ resonance can be used as a proxy for these channels.

The impact of these future measurements is examined by repeating the procedure from the previous section introducing two benchmark points common to all non-

Scenario	NP Significance
Current data	4.3 σ
Current data + $R_X = 0.8$	5.4 σ
Current data + $R_X = 1.0$	3.8 σ

Table 5.2 Change of the significance of the new-physics hypothesis in $b \rightarrow s\ell^+\ell^-$ decays adding hypothetical measurements of R_{pK} , $R_{K\pi}$, and $R_{K\pi\pi}$, with full run I and run II statistics, under two different hypotheses for the central values.

exclusive LFU ratios: $R_X = 1.0$ (SM) and $R_X = 0.8$ (NP). The latter is chosen being broadly consistent with current global fits. Figure 5.3 (top) shows the distribution of the likelihood ratio when including these new R_X observables under the NP hypothesis. A large increase in the significance from 4.3 σ to 5.4 σ when including the R_X observables is seen. If the new measurements are set to the SM prediction of $R_X = 1.0$, a reduction to 3.8 σ can be expected. These measurements can therefore have a large impact on the clarification of lepton universality violation in $b \rightarrow s\ell^+\ell^-$ decays.

In order to investigate the dependence of the significance with respect to the freedom given to the hadronic parameters, we have repeated the fit fixing the $\langle\eta_X^i\rangle$ to their central values. The result is also shown in Fig. 5.3 (bottom). As expected, in this case the additional measurements do not increase the effective degrees of freedom in the system. The exact knowledge of all hadronic nuisance parameters would lead to a significance of 5.9 σ , i.e. an increase in significance of 0.5 σ compared to when they are treated as nuisance parameters. This relatively small increase provides an a posteriori confirmation that they play a minor role in the fit. We also compare the results obtained with the ranges for the $\langle\eta_X^i\rangle$ set to the default values in Table 5.1 vs. the case of large contributions from four-fermion operators (Table 5.1, right column). In the latter case the significance decreases by 0.03 σ , which reaffirms the small impact the non-local contributions in this analysis. Finally, we also decrease the limits allowed for $\langle\eta_X^{77}\rangle$ to 60, appropriate if the R_{pK} ratio was measured setting q_{\min}^2 above 1 GeV². A negligible difference in discovery potential is seen, which indicates that the exact kinematic range is not crucial for the subsequent interpretation.

5.5 Conclusions

In summary, we have introduced a method to include any LFU ratio in global fits by treating the hadronic uncertainties as nuisance parameters. This method is not

designed to replace the existing theoretical description of R_K or R_{K^*} , where we can take advantage of a detailed knowledge of all the components of the transition amplitudes. It is conceived for interpreting LFU ratios where we lack precise information about the underlying hadronic dynamics.

To demonstrate the method, we have updated the global fit of Ref. [33] to include the LHCb measurement of R_{pK} . With current data, we find that R_{pK} has a marginal effect on the global significance of new physics in $b \rightarrow s\ell^+\ell^-$ decays. However, when extrapolating to the full LHCb dataset, and including also hypothetical measurements of $R_{K\pi}$ and $R_{K\pi\pi}$, we find that the increase in the significance can be large.

In this paper we concentrated on the three non-exclusive LFU ratios which are more promising from the experimental point of view. However, the method proposed here can be extended to include other channels, such as $B_s \rightarrow K^+K^-\ell^+\ell^-$. An interesting experimental feature of some of the non-exclusive channels is that, due to the large invariant mass of the hadronic systems, they suffer much less from partially reconstructed backgrounds compared to the *golden modes* $B^0 \rightarrow K^{*0}\ell^+\ell^-$ and $B^+ \rightarrow K^+\ell^+\ell^-$. This additional experimental advantage reduces the risk of hypothetical mis-modelling of backgrounds, which right now are among the leading systematic uncertainties in the LFU measurements. The inclusion of the non-exclusive R_X using the method proposed here will therefore not only increase the new-physics sensitivity from a pure statistical point of view, but also enhance the redundancy of the experimental results.

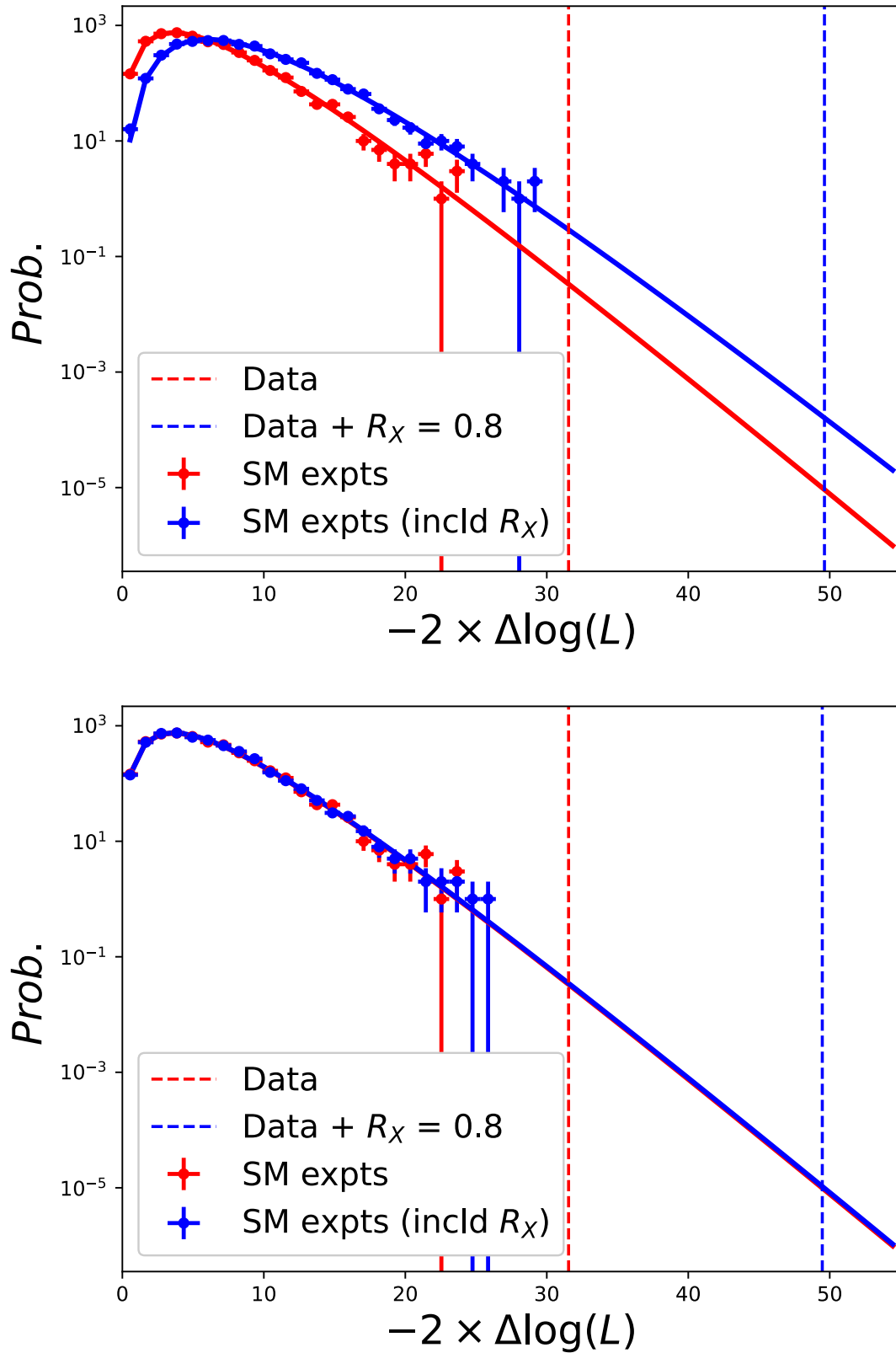


Fig. 5.3 Distribution of the likelihood ratio for pseudo-experiments under the SM hypothesis along with the value obtained from data. The distribution is overlaid with a scenario including hypothetical non-exclusive R_X measurements along with their expected sensitivities (blue). An azimov dataset [27] is used to estimate the expectation value for the significance.

References

- [1] Aaboud, M. et al. (2019). Study of the rare decays of B_s^0 and B^0 mesons into muon pairs using data collected during 2015 and 2016 with the ATLAS detector. *JHEP*, 04:098.
- [2] Aaij, R. et al. (2013). Measurement of Form-Factor-Independent Observables in the Decay $B^0 \rightarrow K^{*0} \mu^+ \mu^-$. *Phys. Rev. Lett.*, 111:191801.
- [3] Aaij, R. et al. (2014a). Differential branching fractions and isospin asymmetries of $B \rightarrow K^{(*)} \mu^+ \mu^-$ decays. *JHEP*, 06:133.
- [4] Aaij, R. et al. (2014b). First observations of the rare decays $B^+ \rightarrow K^+ \pi^+ \pi^- \mu^+ \mu^-$ and $B^+ \rightarrow \phi K^+ \mu^+ \mu^-$. *JHEP*, 10:064.
- [5] Aaij, R. et al. (2014c). Test of lepton universality using $B^+ \rightarrow K^+ \ell^+ \ell^-$ decays. *Phys. Rev. Lett.*, 113:151601.
- [6] Aaij, R. et al. (2016a). Angular analysis of the $B^0 \rightarrow K^{*0} \mu^+ \mu^-$ decay using 3 fb^{-1} of integrated luminosity. *JHEP*, 02:104.
- [7] Aaij, R. et al. (2016b). Differential branching fraction and angular moments analysis of the decay $B^0 \rightarrow K^+ \pi^- \mu^+ \mu^-$ in the $K_{0,2}^*(1430)^0$ region. *JHEP*, 12:065.
- [8] Aaij, R. et al. (2016c). Measurements of the S-wave fraction in $B^0 \rightarrow K^+ \pi^- \mu^+ \mu^-$ decays and the $B^0 \rightarrow K^*(892)^0 \mu^+ \mu^-$ differential branching fraction. *JHEP*, 11:047. [Erratum: *JHEP* 04, 142 (2017)].
- [9] Aaij, R. et al. (2016d). Measurements of the S-wave fraction in $B^0 \rightarrow K^+ \pi^- \mu^+ \mu^-$ decays and the $B^0 \rightarrow K^*(892)^0 \mu^+ \mu^-$ differential branching fraction. *JHEP*, 11:047. [Erratum: *JHEP* 04, 142 (2017)].
- [10] Aaij, R. et al. (2017a). Test of lepton universality with $B^0 \rightarrow K^{*0} \ell^+ \ell^-$ decays. *JHEP*, 08:055.

- [11] Aaij, R. et al. (2017b). Test of lepton universality with $B^0 \rightarrow K^{*0}\ell^+\ell^-$ decays. *JHEP*, 08:055.
- [12] Aaij, R. et al. (2019). Search for lepton-universality violation in $B^+ \rightarrow K^+\ell^+\ell^-$ decays. *Phys. Rev. Lett.*, 122(19):191801.
- [13] Aaij, R. et al. (2020a). Angular analysis of the $B^+ \rightarrow K^{*+}\mu^+\mu^-$ decay.
- [14] Aaij, R. et al. (2020b). Measurement of CP -Averaged Observables in the $B^0 \rightarrow K^{*0}\mu^+\mu^-$ Decay. *Phys. Rev. Lett.*, 125(1):011802.
- [15] Aaij, R. et al. (2020c). Strong constraints on the $b \rightarrow s\gamma$ photon polarisation from $B^0 \rightarrow K^{*0}e^+e^-$ decays. *JHEP*, 12:081.
- [16] Aaij, R. et al. (2020d). Test of lepton universality with $\Lambda_b^0 \rightarrow pK^-\ell^+\ell^-$ decays. *JHEP*, 05:040.
- [17] Aaij, R. et al. (2021a). Analysis of neutral B -meson decays into two muons.
- [18] Aaij, R. et al. (2021b). Branching fraction measurements of the rare $B_s^0 \rightarrow \phi\mu^+\mu^-$ and $B_s^0 \rightarrow f_2'(1525)\mu^+\mu^-$ decays.
- [19] Aaij, R. et al. (2021c). Measurement of the $B_s^0 \rightarrow \mu^+\mu^-$ decay properties and search for the $B^0 \rightarrow \mu^+\mu^-$ and $B_s^0 \rightarrow \mu^+\mu^-\gamma$ decays.
- [20] Aaij, R. et al. (2021d). Test of lepton universality in beauty-quark decays.
- [21] Algueró, M., Capdevila, B., Descotes-Genon, S., Matias, J., and Novoa-Brunet, M. (2021). $\mathbf{b} \rightarrow \mathbf{s}\ell\ell$ global fits after moriond 2021 results.
- [22] Altmannshofer, W. and Stangl, P. (2021). New Physics in Rare B Decays after Moriond 2021.
- [23] Beneke, M., Bobeth, C., and Szafron, R. (2019). Power-enhanced leading-logarithmic QED corrections to $B_q \rightarrow \mu^+\mu^-$. *JHEP*, 10:232.
- [24] Bordone, M., Isidori, G., and Pattori, A. (2016). On the Standard Model predictions for R_K and R_{K^*} . *Eur. Phys. J. C*, 76(8):440.
- [25] Ciuchini, M., Fedele, M., Franco, E., Paul, A., Silvestrini, L., and Valli, M. (2021). Lessons from the $B^{0,+} \rightarrow K^{*0,+}\mu^+\mu^-$ angular analyses. *Phys. Rev. D*, 103(1):015030.

- [26] Cornella, C., Faroughy, D. A., Fuentes-Martín, J., Isidori, G., and Neubert, M. (2021). Reading the footprints of the B-meson flavor anomalies.
- [27] Cowan, G., Cranmer, K., Gross, E., and Vitells, O. (2011). Asymptotic formulae for likelihood-based tests of new physics. *Eur. Phys. J. C*, 71:1554. [Erratum: *Eur.Phys.J.C* 73, 2501 (2013)].
- [28] Fuentes-Martín, J., Isidori, G., Pagès, J., and Yamamoto, K. (2020). With or without U(2)? Probing non-standard flavor and helicity structures in semileptonic B decays. *Phys. Lett. B*, 800:135080.
- [29] Geng, L.-S., Grinstein, B., Jäger, S., Li, S.-Y., Martin Camalich, J., and Shi, R.-X. (2021). Implications of new evidence for lepton-universality violation in $b \rightarrow sl^+\ell^-$ decays.
- [30] Hiller, G. and Kruger, F. (2004). More model-independent analysis of $b \rightarrow s$ processes. *Phys. Rev. D*, 69:074020.
- [31] Hiller, G. and Schmaltz, M. (2015). Diagnosing lepton-nonuniversality in $b \rightarrow s\ell\ell$. *JHEP*, 02:055.
- [32] Hurth, T., Mahmoudi, F., Santos, D. M., and Neshatpour, S. (2021). More Indications for Lepton Nonuniversality in $b \rightarrow sl^+\ell^-$.
- [33] Isidori, G., Lancierini, D., Owen, P., and Serra, N. (2021). On the significance of new physics in $b \rightarrow sl^+\ell^-$ decays. *Phys. Lett. B*, 822:136644.
- [34] Isidori, G., Nabeebaccus, S., and Zwicky, R. (2020). QED corrections in $\bar{B} \rightarrow \bar{K}\ell^+\ell^-$ at the double-differential level. *JHEP*, 12:104.
- [35] Khachatryan, V. et al. (2015). Observation of the rare $B_s^0 \rightarrow \mu^+\mu^-$ decay from the combined analysis of CMS and LHCb data. *Nature*, 522:68–72.
- [36] Lisovskyi, V. (2019). Study of rare b -baryon decays and test of lepton universality at LHCb. Presented 09 Sep 2019.
- [37] Lu, C.-D. and Wang, W. (2012). Analysis of $B \rightarrow K_j^*(\rightarrow K\pi)\mu^+\mu^-$ in the higher kaon resonance region. *Phys. Rev. D*, 85:034014.
- [38] Sirunyan, A. M. et al. (2020). Measurement of properties of $B_s^0 \rightarrow \mu^+\mu^-$ decays and search for $B^0 \rightarrow \mu^+\mu^-$ with the CMS experiment. *JHEP*, 04:188.

- [39] Straub, D. M. (2018). `flavio`: a Python package for flavour and precision phenomenology in the Standard Model and beyond.

Conclusions

*Not only is the Universe stranger
than we imagine,
it is stranger than we can imagine.*

A. Eddington

One of the most active and promising areas of research for physics beyond the Standard Model (SM) is the Flavour sector. As discussed throughout this dissertation, $b \rightarrow s\ell^+\ell^-$ decays to light leptons provide crucial insight on possible deviations from precise Standard Model predictions, which are a smoking gun for New Physics effects. In this thesis both the experimental and theoretical aspects of analyses involving this class of decays have been presented, together with a pristine and general method of interpreting the global significance of results connected by the underlying $b \rightarrow s\ell^+\ell^-$ transition.

The correct modelling of effects that can mimic Lepton Flavour Universality (LFU) violation within the Standard Model is of great importance when obtaining the simulated samples needed for analyses measuring the related observables. The most important of these effects on the SM prediction of LFU probes, such as R_{H_s} of Eq. (1.100) are radiative corrections. In Chapter 2 we have shown that these are safely taken into account with the currently deployed PHOTOS software package. Moreover, our custom simulation allowed us to cross check that neglecting the interference between resonant and non-resonant modes in the simulated samples has next to no impact on the efficiencies determination, provided that the upper limit on the dielectron invariant mass window is chosen far enough from the resonance, as is currently done.

The measurement of R_K using pp collision data collected during Run I and Run II of LHCb operation was presented in Chapter 3. It is the most precise measurement of a LFU sensitive probe, and the first one exhibiting a 3σ deviation with respect to the SM expectation. The measured value, combined with previous measurements of the decay rate of $B^+ \rightarrow K^+e^+e^-$ indicate a deficit of the same decay rate proceeding

to muons in the final state, in line with the set of deviations in $b \rightarrow s\ell^+\ell^-$ branching fractions presented in Chapter ???. As opposed to those, however, this result is not affected by potentially underestimated hadronic uncertainties as they cancel out in the SM prediction of the ratio of $b \rightarrow s\ell^+\ell^-$ branching fractions.

A method to evaluate the Look Elsewhere Effect (LEE) for the set of anomalies in $b \rightarrow s\ell^+\ell^-$ decays was introduced for the first time in Chapter 4. This not only allows to calculate the global significance of the hypothesis of New Physics in $b \rightarrow s\ell^+\ell^-$ decays of short-distance origin but also to adopt a very conservative approach towards theory uncertainties arising from long-distance effects such as charm-loop mediated decays. Including the latest LFU measurements of R_{K,K^*} , together with results from $B^0 \rightarrow K^{*0}\mu^+\mu^-$ angular analysis results and information on the $B_s \rightarrow \mu^+\mu^-$ decay rate, a significance of 4 standard deviations is obtained.

Finally, a general expression for R_{H_s} in terms of Wilson Coefficients and hadronic nuisance parameter, was presented in Chapter 5. It allows to extend the set of observables included in the global significance estimate to those for which the form factors are still unknown. The measurement of R_{pK} is hence included for the first time in the determination of a combined significance of the New Physics hypothesis, together with different scenarios obtained by including the planned measurements of R_{pK} , $R_{K\pi}$ and $R_{K\pi\pi}$, proving their drastic discovery potential.

Rare $b \rightarrow s\ell^+\ell^-$ transitions are an important resource and physics laboratory for advancing our understanding of the flavour structure of the Standard Model, and ultimately of New Physics. The LHC and LHCb experiments are an ideal environment to perform such compelling measurements, and the full potential of the dataset collected until now has not been still fully exploited. Several measurements are being performed at the time of writing, such as the angular $B^0 \rightarrow K^{*0}e^+e^-$ analysis which is of crucial importance in disentangling the P'_5 anomaly observed in the muons from a sheer SM effect. Of great relevance are also the efforts in setting an upper limit to the $B^0 \rightarrow K^{*0}\tau^+\tau^-$ branching fractions, due to the fact that most credited models conceived to explain the anomalies predict a stronger coupling of NP mediators to the heavier fermion families. Results from other LFU observables are also awaited exploiting the full dataset collected at LHCb, such as $R_{K\pi}$ and $R_{K\pi\pi}$, or in the high dilepton invariant mass region, such as R_K and R_{K^*} at high q^2 , and the cross check of our understanding of the efficiencies at low dilepton invariant mass, $R_{\phi\pi}$.

This is a placeholder for the dedication

